Investigating spinal biomechanics and mechanobiology to predict disease progression and treatment effects in oncology patients.

Fiona Gibson

A thesis submitted in partial fulfilment of the requirements for the degree of Doctor of Philosophy

The University of Sheffield

Faculty of Engineering

School of Mechanical Aerospace and Civil Engineering

February 2025

ACKNOWLEDGEMENTS

I would first like to thank my supervisor Stefaan Verbruggen for giving me the opportunity to work on this project and the unwavering support throughout my PhD. Thank you also to my supervisors here in Sheffield, Xinshan Li and Enrico Dall'Ara, for the guidance and always insightful conversations.

I would also like to thank all my colleagues who have contributed in many different ways to the development of this PhD. Thank you to Prof. Julia Shelton for developing the ideas for the project with Stefaan and your continuous positivity towards my work. Thank you to Sean Molloy and Prashant Thayaparan at the Royal National Orthopaedic Hospital for collating and providing the myeloma CT data. Thank you to Dr Margaret Paggiosi and Prof. Janet Brown for the collection and permission to use the ANTELOPE database. Thank you to Dr Rebecca Andrews, Dr Michelle Lawson and Dr Andrew Chantry for providing the CT and biomarker dataset, and particularly Becky for always being so enthusiastic about our collaboration and work. Moreover, a massive thank you to all my colleagues and friends in Insigneo for being there for me when I needed it.

I would also like to thank my family; without their support it would have been much harder to complete this work. Another person I could not have done this without is my partner, Will, who never failed to raise my spirits and constantly tell me I am good enough. The final year of my PhD was particularly difficult losing my Grandma and Grandad, both of you have always been there for me, I hope I have done you proud.

Finally, I would like to acknowledge my funding from the ESPRC. Additionally, I would like to acknowledge Springer, Elsevier, World Scientific, Openstax, The Editors of Encyclopaedia Britannica, The AO Foundation, World Scientific and Dovepress for the use of their figures and images.

ABSTRACT

Primary cancers, such as prostate cancer and multiple myeloma (MM), frequently metastasise to the skeleton, disrupting bone remodelling, reducing vertebral strength, and increasing fracture risk. As treatments extend survival, more patients are living with structurally compromised vertebrae. To assess the vertebral strength in cancer patients using clinical CT scans, a finite element (FE) pipeline was first developed. Its development highlighted the impact of image quality on segmentation reproducibility and showed comparable results between phantom and phantomless calibration methods.

In Chapter 4, the effect of androgen deprivation therapy (ADT) on vertebral strength in prostate cancer patients was investigated using a combination of DXA-derived areal bone mineral density (aBMD), CT-derived volumetric BMD (vBMD), and mechanical properties from the FE pipeline. Significant reductions in densitometric and mechanical properties were found after 12 months of ADT. Furthermore, vBMD outperformed aBMD in predicting vertebral strength, suggesting that these clinically accessible measures may better assess fracture risk.

Chapter 5 applied the FE pipeline to MM patients treated non-surgically. Changes in CT-derived densitometric and FE-derived mechanical properties over time were quantified. In vertebrae with large lesions (>50% of the vertebral body), remineralisation around the lesion was observed, resulting in increased strength. To investigate the mechanisms behind this, a mechanobiological model was developed in Chapter 6. This multi-scale model combined organ-level FE simulations with a cell-level bone adaptation algorithm and was optimised for each patient. While the model accurately predicted mineral and strength changes in vertebrae with smaller lesions, it failed in vertebrae with extensive lesions, suggesting that standard bone remodelling principles are insufficient in myeloma-affected bone. Additionally, its reliance on longitudinal scans limited its prospective use.

To enable prospective use, Chapter 7's pilot study incorporated serum bone turnover markers at 1, 2, and 3 months into the mechanobiological model, allowing for successful prediction of 12-month mechanical outcomes in 3 out of 5 patients from baseline imaging alone. This biomarker-informed model marks the first use of biomarkers to drive personalised vertebral strength prediction. Together, these innovations offer a foundation for improved treatment monitoring, early fracture risk prediction, and decision-making in metastatic bone disease.

PUBLICATIONS

Journal Articles

- Gibson F, Paggiosi, A, Handforth C, Brown J E, Li X, Dall'Ara E, Verbruggen S (2024) "Altered vertebral biomechanical properties in prostate cancer patients following androgen deprivation therapy", *Bone, 195:117465* https://doi.org/10.1016/j.bone.2025.117465
- Gibson F, Andrews R, Lawson S, Chantry A, Shelton J, Paggiosi A, Handforth C, Brown J E, Thayaparan P, Molloy S, Shelton J, Li X, Dall'Ara E, Verbruggen S "Patient specific computational prediction of vertebral bone changes in patients with multiple myeloma", *In preparation*

Conference Presentations

Peer Reviewed International Conferences

- Poster presentation at the Annual meeting of the Cancer and Bone Society, Sheffield, UK, July 2024
- Podium presentation at the 29th Annual Conference of the European Society of Biomechanics, Edinburgh, UK, July 2024
- Poster presentation at the Orthopaedic Research Society, Long Beach, Los Angeles, USA, February 2024
- Poster and Podium presentation at the Annual meeting of the European Calcified Tissue Conference, Liverpool, UK, April 2023
- Podium presentation at the 11th Annual Meeting of the European Solid Mechanics Conference, Galway, Ireland, July 2022 – Awarded the Young Female Investigator Award

Peer Reviewed National Conferences

- Podium presentation at the Annual conference of the British Orthopaedic Research Society, Sheffield, UK, July 2024 – Runner up for the Young Investigator Award
- Poster presentation at the Annual meeting of the Association of Biomedical Engineers, Medical Engineers and Bioengineers, London, UK, September 2024

- Podium presentation at the Annual conference of the Bone Research Society, Sheffield, UK, July 2024 – Awarded the Young Investigator Award
- Podium presentation at the Annual meeting of the Insigneo Showcase, Sheffield, UK, July 2023
- Poster presentation at the Annual conference of the Bone Research Society, Sheffield, UK, April 2023
- Podium presentation at the Mellanby Centre Annual Research Day, Sheffield, UK, March 2023

NOMENCLATURE

Greek Letters

ε	Strain
σ	Stress
ρ	Density

Acronyms

ADT	Androgen Deprivation Therapy
BAFF	Activin A and B-cell activating factor
BMC	Bone Mineral Content
BMD	Bone Mineral Density
BMSC	Bone Marrow Stromal Cells
BTM	Bone Turnover Marker
CSA	Cross Sectional Area
CTX	Carboxy Terminal Collagen Crosslinks
DcR3	Decoy receptor 3
DKK1	dickkopf-1
DOF	Degrees of Freedom
DXA	Dual Energy X-rays Absorptiometry
ES	Erector Spinae
FE	Finite Element
HU	Hounsfield Unit
HR-pQCT	High Resolution peripheral Quantitative Computed Tomography
IL-6/IL-7	Interleukin-6/ Interleukin-7

IM	Internal Material
MM	Multiple Myeloma
MMP	Matrix Metalloproteinase
MRI	Magnetic Resonance Imaging
MSC	Mesenchymal Stem Cell
OPG	Osteoprotegerin
P1NP	Procollagen 1 N-terminal Propeptive
PCa	Prostate Cancer
PTH	Parathyroid Hormone
QCT	Quantitative Computed Tomography
RANK	Receptor activator of nuclear factor kappa-B
RANKL	Receptor activator of nuclear factor kappa-B ligand
ROI	Region of Interest
SAT	Subcutaneous Adipose Tissue
SED	Strain Energy Density
TGF-β	Transforming Growth Factor-beta
TLSO	Thoracolumbar sacral orthoses
TNF	Tumour Necrosis Factor
3D	Three-dimensional

TABLE OF CONTENTS

1 INTRODUCTION

Bone is a highly dynamic tissue that continuously remodels in response to mechanical stimulation and biochemical cues. This process is crucial for maintaining skeletal integrity, adapting to mechanical loads, and repairing microdamage (Cowin, 2001). However, in the presence of disease, particularly cancer, bone homeostasis can be severely disrupted (Bussard, Gay and Mastro, 2008). Metastatic cancers commonly affect the skeleton, leading to either osteolytic lesions, where more bone is resorbed than formed (Suva, Griffin and Makhoul, 2009), or osteoblastic lesions, where excessive, disorganised bone is formed (Macedo *et al.*, 2017). These changes significantly weaken the structural integrity of bone, increasing the risk of fractures and other skeletal complications (Mercadante, 1997). Understanding how different cancers and their treatments influence bone remodelling is essential for improving patient management and therapeutic strategies.

Prostate cancer (PCa) is the second most common cancer among men with approximately 26.5% of the male population having been diagnosed with prostate cancer worldwide (Wong *et al.*, 2019). Androgen deprivation therapy (ADT) is the most common treatment for advanced disease due to the role of the androgen receptor signalling pathway in prostate cancer development (El Badri, Salawu and Brown, 2019). When ADT is administered, the levels of testosterone and oestradiol fall rapidly and significantly, leading to dysregulated bone remodelling. This in turn causes a decrease in bone mineral density (BMD) and bone integrity whilst increasing fracture risk. The correlation of fractures with ADT in PCa patients was evaluated by three large retrospective studies that reported these patients having a 21-37% higher risk of fracture compared to PCa patients who were not treated with ADT (Shahinian *et al.*, 2005; Smith *et al.*, 2005, 2006). Smith and colleagues, also reported that vertebral fractures were 18% more likely to occur following ADT, as well as an overall fracture risk increase of 13% (Smith *et al.*, 2006). Despite studies investigating the effect of ADT on the peripheral strength of the distal radius using HR-pQCT (High resolution peripheral QCT) (Dalla Via *et al.*, 2019), and femoral strength and fracture risk using biomechanical computed tomography (BCT) (Lin *et al.*, 2023), vertebral strength is yet to be obtained using FE models based on QCT images of vertebra. Therefore, the first hypothesis of this thesis is “The vertebral strength of prostate cancer patients reduces when ADT is administered”.

Multiple Myeloma (MM) represents around 2% of new cancers every year in the UK and the number of cases and deaths has more than doubled worldwide in the last 30 years (Zhou *et al.*, 2021). Patients with MM are most commonly affected by spinal involvement (80-90%) (Bird *et al.*, 2011) with 34-36% of patients suffering from spinal fracture (Anselmetti, Manca and Montemurro, 2012). Anti-myeloma treatments have significantly improved over the last 30 years, increasing the 5-year survival rate for patients with MM from 12 to 50% and 11 to 44% in men and women respectively (Cancer Research UK, 2014; Bird and Boyd, 2019). Nevertheless, due to the destructive nature of MM, patients are left with unstable and weak spines and therefore, most patients are still in need of intervention to stabilise the spine and prevent vertebral collapse and spinal cord damage. Surgery is currently the most common intervention. However, due to the older age of most patients at diagnosis (>70 years), surgery is associated with increased morbidity due to the frailty of MM patients (Nucci and Anaissie, 2009).

In more recent years, orthopaedic bracing has been presented as an alternative to surgery. The brace is intended to encase the whole spine, providing structural stability, and preventing movement of the spine. Case reports have shown that under treatment with bracing, bone lost by the cancer has started to 'heal' or remineralise. Remineralisation was detected in 48% of bone lesions in a study that also concluded that there was a linear relationship between radiation dose and the likelihood of remineralisation (Matuschek *et al.*, 2015). Mose et al., conducted a similar study and found remineralisation in 46.4% of patients (Mose *et al.*, 2000). A slightly lower number of patients with remineralisation (24%) was reported by Balducci et al., who also estimated the time to achieve remineralisation was around 6 months (Balducci *et al.*, 2011). This phenomenon has only been observed and reported anecdotally through clinical Computed Tomography (CT) scans, with no quantification conducted nor investigation of the effect of the remineralisation on the structural properties of the vertebra. Patient-specific models have been utilised to evaluate the mechanical properties of vertebrae that have been affected by other metastatic cancers, but as yet, no study has researched the implications of remineralisation in patients with MM on vertebral mechanics and spinal stability. Therefore, the second research hypothesis of this thesis is "The remineralisation following bracing treatment for MM patients leads to an increase in vertebral strength".

Key to the ability of bone to heal and remineralise is mechanobiology, the study of how mechanical forces influence cellular behaviour and tissue adaptation. In bone, mechanical loading plays a critical role in maintaining mass and structure, as described by Wolff's Law (Wolff, 1892) and Frost's Mechanostat Theory (Frost, 1987). Given the challenge of investigating this phenomenon experimentally, various computational models have been developed to predict bone adaptation in response to different mechanical environments, particularly in conditions such as osteoporosis (Lerebours *et al.*, 2016; Martin *et al.*, 2020). However, the application of mechanobiological principles to MM remains largely unexplored. Given that bracing alters the mechanical environment of the spine, it is possible that the observed increase in mineralisation in MM vertebrae results from mechanical stimulation. However, the bracing could also just be acting as a support to ensure there is no fracture, while biological responses influenced by the myeloma cells are what is driving the remineralisation. Understanding this response through a mechanobiological lens could provide valuable insights into how myeloma-affected bone adapts to external mechanical interventions and whether similar mechanisms to those observed in other bone pathologies apply to this condition. Therefore, the third research hypothesis of this thesis is "Normal mechanobiology principles cannot explain the bone changes in MM patients' vertebrae treated non-surgically".

Bone turnover markers (BTMs) play a crucial clinical role in assessing bone metabolism and predicting changes in fracture risk (Vasikaran *et al.*, 2011). Markers of bone formation, such as procollagen type 1 N-terminal propeptide (P1NP), provide insight into osteoblastic activity, while markers of bone resorption, including Carboxy Terminal Collagen Crosslinks (CTX), reflect osteoclastic activity (Kuo and Chen, 2017). These biochemical indicators are widely used in conditions like osteoporosis to monitor treatment efficacy and disease progression (Kuo and Chen, 2017). In MM, where bone remodelling is profoundly dysregulated, incorporating such BTMs could help elucidate the mechanisms driving mineralisation changes. By combining biomarker analysis with mechanobiological models, it may be possible to improve predictions of bone adaptation in MM vertebrae, ultimately informing more effective treatment strategies. Therefore, the final hypothesis of this thesis is "Mechanobiological models incorporating bone turnover markers can predict bone changes in vertebrae of patients with multiple myeloma".

1.1 Objectives and Hypothesis

The overall aim of this thesis was to understand the biomechanical changes in vertebra with metastatic and non-metastatic cancer. The first specific objective was to develop patient-specific computational FE models to determine biomechanical stability of vertebrae in patients with cancer. The secondary specific objective was to apply the FE pipeline to a dataset of longitudinal CT scans of prostate cancer treated with ADT and of MM patients treated with orthopaedic bracing. The third specific objective was to develop adaptive FE model to predict spatio-temporal bone structure post-anti-cancer treatment of MM based on understanding of cancer cell regulation of mechanobiology. These objectives will address four hypotheses, each of which will aim to fill the identified gaps in the literature and underpin the research of Chapters 4-7 of this thesis.

Hypothesis 1: “The vertebral strength of prostate cancer patients reduces when ADT is administered”

Hypothesis 2: “The remineralisation following bracing treatment for MM patients leads to an increase in vertebral strength”

Hypothesis 3: “Normal mechanobiology principles cannot explain the bone changes in MM patients' vertebrae treated non-surgically”

Hypothesis 4: "Mechanobiological models incorporating bone turnover markers can predict bone changes in vertebrae of patients with multiple myeloma"

1.2 Thesis Outline

This thesis comprises the work completed for the duration of the candidate's PhD studies. First, a thorough review of the background and literature is presented in Chapter 2, outlining the hierarchal structure of bone and its mechanical properties, multiple myeloma and prostate cancer and their effect on bone, current treatment strategies for MM and their advantages and disadvantages, the FE method, the current state of the art in treatment and prediction of vertebral strength in metastatic patients, as well as predictive models of bone remodelling, highlighting the gap within the literature and motivation behind the studies in this thesis. Chapter 3 then uses the methodologies described in Chapter 2 to develop a finite element pipeline from clinical CT images of vertebrae. Chapter 4 reports the application of

the FE method (described in Chapter 3) to a dataset of PCa patients treated with ADT, testing Hypothesis 1. Chapter 5 then investigates Hypothesis 2 by applying the FE method in Chapter 3 to a dataset of MM patients' vertebrae, treated non-surgically. The development of a mechanobiological model to predict bone changes in MM vertebra is then detailed in Chapter 6 to evaluate Hypothesis 3. The incorporation of biomarkers into the mechanobiological model to improve the prediction of bone changes is then assessed in Chapter 7, evaluating Hypothesis 4. Finally, Chapter 8 summarises the key findings, putting them in the context of current assessment of vertebral biomechanics, cancer and mechanobiology, along with recommendations for future research in these fields.

2 BACKGROUND AND LITERATURE REVIEW

2.1 Bone Anatomy

The human skeleton provides structural support and protection of internal organs, permits movement and maintains a constant environment for haematopoiesis within the marrow (Taichman, 2005). Bone is composed of 50-70% inorganic mineral content, of which hydroxyapatite [$Ca_{10}(PO_4)_6(OH)_2$] is the most abundant, and 20-40% organic matrix which contains approximately 90% type-1 collagen and 5-10% water (Clarke, 2008). The adult human skeleton is composed of 80% cortical bone and 20% trabecular bone (Figure 2.1) (Ott, 2018). Cortical and trabecular bone are usually formed in a lamellar pattern where the collagen fibres are stacked unidirectionally in alternating orientations (Keaveny, Morgan and Yeh, 2004). Cortical bone is the dense outer layer where the lamellae are tightly packed and formed into concentric rings measuring approximately 200µm in width (Dahl and Thompson, 2011). In contrast, trabecular bone is a highly porous bone tissue in which the lamellae form a network of rod or plate shapes that are around 100µm to 300µm thick (Keaveny, Morgan and Yeh, 2004).

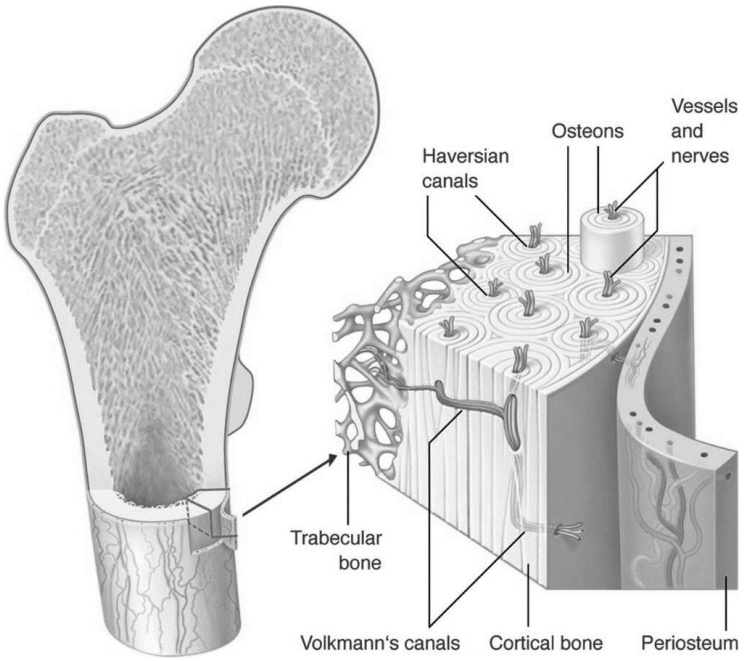

Figure 2.1 - Structure of a femoral bone from the organ level to the tissue level. A zoom in of a portion of cortical and trabecular bone. (Bartl and Bartl, 2019)

2.1.1 The Human Vertebra

The vertebral column has various functions: (i) providing structural support to the skull and trunk whilst allowing their movement; (ii) providing protection of the spinal cord; (iii) absorbing the stresses produced by walking and lifting and (iv) providing attachment for the limbs, ribs and muscles whilst facilitating coordinated movement (Saladin, Gan and Cushman, 2017). The spine is divided anatomically into 5 sections, as shown in Figure 2.2: (a) the cervical (neck) section consists of 7 vertebrae (C1-C7) with a primary function of head support and allowing a wide range of motion of the head (Bogduk and Mercer, 2000), (b) the thoracic section consists of 12 vertebrae (T1-T12) and connects to the rib cage, protecting vital organs in the chest (Edmondston and Singer, 1997), (c) the lumbar section contains 5 vertebrae (L1-L5) and bears the majority of the body weight whilst allowing for flexibility and movement in the lower back (Boszczyk, Boszczyk and Putz, 2001), (d) the sacrum which consists of five fused vertebra (S1-S5) which connects the trunk to the lower body (Agur, Dalley and Grant, 2013) and (e) the coccyx which consists of three to five fused vertebrae connected to the bottom of

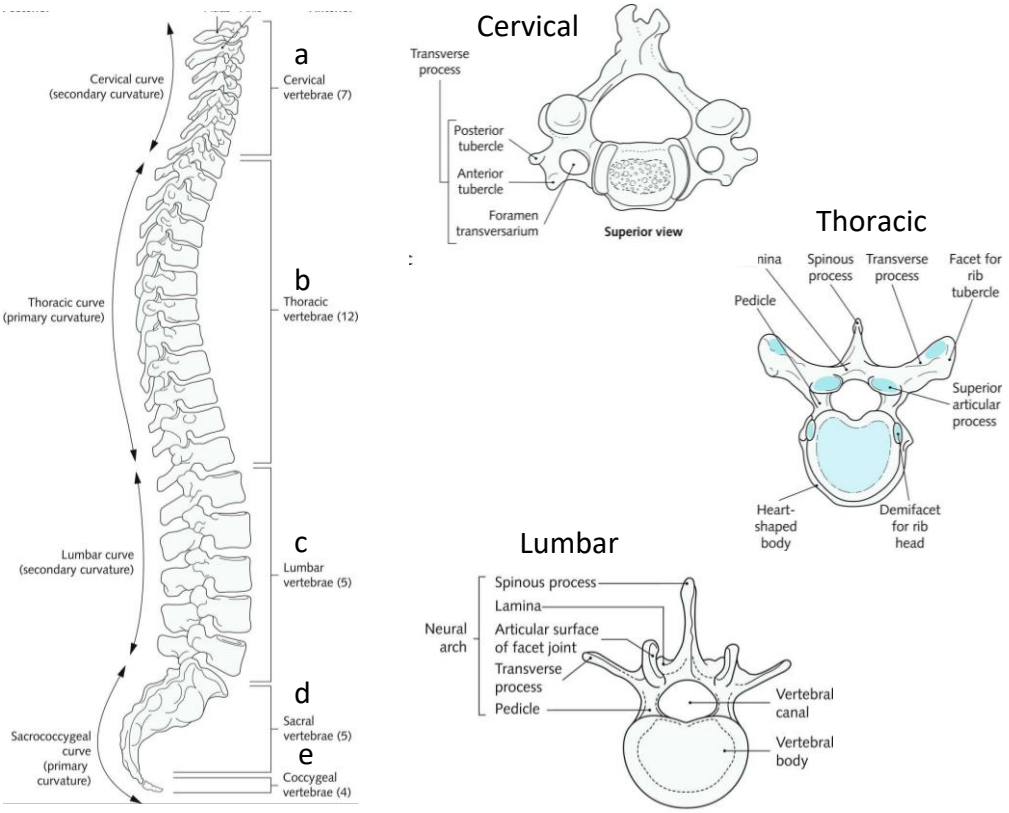

Figure 2.2 - The vertebral column (left) and the three types of vertebrae (right) (a) cervical, (b) thoracic and (c) lumbar modified with permission from (Hall and Stephens, 2018)

the sacrum with its main function to support and stabilise the body whilst in a sitting position (Lirette *et al.*, 2014). Each of these regions is composed of several vertebral bodies connected by intervertebral discs and facet joints (Figure 2.2). Vertebral bodies are comprised of a thin outer layer of cortical bone, which varies from 268µm to 329µm in thickness (Ritzel *et al.*, 1997), that encloses an inner area of trabecular bone (mean trabecular thickness: 100 µm to 400 µm) (Bevill and Keaveny, 2009). The vertebral body is composed of about 25% cortical bone and 75% trabecular bone (Clarke, 2008). From the vertebral body, spinous and transverse processes along with various facets make up the rest of a vertebrae. Within the thoracic region, T1-10, the transverse facets at the end of the transverse processes provide a second point of attachment and articulation for the ribs. The arrangement of the superior and inferior processes in the lumbar vertebra also provides a high resistance to twisting (Saladin, Gan and Cushman, 2017).

2.2 Bone Tissue

There are two main types of bone tissue: cortical and trabecular. In long bones, cortical bone consists of concentric lamellae connected by canaliculi which surround a central (Haversian) canal (Saladin, Gan and Cushman, 2017). The main structural unit for cortical bone is an osteon which consists of the lamellae and central canal (Saladin, Gan and Cushman, 2017). Osteocytes reside in the small spaces between the individual lamellae (lacunae) and are arranged circumferentially around the central canal and connected by fine canaliculi to allow for osteocyte communication (Mellon and Tanner, 2012). The haversian canals accommodate a microvascular network, essential for blood supply to the osteocytes (Cowin, Moss-Salentijn

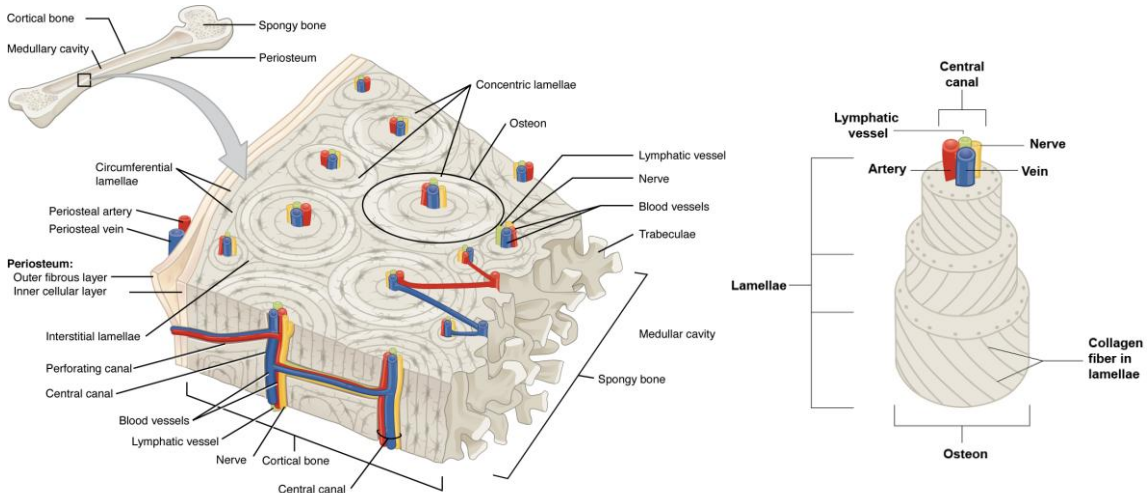

Figure 2.3 - Organisation of cortical bone and an osteon in long bones (Betts *et al.*, 2022)

and Moss, 1991). Collagen fibres are arranged in a 'corkscrew' around each individual lamellae, alternating in direction around adjacent lamellae. This orientation enhances the strength of bone. Cortical bone provides a higher resistance to compression than tension (percentage strength-to-modulus ratio is around 1.12 for longitudinal compression and 0.78 for tension) (Keaveny, Morgan and Yeh, 1981). Cortical bones' Young's Modulus varies between 7 and 25 GPa depending on orientation, age, disease and other contributing factors (Bonfield and Datta, 1974; Currey, 1979).

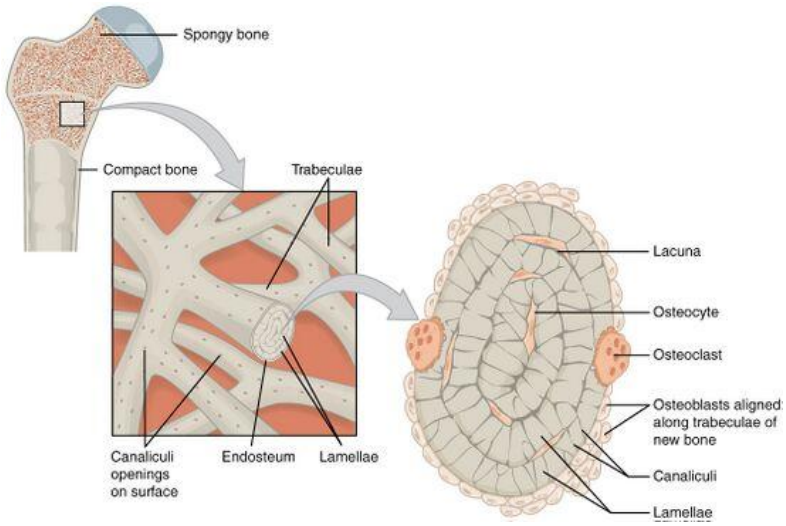

Figure 2.4 - Where the bone cells reside within the bone (Betts *et al.*, 2022)

Trabecular bone consists of rodlike structures arranged in a lattice, which is permeated by spaces filled with bone marrow (Saladin, Gan and Cushman, 2017). Osteocytes are arranged concentrically, residing between lamellae. Unlike cortical bone, trabecular bone does not need a central canal for the supply of blood as the osteocytes are close enough to the blood supply within the bone marrow (Mellon and Tanner, 2012). The structure of trabecular bone is not random and is formed along the lines of highest stress within the bone (Saladin, Gan and Cushman, 2017). Trabecular bone, being a more porous material, has a lower Young's Modulus which varies from 0.6 to 2 GPa depending on the orientation of loading (Ashman and Jae Young Rho, 1988; Keaveny *et al.*, 1993).

Bone tissue contains four types of cells: osteoblasts, osteocytes, bone lining cells and osteoclasts. Osteocytes are derived from mature osteoblasts, osteoblasts develop from mesenchymal stromal cells (osteoprogenitor cells), while osteoclasts come from haemopoietic stem cells (Downey and Siegel, 2006). Osteoblasts constitute 4-6% of the total bone cells and are known for their bone forming function (Capulli, Paone and Rucci, 2014).

They usually reside within the bone canals, endosteum and periosteum and may enter by migrating from surrounding tissue or from the blood (Mellon and Tanner, 2012). Osteocytes reside in the lacunae (spaces between the lamellae) and are formed during bone deposition by osteoblasts and make up 90% of the bone cells (Mellon and Tanner, 2012). Bone lining cells cover up to 95% of the bone surface and communicate with the osteocytes through the processes in the canalicular system (Mellon and Tanner, 2012). Osteoclasts' main function is to remove (resorb) bone and are found on the surface of bone during resorption (Figure 2.4) (Saladin, Gan and Cushman, 2017).

2.3 Bone Physiology

2.3.1 Bone Remodelling

While bone is first laid down using various bone modelling processes, in the adult skeleton, the primary physiological activity of bone is bone remodelling. Bone undergoes constant remodelling by osteoclasts and osteoblasts, whereby old bone tissue is removed and replaced by new bone tissue. The process of remodelling is crucial for maintaining the load bearing capacity of bone, the regulation of mineral homeostasis and haematopoiesis and to repair structural damage (Cowin, 2001). Remodelling sites mostly develop in a random manner but are also found to target areas that require repair (Burr, 2002). The duration of the remodelling process for cortical and trabecular bone is shown in Table 2.1 where the cycle for cortical bone is longer than that for trabecular bone.

Table 2.1 - Comparison of cortical and trabecular bone structural units (Cowin, 2001).

Parameter	Cortical	Cancellous
Length (mm)	2.5	1.0
Circumference (mm)	0.6	0.6
Wall thickness (mm)	0.075	0.040
Number/mm^3 bone volume	15	40
Total number in skeleton	21 X 10^6	14 X 10^6
Duration of resorption (days)	24	21
Duration of formation (days)	124	91
Remodelling period (days)	148	112
Bone turnover rate (%/year)	43	26

The remodelling process is controlled by three cells: osteocytes, osteoclasts, and osteoblasts (Figure 2.5). It involves a continuous cycle whereby osteocytes detect mechanical stimuli, including changes in strain magnitude or direction, activating the resorption and deposition of bone by osteoclasts and osteoblasts respectively (Cowin, 2001).

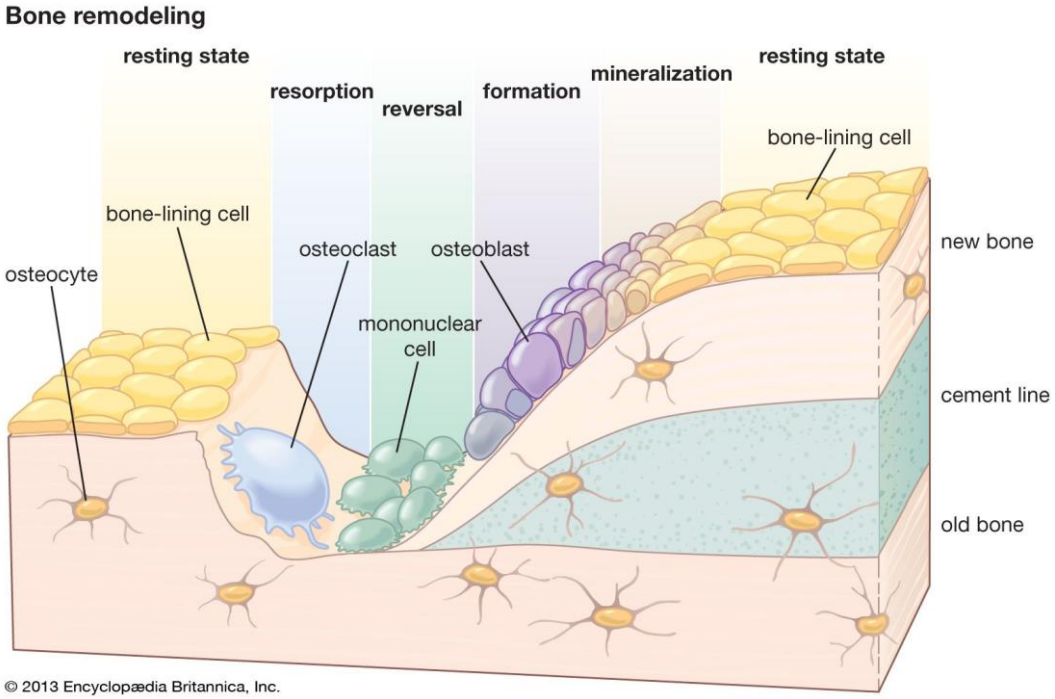

Figure 2.5 - Bone cells and the bone remodelling process (The Editors of Encyclopaedia Britannica, 2020)

Osteocytes regulate the receptor activator nuclear factor-kappa B (RANK), its ligand RANKL, and the osteoprotegerin (OPG) signalling pathway (Terpos, Christoulas and Gavriatopoulou, 2018). Osteoclast development and differentiation is determined by RANK-RANKL signalling. OPG is a decoy receptor for RANKL which intercepts the RANK-RANKL pathway, therefore reduces osteoclastogenesis. The ratio between RANKL and OPG is crucial for maintaining the appropriate number of osteoclasts for normal remodelling. An abnormal RANKL/OPG ratio has been found in both benign and malignant bone diseases (Hofbauer *et al.*, 2000). Osteocytes also regulate osteoblast activity through the secretion of cytokines: sclerostin and dickkopf-1 (DKK1). The Wnt pathway leads to the expression of osteoblastic target genes (Westendorf, Kahler and Schroeder, 2004). DKK1 binds to low density lipoprotein receptors on the surface of osteoblasts, blocking the Wnt pathway (Bonewald, 2011). Sclerostin also

inhibits the Wnt pathway. Both cytokines supress the Wnt-signalling and therefore reduce osteoblast function.

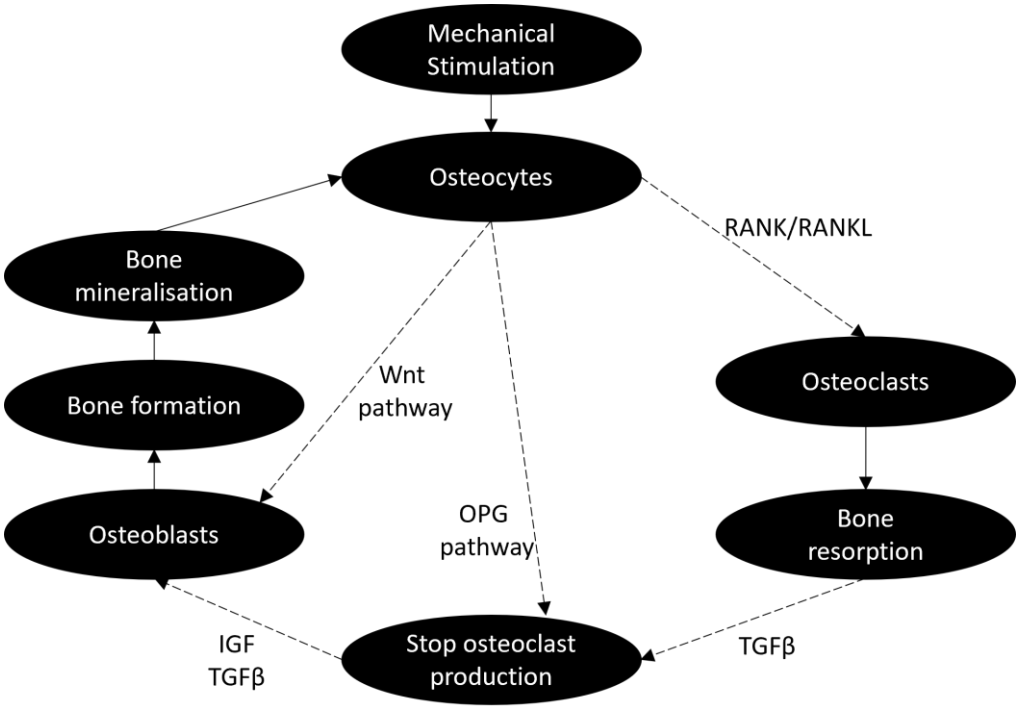

Figure 2.6 - A schematic representation of the bone remodelling process and some of the pathways that affect the resorption and deposition of bone.

2.3.2 Bone Turnover Markers

Bone turnover markers (BTMs) are released into the blood or urine following bone remodelling. Procollagen 1 N-terminal Propeptide (P1NP) is a known BTM of bone formation. When osteoblasts form bone, they produce type 1 collagen which starts as a precursor molecule, procollagen (Hlaing and Compston, 2014). When procollagen is secreted into the extracellular matrix, enzymes cleave propeptides which are extra sequences at both ends of procollagen (Hlaing and Compston, 2014). This process releases P1NP from the N-terminal end and P1CP (Procollagen Type I C-terminal Propeptide) from the C-terminal end (Burtis, 2015). P1NP is more extensively described in literature than P1CP and the use of P1NP as a reference marker for bone formation in studies evaluating fracture risk assessment and treatment response has been recommended by the International Federation of Clinical Chemistry and Laboratory Medicine (IFCC) and the International Osteoporosis Foundation (IOF) (Vasikaran *et al.*, 2011).

Carboxy terminal collagen crosslinks (CTX) has been found to be a specific and sensitive biomarker of bone resorption (Kuo and Chen, 2017) and was also recommended by the IFCC and IOF as a reference marker for bone resorption (Vasikaran *et al.*, 2011). CTX is released when the collagen matrix is degraded by enzymes such as MMP's (matrix Metalloproteinase) following bone resorption by osteoclasts (Burtis, 2015).

Sclerostin is known to be another indicator of bone turnover. Sclerostin is secreted by osteocytes, and inhibits the differentiation and proliferation of osteoblasts (Winkler *et al.*, 2003) by blocking the Wnt pathway (Moester *et al.*, 2010). While less commonly used to monitor bone turnover than CTX and P1NP, sclerostin levels have been shown clinically to reflect inhibition of bone formation (Anastasilakis *et al.*, 2013).

2.4 Bone Biomechanics

The anatomy and physiology described thus far play a significant role in establishing the mechanical behaviour of bone as a material. Bone is a heterogeneous and anisotropic material, and undergoes elastic and plastic deformation, before and after yield respectively (Hart *et al.*, 2017). The mechanical behaviour of bone can be classified into three stress-strain regions: (I) elastic region, (II) non-linear post-yield region and (III) fracture (Figure 2.7b). In region I, the bone deforms elastically and reversibly, following Hooke's Law, whereby the change in length is proportional to the load applied. Bone stiffness can be calculated as the gradient of this region on the force-displacement curve (Figure 2.7a), while normalised stiffness (modulus of elasticity, E) can be calculated as the linear slope in the equivalent stress-strain curve (Figure 2.7b). Reversibility remains until yield (σ_y), which is estimated by the 0.2% strain-offset method (Figure 2.7b, region II). Due to its ductile nature, bone plastically deforms after yield (Figure 2.7b, region II). Constitutive models, such as the Drucker-Prager and quadric yield criterion, have been used to describe the yield behaviour of bone (Schwiedrzik, 2014). Beyond yield, stress is not uniformly distributed in bone and depends on the loading direction, therefore, there is asymmetry of strength in tension and compression (Currey, 2001). Plasticity continues until it reaches its ultimate stress (σ_u), after which the process of fracture begins (Figure 2.7b, region III).

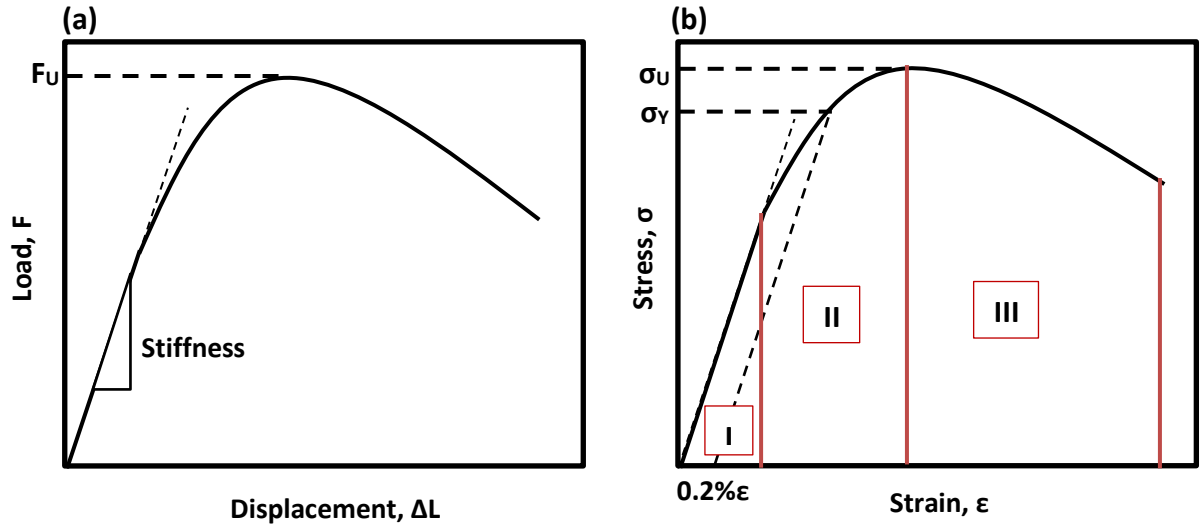

Figure 2.7 - (a) Typical load-displacement curve and (b) normalised stress-strain curve of bone highlighting the three domains of the mechanical behaviour of bones: (I) elastic, (II) post-yield, and (III) fracture

Bone density and microstructure in both cortical and trabecular bone vary due to factors such as age, gender, disease and anatomical site (Cowin, 2001). At organ scale, these differences affect the mechanical response of bone under loading (Pahr and Zysset, 2009). Bone mass, geometric tissue distribution and material properties are known to directly influence bone stiffness and strength (Cole and Van Der Meulen, 2011). Material properties of bone are not uniform across the population and therefore computational studies, such as those planned in this thesis, must account for these variations by applying patient specific properties. Material mapping is often conducted using a computational software that derives bone density from CT attenuation. The density can then be converted to elastic modulus using a set of equations (see more in Section 2.6).

2.4.1 Vertebrae Biomechanics

Spinal instability has been defined as ''the loss of the ability of the spine under physiologic loads to maintain its patterns of displacement'' (White and Panjabi, 1978). The structural stability of the spine depends on vertebral architecture and bone mineral density, disc-intervertebral joints, facet joints, ligaments and anatomical curvature (Izzo *et al.*, 2013). The load-bearing ability of each vertebra depends on the size and shape, integrity of the trabecular system and bone density (Izzo *et al.*, 2013). In compression, the role of the cortical shell is substantial, carrying around 45% of the compressive load (Eswaran *et al.*, 2006). The

posterior elements are also involved in the stability of the spine as they control the direction and amplitude of movement and share the loads (Izzo *et al.*, 2013). The posterior facets usually carry up to 33% of the compressive load but can rise to 70% due to high and prolonged weight loading and disc degeneration (Dunlop, Adams and Hutton, 1984).

Axial compression and bending play the largest role in the loading of the spine. Studies have shown that, in the presence of muscles, the spine is subject to large axial compressive loads but an insignificant amount of bending due to muscle involvement (Goel *et al.*, 1995). The compressive strength of the vertebral bodies increases with distance down the spine due to the increase in size of the endplates (Brinckmann, Biggemann and Hilweg, 1989).

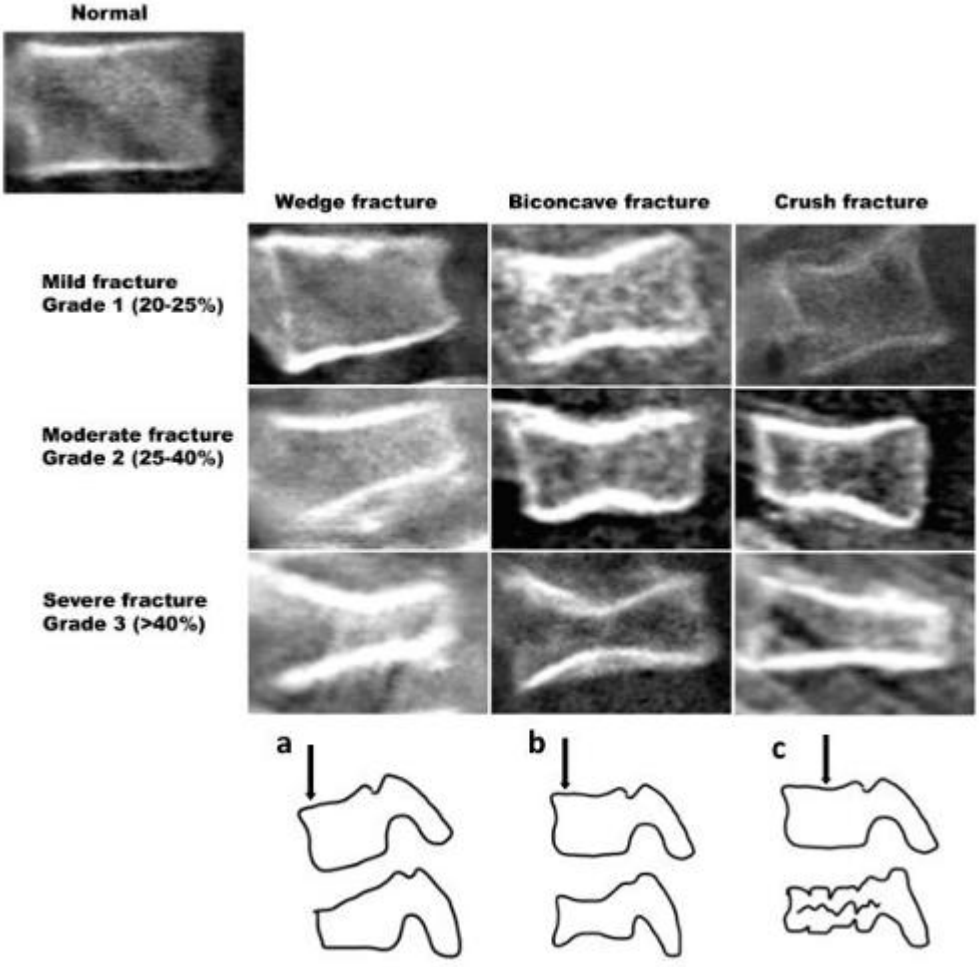

Figure 2.8 - At the top, example scans of a vertebra with multiple fractures with each fracture mode labelled with a diagram (a) wedge fracture, (b) biconcave fracture and (c) crush fracture (Alqahtani and Offiah, 2019).

Vertebral fractures occur when the applied load exceeds the strength of the vertebral body. Compression fractures account for 75% of all thoracolumbar fractures (Proudfoot, 2003). The failure pattern of compression fractures has been attributed to the variations in trabecular microstructure adjacent to the superior endplate (Hussein *et al.*, 2018). For axial compressive loading (Figure 2.8B,C), the fracture initiates more centrally on the superior endplate and progresses into a crushed or biconcave shape (Jackman *et al.*, 2015). A combination of axial compression and anterior bending (Figure 2.8A,B) induces a large deflection towards the anterior of the superior endplates, either creating a wedge fracture (A) or a biconcave shape (B) (Jackman *et al.*, 2015).

2.5 Cancer and bone metastases

Primary bone cancer, while devastating, is a rare occurrence, comprising of only 0.2% of all cancers in Europe (Gatta *et al.*, 2017). However, common primary cancers, such as breast, prostate (PCa) and multiple myeloma (MM) have a high incidence of bone metastases (Cecchini *et al.*, 2005). Metastatic disease in the skeleton is a major cause of morbidity due to severe pain, vertebral fractures and spinal cord compression (Mercadante, 1997). Hypercalcemia, an increase in calcium in the blood which correlates to a loss of mineral and weakened bones, also occurs in 5-10% of all cancer patients with advanced disease, most commonly effecting breast cancer and MM patients (Clines and Guise, 2005).

Bone metastases form when the cancer spreads from the primary site to another part of the body. Cancerous cells can travel through the bloodstream or lymphatic system to other sites, with bone being one of the most common. The spine is most affected by bone metastasis, as well as the long bones in the leg, the pelvis and the skull (Feller, Kramer and Lemmer, 2011). Prostate and breast cancer are responsible for the majority of cases, up to 70%, of the skeletal metastases (Cecchini *et al.*, 2005). There is approximately 65-75% bone involvement in advanced breast and PCa (Macedo *et al.*, 2017) in comparison to MM where bone involvement presents in 95-100% (Yee and Raje, 2018). Metastatic lytic bone lesions reduce bone strength leading to an increased risk of fracture (Confavreux *et al.*, 2021). Complications arising from these lesions, such as vertebral compression fractures, are often the cause of pain and morbidity as opposed to the primary cancer (Mansoorinasab and Abdolhoseinpour, 2018).

There are three types of bone metastases: osteolytic, osteoblastic and mixed which are classified according to the mechanism of interference with normal bone remodelling (Macedo *et al.*, 2017). Osteolytic lesions are present in multiple myeloma, breast cancer, melanoma and thyroid cancer and are characterised by the destruction of normal bone (Mundy, 2002). The bone destruction is led by an increase in osteoclast activity leaving the bone with large spaces within the extracellular matrix (Tian *et al.*, 2009). Tumour cells grow within this space, forming the lytic lesion. Osteoblastic lesions are formed due to an increase in osteoblast activity, increasing the amount of bone tissue deposited (Dai *et al.*, 2005). Osteoblastic lesions are predominantly found in PCa patients (Zhang, Jiang and Wang, 2023). Both types of metastases show evidence of increased osteoclast activity, despite the sclerotic nature of osteoblastic lesions (Mundy, 2002). In some cases, both osteolytic and osteoblastic lesions are present in the same bone, which are known as mixed lesions.

2.5.1 Prostate cancer and bone metastases

PCa is the second most common cancer among men with approximately 26.5% of the male population having been diagnosed with PCa worldwide (Wong *et al.*, 2019). The 10-year survival rate for PCa patients in the UK has tripled in the last 40 years, which can be attributed to the advances in treatment as well as early detection and screening (Cancer Research UK, 2019). Long term effects of PCa and treatments on bone health are now of increasing concern due to patients living longer with prostate cancer (El Badri, Salawu and Brown, 2019).

Androgen deprivation therapy (ADT) is the most common treatment for advanced disease due to the role of the androgen receptor signalling pathway in PCa development (El Badri, Salawu and Brown, 2019). Oestrogens, such as oestradiol, produced via aromatisation of androgens in males, influence the osteoclast activity through the regulation of the RANK/RANKL/OPG pathway (Almeida *et al.*, 2017). Androgens, such as testosterone, play a key role in bone homeostasis. When ADT is administered, the levels of testosterone and oestradiol fall rapidly and significantly, leading to dysregulated bone remodelling. This in turn causes a decrease in bone mineral density (BMD) and bone integrity whilst increasing fracture risk. The reduction in BMD has shown to be most significant in the first 12 months of ADT (Greenspan *et al.*, 2005), with the BMD progressively declining up to 10 years after commencing ADT (Kiratli *et al.*, 2001).

2.5.2 Multiple Myeloma and bone metastases

MM is a cancer of the plasma cells, a type of white blood cell that makes antibodies as part of the immune defence system. Abnormal plasma cells proliferate in the bone marrow, forming osteolytic bone lesions (Figure 2.9). In recent years, therapeutic treatments for this cancer have significantly improved leading to increased survival (Bird and Boyd, 2019). Bone fractures resulting from weakened vertebrae in the spine necessitate surgical intervention. However, surgery is associated with increased morbidity due to the frailty of MM patients, who have lower bone quality and a lower resistance to infection (Nucci and Anaissie, 2009).

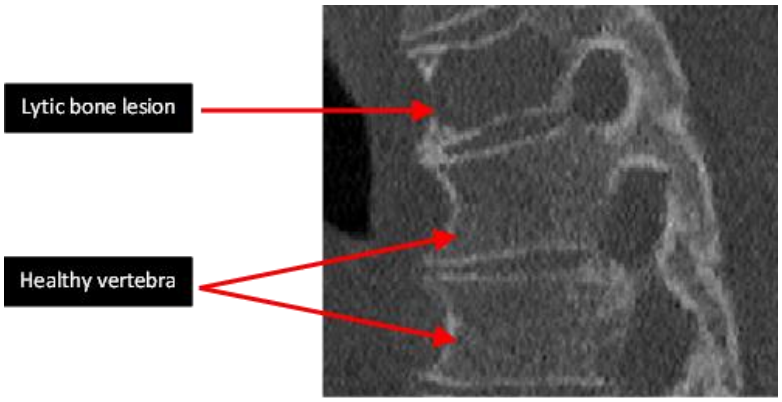

Figure 2.9 - Zoom in of a CT scan of the spine showing three vertebra, one lytic (top) and two healthy (middle and bottom).

2.5.2.1 MM Metastatic Lesion Formation

In MM patients, there is an imbalance in the remodelling cycle, whereby the osteoclast differentiation and resorption rate are increased while osteoblastogenesis is decreased (Figure 2.10). MM cells and bone marrow stromal cells (BMSCs) disrupt the bone marrow microenvironment. MM cells increase the differentiation and activation of osteoclasts by producing decoy receptor 3 (DcR3) and upregulating RANKL, IL-6, activin A and B-cell activating factor (BAFF) (Giuliani, Rizzoli and Roodman, 2006; Oranger *et al.*, 2013). The overexpression of DcR3 increases the tumour growth as it belongs to the tumour necrosis factor (TNF) receptor family (Colucci *et al.*, 2009). IL-6 increases the survival of myeloma cells by protecting them from apoptosis (Gupta *et al.*, 2001) whilst upregulating IL-7 and increasing the expression of RANKL and osteoclastogenesis (Giuliani, Rizzoli and Roodman, 2006). Activin A, in addition to activating osteoclasts, also inhibits osteoblast differentiation (Luisi *et al.*, 2001). Osteoblast differentiation is stimulated by the Wnt signalling pathway (Hameed *et al.*,

2014). In MM patients DKK1 is increased, which antagonises the Wnt pathway resulting in the inhibition of osteoblast maturation (Qiang *et al.*, 2008). The upregulation of osteoclastogenesis and downregulation of osteoblastogenesis combined with an increase in tumour growth factors creates a vicious cycle of bone destruction and tumour expansion. In contrast to cancers such as prostate and breast where the osteoblast activity also increases, no new bone is formed with MM creating a more destructive disease (Roodman, 2009).

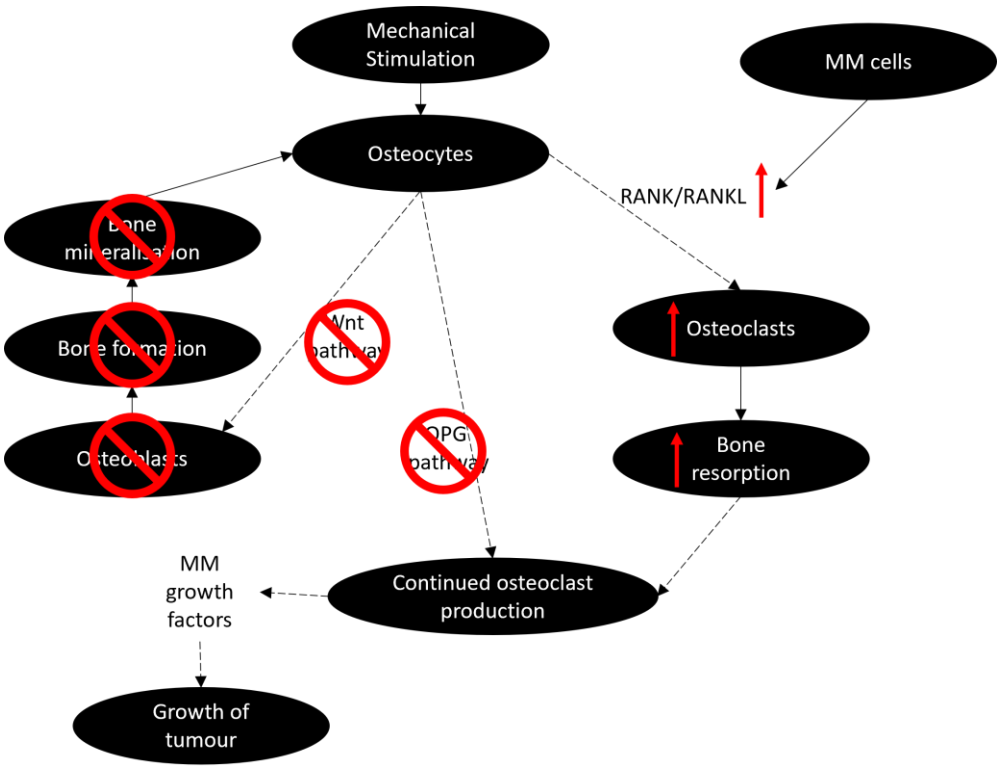

Figure 2.10 - Flow diagram showing how the remodelling cycle of bone is affected by MM.

2.5.2.2 Clinical Management of Multiple Myeloma

As a result of MM, 70-80% of patients endure bone pain whilst 2-3% ultimately suffer from spinal cord compression (Hameed *et al.*, 2014). The approach to treatment can be split into two areas: (1) effective treatment of myeloma and (2) use of ''bone-modifying'' treatment to support bone recovery and prevent further bone loss and fractures.

An example of the management process used with MM is shown in Figure 2.11. Patients usually present bone pain and neurological signs when first diagnosed. A whole spine MRI is performed to assess whether there is cord compression and soft tissue involvement (Terpos *et al.*, 2021). If the patient presents spinal cord compression on diagnosis, it is classed as a medical emergency and decompression surgery is conducted immediately followed by local

radiotherapy to target the soft tissue disease (Bird *et al.*, 2011). If no cord compression is present, the first treatment process is controlling the disease. The soft tissue involvement is treated depending on the patients age and their suitability (Hameed *et al.*, 2014). Stem cell transplant, chemotherapy and radiation therapy and high dose therapy, whereby a higher than standard dose of chemotherapy or radiotherapy is used as a more aggressive treatment, are among the treatments considered for controlling myeloma. Once the disease is controlled, bisphosphonate therapy is used to prevent further bone loss by inhibiting osteoclast formation and maturation and to enhance osteoclast apoptosis (Van Beek *et al.*, 1999).

Spinal lesions are often treated using localised radiotherapy, but in the cases of collapsed vertebrae, vertebroplasty and kyphoplasty are also considered (Figure 2.12a) (Snowden *et al.*, 2011). Vertebroplasty, the injection of cement into fractured vertebra, and kyphoplasty, insertion of a balloon into the fractured bone to create space for the injection of cement, should be performed soon after the vertebral body collapses (Molloy *et al.*, 2015). Surgical intervention should only be considered in the event of spinal instability or neurological deficit from cord compression in patients with vertebral osteolysis of more than 30% (Rao *et al.*, 2006; Flouzat-Lachaniette *et al.*, 2013). However, the use of surgery must also be carefully considered as MM patients are often elderly and immunocompromised putting them at higher risk of complications (Cawley *et al.*, 2019). The survival rate post-surgery has been evaluated in several studies, indicating a 5-year survival rate between 34%-50% (Quidet *et al.*, 2018; Galán-Olleros *et al.*, 2021). However, two similar studies, evaluating multiple surgeries, showed a decrease in survival rate from 48% (2002) to 40% (2011), suggesting it is not surgical techniques that have improved the survival rate (Roland Dürr *et al.*, 2002; Utzschneider *et al.*, 2011). The rate of complications following surgery have also been reported and range between 20% (Galán-Olleros *et al.*, 2021) and 75% (Quidet *et al.*, 2018). If necessary, surgery is conducted upon diagnosis meaning post-operative recovery could delay the start of anti-myeloma treatments such as chemotherapy (Flouzat-Lachaniette *et al.*, 2013). The risks associated with surgery for most patients outweigh the benefits and therefore alternatives must be identified (Fahed *et al.*, 2015).

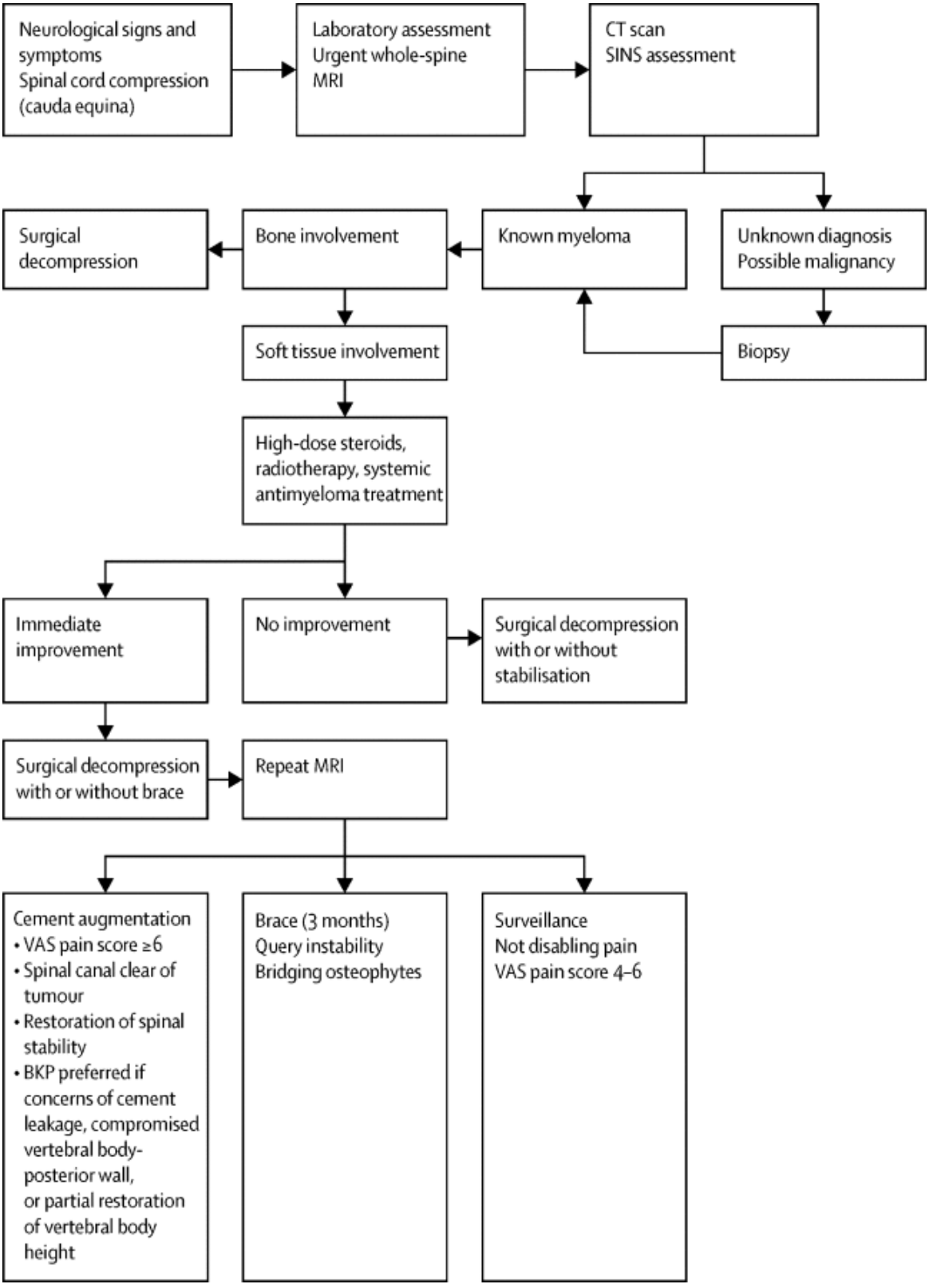

Figure 2.11 - Flow diagram representing the management of MM upon diagnosis. (Terpos *et al.*, 2021)

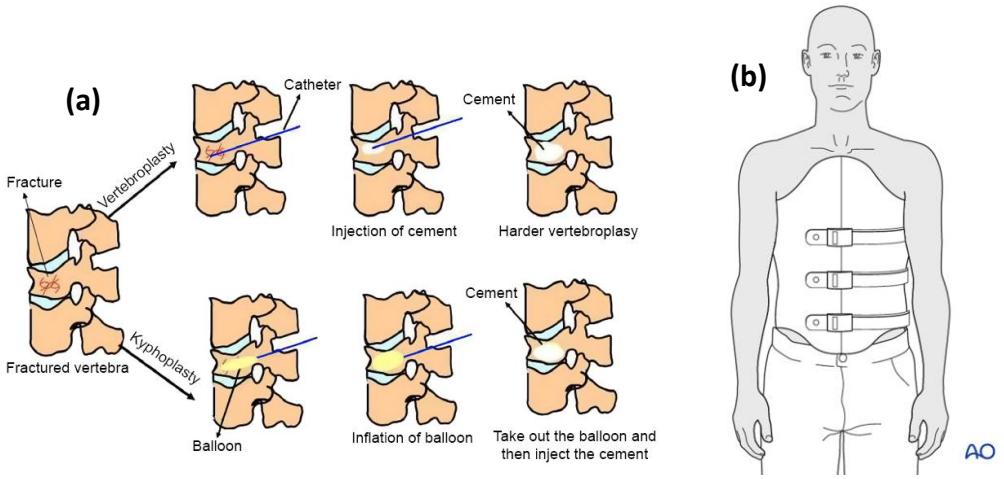

Figure 2.12 - (a) illustration of vertebroplasty and kyphoplasty (Gao *et al.*, 2015) **(b) illustration of an example of orthopaedic bracing (Copyright by AO Foundation, Switzerland, Source: AO Surgery Reference, www.aosurgery.org.)**

Alternatively, the spine can be stabilised using external orthopaedic bracing (Figure 2.12b). Spinal orthoses stabilise the spine by holding it in an extended position, minimising the loading on the weakened vertebrae (Delank *et al.*, 2011). Figure 2.13 indicates how chemotherapy treatment reduces the number of myeloma cells and how structural integrity is increased through bracing for patients with multiple myeloma. The brace is worn until the bone integrity has entered the 'stable' region with the hope that, when removed, the spine has been stabilised through bone remodelling and is no longer at risk of fracture.

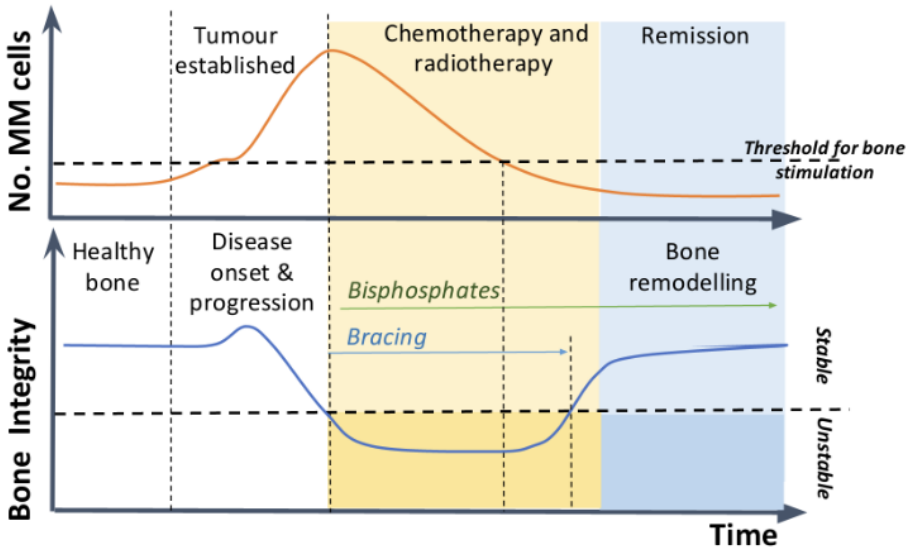

Figure 2.13 - Graphs describing the hypothesis behind the treatment of MM for the number of MM cells throughout treatment (top) and the integrity of bone throughout treatment (bottom).

Most of the orthoses used in previous studies for MM have been rigid, which can lead to discomfort beyond 3 months. Therefore, they are currently only used for short-term control of pain (Molloy *et al.*, 2015). More flexible collars are yet to be studied with MM but have been evaluated for the rehabilitation of osteoporotic patients. Meng Li et al. (2015), and Pfeifer et al. (2004), reported a significant reduction in pain and gain in functional mobility using a more flexible brace (Pfeifer, Begerow and Minne, 2004; Li *et al.*, 2015). Custom made thoracolumbar sacral orthoses (TLSO) are used most when evaluating the efficacy of braces. Several studies have reported that using a TLSO (between 3 and 6 months) alongside radiotherapy, for a lesion classed as unstable and at significant risk of neurological damage, significantly reduced pain and restored neurological function (Aligizakis *et al.*, 2002; Gokaraju *et al.*, 2016; Malhotra, Lui, *et al.*, 2016). Alongside a reduction in pain, osseous bone formation has been observed post-bracing, which conferred additional stability (Rao *et al.*, 2006; Malhotra, Lui, *et al.*, 2016; Gokaraju *et al.*, 2019; Belo, Reis and Teixeira, 2021). Mineralisation was subsequently detected around the lesion, between lytic vertebra and along fracture lines. It has been concluded that the benefit of non-surgical treatment outweighed the risks associated with surgery (Gokaraju *et al.*, 2016) if the bracing was implemented within six months of presenting (Malhotra, Butler, *et al.*, 2016).

Alongside the abovementioned research regarding remineralisation following bracing, other studies have reported similar results following radiotherapy alone (Mose *et al.*, 2000; Balducci *et al.*, 2011; Matuschek *et al.*, 2015). The percentage of lesions that remineralised varied between studies, showing the variability of bone remodelling between cohorts. Remineralisation was detected in 48% of bone lesions in a study that also concluded that there was a linear relationship between radiation dose and the likelihood of remineralisation (Matuschek *et al.*, 2015). Mose et al., conducted a similar study and found remineralisation in 46.4% of patients (Mose *et al.*, 2000). A slightly lower number of patients with remineralisation (24%) was reported by Balducci et al., who also estimated the time to achieve remineralisation was around 6 months (Balducci *et al.*, 2011). All the results in the studies mentioned were calculated from CT and/or MRI images of the patient's bone, and no mechanical analysis was performed.

2.6 Spinal Imaging

To assess the patient's risk of vertebral fracture in clinics, two methods have been previously adopted: Dual Energy X-rays Absorptiometry (DXA) and Quantitative Computed Tomography (QCT). QCT provides images obtained from a CT machine where either an inline or offline (retrospective) calibration phantom could also be scanned. Calibration phantoms are used to convert the image's Hounsfield units into apparent bone mineral density (BMD) and subsequently elastic modulus through a set of calibration and conversion functions. While both DXA and QCT are used in clinical practice to measure BMD, QCT has the advantage of providing volumetric measurements of BMD in both cortical and trabecular bone (Demirbağ Kabayel, 2016). DXA produces a 2D image which has known limitations in incorrectly classifying the risk of fracture, exemplified by a recent study in which 70% of osteoporotic fracture patients had normal DXA aBMD (Jiang et al., 2020). Despite this, DXA is still the gold standard in the clinic due to the low radiation exposure (5-20 µSv by DXA vs. 60-90 µSv by QCT) (Demirbağ Kabayel, 2016).

For QCT, after each axial translation across the subject of the tube and detector, the tube-detector assembly is rotated to a different angle, see Figure 2.14 (Goldman, 2007). The 3D images are reconstructed by combining the 2D images captured at each angle. Each slice taken is in the X-Y plane with the Z-direction representing the slice thickness. The 2D slices are used to reconstruct 3D models which are composed of a matrix of 3-dimensional hexahedral boxes, called voxels (Goldman, 2007).

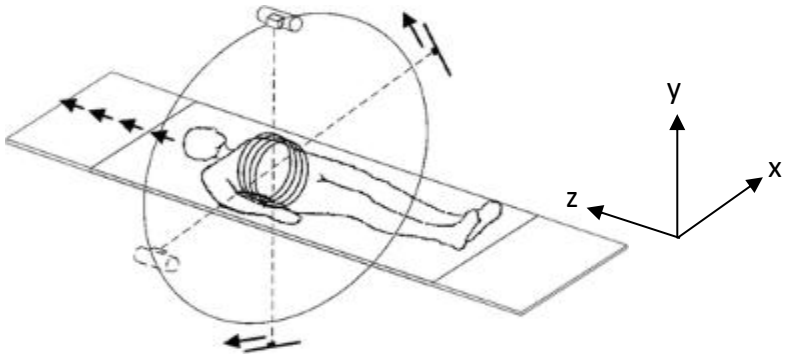

Figure 2.14 - Representation of the system used in the current CT scanners which implies the continuous rotation of the X-ray source-detector around the patient while they translate through. Image reproduced from (Cierniak, 2011)**.**

The brightness and intensity of the grey value (measured in Hounsfield units, HU) is proportional to the mineral content of the tissue and is calculated using Equation 2.1.

$$CT\ number\ (Houndsfield\ units, HU) = [K \times (u_{voxel} - u_{water})]/u_{water}$$

Equation 2.1

Where K is a constant, u_{voxel} is the linear attenuation coefficient of the material of interest and u_{water} is the linear attenuation coefficient of water. The distribution HU is then converted into BMD using a densitometric calibration equation, which is derived from a calibration phantom. The phantom is usually placed within the scanner (i.e. inline phantom) and is composed of insertion rods of known densities (example in Figure 2.15).

To obtain the BMD values of a CT scan, a linear regression analysis is performed between the known values of BMD of the rods and the actual values of HU within the CT scan to estimate parameters a and b in the equation:

$$\rho_{QCT} = \mathrm{a} + \mathrm{b}HU$$

Equation 2.2

Where ρ_{QCT} represents the QCT equivalent BMD, HU represents the Hounsfield unit values in the image and a and b are constants from the linear regression analysis performed. This equation can then be applied to estimate BMD of the bone. From this equation, the apparent density and the elastic modulus of the tissue are calculated using the following relationships.

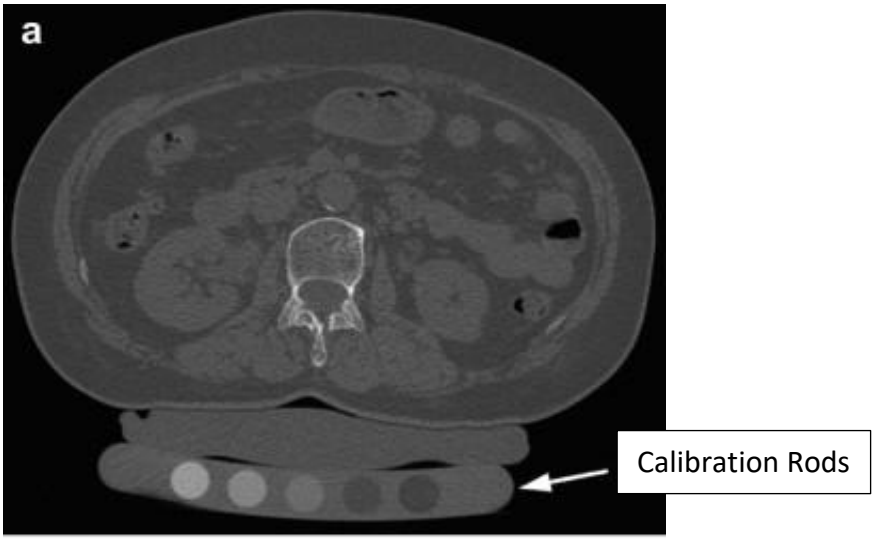

Figure 2.15 - QCT image of a human vertebra scanned with a calibration phantom composed by 5 insertion rods with equivalent densities of 0, 50, 100, 150, and 200 mg/cm^3 used to calibrate the image grey levels in equivalent BMD (Griffith and Genant, 2008)**.**

The density determined by CT (ρ_{QCT}) and ashing density (ρ_{ash}) is highly correlated (Schileo *et al.*, 2008), therefore it is assumed that $\rho_{QCT} = \rho_{ash}$.

$\rho_{ash} = \rho_{app} \times 0.6\ [g/cm^3]$; (Schileo *et al.*, 2008)

Equation 2.3

Where ρ_{QCT} is the QCT equivalent BMD and ρ_{app} is the apparent density.

$E = 4730{\rho_{app}}^{1.56}\ [MPa]$; (Morgan, Bayraktar and Keaveny, 2003)

Equation 2.4

Where E defines the elastic modulus as a function of the apparent density, ρ_{app}.

The role of CT technology has grown extensively due to its effectiveness in skeletal assessment for diagnosis and continuous monitoring of MM (Duvauferrier *et al.*, 2013). This imaging technique provides essential information for assessing spinal stability by allowing for the identification of osteopenia, lytic lesions, soft-tissue involvement and fractures (Mahnken *et al.*, 2002). The main concern with CT use is the exposure to significantly higher doses of radiation in comparison to standard X-ray graphs (Winterbottom and Shaw, 2009). Despite this, evidence suggests that low-dose whole body CT is effective in producing high resolution images that provide the information necessary for assessing spinal stability (Gleeson *et al.*, 2009).

2.6.1 Phantomless calibration of CT

The calibration of CT scans usually utilises an external phantom as described in the previous section; however, routine CT scans are often conducted without a calibration phantom as its usage increases the logistical burden of clinical imaging (Lee *et al.*, 2017). To account for this, numerous methods for phantomless calibration have been developed (Michalski *et al.*, 2020; Bartenschlager *et al.*, 2021). Calibration is necessary as the attenuation values depend on the type of scanner and protocol (Pickhardt *et al.*, 2013; Carpenter *et al.*, 2014). One approach is to pre-calibrate the scanner using either DXA measurements or a calibration phantom and apply this general pre-calibration factor to prospective CT scans (Budoff *et al.*, 2013; Pickhardt *et al.*, 2015). Even though this is an improvement from no calibration, it does not consider the patient specific differences as well as scanner and protocol changes.

The most widely used phantomless approach is to utilise internal tissues as the reference materials. The choice of tissues has been varied and depend on scan location, with some

authors choosing air, fat and blood (Lee *et al.*, 2017; Schwaiger *et al.*, 2017), while others have used fat and muscle (Weaver *et al.*, 2015; Saffarzadeh *et al.*, 2016) and shown similar results. Bartenschlager *et al.* compared different combinations of two internal tissues, reporting the lowest error for any combination with air (<5%), particularly air and blood and the highest errors arising when using muscle in the combination (Bartenschlager *et al.*, 2021). These authors also concluded no significant difference when applying the combinations to different scanners.

2.7 Finite Element (FE) Modelling theory and global equation

The FE method is a numerical technique that has been used in the field of biomechanics to computationally study the mechanical properties of bone for over 40 years (Zysset *et al.*, 2013). This technique's success is derived from the use of discretisation which splits larger, complex problems into many smaller problems, using finite elements, to approximate a solution to the overall problem (Heller, 2022). Each finite element is composed of a set number of nodes, depending on shape and element order (linear, quadratic etc), that are associated with degrees of freedom (DOF) (e.g. for a 3D body, three cartesian components for translations and three angles of rotations make up 6 DOFs). The element order can be linear, quadratic or a higher order polynomial and it defines the shape function used in numerical integration. The global stiffness matrix [Equation 2.12] represents the system of linear equations that approximate the solution to the problem and is the sum of the stiffness matrix from each finite element within the model [Equation 2.11]. Once the model has been fully defined by assigning material properties and boundary conditions (displacement or force), Equation 2.13 is solved to find the unknown displacement or force for each element.

First, the displacements of the element are converted to the nodal displacement using a shape function:

$$\{u^{(e)}\} = [N^{(e)}]\{U^{(e)}\}$$

Equation 2.5

Where $\{u^{(e)}\}$ represents the vector of displacements, $[N^{(e)}]$ is the shape function specific to the element type chosen and $\{U^{(e)}\}$ is the unknown nodal displacement vector.

The deformation of a 3D body can be described by strains derived from the displacement. For the linear elastic theory, strains (and deformations) are assumed to be small (Younis, 2009).

Strains in a 3D structure are described by three normal strains and three shear strains in the global coordinate system: $\{\varepsilon\} = [\varepsilon_x \quad \varepsilon_y \quad \varepsilon_z \quad \varepsilon_{xy} \quad \varepsilon_{yz} \quad \varepsilon_{zx}]^T$ (Cook et al., 2001). Principal strains can be described as the normal strains that act along the principal planes where their shear strain is zero. The three principal strains, denoted ε_{p1}, ε_{p2}, and ε_{p3}, are defined as the normal strains acting on mutually orthogonal planes where shear strain is zero. They are conventionally ordered such that $\varepsilon_{p1} \geq \varepsilon_{p2} \geq \varepsilon_{p3}$. While ε_{p1} is the largest and ε_{p3} the smallest, all three principal strains may be either tensile (positive) or compressive (negative), depending on the deformation state. The ordering indicates relative magnitude, not the nature of the strain.

The strain-displacement relationship is calculated as the product of the matrix of differential operator and the derivative of the element shape function and the nodal displacement vector:

$$\left\{\varepsilon^{(e)}\right\} = \left[B^{(e)}\right]\left\{U^{(e)}\right\}$$

Equation 2.6

$$\left[B^{(e)}\right] = [L]\left[N^{(e)}\right]$$

Equation 2.7

By introducing the matrix of differential operator formulated as:

$$[L] = \begin{bmatrix} \frac{\partial}{\partial x} & 0 & 0 \\ 0 & \frac{\partial}{\partial x} & 0 \\ 0 & 0 & \frac{\partial}{\partial x} \\ 0 & 0 & \frac{\partial}{\partial x} \\ \frac{\partial}{\partial x} & 0 & \frac{\partial}{\partial x} \\ \frac{\partial}{\partial x} & \frac{\partial}{\partial x} & 0 \end{bmatrix}$$

Equation 2.8

In the region of linear elasticity, Hooke's law is used to calculate the element stresses based on the strains:

$$\left\{\sigma^{(e)}\right\} = [D^e]\left\{\varepsilon^{(e)}\right\}$$

Equation 2.9

Where [D] represents the elasticity of an isotropic material in which E is the elastic modulus and v is the Poisson's ratio:

$$[D^e] = \frac{E}{(1+v)(1-2v)} \begin{bmatrix} 1-v & v & v & 0 & 0 & 0 \\ v & 1-v & v & 0 & 0 & 0 \\ v & v & 1-v & 0 & 0 & 0 \\ 0 & 0 & 0 & \frac{1-2v}{2} & 0 & 0 \\ 0 & 0 & 0 & 0 & \frac{1-2v}{2} & 0 \\ 0 & 0 & 0 & 0 & 0 & \frac{1-2v}{2} \end{bmatrix}$$

Equation 2.10

The local stiffness matrix $\left[K^{(e)}\right]$ can then be derived from:

$$[K^e] = \int \left[B^{(e)}\right]^T [D^e] \left[B^{(e)}\right] dV$$

Equation 2.11

The unknown displacement $\left\{U^{(e)}\right\}$ for each element can then be solved by balancing the equilibrium equation for all elements against the vector of nodal forces for each element $\left\{F^{(e)}\right\}$:

$$\sum_{e=1}^{e} \left(\left[K^{(e)}\right] \left\{U^{(e)}\right\} - \left\{F^{(e)}\right\} \right) = 0$$

Equation 2.12

To compute the deformation across the whole structure, each element's local stiffness matrix is assembled into a global system called the global stiffness matrix [K]:

$$[K]\{U\} = \{F\}$$

Equation 2.13

Where {*U*} and {*F*} represent the global vectors of unknown nodal displacements and nodal forces, respectively.

2.8 Finite element solution procedure

The mechanical behaviour of bone is non-linear, which must be accounted for within the FE analysis. For a non-linear analysis, the stiffness matrix will change for every iteration of the analysis due to material non-linearity, where the material properties are functions of the stress or strain, contact non-linearity, where gaps may open or close between components, or geometric non-linearity, where the deformation is large enough that the equilibrium

equations must be solved according to the deformed geometry (Cook *et al.*, 2001). One of the most common methods for solving a non-linear problem is the Newton-Raphson method, see Figure 2.16. This method solves the non-linear load-displacement relationship iteratively at steps, n, that are generated by load increments ΔF_n, which is defined as:

$$\{\Delta F\}_n = \{F^{ext}\}_{n+1} - \{F^{int}\}_{n+1}^{i-1}$$

Equation 2.14

Where $\{F^{ext}\}_{n+1}$ is the externally applied forces at each load step (n) and $\{F^{int}\}_{n+1}^{i-1}$ defines the element nodal forces at each iteration (i) and load step (n).

It is assumed that at load step n=1, $\{F\} = \{F\}_n$, $\{U\}_n$ is known. For the applied load $\{F\}_{n+1} = \{F\}_n + \{\Delta F\}_n$, the solution for $\{U\}_{n+1}$ must be computed. For each iteration, $\{\Delta U\}^i$ is calculated by the product of the new stiffness matrix and the load increment ΔF_n, both at the ith iteration of load step $n+1$,.

$$\{\Delta U\}^i = [K_T]_{n+1}^{i-1}\{\Delta F\}_n$$

Equation 2.15

The corresponding nodal displacements, $\{U\}_{n+1}^i$, are then approximated as:

$$\{U\}_{n+1}^i = \{U\}_{n+1}^{i-1} + \{\Delta U\}^i$$

Equation 2.16

This process continues using Equation 2.16 and Equation 2.17 until the residual forces, $\{\Delta R\}_{n+1}^i$, and nodal displacements $\{\Delta U\}_{n+1}^i$ are sufficiently small to accept the solution has converged.

$$\{\Delta R\}_{n+1}^i = \{F^{ext}\}_{n+1} - \{F^{int}\}_{n+1}^{i-1}$$

Equation 2.17

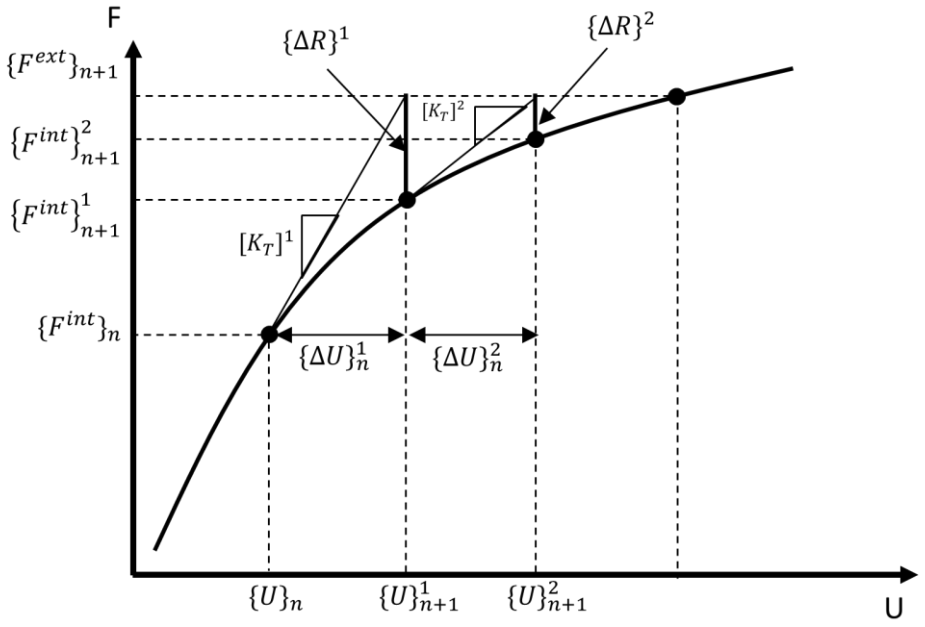

Figure 2.16 - Newton-Raphson method showing the iterative process of the applied load step n+1. (Adapted with permission: Classical and Computational Solid Mechanics, YC Fung, Pin Tong & Xiao Hong Chen, Copyright @2017 by World Scientific Publishing Co. Pte. Ltd.)

2.8.1 Vertebral FE models

The use of FE models to analyse how lytic lesions affect the stability of the spine and mechanical properties of individual vertebrae were initially applied to idealised geometry with lesions (Mizrahi, Silva and Hayes, 1992; Whyne, Hu and Lotz, 2001, 2003; Tschirhart, Finkelstein and Whyne, 2007). Further development of these models utilised patient-specific data of vertebrae with simulated lesions (Matsuura *et al.*, 2014; Galbusera *et al.*, 2018) and real lesions (Campbell *et al.*, 2017).

Vertebral boundary conditions in FE models have been assigned to apply load through adjacent vertebral bodies or embedded endplates. Applying an axial compressive load over the endplate (simulating a vertebra embedded in resin) has been considered an acceptable method for most applications. Despite these methods proving to be equivalent when predicting the ultimate force and damage distribution (Maquer, Dall'Ara and Zysset, 2012), modelling a single vertebra does not represent the loading conditions of the whole spine, including the intervertebral discs (Jackman *et al.*, 2015). However, Lu et al., concluded that the prediction of vertebral strength was not improved by the inclusion of intervertebral discs

(Lu *et al.*, 2014). For a clinical tool, modelling the whole spine would give the advantage of assessing the fracture risk of every vertebra, as in most cases, the vertebrae adjacent to a lytic vertebra are also at high risk of fracture due to the alteration of biomechanical properties resulting from the cancer (Anitha *et al.*, 2017).

The effect of lytic lesions on the mechanical properties of bone has been studied using several plasticity laws. Campbell et al., whose study focused on MM patients with and without fracture, reported high accuracy when using a simple elastic-perfectly plastic model to predict the stiffness, yield force and work-to-yield (Campbell *et al.*, 2017). The inclusion of bilinear elastic-plastic constitutive laws provides a more accurate representation of the material properties, and has proven to be highly accurate when predicting the ultimate forces in compression for vertebra without lesions (Buckley, Loo and Motherway, 2007; Wang *et al.*, 2012). This plasticity model has also been used when validating the prediction of structural properties of human vertebra with lytic lesions (Matsuura *et al.*, 2014), showing a high degree of accuracy as the FE models were highly correlated to the experimental values for fracture load (R^2=0.78). Nevertheless, Groenen et al., reported the limited ability of predicting ultimate loads ($0.22 \leq R^2 \leq 0.25$) when using simple plasticity models despite good estimations of stiffness ($0.64 \leq R^2 \leq 0.69$) (Groenen *et al.*, 2018).

2.9 Mechanobiological Modelling

The bone remodelling process in healthy bone, described above in Section 2.3.1, is a continuous process whereby new bone is formed to replace mature and damaged bone. Osteoclasts and osteoblasts remove and form bone respectively, working together to create a balance between bone formation and resorption. If this balance is disrupted, it will lead to the development of certain bone pathologies, such as osteoporosis (Feng and McDonald, 2011).

Bone remodelling differs between cortical and trabecular bone. Trabecular bone remodelling occurs on the surface of the trabeculae, where osteoclasts create a resorption lacuna followed by osteoblasts that fill this lacuna with new bone. This process lasts around 180 days (30-40 days for resorption and 150 days for formation) (Pant *et al.*, 2021). In contrast, the cortical bone remodelling cycle is shorter (around 120 days) (Agerbæk *et al.*, 1991) and works by a group of osteoclasts cutting through the bone, forming canals, followed by osteoblasts

that lay down osteoid (Pant *et al.*, 2021). Bone changes can be categorised into remodelling, which is remodelling to repair damage and adapt to loading and modelling or shaping of the bone, which dictates the modification of the bone shape (Cowin and Van Buskirk, 1979).

2.9.1 Mechano-regulation modelling

Previous studies have explored mechano-adaptive remodelling extensively to mimic how bones react to local mechanical forces. Wolff's law, originally articulated by Julius Wolff in 1892, posits that bones adapt their internal structure in response to the magnitude and direction of the loading (Wolff, 1892). Mathematical models were then developed to incorporate Wolff's Theory along with Frost's Mechanostat Theory (Frost, 1987; Beaupré, Orr and Carter, 1990; Weinans, Huiskes and Grootenboer, 1992). The Mechanostat theory describes how the mechanical stimulus influences bone density and is split into four regions (Figure 2.17: (1) low stimulus and resorption, (2) moderate stimulus and quiescence, (3) high stimulus and apposition and (4) very high stimulus and failure (Frost, 1987). Additionally, implants that disrupt stress and strain fields can alter the internal mechanical environment, triggering remodelling even when physiological loading limits are not exceeded (Weinans *et al.*, 2000). Consequently, mechano-regulation models require an understanding of both the physiological and pathophysiological reactions of bone to mechanical loading.

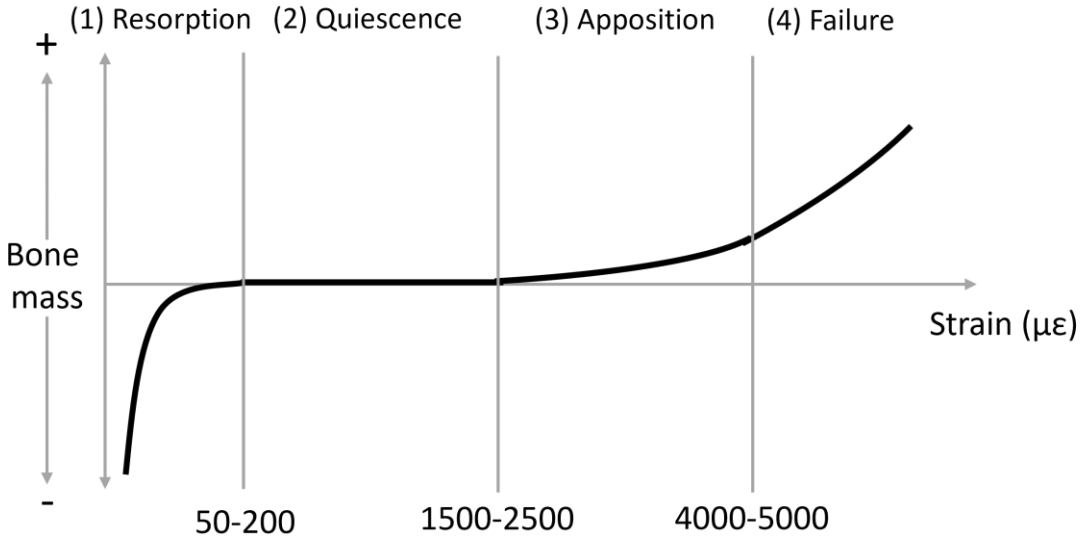

Figure 2.17 - Frost's Mechanostat Theory of bone adaptation to mechanical stimuli.

Over the past four decades, numerous computational models using the FE method have emerged to simulate mechano-adaptive bone responses. Several forms of mechanical stimuli have been adopted in these models, including stress, strain, strain energy density (SED), the gradient of SED, damage and fluid flow. SED (Weinans, Huiskes and Grootenboer, 1992; Huiskes *et al.*, 2000) as well as the gradient of SED (Webster *et al.*, 2015) have frequently served as the primary stimulus for remodelling. An early remodelling algorithm using SED was developed by Huiskes et al. to investigate bone remodelling in an FE model of an idealised femur (Huiskes *et al.*, 1987). Huiskes' model was then built upon by Carter et al. who applied the algorithm to a 2D cross section of a femur (Carter, Orr and Fyhrie, 1989). Within these models, the reference SED, which was compared to the SED per element, dictated if there was bone formation or resorption. The reference SED also determined the size of the lazy zone, which was defined as the range of remodelling stimulus where no remodelling takes place. Another author used the SED stimulus from an FE analysis to drive a function that described the velocity at which bone was added or resorbed from the bone surface (Schulte *et al.*, 2013).

SED has been employed to model both internal and external remodelling processes. For instance, Wang et al. developed a model predicting changes in tooth density (internal) and position (external) based on SED as the stimulus (Wang *et al.*, 2014). The reference SED remodelling algorithm was used to mimic internal remodelling and changes in tooth density, whereas the velocity-based function was employed to describe the tooth movement and position over time. An earlier model by Beaupre et al. introduced a time-dependent approach that combined internal and external remodelling processes, assuming that the disparity between expected (reference) and actual mechanical stress drove the remodelling process (Beaupré, Orr and Carter, 1990).

More recently, instead of using the SED per element as the stimulus for bone remodelling, studies have utilised the SED per unit mass to drive the bone remodelling process (Behrens *et al.*, 2009). This approach has been adopted by a number of studies to investigate periprosthetic femurs and implant loading (Mellal *et al.*, 2004; Behrens *et al.*, 2009; Lin, Lin and Chang, 2010). However, it's important to note that bone cells cannot directly sense SED,

which is a combination of stress and strain; they can only detect stimuli in their mechanical environment.

Studies have utilised other mechanical stimuli, as well as a combination of SED with other mechanical stimulus, such as damage, within bone remodelling algorithms. Wang et al. used the combination of damage and SED within a basic multicellular unit (BMU) to drive the remodelling algorithm (C. Wang *et al.*, 2011). The damage was calculated according to the number of cycles to failure, which was dependant on the stress and other material properties from previous works (Carter, Hayes and Schurman, 1976; McNamara and Prendergast, 2007). In Wang *et al.*'s (2011) model, if the damage was below a certain threshold, remodelling occurred depending on the difference between the reference SED and calculated SED (C. Wang *et al.*, 2011). However, if it was above a critical value, the decision if the element would undergo remodelling was dictated by a random number generator. Wang *et al*.'s (2011) model was only applied to a 2D cross section of a vertebral body, limiting its applicability (C. Wang *et al.*, 2011).

Mellal *et al*. evaluated the use of SED per unit mass, peak strain and stress individually as the mechanical stimulus for bone remodelling around an implant (Mellal *et al.*, 2004). These authors concluded that the stimulus based on the peak strain and SED was consistent with *in vivo* data, however it produced lower compressive stresses than expected (Mellal *et al.*, 2004). Strain was also used as the stimulus by Dunlop to compare four remodelling rules, a step relationship where a strain threshold was used to dictate if there was formation, Frost's Law (Frost, 1987) and two linear relationships between strain level and the probability of resorption and deposition to test the use of different treatments, exercise and anti-resorptive treatments on the bone volume (Dunlop *et al.*, 2009). All four remodelling rules in Dunlop's study predicted a higher frequency of smaller trabeculae than experimental data, however, the step wise rule showed the strongest agreement with experimental data when modelling the antiresorptive treatment (Dunlop *et al.*, 2009). This suggests the response to a mechanical stimulus should be initiated at a certain threshold rather than a linear relationship with strain.

2.9.2 Mechanobiological regulation modelling

The introduction of biological regulation in FE modelling of mechano-adaptation first came from Lemaire et al. (Lemaire *et al.*, 2004), who proposed a model employing a system of

differential equations to depict the temporal evolution of bone cells. This model also accounted for critical factors such as osteoblast-osteoclast coupling, the RANK-RANKL-OPG pathway, parathyroid hormone (PTH) administration, and TGF-β (transforming growth factor-beta). Despite its simplicity and a lack of experimental validation, Lemaire's model laid a solid foundation for potential therapeutic interventions in bone-related conditions. Building upon this work, Pivonka further expanded the modelling framework by describing the behaviour of basic multicellular units (BMUs) based on bone-cell dynamics (Pivonka *et al.*, 2008). Additionally, Pivonka's model considered changes in bone volume resulting from BMU behaviour and identified a limited set of parameter combinations that produced physiologically realistic bone remodelling simulations. Notably, these early models did not explicitly incorporate mechanical stimuli, but they paved the way for future developments that could integrate mechanical factors into the modelling process.

Algorithms have been developed from the original work of Lemaire and Pivonka to couple the mechanical and biological response of bone. Scheiner et al. extended the work of Pivonka et al (Pivonka *et al.*, 2008, 2010) to include a mechanoregulatory feedback response using micro-mechanical strains to regulate pre-osteoblast evolution and known pathways, such as TGF- β, RANKL and OPG to regulate osteoclast evolution and bone cell concentrations. Bone cell populations and formation and resorption rates then dictated the bone volume fractions (Scheiner, Pivonka and Hellmich, 2013). Another example of a bone remodelling algorithm is described by Komarova et al. whereby a mathematical model was constructed to describe the temporal changes in osteoblast and osteoclast populations and therefore bone mass at a specific site (Komarova *et al.*, 2003). Komarova (2003) established two modes of remodelling, where one is targeted, a single re-modelling cycle in response to an external stimulus, and one is random, a series of internally initiated cycles of bone remodelling (Komarova *et al.*, 2003). This suggests that, as well as mechanically induced remodelling, there is an additional algorithm that must be developed to explain further changes within the bone (Komarova *et al.*, 2003). The algorithm resulted in non-linear behaviour of bone cells and subsequent bone mass, showing similar behaviour to what is observed *in vivo*. These models, however, are purely mathematical and not applied to real bone geometry.

To bridge the gap between mathematical modelling and FE models, authors have applied previously developed algorithms to 2D or 3D FE models. The mechano-regulatory model previously mentioned by Huiskes (Huiskes *et al.*, 1987), was continuously updated to incorporate a separate description of osteoclastic resorption and osteoblastic formation, an osteocyte mechanosensory system, and the role of microdamage (Huiskes *et al.*, 2000). This model was applied to a 2D, and later a 3D FE model to demonstrate the theory's prediction of cancellous bone formation (Huiskes *et al.*, 2000; Ruimerman *et al.*, 2003). Komarova's (2003) algorithm (Komarova *et al.*, 2003) was also tested and developed in Hambli's study using an idealised 3D FE model of a proximal femur (Hambli, 2014). Hambli (2014) used damage as the mechanical stimulus to influence the osteoclast and osteoblast formation, as well as rates of bone formation and resorption which updated the bone density accordingly. The algorithms prediction of the BMD distribution in the femur showed many architectural features that are observed clinically (Hambli, 2014). To improve the model, these authors suggested the use of imaging data (DXA/CT) to incorporate patient specific material properties as well as 3D geometry (Hambli, 2014). The purpose of Hambli's (2014) study was to establish a framework to explore the development of new therapeutic treatments for pathological conditions and bone disorders such as osteoporosis (Hambli *et al.*, 2016). As with most computational studies, there is no experimental work to validate Hambli's study. However, in 2017 Dao et al. (Dao, 2017) combined the FE remodelling framework of Hambli with an agent based model to describe the cellular dynamics. Dao (2017) noted the qualitatively comparable bone cell evolution and population during a simulation to a follow-up section obtained using the HR-pQCT technique (Christen *et al.*, 2014).

While all the studies described in this section thus far depict normal bone remodelling, some authors have extended this to include disease progression and the effect of therapeutics. For example, the mechano-regulatory models developed by Pivonka and Scheiner (Pivonka *et al.*, 2008, 2010; Scheiner, Pivonka and Hellmich, 2013) were extended by Lerebours et al. to simulate osteoporosis in a femur (Lerebours *et al.*, 2016). The model incorporated both biological, hormonal regulation and biochemical coupling of bone cell populations, and mechanical adaption of the tissue. Their findings were in accordance with experiments, simulating endocortical bone loss and cortical wall thinning (Lerebours *et al.*, 2016). Martin et al. then studied the efficacy of bone remodelling treatments for osteoporosis (Martin *et*

al., 2020). Their simulation results for bone mineral density at different time points post-treatment agreed well with the data reported in the literature. In addition, Wang et al. simulated the interaction between multiple myeloma (MM) and the bone microenvironment (Y. Wang *et al.*, 2011). Their algorithm was based on the model by Pivonka et al. (Pivonka *et al.*, 2008) and developed to clarify the most important cell signalling pathways in MM disease progression, including TGF-β, IGF-β and RANKL/OPG (Y. Wang *et al.*, 2011).

FE has also been used to simulate the effect of pharmacological treatments on bone remodelling. Hambli (2016) developed a bone remodelling algorithm to simulate the effect of denosumab on the proximal femoral bone remodelling (Hambli *et al.*, 2016). They combined a model to describe the denosumab absorption in blood serum (Scheiner *et al.*, 2014) with their previously developed FE mechanobiological model (Hambli, 2014). They assumed the mechanical stress drove the behaviour of osteoclasts and osteoblasts, while the populations of osteoclasts and osteoblasts were predicted by the Komarova et al. (2003) model (Komarova *et al.*, 2003). In another similar study, Bahia et al. (2020) used SED as the mechanical stimulus to assess the effect of antiresorptive drugs on bone remodelling on a proximal femur (Bahia *et al.*, 2020). The drug concentration and the SED determined the bone cell populations and dynamics which updated the bone mineral density accordingly. The model was able to qualitatively capture realistic behaviour in response to mechanical and pharmacological stimulus.

2.10 Gap in the Literature

The literature review highlighted the extensive use of FE for evaluating mechanical properties of vertebra. However, this has yet to be applied to a dataset of prostate cancer patients treated with ADT. The literature also demonstrated several promising findings showing that remineralisation occurred following the use of bracing to treat instability, suggesting that this could be a successful alternative to surgery. However, these studies were purely clinical and observational, and do not relate the remineralisation to any change in structural mechanical properties or dynamic physiological processes of bone. Therefore, the first objective of the thesis was to develop an FE pipeline to pipeline to assess clinical CT images of vertebra with and without metastases. This pipeline was then used to evaluate the effect of ADT on the mechanical properties of vertebra in addition to assessing if there was an increase in mineral

content and subsequent increase in mechanical properties in MM patients treated non-surgically following anti-cancer treatment.

The mechanobiological models previously developed to assess bone changes have been applied to idealised geometry, the femur or are purely mathematical. Similarly, any mechanobiological models predicting bone changes applied to MM patients have been mathematical and to understand the development of lesions instead of the post anti-cancer treatment. Clinical case studies evaluating the use of radiotherapy and bracing as a non-surgical treatment for MM vertebral metastatic lesions have shown promising results where remineralisation has occurred around and into the lesion, reducing the size of the lesion. However, how this remineralisation occurred and whether it was driven by normal mechanobiological principles or additional biological mechanisms influenced by the cancer is unknown. To bridge the gap between current knowledge of mechanobiological pathways and bone changes in MM patients treated non-surgically following anti-cancer treatment, a mechanobiological predictive model was developed.

3 DEVELOPMENT OF A PATIENT SPECIFIC FE PIPELINE TO ASSESS BIOMECHANICAL CHANGES IN VERTEBRA WITH METASTATIC CANCER

3.1 Introduction

This chapter outlines the datasets used within the thesis as well as the development of the finite element (FE) pipeline from a clinical computed tomography (CT) scan through to the prediction of mechanical properties of vertebrae from cancer patients. In addition, it details three stages of the pipeline that were further developed or optimised; segmentation, material property calibration from CT scans and the meshing stage of the FE set up.

3.2 Datasets

3.2.1 ANTELOPE trial

The first dataset included in this study is a time series QCT dataset from the ANTELOPE trial (Handforth *et al.*, 2024). Ethical approval was obtained from the South Yorkshire Research Ethics Committee in October 2016 (IRAS ID 206171). QCT scans of the T12 vertebra were taken at baseline and 12 months after baseline. This dataset included 31 patients in Group A, androgen deprivation therapy (ADT) treated group, of which 29 patients completed all study assessments and 26 had a matched control. One patient's QCT scan was unable to be reconstructed due to overlapping vertebra so 25 patients make up the cohort within this thesis. An overview of the patient demographics data is shown in Table 3.1.

The first cohort from 2017 was scanned using the GE LightSpeed VCT (GE Healthcare, Milwaukee, WI) in the radiology department at the Northern General Hospital, Sheffield, whilst the follow-up scans in 2018 along with all second cohort scans were scanned using the Toshiba Aquilion ONE (Toshiba Medical Systems, Tokyo, Japan) at the same hospital. Quality assurance was performed once per month using a Mindways phantom (Mindways Software, Inc., Austin, TX, USA) on both scanners. All scans were performed in the anteroposterior position, using the same noise index. The QCT protocol included a single scan from the superior edge of the T12 vertebra to the T12/L1 margin. For the GE scanner, the tube voltage was 120 kV and the mean tube current was set at 360 mA, with a voxel size of

0.937x0.937x0.625 mm^3. For the Toshiba scanner, the tube voltage was also 120 kV, the mean tube current was set at 250 mA and a voxel size of 0.976x0.976x0.5 mm^3.

Table 3.1 - Patient demographics data for the ANTELOPE treated and control groups (25 subjects per group) including age, height, and BMI.

Treated	Age (years)	Height (cm)	BMI (kg/m^2)	Matched Control	Age (years)	Height (cm)	BMI (kg/m^2)
A01	72	178.8	29 .0	**C01**	74	192.3	31.4
A02	80	173.9	26.7	**C15**	80	175.2	26.3
A03	67	165.9	21.9	**C32**	64	171.7	23.5
A05	67	179.2	27.3	**C25**	71	182.0	24.9
A06	70	180.6	31.0	**C06**	68	182.8	27.1
A07	72	173.2	23.1	**C26**	71	173.0	20.4
A10	71	191.1	32.7	**C09**	63	188.1	29.6
A13	65	169.7	27.3	**C16**	82	169.0	29.7
A16	82	169.8	32.7	**C11**	79	175.0	30.7
A17	76	181.0	24.1	**C20**	73	178.0	24.2
A19	79	180.3	24.1	**C30**	75	181.0	25.5
A20	74	181.7	28.6	**C03**	77	180.1	30.1
A21	71	167.7	25.8	**C14**	74	168.2	26.8
A23	64	172.4	25.9	**C08**	53	184.4	26.9
A24	78	174.2	25.8	**C02**	76	169.0	22.3
A25	73	170.8	28.3	**C04**	73	173.3	26.2
A27	80	167.6	25.8	**C05**	78	170.4	26.9
A28	76	175.4	27.8	**C12**	78	179.0	32.1
A30	76	176.9	30.1	**C19**	75	180.8	34.9
A32	80	160.7	26.9	**C21**	78	159.8	22.7
A33	76	163.4	34.4	**C23**	77	163.2	31.8
A34	72	175.4	31.3	**C31**	71	171.0	27.6
A35	73	182.2	24.3	**C24**	73	184.5	23.9
A37	80	171.3	23.9	**C17**	78	169.0	24.9
A38	67	165.4	23.9	**C10**	70	161.0	29.3
Average (±SD)	74 ±5	174.3 ±6.8	27.4 ±3.3	**Average (±SD)**	73 ±6	175.9 ±8.0	27.1 ±3.5

3.2.2 Royal National Orthopaedic Hospital (RNOH)

Clinical CT data was obtained from the RNOH which included ten patients each with a baseline and follow-up scan at varying months apart (16 ±15 months), seen in Table 3.2 Ethical

approval was obtained from the University Research Ethics Committee at the University of Sheffield (Reference Number: 044189)

Three different scanners were used: Phillips ingenuity (Phillips, Amsterdam, Netherlands), Phillips brilliance 64 and GE Lightspeed VCT. All protocols had the tube voltage set to 120kV while the mean tube current varied from 101-305 mA, the voxel size varied from 0.3417x0.3417x1 mm^3 to 0.6875x0.6875x3 mm^3 between protocols. The lytic vertebral level was selected by the vertebra with the largest lesion present within both baseline and follow-up CT scans.

Table 3.2 - Patient demographics data for the RNOH MM data including age, sex, time between baseline and follow-up, vertebral level used within the scan and the condition of the vertebra.

Patient ID	Age	Sex	Time between baseline and follow-up (months)	Vertebral Level	Condition
P1a	77	M	3	T4 T3	Control Lytic
P3	66	M	12	T10 T11	Control Lytic
P3a	63	M	12	T10 T11	Control Lytic
P5	74	M	8	T4 T6	Control Lytic
P5a	73	M	37	T1 C7	Control Lytic
P8	47	M	2	T4 T3	Control Lytic
P9	61	M	37	L3	Lytic
P9a	49	M	9	T10 T11	Control Lytic
P11	77	M	38	L3 L4	Control Lytic
P12	34	M	4	T3 T4	Lytic Lytic
Average (±SD)	62 ±15		16 ±15		

3.2.3 Sheffield Teaching Hospitals (STH)

Clinical CT data at baseline and 12 months along with bone turnover marker (BTM) data (CTX, P1NP and sclerostin) at 1-, 2- and 3-months post baseline was obtained from Sheffield

Teaching Hospitals (Table 3.3, Table 3.4). The study was conducted according to the guidelines of the Declaration of Helsinki and approved by the Health Research Authority and Health and Care Research Wales (HCRW), and the Yorkshire & The Humber – Bradford Leeds Research Ethics Committee, United Kingdom (REC 18/YH/0275). Two CT scanners were used; Toshiba Aquillon ONE and Toshiba Aquillon PRIME SP both using a tube voltage of 120 kV and a voxel size of 1x1x1 mm^3.

Table 3.3 - Patient demographics data for the STH MM data including age, sex, vertebral level used within the scan, the condition of the vertebra and whether the patient had bone turnover marker (BTM) data.

Patient ID	Age	Sex	Level	Condition	BTM Data
BRATS001	64	M	T4	Lytic	Yes
BRATS002	66	M	T2	Control	No
BRATS003	64	M	T8	Control	No
BRATS005	68	M	T12	Control	Yes
BRATS006	60	F	T12	Lytic	Yes
BRATS009	64	M	T12	Control	Yes
BRATS011	66	F	T11	Lytic	Yes

Table 3.4 - Carboxy Terminal Collagen Crosslinks (CTX), Procollagen 1 N-terminal Propeptide (P1NP) and Sclerostin data for each patient at 1-, 2- and 3-months post Baseline.

CTX (ng/mL)

Patient ID	Month 1	Month 2	Month 3
BRATS001	0.062	0.033	0.062
BRATS005	0.373	0.138	0.053
BRATS006	1.386	0.116	0.07
BRATS009	0.091	0.033	0.003
BRATS011	0.233	0.033	0.033

P1NP (ng/mL)

Patient ID	Month 1	Month 2	Month 3
BRATS001	44.13	36.71	41.41
BRATS005	86.86	54	4.98
BRATS006	230	21.46	25.02
BRATS009	17.79	7.84	8.54
BRATS011	78.98	67.94	13.43

Sclerostin (pmol/L)

Patient ID	Month 1	Month 2	Month 3
BRATS001	15.267	13.568	19.603
BRATS005	35.979	31.153	31.108
BRATS006	42.285	33.727	21.444
BRATS009	24.44	21.911	18.291
BRATS011	29.506	24.44	26.93

3.3 Introduction to the FE Pipeline

The finite element pipeline developed for this thesis involved taking CT images, converting them into 3D models through segmentation, applying material properties and constraining the body for simulation to assess the mechanical properties, Figure 3.1. The FE pipeline has been used extensively to evaluate the mechanical properties of vertebrae with (Campbell *et al.*, 2017) and without lesions (Buckley, Loo and Motherway, 2007; Wang *et al.*, 2012). Manual segmentation is currently still the gold standard method for segmenting CT images of vertebrae with lesions, however, this process has not been investigated for reproducibility or the effect of the image quality on the segmentation, inherently affecting the prediction of mechanical properties.

Separately, phantom calibration is currently the gold standard for calibrating CT scans; however, it restricts analyses to prospective studies or studies within radiological departments where phantoms are scanned routinely. Conversely, in oncology departments, it is not routine to scan with phantoms, therefore a phantomless procedure would enable the processing of several retrospective datasets. Thus, the use of a phantomless calibration method as opposed to a phantom calibration has not been compared in vertebrae to date, despite the obvious advantages for both resource-poor settings and investigating retrospective datasets. Finally, the meshing stage of the pipeline must be optimised for the dataset and pipeline to ensure there is no influence of the mesh on the prediction of the mechanical properties.

Therefore, three stages of the pipeline were highlighted to fill a gap in the literature and optimise the current pipeline: (1) segmentation, (2) CT densitometric calibration and (3) meshing. The segmentation reproducibility was assessed through comparing repeated segmentations from the same user using the Dice similarity coefficient (DSC) and Hausdorff distance. The CT calibration methods, phantom and phantomless were evaluated and compared using the prediction of the volumetric Bone Mineral Density (BMD). Finally, the meshing stage was optimised by conducting a mesh refinement study.

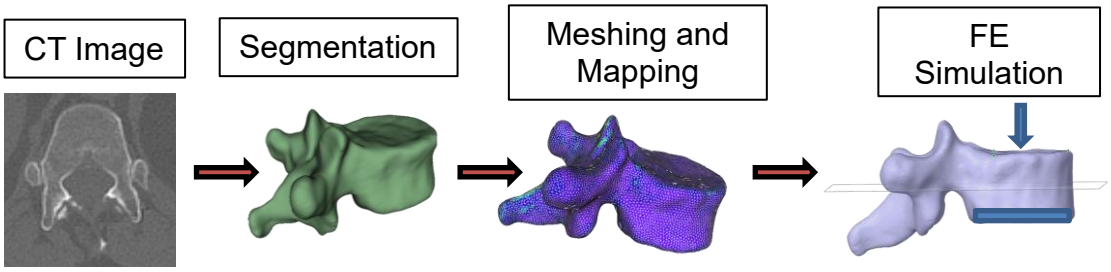

Figure 3.1 – Overview of a finite element pipeline commonly used in literature.

3.4 Intra-observer reproducibility of manual segmentation procedure

Segmentation is the process whereby a medical image is used to separate the object of interest from the background. The use of manual segmentation has been evaluated for reproducibility (DeVries *et al.*, 2008) and validated for FE studies of bone strength (Garavelli *et al.*, 2022) but the impact of lesions on the reproducibility has not been assessed. Therefore, the objective of this subchapter was to assess the intra-observer variability of a single operator in segmenting vertebrae. Segmentations were performed on QCT scans of individual

vertebra in 3D slicer. To evaluate the reproducibility of the segmentations, the Dice Similarity Score (DSC), a measure of the overlap between two segmentations, mean Hausdorff distance, the mean of the maximum surface-to-surface distances between two segmentations and 95% Hausdorff distance, which reduces sensitivity to outliers compared to the mean Hausdorff distance by taking the 95th percentile, were used.

3.4.1 Introduction

Segmentation of medical images has numerous applications including diagnosis and monitoring disease progression (Wehrli *et al.*, 2006) and analysis of mechanical properties using finite element modelling (Saillard *et al.*, 2024). MRI, CT and PET/CT have been used in the above applications for the segmentation of bone (Liu *et al.*, 2021; Aldieri *et al.*, 2024; Majcher *et al.*, 2024; Saillard *et al.*, 2024). For assessing the risk of fracture of bone with lesions, CT is the modality of choice due to the ability to visualise both trabecular and cortical bone with high resolution (Heindel *et al.*, 2014). Despite CT being limited when analysing soft tissues compared to MRI, CT still allows for the detection and segmentation of metastatic lesions (Aldieri *et al.*, 2024).

Segmentation modalities have been compared to assess the reproducibility of each technique depending on the application. To detect and segment tumours, automatic segmentation methods have been applied previously, with U-Net being the most popular algorithm of choice (Cheng *et al.*, 2021; Liang *et al.*, 2024). Segmentation of lesions in soft tissue have shown low repeatability (DSC 0.6-0.73) (Nishio *et al.*, 2021; von Schacky *et al.*, 2021) and segmentation of lesions within bone have also shown similar results (DSC 0.67-0.72) (Xu *et al.*, 2018). Recent studies have successfully applied an automated segmentation algorithm to a dataset of healthy vertebrae (DSC 0.93) (Liang *et al.*, 2024), vertebrae with lytic lesions (DSC 0.93) (Faghani *et al.*, 2023), and fractured vertebrae (DSC 0.93-0.94) (Park *et al.*, 2022). However, these algorithms have not been validated for use in FE applications.

Manual methods such as thresholding have also been applied and validated to laser surface scans resulting in minor mean differences (0.2 mm) (DeVries *et al.*, 2008). The inter-operator variability in this study was also low, having high relative overlaps in all segmentations (0.89-0.93). The high reliability was attributed to the high resolution of the CT and high contrast

between bony structures and surrounding tissue. Similarly, Rathnayaka et al. utilised intensity thresholding and found similar mean differences (0.18 mm) which they deemed an acceptable level due to the error being less than the resolution of the scan (Rathnayaka *et al.*, 2011). Thresholding with manual editing has been utilised in a validation study of finite element models of osteoporotic vertebrae and found excellent correlation with experimental results (R^2=0.94-0.98) (Garavelli *et al.*, 2022). Manual segmentation was also adopted in other FE studies to assess the mechanical properties of vertebrae with metastatic lesions (Costa *et al.*, 2019).

Evaluating intra-operator variability is important for accurate FE model creation. The geometry is highly influential in the accuracy of the FE simulations, so consistent segmentation results in more accurate representation of anatomical structures of interest (Wysocki and Doyle, 2022). Additionally, the segmentation has a direct influence on the material property assignment. For example, if the segmentation varies substantially, the cortical shell may include more or less high-density bone depending on where it is segmented. Another reason for consistent segmentation is to ensure the results of the FE are reproducible. This is important for validating and comparing results across different simulations. Therefore, the aim of this study was to evaluate the intra-operator variability when segmenting healthy vertebrae and vertebrae with lytic lesions. The image quality, a combination of pixel size, slice thickness and tube current, was also compared to the evaluation metrics for reproducibility to understand what has the greatest effect.

3.4.2 Patient Data

QCT scans of healthy control (n=5) vertebra from the ANTELOPE study (Handforth *et al.*, 2024) (Table 3.1 for description of dataset) and of MM patients from clinical data (n=5) (Table 3.2 for description of dataset). The vertebrae segmented in the MM group were selected based off the segment with the largest lesion including cortex infiltration.

3.4.3 Methods

Segmentation software 3D Slicer (3D-slicer 5.6.2, [https://www.slicer.org/] (Fedorov *et al.*, 2012)) was used to generate 3D models of each vertebra. Each vertebra was segmented three times by a skilled operator with the segmentations taking place more than 6 days apart to

reduce memory effects. Masks were created for each vertebrae which represented a number of voxels defining the shape of an anatomical component (Cook *et al.*, 2012). Initially, thresholding was applied to define which voxels were included in the mask depending on their grey level. The threshold was adjusted by the operator until the mask was optimised for the maximum amount of bone and a well-defined cortex whilst minimising soft tissue. Once the thresholding was optimised, the mask was assessed for any bridging, areas between vertebrae where no bony tissue exists, and manually resolved to ensure only bone was included in the mask. The interior of the mask was then filled manually based on the mask boundaries in the sagittal plane. Manual detailing was necessary when the initial thresholding over or under selected the vertebrae. A final check was conducted to ensure all anatomical views of the vertebra were defined by the mask Figure 3.2.

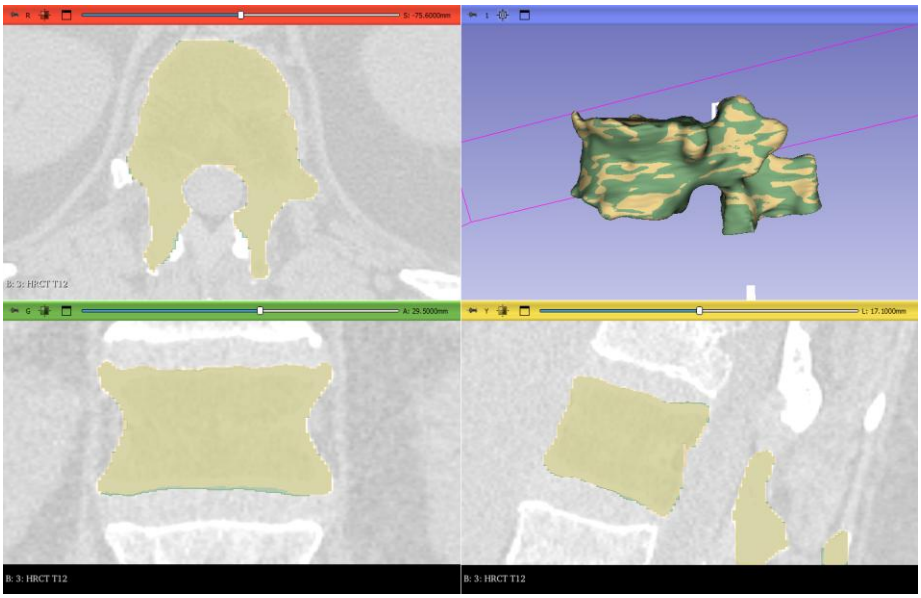

Figure 3.2 - Example of segmentation comparison process in 3D slicer. Two segmentations (1) in yellow and (2) in green.

To evaluate the reproducibility of the segmentations, two evaluation metrics were selected: DSC and Hausforff distance (HD). DSC is a good overall measure of how well something matches by assessing the overlap where a higher value indicates better agreement. HD is useful for assessing differences when there is a complex boundary which is applicable in this case as vertebrae are irregular bones (Taha and Hanbury, 2015). HD is the maximum distance between the points on the boundary of one mask and the closest points on the boundary of the other where lower values indicate better agreement.

DSC:

$$DSC = \frac{2|X \cap Y|}{|X| + |Y|}$$

Equation 3.1

Where X and Y are the two masks being compared, |X ∩ Y| is the size of the overlap between X and Y and |X| and |Y| are the sizes of the masks X and Y respectively.

Hausdorff Distance:

$$H(X,Y) = \max\left(h(X,Y), h(Y,X)\right)$$

Equation 3.2

Where X and Y are two sets of points on masks X and Y respectively and $h(X,Y)$ is the distance between points a and b.

To assess how the image quality affects the reproducibility of the segmentation, the relationship between three parameters and the DSC and HD were evaluated: pixel size, tube current and slice thickness. Pixel size is defined by the distance between the centres of two adjacent pixels in the imaging plane. Smaller pixel size usually results in higher spatial resolution, meaning more detail can be captured in the image and lower partial volume effects. Slice thickness is the distance between the centres of adjacent slices. Smaller slice thickness provides a more continuous coverage of the scanned volume, which can improve the accuracy of volumetric measurements. Tube current is the flow of electric charge through the X-ray tube's filament, measured in milliamperes (mA). Higher tube current results in more X-rays being generated, which can improve the image quality by increasing the signal-to-noise ratio. However, Increasing the tube current increases the amount of radiation delivered to the patient so this needs to be balanced to get the highest image quality without needlessly damaging the patient.

To assess the variability of using the DSC and HD the mean and standard deviation was calculated. To compare the reproducibility of the control and MM groups, a Mann-Whitney U-test was applied where significance was recognised at $P < 0.05$. To compare the variance in segmentation per patient between each group, Levene's test was conducted where $p < 0.05$ indicated significance. The metrics were also compared to pixel size, slice thickness and tube

current using a Spearman rank correlation. Due to the small sample size, an $r \leq 0.5$ represents a weak correlation, $0.5 < r < 0.9$ is moderate correlation and $0.9 < r \leq 1$ is a strong correlation, with p-values where significance was considered for $p < 0.05$. To evaluate the combined use of the image quality parameters, a multivariate linear regression analysis was performed with p-values where significance was considered for $p<0.05$.

3.5 Results

Table 3.5 shows the overall results for the DSC, average and 95% maximum Hausdorff distance, pixel sizing, slice thickness and tube current for both the control and MM groups. There was no significant difference between the control and MM group for both DSC (Control: 0.97 ±0.02, MM: 0.95 ±0.03), mean Hausdorff Distance (Control: 0.27 ±0.22 mm, MM: 0.34 ±0.22 mm) and 95% Hausdorff distance (Control: 0.79 ±0.38 mm, MM: 1.00 ±0.31 mm). There was a trend towards higher reproducibility for the control group, but this would need testing with a larger dataset.

Table 3.5 - Results overview of the DSC, average and 95% Hausdorff distance, pixel size, slice spacing and mean tube current for the control and MM dataset.

	DSC (avg ±std)	Average Hausdorff Distance (mm) (avg ±std)	95% Hausdorff Distance (mm) (avg ±std)	Pixel size (mm) (avg ±std)	Slice Thickness (mm) (avg ±std)	Mean tube Current (mA) (avg ±std)
Control 1	0.98 ±0.009	0.18 ±0.09	0.73 ±0.37	0.9375	0.3	360
Control 2	0.96 ±0.03	0.33 ±0.27	0.66 ±0.57	0.9375	0.3	360
Control 3	0.95 ±0.03	0.43 ±0.33	0.97 ±0.58	0.9375	0.3	360
Control 4	0.97 ±0.02	0.30 ±0.3	0.73 ±0.37	0.9375	0.3	360
Control 5	0.99 ±0.004	0.11 ±0.03	0.88 ±0.11	0.9375	0.3	360
Lytic 1	0.96 ±0.02	0.28 ±0.1	0.8 ±0.2	0.39	0.5	305

Lytic 2	0.95 ± 0.02	0.41 ±0.17	1.38 ±0.2	0.67	1.5	298
Lytic 3	0.95 ±0.02	0.30 ±0.13	0.74 ±0.19	0.39	0.5	186
Lytic 4	0.92 ±0.04	0.60 ±0.34	1.22 ±0.34	0.69	1.25	101
Lytic 5	0.98 ±0.003	0.14 ±0.013	0.87 ±0	0.34	0.5	226
Control avg	0.97 ±0.02	0.27 ±0.22	0.79 ±0.38	0.9375 ±0	0.3 ±0	360 ±0
MM avg	0.95 ±0.03	0.34 ±0.22	1.00 ±0.31	0.4968 ±0.15	0.85 ±0.45	216 ±70
p - value	0.095	0.69	0.2	0.0079	0.0079	0.0079
p - value	0.095	0.69	0.2	0.0079	0.0079	0.0079

Figure 3.3 shows the grouped and individual data for both evaluation metrics for the control and MM groups. The data for the average Hausdorff distance was equally distributed in both the control and MM groups (Figure 3.3, B), as well as having a similar range. The range of DSCs and 95% Hausdorff distance was larger for the MM group compared to the control (Figure 3.3, A & C). For the MM group, the patients whose DSC were the highest (Lytic 1 and Lytic 5) had more similar scan properties to that of the controls (Table 3.5, Figure 3.4 A) which allowed for more consistent segmentation compared to the rest of the cohort. In particular, the patient with the lowest DSC (Lytic 4) has a scan of lower quality, larger pixels and slice thickness and lower tube current (Table 3.5, Figure 3.4 B).

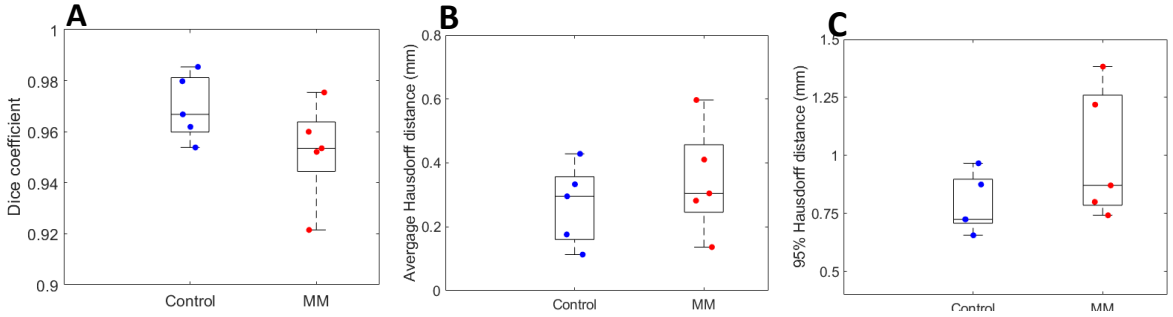

Figure 3.3 - Box plots showing the DSC (A), average Hausdorff distance (B) and 95% Hausdorff distance (C) for the control and MM datasets.

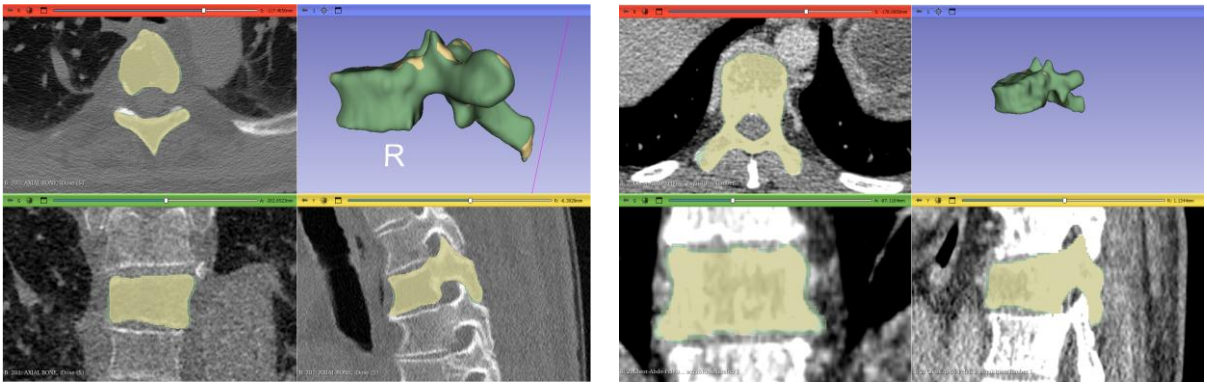

(A) (B)

Figure 3.4 - Representative segmentations of (A) Lytic 1 – CT scan with the best scan quality (B) and Lytic 4 – CT scan with the worst scan quality.

Due to the difference in segmentation consistency in the MM group, the relationship between the evaluation metrics and the current, pixel size and slice thickness were evaluated. Linear regressions were constructed, and the significance of the correlation was determined (Figure 3.5). The current had a weak and insignificant correlation with the DSC ($r = 0.5$, $p = 0.45$) and the Hausdorff distance ($r = -0.5$, $p = 0.45$). However, the Pixel size had a strong but insignificant correlation with the DSC (-0.9, $p = 0.08$) and a moderate but insignificant correlation the Hausdorff distance ($r = 0.8$, $p = 0.13$). Similarly, the slice thickness had a moderate but insignificant correlation with both the DSC ($r = -0.78$ $p = 0.2$) and Hausdorff distance ($r = 0.78$, $p = 0.2$).

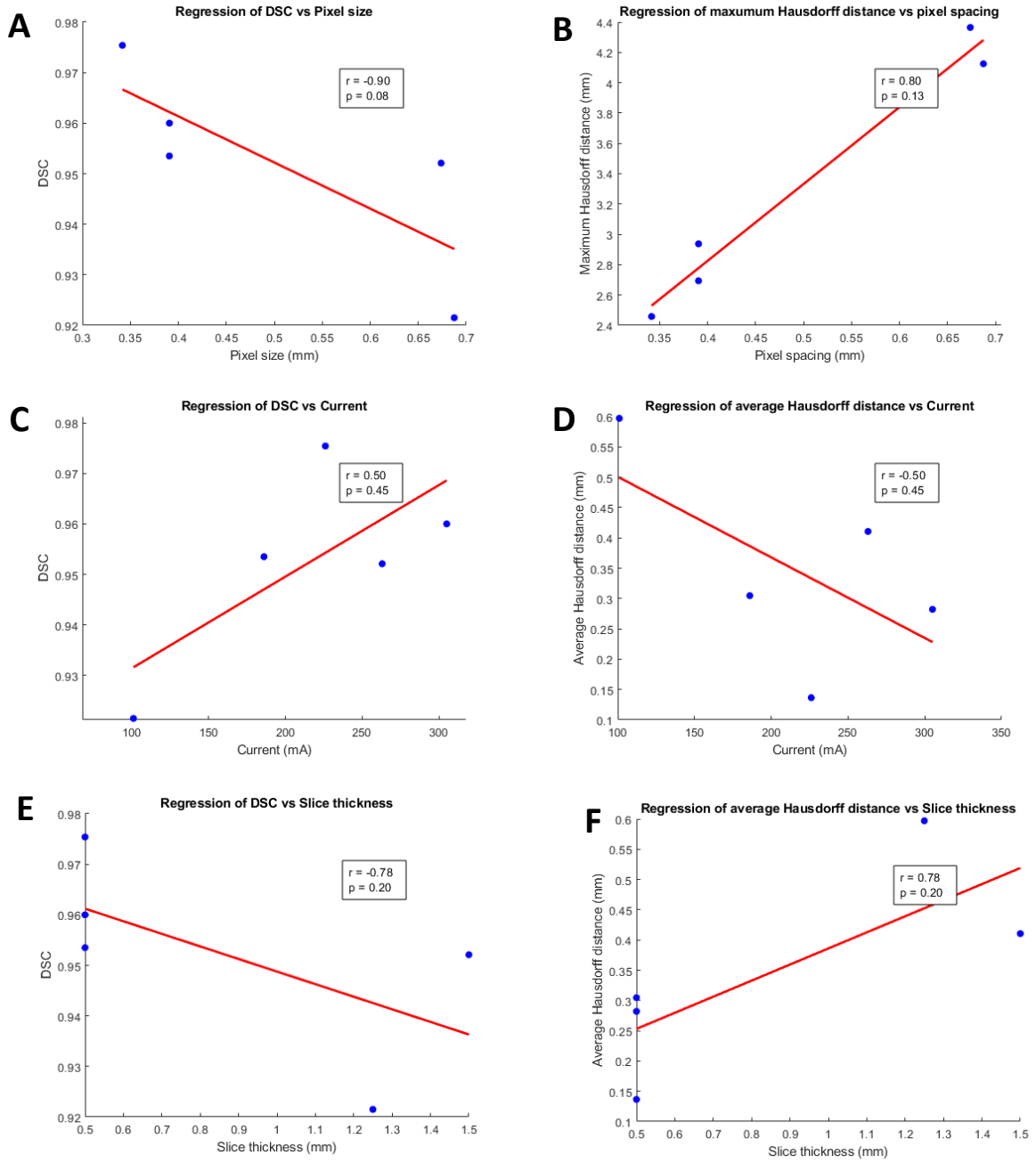

Figure 3.5 - Linear regression analysis between (A) Pixel size and DSC, (B) Pixel thickness and Hausdorff distance, (C) Tube current and DSC, (D) Tube current and Hausdorff distance (E) Slice thickness and DSC and (F) Slice thickness and Hausdorff distance.

As the relationship between the evaluation metrics and pixel size and slice thickness was moderate to strong but not significant, a multivariate analysis was conducted to understand whether the combination of these two scan properties significantly influenced the segmentation reproducibility (Figure 3.6). The pixel size and slice thickness could significantly ($p = 0.014$) explain 98.6% of the variance in the DSC. There was a significant, strong, negative

relationship between pixel size and the DSC (p = 0.011) and a significant positive relationship between the slice thickness on the DSC. The pixel size and slice thickness could significantly (p = 0.006) explain 99.4% of the variance in the Hausdorff distance. In comparison to the DSC, pixel size had a significant, positive relationship on the Hausdorff distance (p = 0.007) while slice thickness had a significant, negative relationship with Hausdorff distance (p = 0.015).

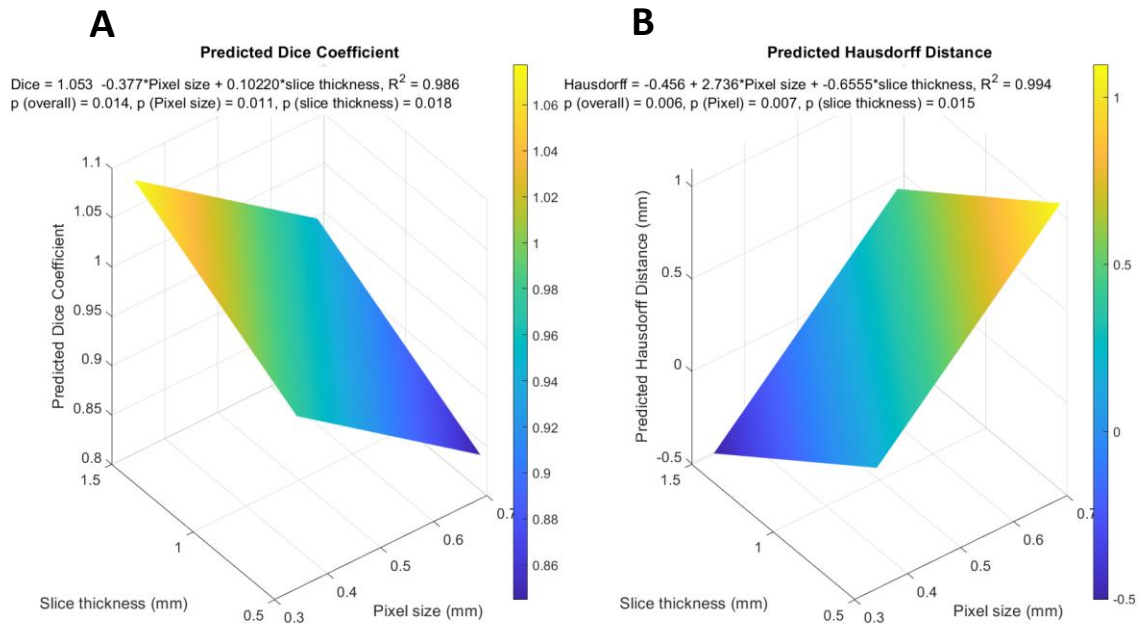

Figure 3.6 - Multivariate analysis of the combined effects of Image quality parameters and the evaluation metrics. (A) predicted DSC from a combination of slice thickness and pixel size, (B) predicted Hausdorff distance from slice thickness and pixel size.

3.5.1 Discussion

The evaluation of the segmentation accuracy revealed better consistency in the control group due to the slightly higher average DSC. However, both groups exhibited high DSC (>0.9), indicating good overall segmentation accuracy. In addition, the MM group had a slightly higher average Hausdorff distance, suggesting slightly worse spatial accuracy.

The correlation between tube current and both evaluation metrics was weak and not statistically significant. This indicates that tube current has a limited impact on segmentation accuracy. The tube current increases image contrast, possibly aiding the thresholding stage of the segmentation. Nevertheless, an increase in tube current can also increase the noise

and degradation of the image, which could explain why higher tube currents are not highly correlated with a high DSC or low Hausdorff distance. The study found a strong but insignificant correlation between pixel size and both the DSC and average Hausdorff distance and a moderate but insignificant correlation between slice thickness and both the DSC and average Hausdorff distance.

To further analyse the use of these parameters in predicting segmentation consistency, the multivariate analysis evaluated combinations of these parameters. The variance in the DSC could be explained by the combination of the pixel size and slice thickness. The pixel size and slice thickness both contribute significantly to the overall image quality, with pixel size primarily effecting the spatial resolution and noise level and slice thickness mainly dictating how much axial volumetric information is gathered. Therefore, as the DSC is a measure of overlap, a smaller pixel size would allow for more consistent selection of the correct pixels and a smaller slice thickness would reduce the differences in the axial direction. For the Hausdorff distance, the combination of both pixel size and slice thickness gave a significant explanation of up to 99% of the variance. The Hausdorff distance in the individual regression analysis was negatively influenced by both pixel size and slice thickness, suggesting that a larger pixel size and slice thickness increased the averaged difference at any two points between the two segmentations.

3.5.2 Conclusion

While the study did not find significant differences between the control and MM groups, it is essential to consider the limitations of the dataset. The sample size was relatively small, and the variability within the MM group may have been limited. Further studies with larger datasets and a wider range of scanning protocols and vertebral levels are needed to confirm the generalisability of these findings.

This study demonstrates the significant impact of image quality on vertebral segmentation in QCT scans. Pixel size and slice thickness emerged as key predictors of segmentation accuracy, with smaller pixel sizes and thinner slices leading to improved results. These findings highlight the importance of optimising image acquisition parameters to enhance the reliability and accuracy of vertebral segmentation. By carefully considering factors such as pixel size and

slice thickness, researchers and clinicians can improve the quality of segmentation results for various applications, including clinical diagnosis, treatment planning, and research.

While the image quality parameters varied in the lytic groups CT scans, influencing the reproducibility, the DSC and Hausdorff distances were considered acceptable for processing through the rest of the FE pipeline. For the following studies in this thesis, segmentations were performed once by the same trained operator to ensure the same consistency as reported in this section.

3.6 Phantom and phantomless densitometric calibration

The aim of this subchapter was to estimate the densitometric calibration laws, with a calibration phantom, which are used in the mapping of the heterogeneous material properties of the QCT-based FE models of vertebrae used in Chapter 4 to study the effect of ADT in prostate cancer patients. The ANTELOPE dataset was then used to validate the phantomless calibration method later used in Chapter 5 to assess the effect of remineralisation of lytic lesions in MM patients following treatment.

3.6.1 Patient Data

The ANTELOPE dataset was utilised for this subchapter where all fifty QCT scans, both control and treated, were used. More information on this dataset can be found in Table 3.1 and Section 3.2.1.

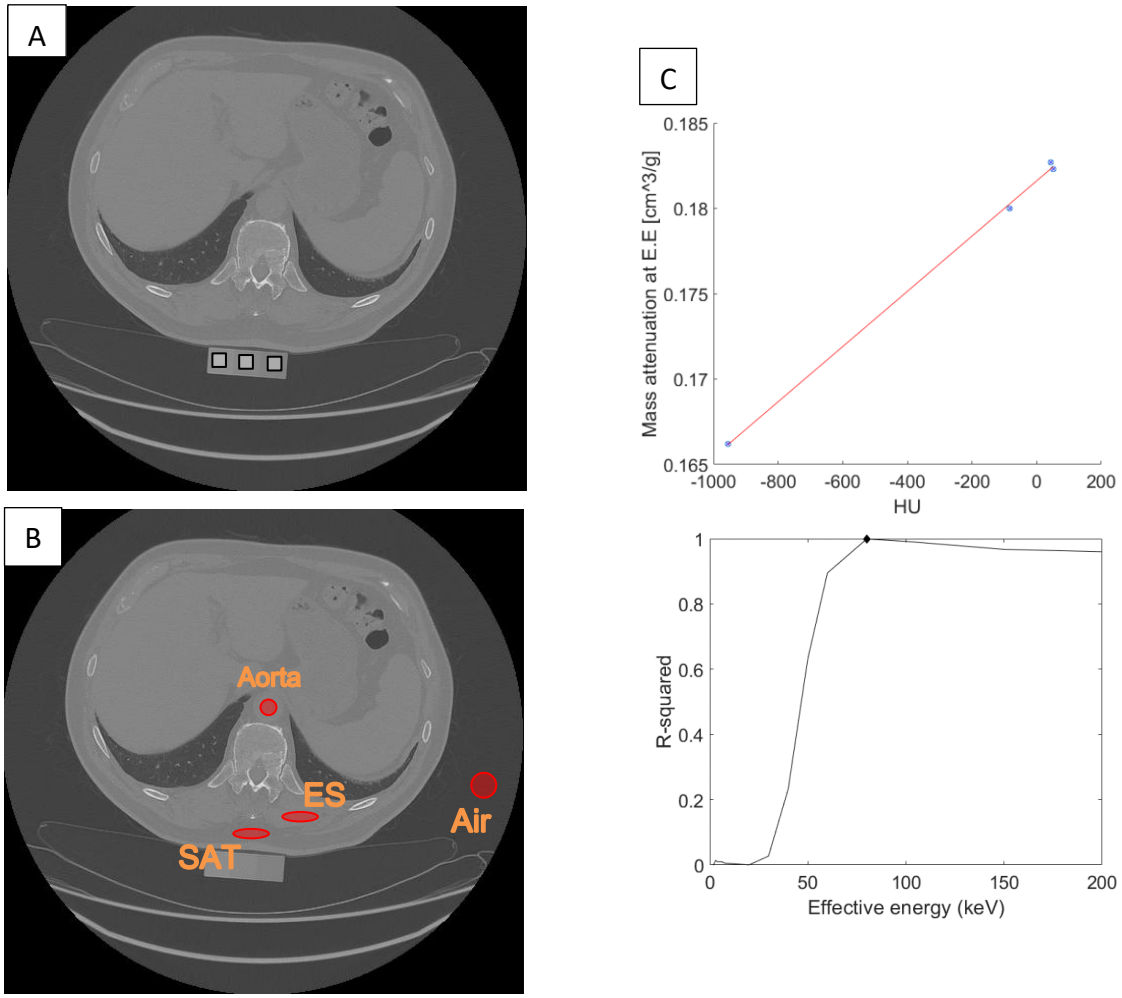

Figure 3.7 - Density calibration methods for quantitative CT analysis. (A) Phantom-based calibration uses the phantom. Each calibration rod is sampled from the image to determine linear conversion between HUs and equivalent density. (B) In scan tissues of reference (adipose (SAT), air, blood (aorta), and skeletal muscle (ES)) are sampled adjacent to the bone of interest for internal calibration. (C) HUs and mass attenuation coefficients for each tissue (circle data points) are correlated by iterating at each effective energy (EE). Scan effective energy is determined by maximizing the coefficient of determination across all effective energies (black diamond).

3.6.2 Calibration with phantom

The QCT scan protocol included a solid inline calibration phantom (Image Analysis, Inc., Columbia, KY, USA) containing rods of 0, 0.075, and 0.15 g/cm^3 equivalent concentration of calcium hydroxyapatite. The densitometric calibration was computed using a standard approach, which assumes a linear relationship between the average Hounsfield units (HU) and the known equivalent mean values of equivalent BMD of each rod. To do so, one region of interest (ROI), Figure 3.7A, was defined manually within each insertion of the phantom (ImageJ) (Rasband, 1997; Schneider, Rasband and Eliceiri, 2012). The ROIs were defined as square regions centred within each calibration rod with length equal to half the edge length of the rod (12.5 mm). For each of the three rods, mean HU values over the same 10 slices were used to perform the linear regression analysis for calibration, Equation 3.3.

$$\rho_{QCT} = \mathrm{a} + \mathrm{b}HU$$

Equation 3.3

Where ρ_{QCT} represents the QCT equivalent BMD, HU represents the Hounsfield unit values of the densitometric calibration law and a and b are constants from the linear regression analysis performed.

3.6.3 Phantomless Calibration

To calculate the phantomless calibration equation, a combination of internal materials (IM) was used. From each scan, tissue ROIs for adipose (SAT), air, aortic blood, and skeletal muscle (ES) were manually sampled from the scan field-of-view, as depicted in Figure 3.7B. To reduce influence of variations in tissue HUs across the scan field-of-view, the ROIs were placed adjacent to the bones of interest (T12 vertebra) for each tissue, and the mean HUs were determined from the tissue sample aggregated histograms of ten 2D slices. Using mass absorption coefficients obtained from the National Institute of Standards and Technology (www.nist.gov National Institute of Standards and Technology, NISTIR 4999), the scan effective energy was estimated by iteratively correlating the ROI-specified HUs and corresponding mass absorption coefficient at each energy level and maximizing the coefficient of determination (Millner *et al.*, 1978), as shown in Figure 3.7C. For compounds as HA (Ca10(PO4)6(OH)2, [24]) that are not tabulated in NIST, mass absorption coefficients can be calculated if the atomic mass fractions and the mass densities are known. Once the scan

effective energy was determined for the scan, the mass absorption coefficients, equivalent density and measured HU values for each material were used in a two-component mass fraction model (Genant and Boyd, 1977) to calculate the associated calibration equation, Equation 3.4.

$$\rho_{QCT} = \frac{\left(\frac{\mu}{\rho}\right)_1 \rho_1 \frac{HU - CT_2}{CT_1 - CT_2} + \left(\frac{\mu}{\rho}\right)_2 \rho_2 \frac{HU - CT_1}{CT_2 - CT_1} - \left(\frac{\mu}{\rho}\right)_w \rho_w}{\left(\frac{\mu}{\rho}\right)_{HA} - \left(\frac{\mu}{\rho}\right)_w \frac{\rho_w}{\rho_{HA}}}$$

Equation 3.4

Where ρ_{QCT} represents the QCT equivalent BMD, HU represents the Hounsfield unit values of the densitometric calibration law, CT_1 and CT_2 represent the averaged grey value of each internal material, ρ_1 and ρ_2 represent the density of each internal material, ρ_w and ρ_{HA} represent the density of water and hydroxyapatite respectively and $\left(\frac{\mu}{\rho}\right)_1$ and $\left(\frac{\mu}{\rho}\right)_2$ represent the mass absorption coefficient for the internal material, $\left(\frac{\mu}{\rho}\right)_w$ and $\left(\frac{\mu}{\rho}\right)_{HA}$ represent the mass absorption coefficients for water and hydroxyapatite respectively.

Table 3.6 - Mass densities of internal calibration materials obtained from the National Institute of Standards and Technology (NIST) database. ES: erector spinae muscle, SAT: subcutaneous adipose tissue.

Material	Density (g/cm^3)
Blood	1.06
Air	1.205 X10^{-3}
ES	1.04
SAT	0.92

In order to validate the theoretically calculated accuracy errors for each of the fifty datasets, measured trabecular CT values of the T12 vertebra were converted to BMD by the linear phantom and phantomless calibration equations. Then for each scan, the difference ΔBMDs between the phantomless calibration and the standard phantom based QCT procedure was determined.

3.6.4 Results

Figure 3.8 shows the absolute BMD differences between phantomless and phantom based calibration. Highest mean ΔBMDs values were found for the combination of air and fat (SAT) (0.0197 g/cm^3) and for the combination of adipose tissue and ES muscle (0.0156 g/cm^3). For all other IM combinations, the mean difference was below 0.015 g/cm^3, with the smallest ΔBMDs mean value for the combination of aorta and air (0.0045 g/cm^3).

Figure 3.9 details the linear regressions of between the phantom and phantomless estimated BMD values for all IM combinations. Spearman's correlation was calculated, and all paired combinations had a strong and significant correlation between phantom and phantomless BMD, with the combination of air and aorta having the strongest correlation ($r = 0.98$, $p < 0.01$).

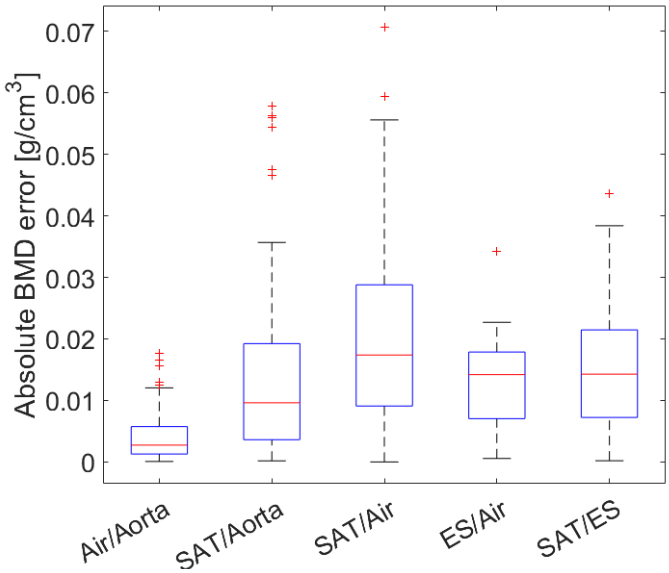

Figure 3.8 - Absolute BMD differences between phantomless and phantom based calibration for five different IM combinations. Top and bottom horizontal borders of the blue box indicate the 25th and 75th percentiles with their distance representing the interquartile range (IR), the red line shows the median. Red points outside the dashed lines (Whisker) are outlies with values > 1.5 × IR.

Therefore, for future studies, in this thesis, using the phantomless calibration method, the combination of air and aorta will be used.

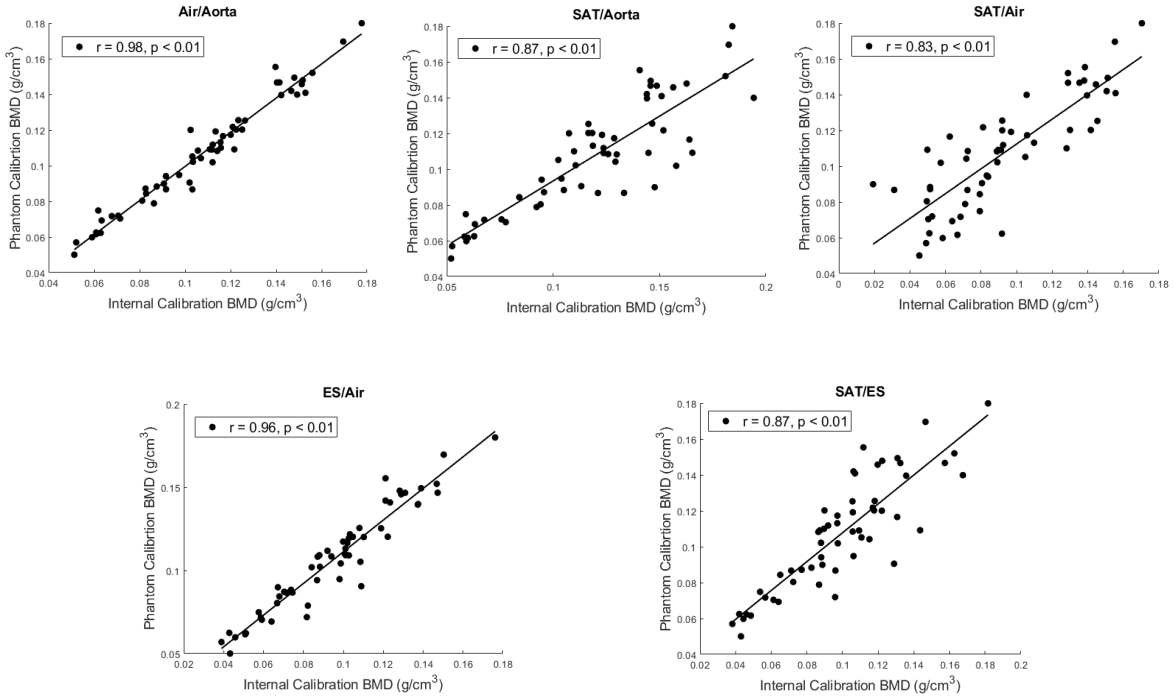

Figure 3.9 - Linear regressions between the phantom and phantomless BMD for all internal material combinations.

3.7 Mesh Convergence Analysis

3.7.1 Patient data

Data relative to one patient was used in this preliminary analysis towards the definition of the FE modelling methodology. The chosen dataset (P1a) was representative of a critical lytic vertebra present within the RNOH multiple myeloma study's cohort (see section 3.2.2). From this patient, three vertebrae were modelled: one with a lytic lesion (T4) and two adjacent controls without lesions (T3 and T5).

3.7.2 Methods

Each vertebra was reconstructed from clinical CT scans into a 3D model using 3D-Slicer (Fedorov *et al.*, 2012). The vertebra models were then aligned to ensure the loading was applied perpendicular to the endplates of the vertebral body. This was conducted by creating

best-fit planes on the superior and inferior endplates and aligning the vertebra to the average of these two planes. This process was completed in Ansys Spaceclaim (Ansys®, [Spaceclaim], 2021R1, ANSYS, Inc). The endplates were also identified and labelled on the vertebral body, in Spaceclaim, to create a surface for ease of applying the boundary conditions (Figure 3.10). Each model was prepared using Spaceclaim to ensure sufficient meshing by removing anomalous sharp edges and floating elements. The models were meshed with quadratic (10 node) tetrahedral elements in Ansys Mechanical (Ansys®, [Workbench Mechanical], 2021R1, ANSYS, Inc).

The minimum edge size of the quadratic tetrahedral elements was set to 0.675mm which is equal to the lowest image resolution of the CT scans. The edge size was increased by a factor of 1.48 to create 3 coarser meshes (esize = 1.00, 1.48 and 2.19mm).

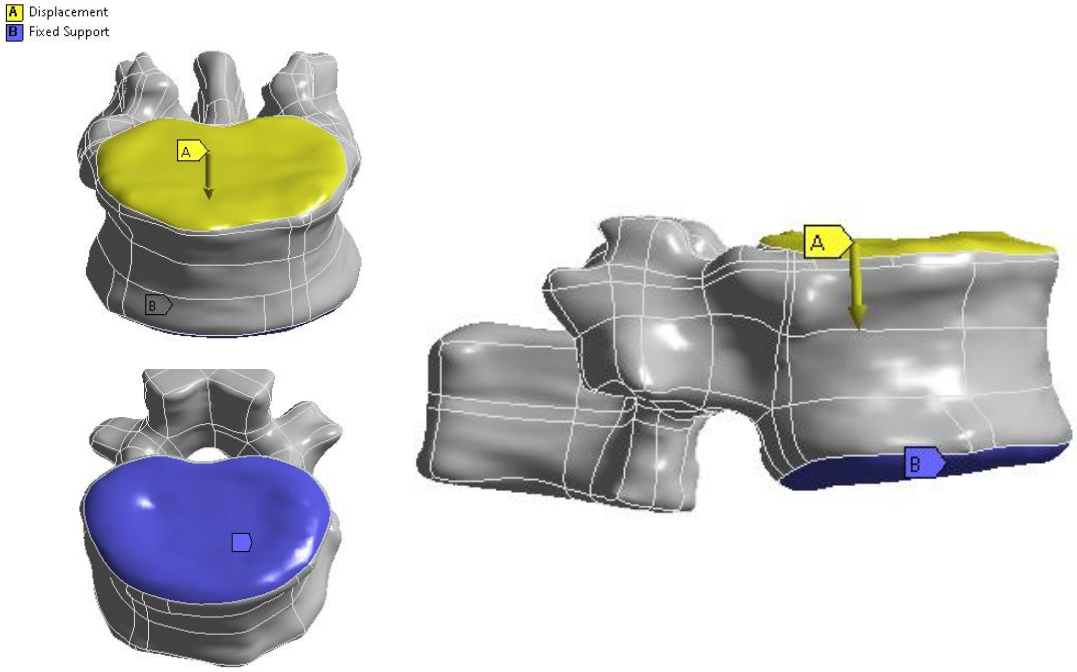

Figure 3.10 - Application of boundary conditions. (A) The displacement applied to the superior endplate. (B) The fixed support applied to the inferior endplate.

Both bone and lytic tissue were modelled as heterogenous, isotropic, and elastic-plastic materials, following the assumption that lytic lesions only affect local bone density (Nazarian *et al.*, 2008). Bonemat (BONEMAT®, 2013) was used to map the linear material properties for each vertebra model using the patient specific densitometry phantomless calibration equation (see Section 3.2) and phenomenological relationships (Equations 3.5 and 3.6). The plastic behaviour of bone was modelled as isotropic and symmetric, where the yield stress

criterion is computed based on a density-strength relationship [Equation 3.7], and a 95% reduction in the post-yield elastic modulus [Equation 3.8] as shown in Figure 3.11. The density determined by CT (ρ_{QCT}) and ashing density (ρ_{ash}) is highly correlated (Schileo *et al.*, 2008), therefore it is assumed that $\rho_{QCT} = \rho_{ash}$.

$\rho_{ash} = \rho_{QCT} = \rho_{app} \times 0.6\ [g/cm^3]$; (Schileo *et al.*, 2008)

Equation 3.5

Where ρ_{QCT} is the QCT equivalent BMD and ρ_{app} is the apparent density.

$E = 4730{\rho_{app}}^{1.56}\ [MPa]$; (Morgan, Bayraktar and Keaveny, 2003)

Equation 3.6

Where E defines the elastic modulus as a function of the apparent density, ρ_{app}.

$\sigma_{y1} = 21.7{\rho_{app}}^{1.52}\ [g/cm^3]$; (Morgan and Keaveny, 2001)

Equation 3.7

Where σ_{y1} represents the yield stress in tension as a function of the apparent density, ρ_{app}.

$E_{py} = 0.05 \times 4730{\rho_{app}}^{1.56}\ [MPa]$; (Niebur *et al.*, 2000; Morgan, Bayraktar and Keaveny, 2003)

Equation 3.8

Where E_{py} symbolises the post-yield elastic modulus as a function of the apparent density, ρ_{app}.

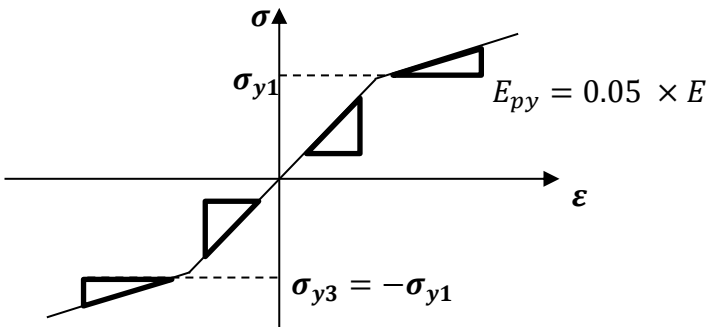

Figure 3.11- Representation of the bilinear, isotropic, and symmetric yield stress criterion used to model the elastic-plastic behaviour of each vertebral model.

The models were loaded in compression on the superior endplate with a displacement of 1.9% of the minimum vertebral height (H) (Figure 3.12). The use of 1.9% apparent deformation has been experimentally proven to produce ultimate stress in vertebral bodies (Crawford, Cann and Keaveny, 2003; Wang *et al.*, 2012; Keaveny *et al.*, 2014). The elements on the inferior endplate were fixed in all directions Figure 3.10.

For each vertebra level, the node containing the maximum compressive strain (EPEL3) in all models was reported. The failure load (FL) was calculated as the sum of the axial forces on the inferior endplate of each vertebral model and displacement was computed from the axial displacement of the central node on the superior endplate. The linear range of the force-displacement curve was used to calculate the stiffness (K). The cross-sectional area (CSA) was calculated as the mean CSA of the vertebral body, excluding the endplates and posterior components. The apparent modulus (E) was calculated using Equation 3.9.

$$E = K \times \frac{H}{CSA}$$

Equation 3.9

Where E is defined by spring stiffness (K) multiplied by the ratio between the vertebral height and CSA of each vertebra. The ultimate strength (σ_U) is calculated using Equation 3.10.

$$\sigma_U = \frac{FL}{CSA}$$

Equation 3.10

Where σ_U is defined as the ratio between the resultant force at 1.9% strain (FL) and the CSA.

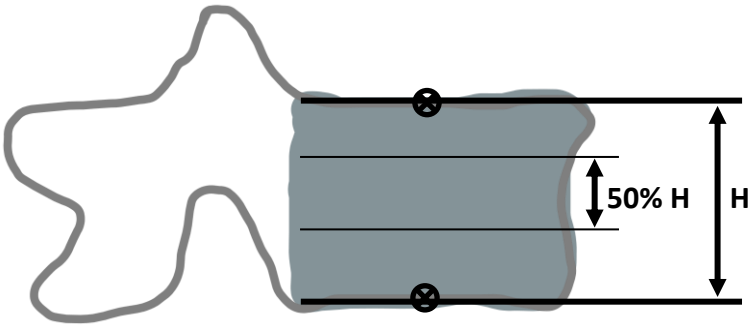

Figure 3.12 - Schematic representation of the region (grey) of the vertebral bodies considered for analysis along with the definition of vertebral height (H) and 50% vertebral height.

The mesh convergence was assessed based on the predicted EPEL3, the apparent modulus (E), and the ultimate strength (σ_U). To reduce the influence of the boundary conditions on the local properties, EPEL3 was evaluated in the central 50% of the vertebral body, excluding all posterior regions that were beyond the vertebral body (Figure 3.12).

To evaluate whether convergence was achieved, the percentage difference (%diff) was calculated with respect to the values obtained from the most refined model (esize = 0.675 mm). If the percentage difference was less than 10% for all results, the model was considered to be converged (Niebur *et al.*, 1999). The distribution of the elastic modulus was also computed for each refined model and vertebra level to assess the uniformity between the most refined models.

3.7.3 Results

For the vertebrae with a lytic lesion (T4) and the controls (T3 and T5), Table 3.7 shows the percentage difference of compressive strains between the two most refined models (0.675 mm and 1 mm) to be <10%. However, as the mesh becomes coarser to element size 1.48 mm, the percentage difference increased to 43% in T3 (control) and 50% in T4 (lytic) whilst the difference for T5 (control) remained small at 3.9%. A similar trend was observed within the predicted properties of ultimate strength and apparent modulus but with much smaller percentage differences. For both predicted values, the percentage difference was <2% between the two most refined models in all vertebrae. Changes in the elastic tissue modulus between the models with element size 0.675 mm and 1mm were minimal (Figure 3.13) and the decrease in element size resulted in a decrease in variability for all vertebrae.

In general, the percentage difference decreased with increasing refinement. This was most likely due to the smoother reconstruction of the geometry. Although the percentage differences of EPEL3 are close to 10%, the smallest percentage differences are found in the predicted properties of ultimate strength and apparent modulus and as this study will focus on the analysis of the predicted mechanical properties, an element size of 1mm is acceptable. In addition, due to the large number of models being simulated for this study, a decrease in computation time of 75% is significant.

Table 3.7 - Report of the element size, computational cost (time) and percentage difference from the most refined model of local and normalised structural properties (EPEL3, σ_U and E).

Level	Condition	Element size (mm)	Time (mins)	Max EPEL3 (ε) (%diff from 0.675 mm)	σ_U (MPa) (%diff from 0.675 mm)	E (MPa) (%diff from 0.675 mm)
T3	Control	2.19	2.58	0.012 **(-60%)**	2.56 **(2.8%)**	763 **(3.4%)**
		1.48	14.2	0.017 **(-43%)**	2.54 **(2%)**	755 **(2.4%)**
		1	38.87	0.028 **(-6.7%)**	2.53 **(1.6%)**	740 **(<1%)**
		0.675	**148**	**0.030**	**2.49**	**738**
T4	Lytic	2.19	4.33	0.028 **(17%)**	3.46 **(-1.7%)**	891 **(<1%)**
		1.48	11 .37	0.012 **(-50%)**	3.51 **(<1%)**	889 **(<1%)**
		1	45.8	0.022 **(-8%)**	3.51 **(<1%)**	891 **(<1%)**
		0.675	**204**	**0.024**	**3.52**	**891**
T5	Control	2.19	5.36	0.012 **(-22%)**	2.94 **(3.5%)**	794 **(4.2%)**
		1.48	11.2	0.016 **(3.9%)**	2.79 **(-1.8%)**	769 **(<1%)**
		1	41.36	0.015 **(2.6%)**	2.88 **(1.4%)**	764 **(<1%)**
		0.675	**156**	**0.015**	**2.84**	**762**

The mesh chosen to use for the rest of this thesis was a maximum edge length of 1 mm. The element size was therefore larger than the CT voxel size and the thickness of the cortical shell (<0.5 mm). Hence, partial volume effects would have been observed on those elements close to the border of the cortical and trabecular bone, because their material properties are derived from the mean of the two bone tissues. One solution to this would be to introduce thin-shell elements when meshing the cortical region (Liebschner *et al.*, 2003; Imai *et al.*, 2006). However, due to the limitations of the material mapping software, Bonemat, the use of smaller elements was not feasible in this study.

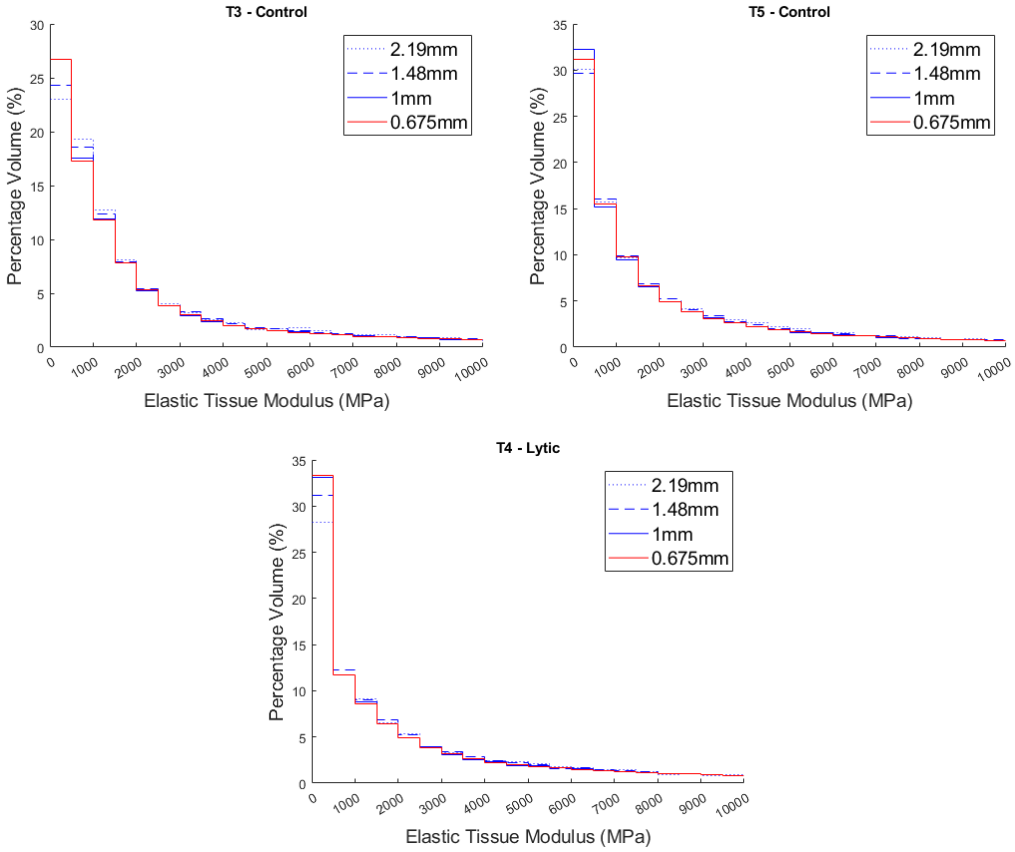

Figure 3.13 - Distribution of the elastic tissue modulus in each of the mesh refinement models generated from the control vertebrae (T3 and T5) and from the vertebra with the lytic lesion (T4).

3.8 Conclusions

This chapter forms the basis for the FE pipeline which will be applied in Chapter 4-Chapter 7 of this thesis. It will be used to; investigate the effect of treatment on vertebral strength of prostate cancer patients (Chapter 4), investigate the effect of treatment on the vertebral strength of multiple myeloma patients (Chapter 5) and develop a mechanobiological model coupling the organ level FE with cell-level interactions (Chapter 6 and Chapter 7).

4 ALTERED VERTEBRAL BIOMECHANICAL PROPERTIES IN PROSTATE CANCER PATIENTS FOLLOWING ANDROGEN DEPRIVATION THERAPY.

4.1 Introduction

As described in Chapter 2, Prostate cancer (PCa) is the most common non-skin cancer among men (Jemal *et al.*, 2010) and the median age at PCa diagnosis is around 66 years (Rawla, 2019). The effects of the disease itself, its treatment and the age of many PCa patients cumulatively give rise to substantial skeletal morbidity (Saylor *et al.*, 2011; Anderson and O'Sullivan, 2022). Androgen deprivation therapy (ADT), which reduces the growth and development of androgen dependant PCa cells, by reducing testosterone levels, is the standard of care for many men diagnosed with PCa. Numerous studies have demonstrated the benefits of ADT in improving survival in patients, with both localised and metastatic PCa (Shore, 2020; Kishan *et al.*, 2022). However, since bone health is also dependent upon androgens, ADT is associated with negative impacts on the skeleton, including a decrease in bone mineral density (BMD) (Abrahamsen *et al.*, 2007) and an increase in fracture risk (Shahinian *et al.*, 2005; Brown *et al.*, 2020; Suarez-Almazor *et al.*, 2022).

Studies have shown that ADT disrupts the bone remodelling cycle. Testosterone and oestradiol levels, important factors in the maintenance of adult bone, are reduced following ADT (Khosla, Joseph Melton and Lawrence Riggs, 2002; Almeida *et al.*, 2017). Greenspan et al described how a reduction in testosterone was significantly correlated with a reduction in areal BMD (aBMD) after 6-12 months of ADT (Greenspan *et al.*, 2005). Other studies have shown a significant decrease in total hip, femoral neck, and lumbar spine areal BMD (aBMD) by 1.5-4.0% annually following commencement of ADT, which exceeds both normal annual bone loss for healthy ageing males and that of postmenopausal women (2.5%) (Higano, 2008; Seifert-Klauss *et al.*, 2012). Despite this, prospective studies reporting bone loss with ADT in men with nonmetastatic PCa have often not evaluated the association of fractures with ADT. However, the correlation of fractures with ADT in PCa patients was evaluated by three large retrospective studies that reported these patients having a 21-37% higher risk of fracture compared to PCa patients who were not treated with ADT (Shahinian *et al.*, 2005; Smith *et*

al., 2005, 2006). Smith and colleagues, also reported that vertebral fractures were 18% more likely to occur following ADT, as well as an overall fracture risk increase of 13% (Smith *et al.*, 2006).

Dual energy X-ray absorptiometry (DXA) is the 'gold standard' clinical method for measuring areal BMD (aBMD, in g/cm^2) and determining fracture risk as part of a comprehensive fracture risk assessment. However, fracture risk is also associated with bone strength, which in turn is dependent on bone quantity and quality. As a 2D projected measurement, DXA cannot provide information on the 3D shape and the large regional variation in vertebral geometries and the distribution of BMD throughout the bone volume. Moreover, DXA measurements of aBMD in the vertebral body are affected by either the presence of the posterior elements (anterior-posterior DXA) or by the ribs or pelvis (lateral DXA). Therefore, to fully capture bone strength, a three-dimensional (3D) quantitative evaluation of the bone biomechanics is necessary. Quantitative computed tomography (QCT) has been used to quantify volumetric BMD (vBMD, in g/cm^3) at various sites such as the spine, hip and femur (Engelke *et al.*, 2008), as a measure that more accurately captures the 3D distribution of mineral in bone tissue. QCT has several advantages over DXA as it can perform sub-regional analysis whilst incorporating the 3D geometry of bone (Engelke *et al.*, 2008).

This more holistic approach has recently been employed in a longitudinal, observational clinical trial of PCa patients commencing ADT (the ANTELOPE trial) (Handforth *et al.*, 2024). In this study, 31 men with non-metastatic PCa, scheduled to commence ADT, were recruited from urology/oncology clinics at the Royal Hallamshire Hospital, Sheffield, along with recruitment of 30 healthy male volunteers matched by age (± 5 years), height (± 5 cm) and body mass index (BMI) (± 5 kg/m^2) to the patients in the ADT treatment group. This patient and volunteer number was chosen to reflect the need for powering the ANTELOPE primary endpoint, which was a change in 12-month vBMD at the distal radius. A range of assessments including aBMD at hip and lumbar spine by DXA scan, vBMD and other microarchitectural parameters at the non-dominant radius by high-resolution peripheral quantitative computed tomography (HR-pQCT), bone turnover markers and other measurements of muscle function and strength and body composition were carried out at baseline and again at 12 months. Overall, the ADT treated group had a significant decrease in lumbar spine aBMD ($p<0.001$), radius trabecular vBMD ($p<0.001$) and cortical vBMD ($p<0.001$), and ultimate failure load at

the radius (p=0.03). Full details of trial design and inclusion/exclusion criteria have been published (Handforth *et al.*, 2024).

Nevertheless, it remains that little is known about the effect of ADT on vertebral strength. QCT images can be used to create 3D biomechanical models, using finite element (FE) analysis of the vertebra to estimate the bone strength. Subject specific FE models have been used extensively to study the biomechanical response of bones to loading (Engelke, van Rietbergen and Zysset, 2016; Schileo and Taddei, 2021). This technique is being used increasingly in bones affected by diseases such as osteoporosis (Matsumoto *et al.*, 2009) and different types of cancer including breast, colorectal and renal cell carcinoma (Costa *et al.*, 2019). It has also been used to study the effect of treatments and has been proven to predict vertebral strength more accurately than DXA in individuals without skeletal diseases (Crawford, Cann and Keaveny, 2003; Dall'Ara *et al.*, 2012) and with osteoporosis (Imai, 2015).

Despite studies investigating the effect of ADT on the peripheral strength of the distal radius using HR-pQCT (Dalla Via *et al.*, 2019), and femoral strength and fracture risk using biomechanical computed tomography (BCT) (Lin *et al.*, 2023), the vertebral strength is yet to be obtained using FE models based on QCT images of the vertebra. Therefore, this chapter aims to address the first hypothesis of this thesis "The vertebral strength of prostate cancer patients reduces when administered with ADT" by uniquely including a comparison of the effect of ADT on the aBMD, measured in the ANTELOPE design, with QCT based vBMD and FE estimated mechanical strength of vertebrae.

4.2 Materials and Methods

4.2.1 Study Design and Participants

The overall study design of the ANTELOPE trial and demographics of the participants have been described elsewhere in Handforth et al. (2024) (Handforth *et al.*, 2024). QCT images of the T12 vertebra for baseline and 12-months were obtained from the ANTELOPE trial, details of patients can be found in Chapter 3. All patients were received intravenous ADT and there was no presence of vertebral fracture in any of the patients T12 vertebra assessed in this study.

4.2.2 DXA and aBMD Measurements

All study participants underwent a posterior-anterior DXA (Discovery A, Hologic, USA) of the lumbar spine, at baseline and 12 months, at the NIHR Clinical Research Facility, Northern General Hospital, Sheffield. Lumbar spine (L1-L4) aBMD (g/cm^2) was also measured.

4.2.3 QCT and vBMD Measurements

The QCT protocol is detailed in Section 3.2.1. The Calibration protocol is detailed in Section 3.6.2, where all scans were individually calibrated to remove any differences in scanning protocol, the type of scanner, and the effect of these on the current study.

For the assessment of trabecular vBMD, from each QCT an ellipse shaped ROI was identified (ImageJ) in the anterior most region of the vertebral body, in the trabecular portion only. The ellipse was identified by creating a circular region of interest in the vertebral body, ensuring the cortical portion was included. The height and the width of the circular region were then reduced by 60% and 20%, respectively. After that, the ellipse was moved to ensure it was in the top half of the vertebral body and 10% away (in terms of width) from all edges. This ROI was extended to include the 10 central slices of the vertebral body. HU values within the ROI for all slices were converted into vBMD using the densitometric calibration identified as described above. For the integral vBMD, the FE software Ansys Workbench (2021R1) was used to select a ROI for all the elements in each vertebral body, excluding the posterior elements and processes, incorporating both the cortical and trabecular regions. The integral vBMD (g/cm^3) was then calculated as the sum of the individual element's bone mineral content (element BMD multiplied by element volume) divided by the total volume of the vertebral body ROI.

4.2.4 FE Models and Mechanical Properties

The models were constructed and simulated using the pipeline described in Chapter 3 and material properties were assigned from the CT image according to the phantom calibration process in Chapter 3. Briefly, CT scans at baseline and follow-up were segmented in 3D-Slicer (Fedorov *et al.*, 2012) to produce 3D models of the vertebrae. They were aligned using the average of two best fit planes, one on the superior endplate and one on the inferior endplate. The models were meshed using a 1mm quadratic tetrahedral mesh following the mesh

refinement study (Chapter 3). A 1.9% strain was applied in axial compression to the superior endplate to simulate failure (Crawford, Cann and Keaveny, 2003; Wang *et al.*, 2012; Keaveny *et al.*, 2014), while the inferior endplate was fixed in all directions. The failure load (FL), stiffness (K), apparent modulus and ultimate strength were calculated as described in Section 3.7.2 and shown in Figure 4.1.

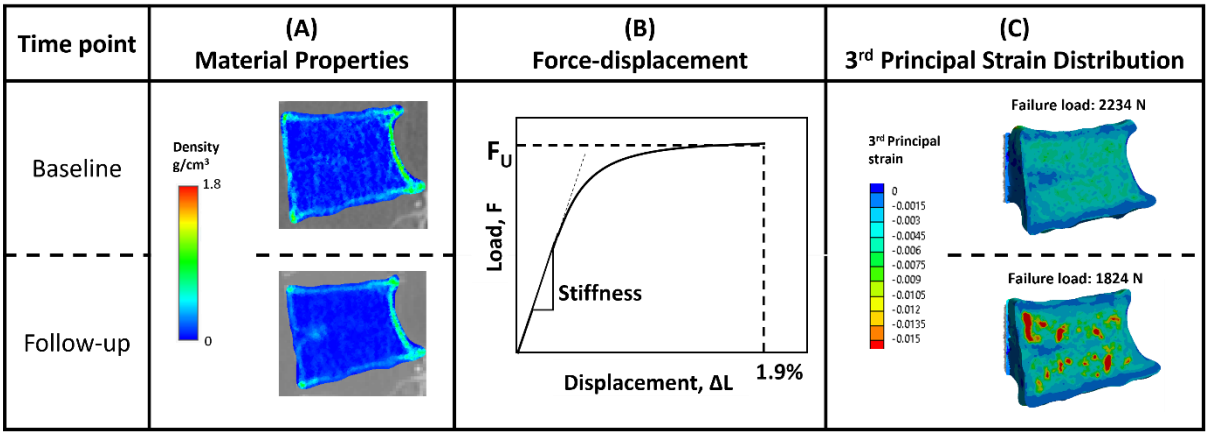

Figure 4.1 - Illustration of the outputs from the FE analysis at both time points. (A) Distribution of the BMD within the vertebral body taken from Bonemat, where blue is low BMD and yellow/red is high BMD. (B) Load-displacement curve used to calculate the stiffness and failure load from the FE results. (C) An example of the 3rd principal strain distribution within a model with the associated failure load.

4.2.5 Statistical Analysis

A Wilcoxon paired test was used to compare the densitometric and FE predicted mechanical properties between baseline and 12 months for both groups (significance was considered at $p<0.05$, *$p<0.05$, **$p<0.01$, ***$p<0.0001$). A Wilcoxon unpaired test (Mann-Whitney U-test) was used to test whether the percentage differences between baseline and 12 months within the treated group was significantly different from the control group. A Wilcoxon paired one tail test was used to evaluate if there was a significantly positive or negative trend in the densitometric, and FE predicted mechanical properties between baseline and 12 months.

Linear regressions were calculated between the percentage difference between the two time points for the FE failure load, failure strength and densitometric variables for the pooled and treated and control groups. The Pearson's correlation coefficients with corresponding p-values of the predictions were calculated for all linear regressions. Where an $r\leq0.3$ represents a weak correlation, $0.3<r<0.7$ is moderate correlation and $0.7<r\leq1$ is a strong correlation, with

p-values where significance was considered for $p<0.05$ and the significance levels were described by *$p<0.05$, **$p<0.01$, ***$p<0.001$.

4.3 Results

ADT reduced both densitometric and mechanical properties in men with PCa (Table 4.1). On average, between the baseline and 12-month visits, the patients receiving ADT displayed a significant reduction in aBMD (aBMD: -4%, $p<0.01$), whilst the aBMD in the control group increased (+2.3%, $p<0.05$). Trabecular vBMD at 12 months had a larger decrease than aBMD for the patients who received ADT (trabecular vBMD: -18%, $p<0.01$), whilst the control group showed no significant change ($p=0.056$). Integral vBMD also had a larger decrease than aBMD for patients receiving ADT (integral vBMD: -11%, $p<0.01$), whilst the control group showed no significant change at 12 months ($p=0.75$). The FE analysis resulted in an even larger decrease in mechanical properties for the patients receiving ADT than both aBMD and integral vBMD but similar to trabecular vBMD (stiffness: -14%, $p < 0.01$; failure load: -16%, $p < 0.01$; normalised stiffness: -14%, $p < 0.01$; failure strength: -16%, $p < 0.01$), compared to the control group. The change between baseline and 12 months in the treated group with respect to the change in the matched control was also significant for all densitometric and mechanical properties (Table 4.1, $p < 0.05$).

Table 4.1. Summarised data for densitometric (aBMD, trabecular vBMD, integral vBMD) and estimated mechanical properties (stiffness, failure load, apparent modulus, and ultimate strength). Average and standard deviation are reported for each group and time point. Percentage differences (% diff) computed between the time points and p-values were reported (1). P-values were also reported to test the significance of the difference between the treated group and the matched control group (2).

.	Control				Treated				p-value[2]
	Baseline	12 Months	% diff	P-value[1]	Baseline	12 Months	% diff	P-value[1]	
aBMD (g/cm^2)	1.09 ±0.18	1.12 ±0.19	+2.3%	**0.0006**	1.14 ±0.17	1.09 ±0.17	-4.0%	**0.0002**	**<0.0001**
Trab vBMD (g/cm^3)	0.11 ±0.036	0.11 ±0.029	-4.9%	0.037	0.13 ±0.06	0.10 ±0.05	-18%	**0.0004**	**0.011**
Integral vBMD (g/cm^3)	0.21 ±0.046	0.20 ±0.035	+0.67%	0.56	0.23 ±0.06	0.20 ±0.05	-11%	**0.0002**	**0.0002**
Stiffness (kN/mm)	39.0 ±16.3	37.7 ±11.4	+6.9%	0.73	45.1 ±18.6	36.6 ±13.8	-14%	**<0.0001**	**0.0004**
Failure load (kN)	3.03 ±1.27	2.94 ±0.93	+2.4%	0.69	3.45 ±1.31	2.76 ±0.91	-16%	**<0.0001**	**<0.0001**
Apparent modulus (MPa)	568 ±218	559 ±136	+7.8%	0.97	754 ±390	618 ±314	-14%	**0.0003**	**0.0004**
Ultimate strength (MPa)	1.79 ±0.61	1.75 ±0.40	+2.9%	0.94	2.25 ±1.10	1.81 ±0.88	-16%	**0.0002**	**<0.0001**

Figure 4.2 shows a representative model from the FE analysis of a subject in the treated group (A19), where the mechanical properties have decreased by 17-20% over 12 months. The resulting decrease in mechanical properties has driven an increase in 3rd principal (compressive) strain within the vertebral body. This is highlighted by the increase in red regions within the vertebral body at follow-up (Figure 4.2A) as well as an increase in frequency of higher strains at follow-up shown in the histogram (Figure 4.2B). The shear strain distributions in Figure 4.3A show the higher shear strain in the 12-month vertebra compared to the baseline for the same patient. The shear strains observed at follow-up are around 10% smaller than the compressive strains, implying compression is the main failure mode. Figure 4.3B highlights the higher plastic strains in similar regions to the high compressive strains, suggesting there is a higher risk of fracture in these regions.

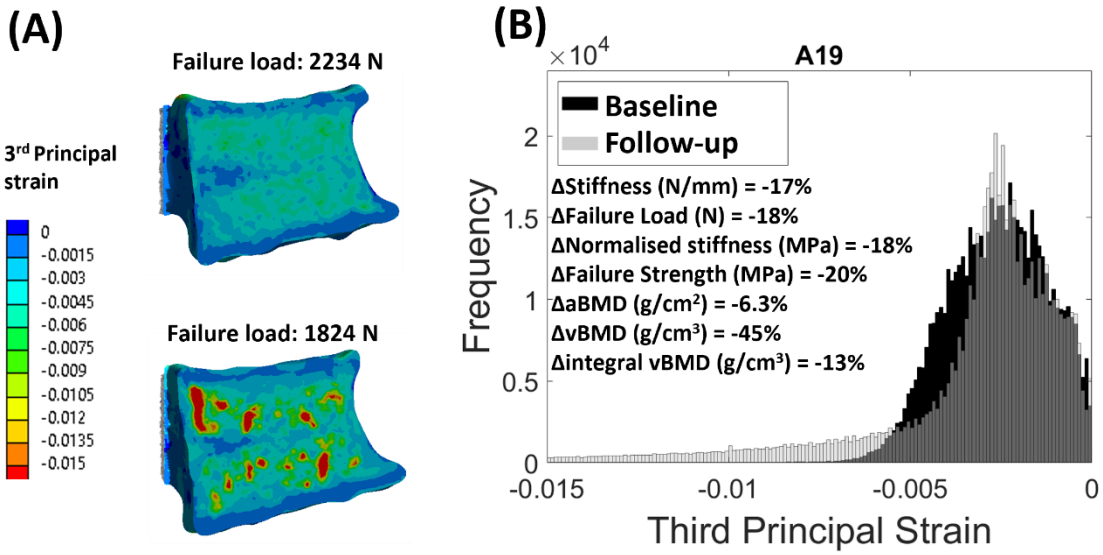

Figure 4.2 - Representative result from the FE analysis showing the local increases (red) in 3rd principal strain distribution (A) in the vertebral body and a histogram of the 3rd principal strain in the vertebral body where time point 2 has a higher proportion of strains in the higher strain region (B).

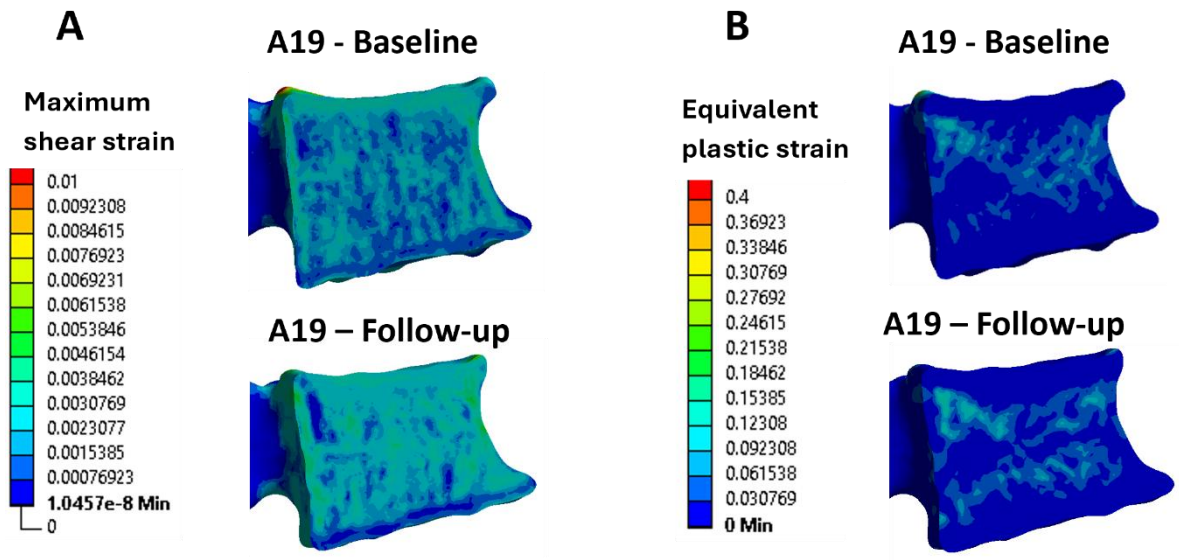

Figure 4.3 - Representative result from the FE analysis showing the local increases in maximum shear strain distribution (A) and equivalent plastic strain (B) in the vertebral body.

Figure 4.4 details the aBMD, vBMD, integral vBMD and failure strength for all patients in the control and treated group at baseline and 12 months. The violin plots of the aBMD show a similar distribution in both the control and treated groups, with the line plots confirming the changes in both groups between baseline and 12 months, where the blue (control) lines had a tendency toward positive gradient (aBMD: $p < 0.001$), whereas the red (treated) lines trended towards a negative gradient (aBMD: $p < 0.001$). Whilst the trabecular vBMD, integral vBMD and failure strength had no trend in the control group, the negative trend in the treated group was significant (trabecular vBMD: $p < 0.001$, integral vBMD: $p < 0.001$, failure strength: $p < 0.001$). The vBMD, integral vBMD and failure strength all had a smaller range in the control group and the treated group.

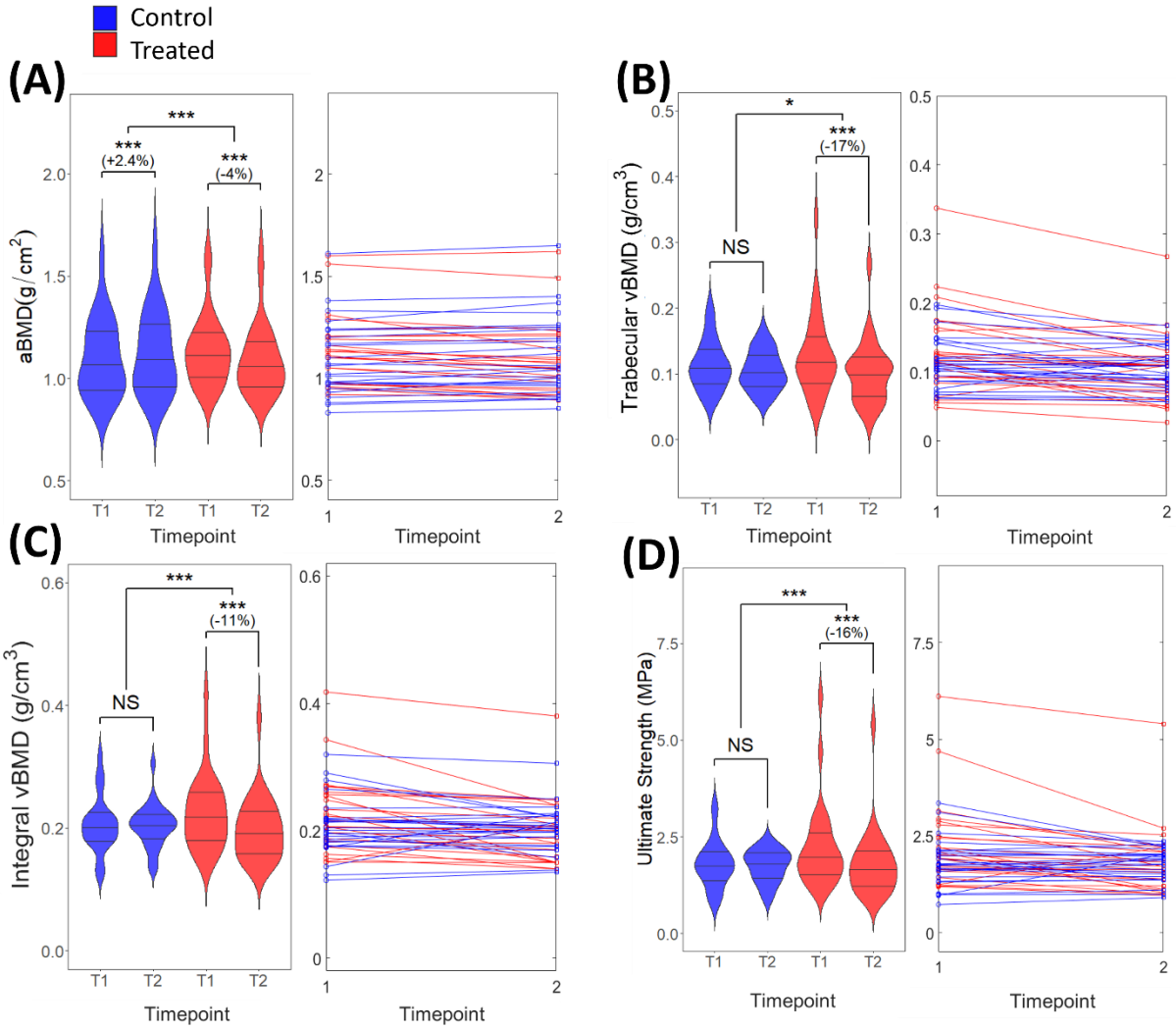

Figure 4.4 - vBMD and failure strength decrease more than aBMD over 12 months in the treated group. Violin plots of both cohorts and both time points and line plots showing the individual patients within each group for (A) aBMD, (B) trabecular vBMD, (C) integral vBMD, and (D) failure strength. *p<0.05, **p<0.01, ***p<0.001

Abbreviations: aBMD – areal BMD, vBMD – volumetric BMD, T1 – baseline, T2 – 12 months

The correlation between the densitometric parameters (aBMD, vBMD and integral vBMD) and the normalised mechanical properties was evaluated for the pooled data as well as the respective treated and control groups at both time points (Figure 4.5). Trabecular vBMD and integral vBMD were both found to be a better predictor of bone strength than aBMD. A weak but significant correlation was found between the percentage change in aBMD and the percentage change in failure load and failure strength for the pooled data ($r = 0.28$-0.44, $p<0.01$). Whereas the correlations between the pooled data for percentage change in trabecular vBMD or integral vBMD and the percentage change in failure load and failure

strength were strong (r=0.78-0.92, p<0.001 for trabecular vBMD; r = 0.88-0.96, p<0.001 for integral vBMD) (Figure 4.5).

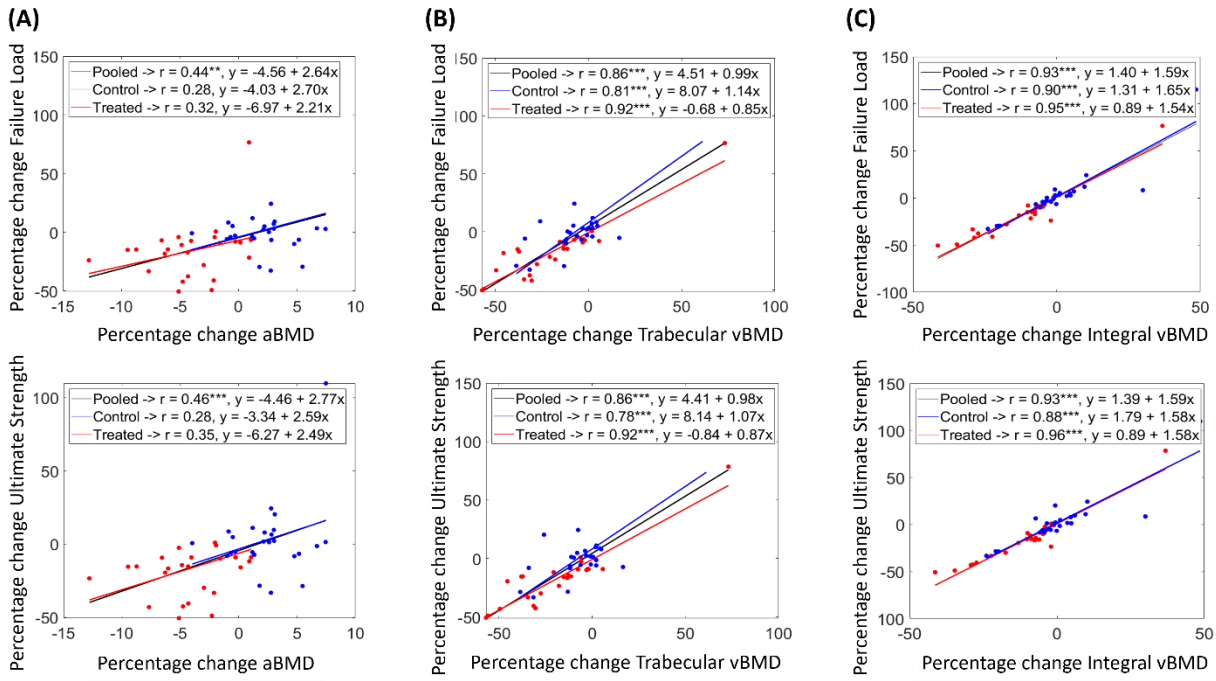

Figure 4.5 - vBMD has a stronger correlation than aBMD with failure load and failure strength. Linear regression analysis for percentage change failure load and percentage change failure strength vs (A) percentage change aBMD, (B) percentage change trabecular vBMD and (C) percentage change integral vBMD. **p<0.01, ***p<0.001.

4.4 Discussion

This study is the first to evaluate the effect of ADT on the biomechanical properties of the vertebra in PCa patients. It demonstrates a more dramatic decrease in vertebral mechanical integrity than those predicted using standard DXA measurements of aBMD. By reconstructing QCT scans, FE models predicted a significant decrease in all densitometric and mechanical properties following 12 months of ADT. It was found that trabecular vBMD and integral vBMD measured via QCT correlated well with FE analyses outputs, indicating a significantly better prediction of mechanical properties at T12 than aBMD measured by DXA at L1-L4.

Previous studies have shown a decrease in aBMD of 1.5-4% annually following commencement of ADT (Higano, 2008; Seifert-Klauss *et al.*, 2012) and the ANTELOPE study also demonstrated a significant decrease in aBMD following ADT after 12 months, at 4%

(Handforth *et al.*, 2024). Due to the high number of trabeculae within the vertebra, the highly vascular nature of trabecular bone, and the intravenous method used to administer ADT, the vertebra is at a higher risk of a reduction in BMD. In this study, similar, but amplified trends were observed in the treated group for trabecular vBMD and integral vBMD, reducing by 17% and 11% respectively over 12 months. QCT scans have been adopted in previous studies to assess the trabecular vBMD and found similar trends after 1 year of ADT (Smith *et al.*, 2001; Sato *et al.*, 2024). Similar amplified trends to this study were observed by Smith et al. (Smith *et al.*, 2001) who reported a reduction of 3.3% in lumbar aBMD and a reduction of 8.5% in vBMD after 48 weeks of ADT. Sato et al. (Sato *et al.*, 2024) reported also significant reduction in lumbar spine vBMD of 17.9% following 12 months of ADT.

The ADT treated group experienced a notable decrease in mechanical properties, with a 14-16% decrease in failure load, stiffness, failure strength, and normalised stiffness, compared to a 4% decrease observed in aBMD. FE analyses has been shown to amplify the changes seen in aBMD from DXA in osteoporotic patients (Keaveny *et al.*, 2007; Imai *et al.*, 2008). This could be explained by accounting for the 3D distribution of BMD, which has been shown to be indicative of strength gains (Keaveny *et al.*, 2007), and cortical thickness, which has also proven to be important when predicting fracture risk (Melton *et al.*, 2010). In addition, FE models are a better predictor of bone strength (failure load) than estimations from aBMD (Imai *et al.*, 2008) and trabecular vBMD (Crawford, Cann and Keaveny, 2003) and are highly correlated with experimental results (Stadelmann *et al.*, 2020).

Areal BMD showed a low predictive ability for mechanical properties (r=0.28-0.46), whereas vBMD and integral vBMD exhibited a strong correlation with mechanical properties (r=0.78-0.92 for trabecular vBMD and r=0.88-0.96 for integral vBMD). The weak correlation between aBMD and mechanical properties may be due to several factors, including overestimating aBMD by central DXA due to anatomical features such as irregular geometry, increased bone marrow fat, non-homogeneous fat distribution and the inclusion of posterior spinous processes (Grashuis, Bolotin and Sieva, 2003; Blake *et al.*, 2009; Almeida *et al.*, 2017). Moreover, DXA cannot provide information on 3D shape, large regional variation in vertebral geometries and the distribution of BMD throughout the bone. Previous studies have also shown that the use of vBMD as a predictor for failure load and failure strength at L3 is stronger

than aBMD (Tatoń *et al.*, 2013). Additionally, DXA measured aBMD at L3 or L2-L4 for predicting mechanical properties of the thoracic vertebrae have been evaluated in a previous study, reporting a weaker correlation for the prediction of T10 (r = 0.62) compared to L3 (r = 0.73) (Burklein *et al.*, 2001). aBMD measured in the lumbar spine is not intended to predict mechanical properties, particularly at different levels of the spine such as T12 due to the differing mechanical and densitometric properties of the vertebra (Burklein *et al.*, 2001). This was further confirmed in our study, which demonstrated that changes in mechanical properties at T12 are not reflected by the changes in spine aBMD (L1–L4).

The highest correlation between densitometric and predicted mechanical properties was observed when using integral vBMD. This can be explained considering that the integral vBMD is calculated across the whole vertebral body and provides information from trabecular and cortical bone compartments, both of which contribute to the vertebral body compressive strength (Fields *et al.*, 2009). The technique adopted here to calculate integral vBMD is not used in the clinical setting. Lower resolution images are acquired clinically and trabecular vBMD is assessed using software available from Mindways (Mindways Software Inc., Austin, TX, USA). However by using integral vBMD, we have demonstrated its improved predictive ability for bone strength compared to aBMD (Keaveny *et al.*, 2007; Melton *et al.*, 2007; Wang *et al.*, 2012). Having shown the feasibility of using FE to predict the mechanical strength of vertebrae, this could underpin further work to see if improvement of fracture prediction is possible.

The study in this chapter has some limitations. Firstly, the material properties of bone were modelled as isotropic. Understanding of the degree of anisotropy can improve the predictive capability of FE models regarding fracture risk in human vertebrae (Vivanco, Anderson and Smith, 2014). The inclusion of anisotropy within a FE study has been known to improve the prediction of bone strength in osteoporotic vertebrae (Fields *et al.*, 2009) and therefore could also improve the biomechanical assessment of PCa patients without the need for higher-dose scans. Nonetheless, the intrinsic anisotropy of the trabecular bone due to the heterogeneous density distribution was modelled by using relatively small element size (below 1mm) and the assignment of heterogeneous material properties in function of the local BMD. Incorporating other loading conditions such as torsion and bending could improve the assessment of the

effect of the ADT on the mechanics of the vertebral body. However, it is well known that compression is the most significant loading condition for most fracture modes and therefore is most used within the field of FE vertebral mechanics (Crawford, Cann and Keaveny, 2003; Buckley, Loo and Motherway, 2007; Wang *et al.*, 2012). Another limitation is introduced through the small cohort size within this study. This particularly plays a role in the linear regression analysis towards the larger percentage change in integral and trabecular vBMD where data is sparse. This could be influencing the overall trend and therefore results would need to be confirmed using a larger dataset.

4.5 Conclusion

In summary, this chapter has shown that ADT treatment for 12 months in a cohort of PCa patients reduces both the densitometric and mechanical properties of vertebrae, confirming the hypothesis for this chapter "The vertebral strength of prostate cancer patients reduces when administered with ADT". Despite a similar trend, an amplified reduction was seen for trabecular vBMD, integral vBMD and bone strength compared to aBMD. In addition, the regression analysis confirmed a stronger correlation of both trabecular vBMD and integral vBMD with the mechanical properties than the aBMD suggesting that the determination of the vBMD might be of higher value when assessing patients bone strength at specific vertebral levels in clinical practice. As well as contributing to the development of a robust computational pipeline, the data from the ANTELOPE trial will be applied as a training dataset in the following chapters.

5 SUBJECT-SPECIFIC FINITE ELEMENT MODELS TO ASSESS THE BIOMECHANICAL CHANGES OF METASTATIC VERTEBRAE IN MULTIPLE MYELOMA PATIENTS TREATED NON-SURGICALLY

5.1 Introduction

Vertebral metastatic lesions are a common complication of multiple myeloma (MM), a cancer of the plasma cells, white blood cells that make antibodies as part of the immune defence system. Abnormal plasma cells proliferate in the bone marrow of vertebrae, forming osteolytic bone lesions. MM represents around 2% of new cancers in the UK and the number of cases and deaths has more than doubled worldwide in the last 30 years (Zhou *et al.*, 2021). Patients with MM are most affected by spinal involvement (80-90%) (Bird *et al.*, 2011) with 34-36% of patients suffering from spinal fracture (Anselmetti, Manca and Montemurro, 2012). Anti-myeloma treatments have significantly improved over the last 30 years, increasing the 5-year survival rate for patients with MM from 12-50% and 11-44% in men and women respectively (Cancer Research UK, 2014; Bird and Boyd, 2019).

Now, this growing population of MM survivors require treatment to stabilise the spine. The current standard of care is invasive surgical intervention, preventing vertebral collapse and spinal cord damage. However, despite the obvious biomechanical component to this challenge, the spinal mechanics of MM patients has not been studied previously. Furthermore, due to the age of most patients at diagnosis (>70 years), the surgery is associated with increased morbidity and high infection risk (Nucci and Anaissie, 2009). It is proposed that by adopting a non-surgical strategy for appropriate MM patients, provided the spine is externally braced (Malhotra, Butler, *et al.*, 2016; Malhotra, Lui, *et al.*, 2016), then significant bone growth and remodelling will internally stabilise the spine. Bone growth has been observed both within the tumour bed and as thickened cortical shells around vertebrae. However, whether this increases the strength of the vertebrae is unknown. Therefore, the aim of this chapter was to assess the change in densitometric and mechanical properties of vertebrae from MM patients treated non-surgically with the aim of confirming or denying the second hypothesis of this thesis “The remineralisation following bracing treatment for MM patients leads to an increase in vertebral strength”.

5.2 Materials and Methods

5.2.1 Patient Data

For this chapter, eight of the patients from the RNOH dataset (Chapter 3, Section 3.2.2) were used (Table 5.1). For each patient, one vertebra with lytic lesions was selected along with a control that had no visible lesions. The vertebrae adjacent to the lytic vertebra were used as controls in all but P5, as the vertebra both above and below were also lytic, hence the T4 vertebra was selected as control in P5 (Table 5.1). QCT protocols for the patients in this cohort are detailed in Section 3.2.2.

Table 5.1 - Details of the cohort including patient's ID, age, sex (M for male), the time between baseline and follow-up, vertebral levels modelled and their condition.

Patient ID	Age	Sex	Time between baseline and follow-up (months)	Vertebral Level	Condition
P1a	77	M	3	T4 T3	Control Lytic
P3	66	M	12	T10 T11	Control Lytic
P3a	63	M	12	T10 T11	Control Lytic
P5	74	M	8	T4 T6	Control Lytic
P5a	73	M	37	T1 C7	Control Lytic
P8	47	M	2	T4 T3	Control Lytic
P9a	49	M	9	T10 T11	Control Lytic
P11	77	M	38	L3 L4	Control Lytic

5.2.2 Finite Element Modelling and Material Properties

The models were constructed and simulated using the pipeline described in Chapter 3 and material properties were assigned from the CT image according to the phantomless calibration process in Chapter 3. Briefly, CT scans at baseline and follow-up were segmented in 3D-Slicer (Fedorov *et al.*, 2012) to produce 3D models of the vertebrae. They were aligned

using the average of two best fit planes, one on the superior endplate and one on the inferior endplate. The models were meshed using a 1mm quadratic tetrahedral mesh following the mesh refinement study (Chapter 3). A 1.9% strain was applied in axial compression to the superior endplate to simulate failure (Crawford, Cann and Keaveny, 2003; Wang *et al.*, 2012; Keaveny *et al.*, 2014), while the inferior endplate was fixed in all directions. Both bone and lytic tissue were modelled as heterogenous, isotropic, and elastic-plastic materials, following the assumption that lytic lesions only affect local bone density (Nazarian *et al.*, 2008). The failure load (FL), stiffness (K), apparent modulus and ultimate strength were calculated as described in Section 3.7.2.

For the assessment of trabecular vBMD (tvBMD), from each QCT an ellipse shaped ROI was identified (ImageJ) in the anterior most region of the vertebral body, in the trabecular portion only. The ellipse was identified by creating a circular region of interest in the vertebral body, ensuring the cortical portion was included, then reducing the height by 60% and the width by 20%. The location of the ellipse was then moved to ensure it was in the top 50% of the vertebral body, 10% away from all edges. This ROI was extended to include the 10 central slices of the vertebral body. HU values within the ROI for all slices were converted into vBMD using the densitometric calibration identified as described in Chapter 3.

5.2.3 Statistics

A Wilcoxon paired test was used to compare the densitometric and FE predicted mechanical properties between baseline and follow-up for both control and lytic vertebrae (significance was considered at $p<0.05$). A Wilcoxon unpaired test (Mann-Whitney U-test) was used to test whether the percentage differences between baseline and 12 months within the lytic vertebrae was significantly different from the control vertebrae (significance was considered at $p<0.05$). Linear regressions were calculated between the percentage difference between the two time points for the FE predicted properties (failure load, stiffness, ultimate strength and apparent modulus) and vBMD variables for the pooled and treated and control groups. The Pearson's correlation coefficients with corresponding p-values of the predictions were calculated for all linear regressions.

5.3 Results

Table 5.2 shows the pooled results for all 8 cases. In all variables (tvBMD, K, FL, E, σ_u), the percentage difference increased between the controls and lytic vertebrae between the two time points. Spring stiffness (K) ranged between 14.5 N/m and 52.4 N/m for the controls and 13.1 N/m and 54.1 N/m for the lytic vertebra. Predicted failure load (FL) ranged from 1.0 kN to 5.6 kN for the control vertebra while predicted FL ranged from 1.09 kN to 5.0 kN for the lytic vertebra. Vertebral ultimate strength (σ_u) varied between 0.82 MPa and 4.9 MPa within the control vertebra and between 0.87 MPa and 5.6 MPa within the lytic vertebra.

Table 5.2 - Differences in densitometric (trabecular vBMD) and estimated mechanical properties (K, FU, E, σU, Average ±Standard Deviation) computed for the vertebrae with or without lytic lesions. Percentage differences (%diff) computed with respect to the controls were also reported.

	Baseline			Follow-up			Average % diff between baseline and follow-up in lytic normalised to control
	Controls (Avg±SD)	Lytic (Avg±SD)	Average % diff Lytic to control	Controls (Avg±SD)	Lytic (Avg±SD)	Average % diff Lytic to control	
tvBMD (g/cm^3)	0.24 ±0.097	0.20 ±0.078	-17 %	0.23 ±0.026	0.21 ±0.03	4 %	9 %
K (kN/mm)	19.8 ±4.5	26.7 ±3.8	28 %	27.4 ±9.4	31.4 ±13.5	25 %	-11 %
F_u (kN)	1.76 ±0.31	1.98 ±0.28	11 %	2.21 ±1.41	2.58 ±1.27	18 %	6.2 %
E (MPa)	525 ± 238	534 ±235	1.9 %	614 ±316	625 ±285	2.5 %	0.83 %
σ_u (MPa)	2.1 ±0.82	2.09 ±0.87	-1.7 %	2.37 ±1.13	2.51 ±1.09	5.3 %	6.2 %

The box plot of the vBMD (Figure 5.1) shows the larger range of values across in the control group (no visible lesions) compared to the lytic lesion group. The vBMD increased in three out of the eight lytic vertebra and two out of the eight controls. Whereas the stiffness and apparent modulus increased for four vertebrae in the lytic group and the failure load and ultimate strength increased for five patients in the lytic group. The lytic group was split into two groups at this point to highlight the effect of the size of lesion (Figure 5.1). The relationship between time between baseline and follow-up and change in mechanical and material properties was assessed, and no relationship was found.

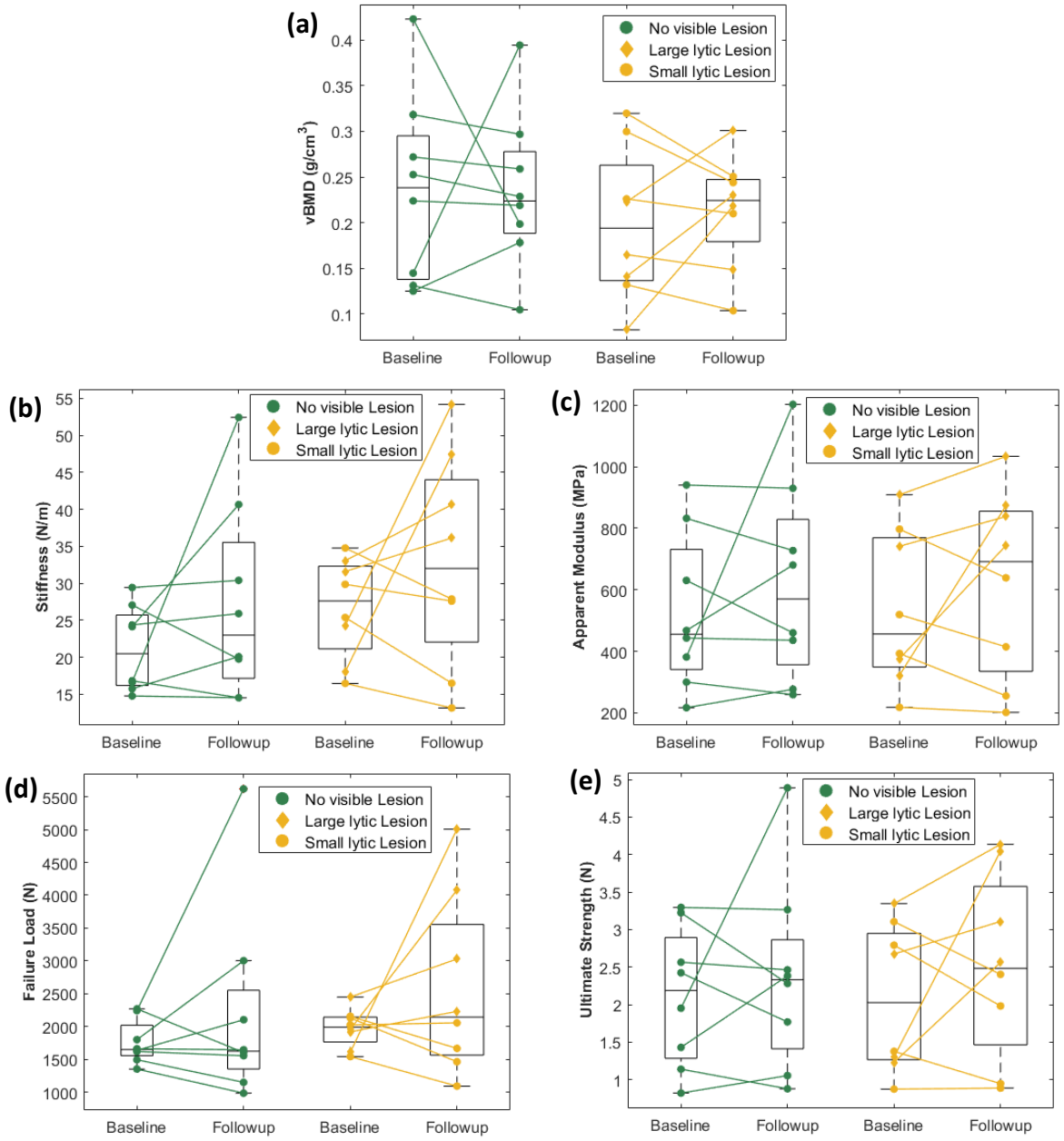

Figure 5.1 – Box plots of the (a) vBMD, (b) stiffness, (c) apparent modulus, (d) failure load and (e) ultimate strength. For each plot, non-lesion vertebrae are shown in green and lytic lesion vertebra are shown in yellow. Vertebrae with large lytic lesions are indicated with a diamond marker. A horizontal line represents data for a single patient connecting baseline to follow-up.

The linear regression analysis between the densitometric properties and mechanical properties are shown in Figure 5.2. There was a strong, significant relationship between all the mechanical properties and the vBMD for the pooled data (stiffness: $r = 0.85$ $p < 0.001$, failure load: $r = 0.89$, $p < 0.001$, apparent modulus: $r = 0.84$, $p < 0.001$, ultimate strength: $r = 0.89$, $p < 0.001$). In addition, the lytic group had a slightly stronger relationship between the vBMD, and stiffness and apparent modulus compared to the control data (stiffness control: r

= 0.84 p < 0.01, stiffness lytic: r = 0.87 p < 0.001, apparent modulus control: r = 0.81, p < 0.05, apparent modulus lytic: r = 0.95, p < 0.001).

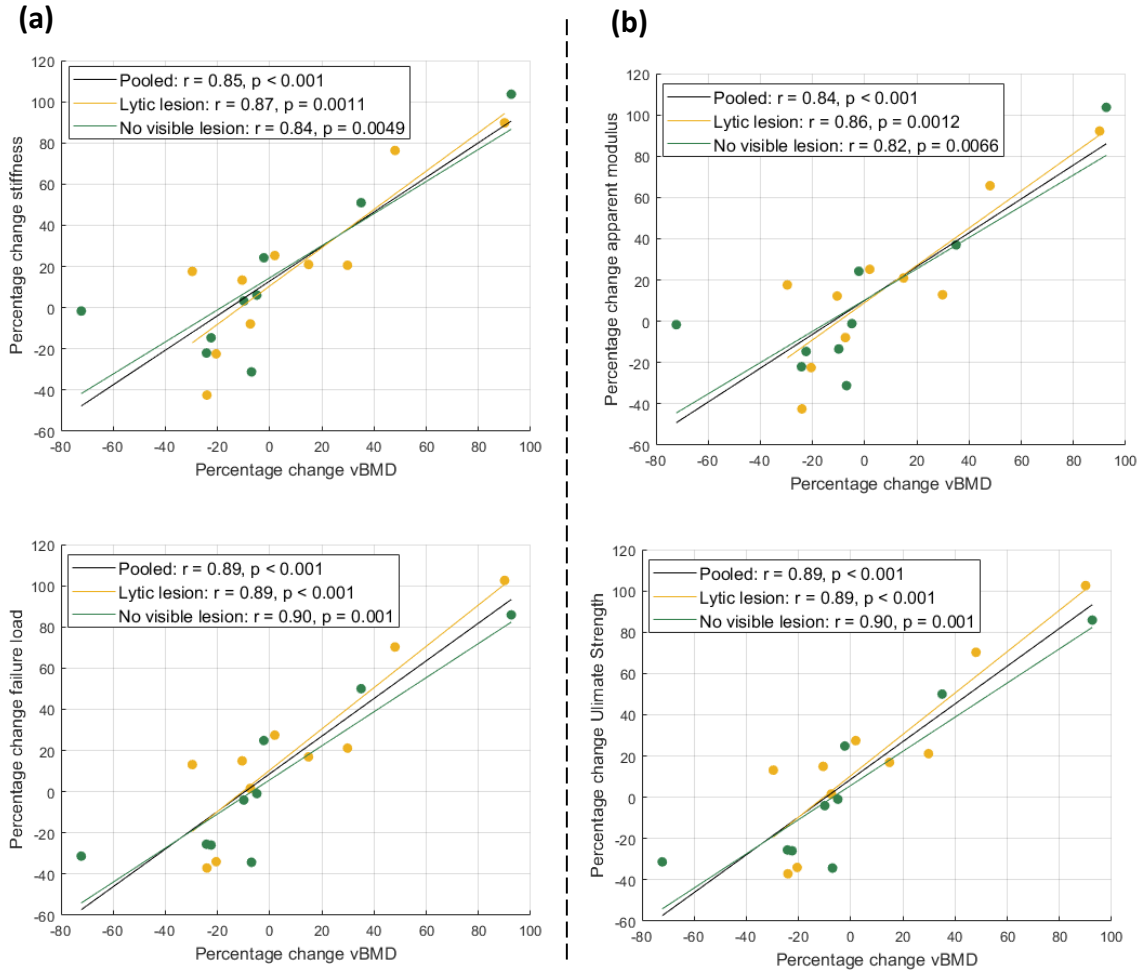

Figure 5.2 - Linear regressions between (a) the change in vBMD and the change in structural mechanical stiffness and failure load and (b) the change in apparent modulus and ultimate strength. Regression equations are reported for pooled data (black), control vertebrae (green) and lytic vertebra (yellow).

Despite the linear regressions showing strong correlations between change in vBMD and the change in mechanical and material properties, some vertebra had a decrease in vBMD while the mechanical and material properties increased. In addition, the size of the lesion varies between patients, four lytic vertebrae had large lesions (>50% of the vertebral body) and four patients' lytic vertebrae had small lesions (<50% of the vertebral body). The effect of the size of the lesion was evident where the four vertebrae with the large lesions increased notably in material and mechanical properties, while the four with small lesions were either stable or decreased in material and mechanical properties. To address these differences, an individual

assessment of patients is necessary to understand the changes occurring in the vertebra. Two vertebrae with large lesions and one with a small lesion were chosen to represent the two groups.

The results for P1a, the first large (>50%) lytic vertebra to be individually assessed is detailed in Figure 5.3. The vBMD in the lytic vertebra for P1a decreased over time, while the other properties (FL, K, E and σ_u) increased (Figure 5.3). The distribution of BMD can be seen in Figure 5.3a for the lytic vertebra in P1a at baseline and follow-up. The region surrounding the lesion has undergone the largest increase in mineral as well as other regions around the cortex (Figure 5.3a). When measuring the vBMD, an ellipse was created in the anterior portion of the vertebral body, not incorporating the cortical region, hence not including the increase in mineral in this region. In addition, the increase in vBMD around the lesion has led to a decrease in minimum principal strain in the same area of P1a's lytic vertebra (Figure 5.3a). This then correlated with the increase in stiffness, failure load, apparent modulus and ultimate strength between baseline and follow-up (Figure 5.3b).

To highlight another vertebra with a large lesion, an overview of P5 is illustrated in Figure 5.4. Unlike P1a, this patient had a notable increase in both vBMD and mechanical and material properties. There is a clear increase in vBMD from baseline to follow-up, particularly in the posterior region of the lesion and vertebral body. This increase in vBMD led to an increase in material and mechanical properties (Figure 5.4d). The minimum principal strain (Figure 5.4c) show a very similar distribution at baseline and follow-up. The strain around the lesion region has reduced slightly which could be attributed to the increase in mechanical and material properties.

One patient, with small lytic lesions, whose vBMD, material and mechanical properties decreased between two timepoints was P8 (Figure 5.5). This example patient shows a new small lesion in the posterior region of the vertebral body (Figure 5.5 b) where the density is lower (lighter purple). This new lesion formation could have started healing after the follow-up but as the time between baseline and follow-up for P8 was 2 months, this remineralisation would not be present at follow-up. The influence of the new lesion can be seen by the increase in minimum principal strain within this region (Figure 5.5c) and the decrease in material and mechanical properties (Figure 5.5d).

(a)

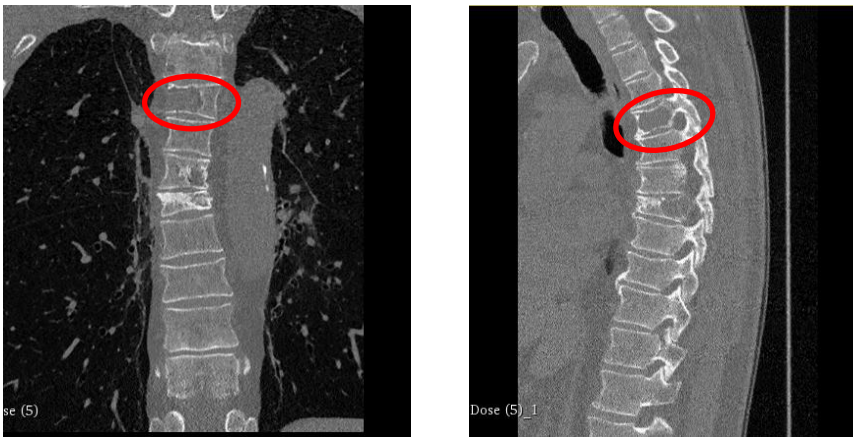

(b)

	Baseline	Follow-up (3 months)
Density distribution (g/cm³)	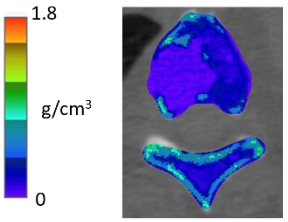	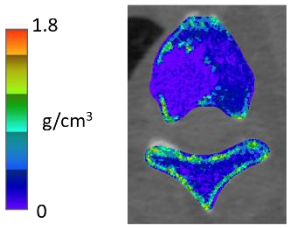
EPEL3 distribution@1.9% strain (mm/mm)	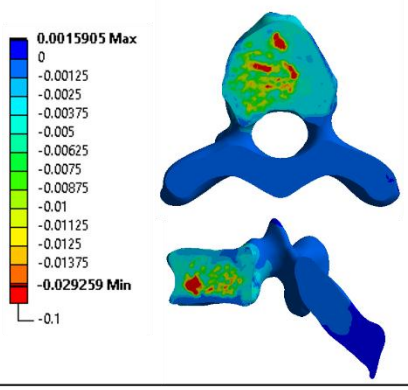	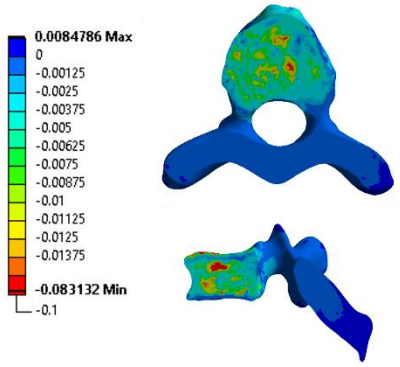

(c)

(d)

Time Point	Condition	tvBMD (g/cm³)	% diff to control	Stiffness (N/m)	% diff to control	Failure load (N)	% diff to control	Apparent Modulus (MPa)	% diff to control	Ultimate Strength (MPa)	% diff to control
Baseline	Control	0.253	-41%	29.4	7.1%	1623	16%	832	-12%	2.57	4.2%
	Lytic	0.165		31.6		1922		742		2.68	
Follow-up (3 months)	Control	0.220	-42%	30.3	17%	1558	35%	728	14%	2.46	23%
	Lytic	0.149		36.1		2233		838		3.11	

Figure 5.3 - Case report for patient 1a (a) CT scan in the coronal and sagittal plane with lytic vertebra highlighted in red, (b) CT scans in the axial plane of the control and lytic vertebra alongside with the material distributions of density for each vertebra, (c) the minimum principal strain (EPEL3) distribution in the axial and coronal planes (where red is high strain and blue is low strain) and (d) table of the mechanical properties for all vertebra at both Time Points, reporting the percentage difference (%diff) between the control and lytic vertebrae.

(a)

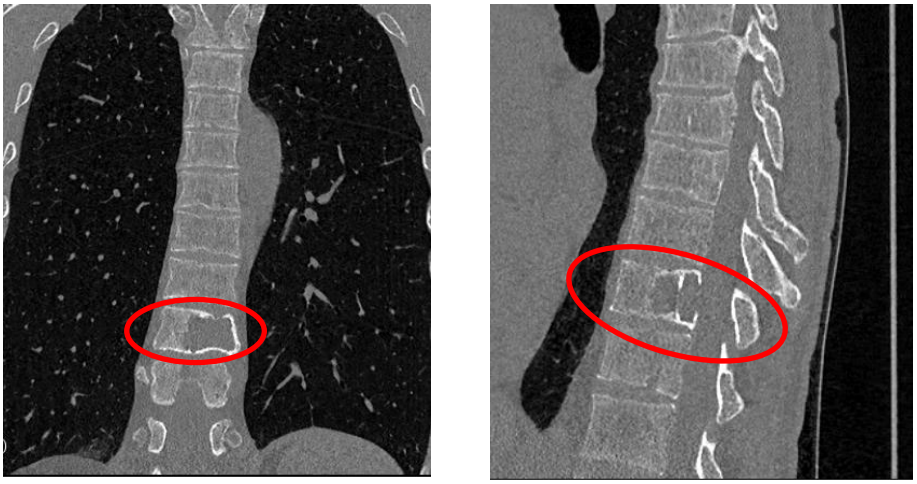

(b)

	Baseline	Follow-up (8 months)
Density distribution (g/cm³)	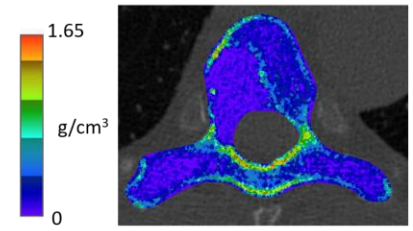	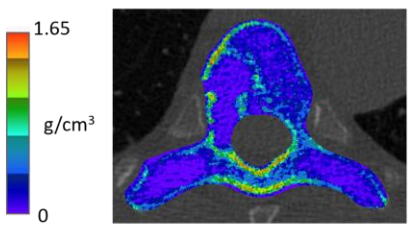
EPEL3 distribution@1.9% strain (mm/mm)	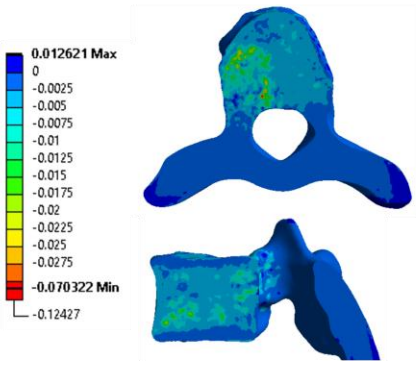	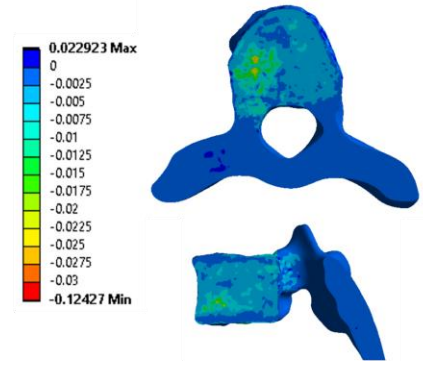

(c)

(d)

Time Point	Condition	tvBMD (g/cm³)	% diff to control	Stiffness (N/m)	% diff to control	Failure load (N)	% diff to control	Apparent Modulus (MPa)	% diff to control	Ultimate Strength (MPa)	% diff to control
Baseline	Control	0.272	-20%	29.4	-19%	1665	38%	940	-3%	3.29	1.5%
	Lytic	0.223		.24.4		2451		909		3.34	
Follow-up (8 months)	Control	0.259	15%	25.9	44%	1649	59%	930	11%	3.27	23%
	Lytic	0.301		40.6		3031		1034		4.14	

Figure 5.4 - Case report for patient 5 (a) CT scan in the coronal and sagittal plane with lytic vertebra highlighted in red, (b) CT scans in the axial plane of the control and lytic vertebra alongside with the material distributions of density for each vertebra, (c) the minimum principal strain (EPEL3) in the axial and coronal planes (where red is high strain and blue is low strain) and (d) table of the mechanical properties for all vertebra at both Time Points, reporting the percentage difference (%diff) between the control and lytic vertebrae.

(a)

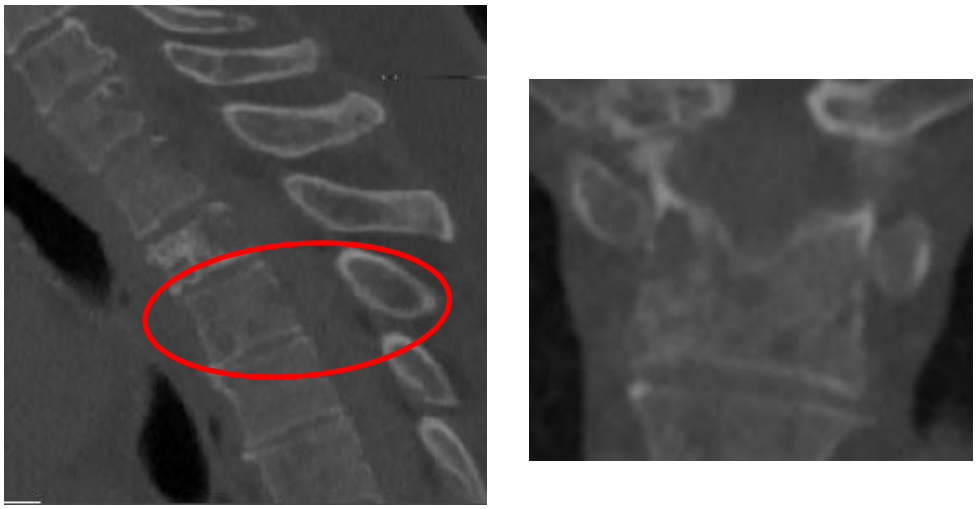

(b)

	Baseline	Follow-up (2 months)
Density distribution (g/cm³)	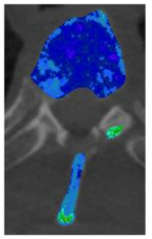	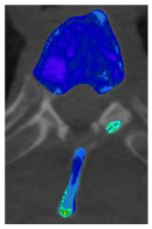
EPEL3 distribution@1.9% strain (mm/mm)	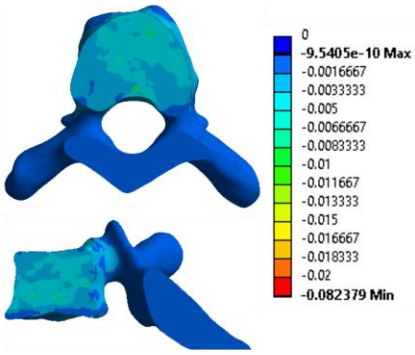	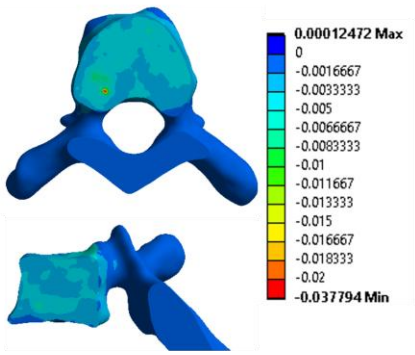

(c)

(d)

Time Point	Condition	tvBMD (g/cm³)	% diff to control	Stiffness (N/m)	% diff to control	Failure load (N)	% diff to control	Apparent Modulus (MPa)	% diff to control	Ultimate Strength (MPa)	% diff to control
Baseline	Control	0.319	-0.3%	34.8	-25%	2158	5%	797	-23%	3.11	3.8%
	Lytic	0.318		27.1		2271		630		3.23	
Follow-up 2 months)	Control	0.251	17%	25.9	-27%	1649	1.3%	639	-32%	2.40	-5.1%
	Lytic	0.297		19.8		1670		461		2.28	

Figure 5.5 - Case report for patient 8 (a) CT scan in the coronal and sagittal plane with lytic vertebra highlighted in red, (b) CT scans in the axial plane of the control and lytic vertebra alongside with the material distributions of density for each vertebra, (c) minimum principal strain (EPEL3) distribution in the axial and coronal planes (where red is high strain and blue is low strain) and (d) table of the mechanical properties for all vertebra at both Time Points, reporting the percentage difference (%diff) between the control and lytic vertebrae.

5.4 Discussion

The aim of this chapter was to evaluate the difference in mechanical properties at two time points of vertebrae with lytic lesions, in relation to adjacent vertebrae without lesions, of MM patients treated with orthopaedic bracing. None of the vertebrae assessed within this study had vBMD values that were classed as osteoporotic (BMD<0.08 g/cm^3) or osteopenic (0.08 g/cm^3<BMD<0.12 g/cm^3) (Zysset *et al.*, 2015). These values were, however, estimations calculated from the QCT images and not from DXA which is the gold standard for classifying low bone density (Cummings, Bates and Black, 2002).

The predicted mechanical properties from the FE models simulated in this study generally agree with previous results from studies of compressive loading on vertebrae. Fracture loads have been reported between 2 kN and 9 kN for the vertebral bodies in the thoracolumbar region (Liebschner *et al.*, 2003; Imai *et al.*, 2006; Fields *et al.*, 2011). This study estimates the predicted fracture load between 1.0 kN and 5.6 kN which almost falls within this range. In addition, for spring stiffness, Dall'Ara et al.'s experimental study observed values ranging from 17 to 54 kN/mm, in agreement with this thesis' study that predicted a range from 13.1 kN/mm to 52.4 kN/mm (Dall'Ara *et al.*, 2012).

Remineralisation and an increase in vBMD were identified in the four patients with large lesions (P1a, P3a, P5 and P9a) at time point 2, with patient 3a (time step of 12 months), P5 (time step of 8 months) and P9a (time step of 9 months) showing the largest area of remineralised tissue. This correlated to the prediction by Balducci et al. of the time taken to remineralise of 6 months (Balducci *et al.*, 2011), suggesting the other patient with a large lesion (P1a, time step of 3 months) was still in the process of remineralisation at the time the second CT scan was taken. The other patients' lytic vertebrae with smaller lesions (P3, P5a, P8) decreased in tvBMD, meaning 38% of patients within this study had an increase in vBMD. Patient P11's lytic vertebra was collapsed. This vertebra saw an increase in vBMD but a decrease in material and mechanical properties. This is most likely due to the mineral increasing on the endplates to stabilise the adjacent vertebra rather than to increase the vBMD in the vertebral body. Additionally, P11's control vertebra experienced an increase in vBMD, material and mechanical properties, suggesting an attempt of the adjacent vertebra to stabilise the spine. Other studies have seen a similar percentage of patients with

remineralisation (24%, 48% and 46.4%) (Mose *et al.*, 2000; Balducci *et al.*, 2011; Matuschek *et al.*, 2015). However, due to the small cohort in this study, it may not be representative of the population.

The lytic vertebrae displayed bimodal changes, with four increasing and four decreasing in mechanical properties. The four lytic vertebrae that increased, all possessed a large lytic lesion (>50% of vertebral body). At baseline, the large lesions decreased the amount of bone in the vertebral body and increased the mechanical stresses on the remaining bone. Through cell signalling and bone remodelling, at time point 2, the regions surrounding the lesion increased in mineral density, regaining the strength of the vertebra. The mechanisms behind the significant mineral increase are currently unknown and should be investigated further. For the four vertebrae with smaller lesions, the lesions are unlikely to change the load bearing of the vertebrae and therefore do not induce the same rapid remodelling as the larger lytic vertebrae.

The linear regression analysis of the densitometric and mechanical properties described a strong correlation between the change in vBMD and failure load and stiffness ($0.88<r<0.96$, $p<0.05$), and between the change in vBMD and apparent modulus and ultimate strength ($0.81<r<0.95$, $p<0.05$). These strong correlations suggested that the densitometric properties, that can be calculated easily in a clinical setting from QCT scans, could be a reliable estimation of the mechanical properties of vertebrae with and without lytic lesions. However, when looking at the individual patients, it was highlighted that P1a had a decrease in vBMD but an increase in all material and mechanical properties. This suggested that there was an increase in cortical BMD that was driving the increase in the FE predicted properties, which was not captured by the current method to evaluate vBMD in these models. It is well known that the cortical shell bears up to 54% of the loading under compression (Eswaran *et al.*, 2006) and therefore an increase in bone density around the cortical shell could substantially increase the strength of the vertebrae.

There are some limitations of this study, the first being the small cohort size of eight patients. However, it was clear from the results that analysis must be conducted on an individual basis despite the number of patients included and, therefore, trends may only be confirmed if the sample size was sufficiently large. The material properties of bone were modelled as

heterogeneous and isotropic. This introduced a further limitation as recent work has suggested that in patients with MM, the degree of anisotropy in trabecular bone is significantly increased (Takasu *et al.*, 2011). The inclusion of this parameter within an FE study has been known to improve the prediction of bone strength in osteoporotic vertebrae (Fields *et al.*, 2009) and, therefore, could also improve the assessment for MM patients without the need for higher-dose scans. However, the loading criterion used within this study was axial compression which would negate the need for modelling anisotropy. The 3D models were assigned material properties according to the CT grey values, which included the lytic tissue, meaning it was modelled as low-density bone tissue. Lytic bone tissue has been previously modelled as a poro-visco-elastic tissue which allows for the evaluation of solid and fluid phases (Whyne *et al.*, 2000; Tschirhart, Nagpurkar and Whyne, 2004). However, due to the fact that the constitution of tumour tissue is not well understood, and the assumption used in this study has been supported by previous work (Nazarian *et al.*, 2008; Stadelmann *et al.*, 2020), this is not seen as a significant limitation.

Compressive loading on a single vertebral body was the method chosen within this study. To improve the accuracy of loading, the model could incorporate physiological loading such as torsion, bending and multi-axial loading. However, it is well known that compression is the most significant loading condition for most fracture modes and therefore is most commonly used within the field of FE vertebral mechanics (Crawford, Cann and Keaveny, 2003; Buckley, Loo and Motherway, 2007; Wang *et al.*, 2012). In addition, the exclusion of the intervertebral discs and articular contacts between facet-joints, which contribute to the transfer of loading between vertebral segments, could have had an effect on the estimation of the mechanical properties and stability (Groenen *et al.*, 2018). For this study, the main focus was the effect of the remineralisation on an individual lytic vertebra in relation to the control vertebra, so this addition was not included. Nonetheless, when more complex problems are introduced that have multiple adjacent lytic vertebrae the loading may be redirected more onto the facet joints and affect the result when estimating the risk of fracture (Whyne, Hu and Lotz, 2003).

5.5 Conclusion

In conclusion, this chapter has shown that, by employing a robust finite element pipeline, significant changes in the mechanical properties of vertebrae with and without lytic lesions

following treatment with orthopaedic bracing occur. From the results, it has been shown that vBMD could be a useful tool in predicting the mechanical properties of vertebrae with lytic lesions. However, for patients with mineralisation primarily in the cortical compartment, vBMD alone could not predict the mechanical properties and an FE analysis was required. Using this method, an estimation of the effect of remineralisation, following treatment, on the mechanical properties of lytic vertebra was made. The results suggested that over time, with remineralisation, the mechanical properties of the large lytic vertebrae improved, confirming the second hypothesis of this thesis "The remineralisation following bracing treatment for MM patients leads to an increase in vertebral strength". In contrast, vertebrae with smaller lesions had either no change or a decrease in densitometric and mechanical properties. However, how and why this remineralisation occurs in certain regions, if it is purely mechanically driven or that there are additional biological mechanisms involved, is unknown. Hence, it is necessary for further investigations into the biological mechanisms behind the remineralisation, in order to build a more accurate picture of how material and mechanical properties change in MM patients following treatment.

6 MECHANOBIOLOGICAL MODEL OF METASTATIC LESIONS IN VERTEBRAE OF MULTIPLE MYELOMA PATIENTS SUGGESTS CANCER-INDUCED REMINERALISATION POST-TREATMENT.

6.1 Introduction

As discussed in Chapter 5, standard bone biomechanics alone does not appear to explain the rapid remineralisation observed in recovering multiple myeloma (MM) patients. In order to investigate the underlying mechanisms for the changes in strength seen in the clinic, we must parse out what part of the remineralisation is driven by response to mechanical stimuli and the degree to which additional biological mechanisms are at play. This chapter will develop a mechanobiological model, a form of study used to investigate how mechanical loads affect biological processes. In bone, mechanobiology is particularly important due to the hierarchical structure where a mechanical stimulus at organ level influences the biological response of bone cells and bone adaptation.

A delicate balance of signalling exists between the three main bone cells involved in remodelling; osteoblasts that form bone, osteoclasts that resorb bone and osteocytes that sense and respond to mechanical stimulus. Depending on the magnitude of the stimulus, osteocytes send signals to increase or decrease osteoclast and osteoblast differentiation and activity. Mechanical loading can stimulate the Wnt signalling pathway which is responsible for the differentiation of preosteoblasts to mature osteoblasts (Baron and Kneissel, 2013). A high mechanical stimulus reduces sclerostin levels, produced by osteocytes to block the Wnt pathway, allowing the Wnt ligands to activate the β-catenin pathway to differentiate osteoblasts (Baron and Kneissel, 2013). Osteocytes can also control the activity of osteoclasts through the RANKL/OPG (Receptor Activator of Nuclear factor Kappa-B Ligand/ Osteoprotegerin) system. A high mechanical stimulus reduces the expression of RANKL and increases OPG, reducing osteoclast differentiation and activity (Tobeiha *et al.*, 2020). There are also signals from the bone matrix when bone is under mechanical stress. TGF-β signalling, which is sequestered within the bone matrix and released during bone degradation, promotes osteoblast differentiation and impedes osteoclast differentiation (Crane, Xian and Cao, 2016).

The combination of these pathways ensures normal bone remodelling and bone homeostasis, and these can be measured clinically via a series of bone turnover markers (BTMs) measured in a patient's blood sample. The whole remodelling process lasts around 180 days (30-40 days for resorption and 150 days for formation) (Pant *et al.*, 2021).

In MM, these pathways are disrupted leading to an imbalance in bone remodelling. The RANKL/OPG signal is upregulated whilst the Wnt signal is downregulated, increasing osteoclast activity and decreasing osteoblast activity respectively (Giuliani, Rizzoli and Roodman, 2006). The combination of bone destruction and no new bone formation leads to the development of lytic lesions within the bone (Qiang *et al.*, 2008). Post anti-cancer treatments, most of the MM cells have been destroyed, allowing the bone to return to normal remodelling (Hinge *et al.*, 2016). As the bone is now left with large areas of destruction, the bone is much weaker and therefore under much higher stress and strain. These conditions, in theory, should lead to higher bone formation due to higher mechanical stimulus. However, clinical and experimental observations have shown bone formation at faster rates than normal in recovering MM patients (Rao *et al.*, 2006; Gokaraju *et al.*, 2019), which gives rise to the question of whether this is driven solely by mechanobiological adaptation or if an additional biological mechanism is involved.

The long history of mechanobiological models, dating back to Frost's Mechanostat Theory is detailed in Chapter 2. However, many previous models have focussed on mathematically modelling bone, not applying the algorithms to 2D/3D geometries. To test these algorithms, Hambli incorporated Komarova's model with an 3D finite element (FE) model of a proximal femur (Hambli, 2014). Hambli's model considered fatigue damage effects to describe the mechanical behaviour of bone which influenced the osteoclast and osteoblast formation, as well as rates of bone resorption and formation which updated the bone density accordingly (Hambli, 2014). However, Hambli (2014) computational study was not validated. Nevertheless, in 2017, Dao *et al.* (Dao, 2017) combined the FE remodelling framework of Hambli with an agent based model to describe the cellular dynamics, and qualitatively validated their model through comparison with an experimental study of the human distal tibia (Christen *et al.*, 2014). For MM specific remodelling, only one study has developed a mathematical algorithm to describe the changes to bone remodelling caused by MM cells (Y.

Wang *et al.*, 2011). Wang *et al.'s* algorithm was based on the model by Pivonka *et al.* (Pivonka *et al.*, 2008) and developed to clarify the most important cell signalling pathways in MM disease progression (Y. Wang *et al.*, 2011). There is currently no mechanobiological model describing bone remodelling in MM patients post anti-cancer treatment. Therefore, the aim of this study was to develop a patient-specific mechanobiological model to predict the temporal changes in site specific bone density and global mechanical properties of vertebra in patients with multiple myeloma post anti-cancer treatment to confirm or deny the third hypothesis of this thesis "Normal mechanobiology principles cannot explain the bone changes in MM patients' vertebrae treated non-surgically".

6.2 Materials and Methods

6.2.1 Patient data

The study participants included 10 non-cancer control patients from the ANTELOPE trial (Handforth *et al.*, 2024) and 10 MM patients from the RNOH dataset. For the controls, high resolution quantitative computed tomography (HR-QCT) scans of the T12 vertebra were acquired at two time points 12 months apart (for further details on the QCT scans see Chapter 3). For the MM patients, two clinical CT scans were acquired at baseline and a follow-up (16 ±15 months) with varying protocols (see Chapter 3 for more information). Within each MM patient, two vertebrae were selected, one 'control' vertebra which had no visible lesions and one 'lytic' vertebra which had a visible lesion (Table 6.1, Figure 6.1). For P12, all vertebrae were classed as 'lytic' so two 'lytic' vertebrae were selected. For P9, there was only one

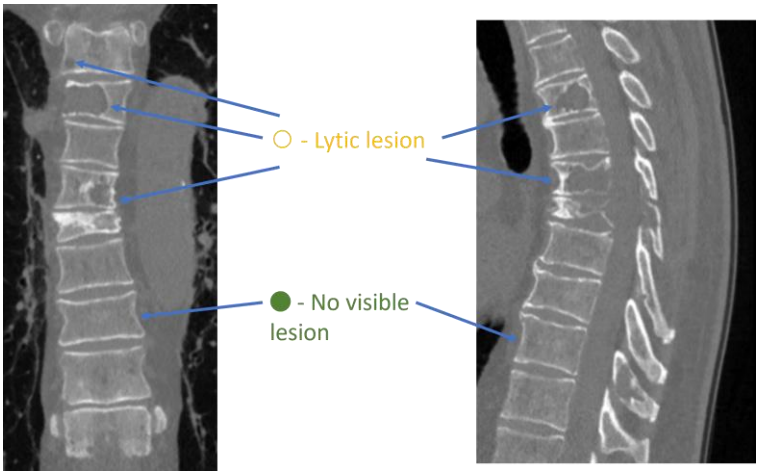

Figure 6.1. Example of which vertebra was classed as 'control' and 'lytic'.

vertebra in the CT scan so only one was selected. For the MM patients, a total of 19 vertebrae were selected.

Table 6.1. Patient data for the MM group with patient ID, time between baseline and follow-up and the vertebra segmented for the 'control' with no visible lesions and the 'lytic' which had a large lytic lesion.

Patient ID Controls	Age	Sex	Patient ID MM	Age	Sex	Time between baseline and follow-up (months)	Vertebral Level	Condition
C01	**74**	M	**P1a**	77	M	3	T4 T3	Control Lytic
C03	**77**	M	**P3**	66	M	12	T10 T11	Control Lytic
C04	**73**	M	**P3a**	63	M	12	T10 T11	Control Lytic
C05	**78**	M	**P5**	74	M	8	T4 T6	Control Lytic
C06	**68**	M	**P5a**	73	M	37	T1 C7	Control Lytic
C08	**53**	M	**P8**	47	M	2	T4 T3	Control Lytic
C10	**70**	M	**P9**	61	M	37	L3	Lytic
C11	**79**	M	**P9a**	49	M	9	T10 T11	Control Lytic
C12	**78**	M	**P11**	77	M	38	L3 L4	Control Lytic
C15	**80**	M	**P12**	34	M	4	T3 T4	Lytic Lytic
Average (±SD)	73 ±8		**Average (±SD)**	62 ±15		16 ±15		

6.2.2 Methods

A mechanobiological model was developed to integrate mechanical stimuli, cellular signaling pathways, and bone remodeling processes to predict changes in bone density and mechanical properties, offering insights into bone adaptation and response to loading conditions (Figure 6.2).

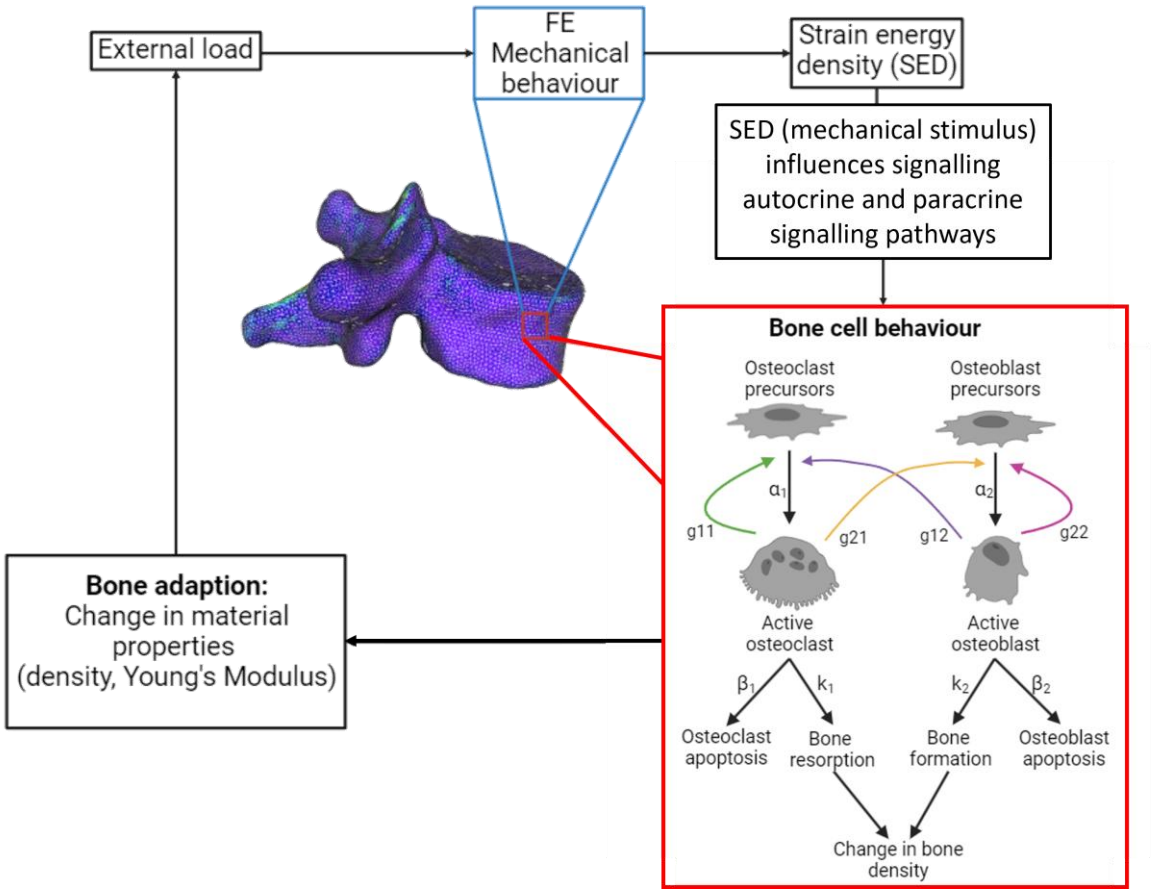

Figure 6.2. Overview of the mechanobiological method. Beginning with an external load applied to the Finite Element (FE) model which outputs the strain energy density (SED) per element. The SED is then imported into the remodelling algorithm which evaluates the interactions and behaviour of bone cells when influenced by a mechanical stimulus (SED). The output of the algorithm is the updated bone density and Young's modulus of each element which is then fed back into the FE model to analyse the predicted mechanical properties.

6.2.2.1 FE setup

Three-dimensional finite element (FE) models of vertebrae were generated from baseline and follow-up computed tomography (CT) scans for control T12 vertebra and selected vertebra for MM patients (Table 6.1). Control CT images were densitometrically calibrated using the phantom calibration method and the MM CT images were calibrated with a phantomless approach (see Chapter 3). The phantom approach was used for the control patients in order to compare the prediction of the clinical MM dataset to a 'gold standard' dataset. The 3D reconstruction of CT scans, meshing, alignment and assignment of material properties are

detailed in Chapter 3. Static simulation up to 0.15% strain was applied uniaxially to the superior endplate, while the inferior endplate was fixed. The strain was calculated using an estimation of the daily compressive forces where combining walking and standing and stair walking is ~900N on L4/L5 (Schäfer *et al.*, 2023), assuming the Youngs modulus is ~300 MPa as vertebra are mainly trabecular bone (Hou *et al.*, 1998; Kopperdahl and Keaveny, 1998; Morgan *et al.*, 2001; Kopperdahl, Morgan and Keaveny, 2002) and cross sectional area (CSA) is ~2000 mm^2 (taken from the L4 vertebra in this study) results in a compressive strain of 0.15% (Equation 7.1). The bracing treatment was not explicitly modelled in this study.

$$\varepsilon = \frac{\sigma}{E} = \frac{F/_{CSA}}{E}$$

Equation 6.1

Where ε is the strain, σ is the stress, E is the Young's Modulus, F is the applied force and CSA is the cross-sectional area.

From the FE 0.15% uniaxial compression model, the SED per element (Figure 6.3) was exported and used as an input in the mechanobiological algorithm. To evaluate the failure load (FL), separate non-linear models were run for baseline and follow-up scans as well as the predicted models. FL was calculated as the load that occurred at an applied apparent strain of 1.9% (Crawford, Cann and Keaveny, 2003; Wang *et al.*, 2012; Keaveny *et al.*, 2014).

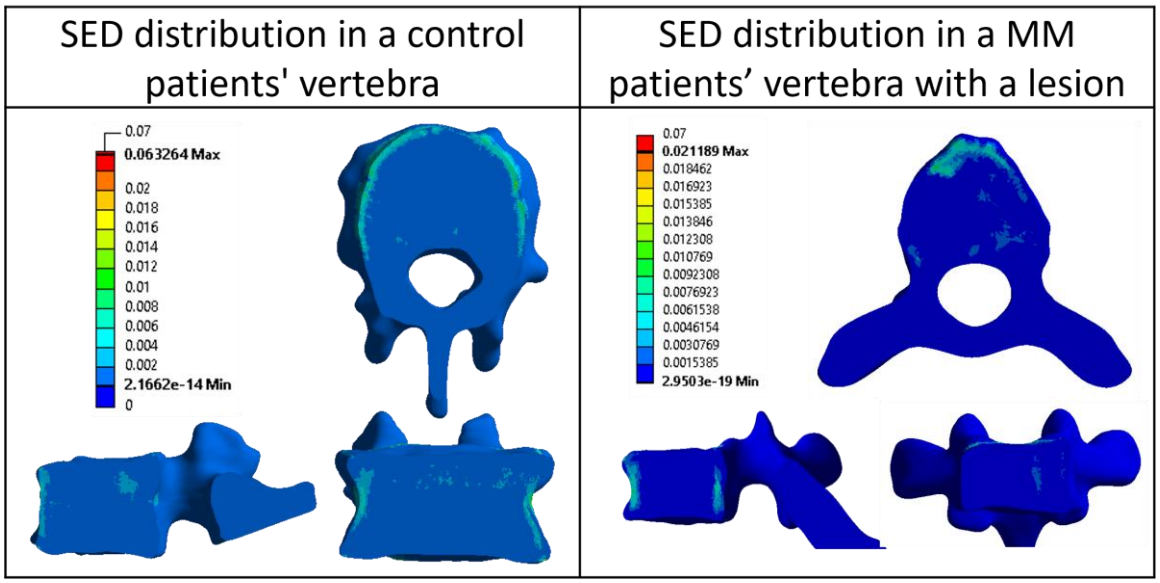

Figure 6.3 – Strain energy density distributions in an example control patient and example MM patient with a lytic lesion.

6.2.2.2 Mechanobiological algorithm

The organ-level FE was coupled with an algorithm representing the cell-level behaviours and interactions of bone cells using differential equations, which adjusted material properties based on biological pathways described by differential equations. The mechanical stimulus was defined based on the difference between the SED/density (SED/ρ) from the FE model and reference stimulus from literature (Hambli, 2014). If the SED/ρ is above this reference value, the mechanical stimulus the element receives will be positive and if the SED/ρ is below this reference value, the mechanical stimulus the element receives will be negative. The value of the stimulus influences the interaction between bone cells and the ratio between formation and resorption. Osteocytes aren't explicitly modelled but their effects are indirectly considered with the osteocyte density (d_k), osteocyte network connectivity (d_0) and mechanosensitvity of the osteocytes (u_k) (Schriefer *et al.*, 2005; Hambli, 2014).

$$S(t) = e^{(-d_k/d_0)} u_k (Sk - (Sk_o + (Sk - Sk_o)(1 - e^{(-\lambda t)})))$$

Equation 6.2

Where d_k= OCd/N_{rem} Osteocyte density/number of remodelling sites, d_0= osteocyte network connectivity, $S(t)$ = mechanical stimulus, u_k= osteocyte mechanosensitivity, Sk =SED/ρ per element, Sk_o= reference SED/ρ, λ =velocity of adaptation.

The bone cell interactions are controlled by the mechanical stimulus which influences the number of active osteoblasts and osteoclasts. g12 represents the signal from osteoblasts to osteoclasts (e.g. TGF-β) and g21 represents the signal from osteoclasts to osteoblasts (e.g. RANKL/OPG). The method of grouping the signalling pathways into two autocrine and paracrine pathways was chosen due to the lack of data on the individual signalling pathways (e.g. RANKL/OPG) (Bonfoh, Novinyo and Lipinski, 2011).

$$g11 = g22 = 0$$
$$g12 = A_1 + B_1 e^{-\gamma_1 S(t)}$$
$$g21 = A_2 + B_2 e^{-\gamma_2 |S(t)|}$$

Equation 6.3

Where g11 and g22 represent the autocrine factors that influence osteoclasts and osteoblasts respectively. A_1 and A_2, B_1 and B_2, γ_1 and γ_2 represent the parameters influencing the paracrine factors.

The change in osteoblasts and osteoclasts is controlled by the mechanical stimulus (above) and parameters that dictate how many of the cells are active over time (Komarova *et al.*, 2003).

$$\frac{dx_C}{dt} = \alpha_1 x_C^{g11} x_B^{g21} - \beta_1 x_C$$
$$\frac{dx_B}{dt} = \alpha_2 x_C^{g12} x_B^{g22} - \beta_2 x_B$$

Equation 6.4

Where x_C is the osteoclast population and x_B is the osteoblast population, α_1 and α_2 represent the rate of formation of osteoclasts and osteoblasts respectively and β_1 and β_2 are the rates of apoptosis for osteoclasts and osteoblasts respectively.

The number of active osteoblasts and osteoclasts is then calculated by taking the steady state populations away from the updated population for that timestep (affected by the mechanical stimulus) (Komarova *et al.*, 2003).

$$\begin{Bmatrix} X_C = x_C - \bar{x}_C & if x_C > \bar{x}_C \\ X_C = 0 & if x_C \leq \bar{x}_C \end{Bmatrix}$$
$$\begin{Bmatrix} X_B = x_B - \bar{x}_B & if x_B > \bar{x}_B \\ X_B = 0 & if x_B \leq \bar{x}_B \end{Bmatrix}$$

Equation 6.5

Where X_C and X_B are the active populations of osteoclasts and osteoblasts, respectively. Steady state populations ($\bar{x}_C$ and $\bar{x}_B$) are calculated by setting $\frac{dx_C}{dt} = 0$ and $\frac{dx_B}{dt} = 0$

The change in density was then based on the number of active osteoblasts and osteoclasts and the rate of formation and resorption respectively (Komarova *et al.*, 2003).

$$\frac{d\rho}{dt} = k_2 X_B - k_1 X_C$$

Equation 6.6

The density was then updated using the forward Euler method and Young's modulus based on the relationship described earlier (Niebur *et al.*, 2000; Morgan, Bayraktar and Keaveny, 2003).

$$\rho_{t+\Delta t} = \rho_t + \Delta\rho$$

Equation 6.7

$$E = 4730\left(\frac{\rho}{0.6}\right)^{1.56}$$

Equation 6.8

Where $\rho_{t+\Delta t}$ is the updated density, ρ_t is the density at the current time step and $\Delta\rho$ is the change in density. E is the Young's modulus and ρ is the density at the end of time.

Table 6.2. Initial Parameters for the mechanobiological model (Komarova *et al.*, 2003; Hambli, 2014)

Parameter	Description	Initial Value
d_0	Osteocyte network connectivity	0.1
OCd (mm^{-3})	Osteocyte density	10625
N_{rem}	Number of remodelling sites	Number of elements
u_k	Osteocyte mechanosensitivity	0.5
Sk_o (J/kg)	Threshold mechanical stimulus	0.0025
λ ($days^{-1}$)	Velocity of adaption	0.002
A_1	Parameter to regulate production of paracrine factors in g12	1.6
B_1	Parameter to regulate production of paracrine factors in g12	-0.49
γ_1	Parameter to regulate production of paracrine factors in g12	33.37
A_2	Parameter to regulate production of paracrine factors in g21	-1.6
B_2	Parameter to regulate production of paracrine factors in g21	0.6
γ_2	Parameter to regulate production of paracrine factors in g21	16.67
k_1	Osteoclast resorption rate	0.00305
α_1 (osteoclasts/day)	Osteoclast formation rate	3
β_1 (osteoclasts/day)	Osteoclast apoptosis rate	0.2
Initial population of osteoclasts	Initial population of osteoclasts	1
k_2	Osteoblast formation rate	0.000016
α_2 (osteoblasts/day)	Osteoblast formation rate	5
β_2 (osteoblasts/day)	Osteoblast apoptosis rate	0.02
Initial population of osteoblasts	Initial population of osteoblasts	15

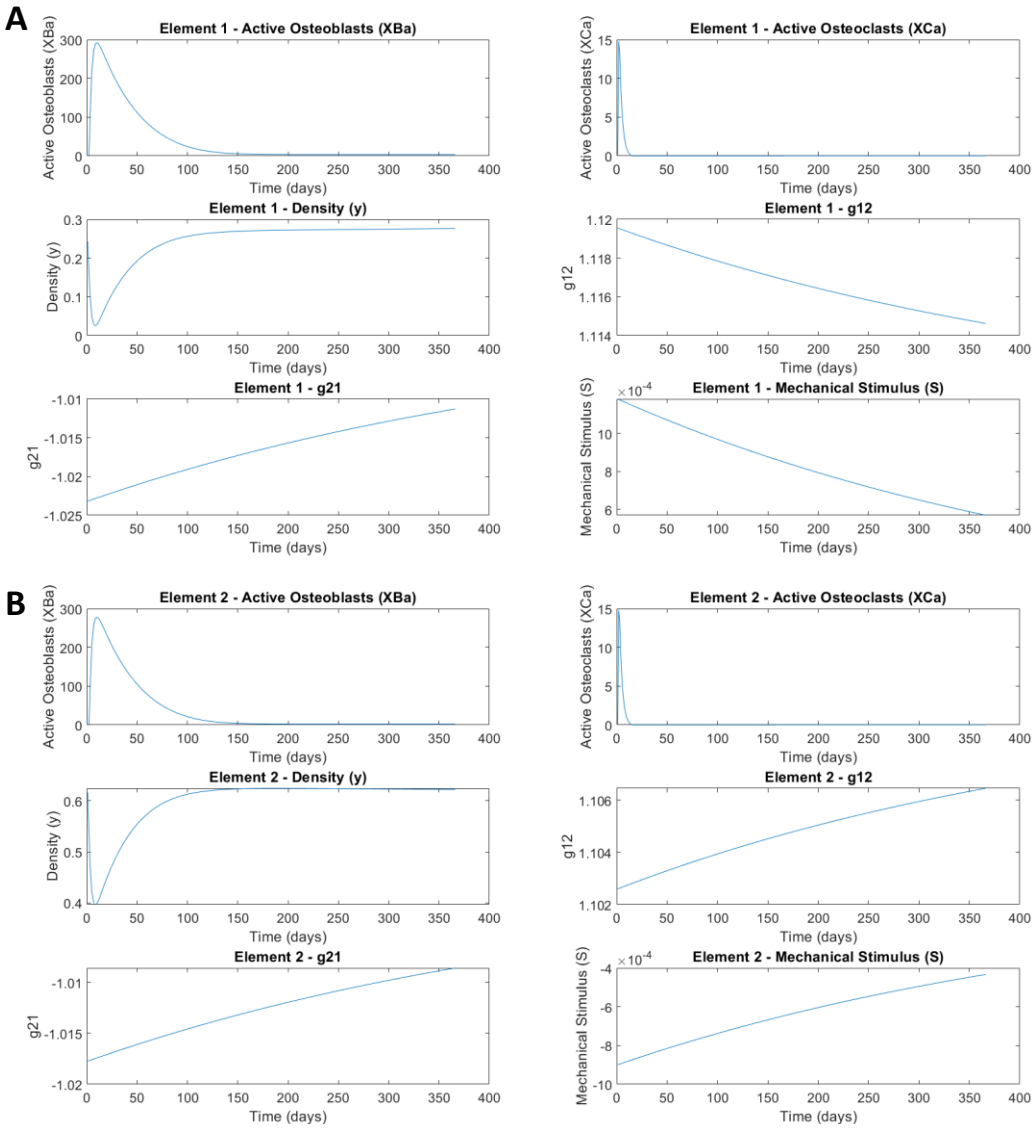

Figure 6.4. Example evolution of two random elements (A and B) for active osteoclasts and active osteoblasts, density, g12, g21 and mechanical stimulus.

In order to visualise the change in mechanical stimulus, g12, g21, active osteoclasts and active osteoblasts and then density, Figure 6.4 shows the evolution of these parameters over time in two randomly sampled elements in one of the vertebral models. The number of active osteoclasts is highest within the first 20-30 days and then the osteoblasts take over until around 150 days where no more remodelling occurs (Figure 6.4). For the first random element, the initial mechanical stimulus is positive meaning there should be a net gain in bone during this remodelling cycle. This can also be seen from g12, signal from osteoclasts to osteoblasts, starting high and decreasing over time, showing the slow decrease in osteoblast differentiation due to a reduction in mechanical stimulus. Similarly, g21, signal from

osteoblasts to osteoclasts slowly increasing over time, meaning an increase in osteoclast differentiation as the mechanical stimulus reduces. The impact of this on the change in density is seen by an initial decrease due to osteoclastic activity and then regaining stability through osteoblastic activity, with the final density dictated by the balance between the two. For the second random element, the initial mechanical stimulus is negative meaning there should be a net loss in density. The positive change in g12 and g21 highlights the increase in signal from osteoclasts to osteoblasts and the signal from osteoblasts to osteoclasts. In this element, these signals are very balanced, with the osteoblastic activity influencing the overall change more than the negative mechanical stimulus. This balance is seen from the density where it stabilises around the same point as the initial density.

6.2.3 Sensitivity and optimisation

For the control patients, a sensitivity analysis was conducted on all parameters individually to see how sensitive the model was to change. Each parameter was increased and decreased by 50% and the local change in density was evaluated then averaged across all elements.

From the sensitivity, parameters were chosen to be optimised for each patient based on how sensitive they were. If they induced a change in density of 20-150%, they were included in the optimisation. To optimise the parameters, a MatLab script (MATLAB 24.1.0.2689473 (R2024a) Update 6) was developed which began by defining an objective function which ran the original mechanobiological algorithm, computing the simulated density and then calculating the standard error between the simulated density and the actual follow-up density. The parameters to be optimised were given initial guesses (Table 6.2) taken from literature (Hambli, 2014) and upper and lower bounds which are set to ±50% of the original value. To evaluate the results of each set of parameters, the function fmincon was used. An options structure for the fmincon function was created to specify how the optimisation algorithm should behave including the display level (iterative) and the algorithm to use sequential quadratic programming (SQP) which means each iteration of the optimisation was solved and stored and with each iteration, the SQP refines its approximation to get closer to the optimal solution). The fmincon function was then called together with the objective function, initial guesses, bounds, and options. This function performs the optimization to minimise the standard error by adjusting the parameters until convergence. Convergence was met when

either the optimality tolerance, the standard error was below 1×10^{-6}, or the step tolerance was below 1×10^{-10}, where further changes in the input parameters did not significantly reduce standard error.

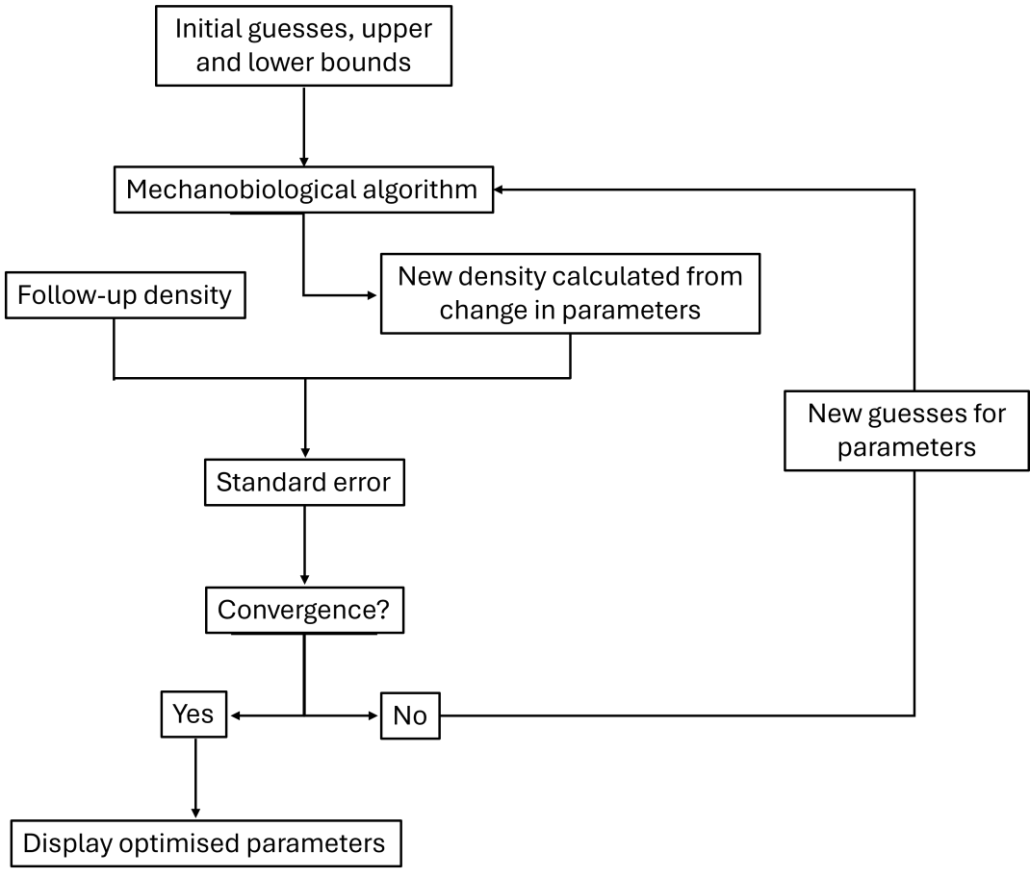

Figure 6.5. Flow-chart of the optimisation

6.2.4 Statistics

To compare the optimised parameters between the control, MM non-lesion and MM lesion groups, Mann-Whitney Unpaired test was used, where significance was defined as $p < 0.05$. To test for significance ($p < 0.05$) between the follow-up BMD and FL and the predicted BMD and FL, a Wilcoxon paired test was used. Linear regression analyses were performed between the follow-up and predicted BMD and FL to assess the variance. A significant result was found when $p < 0.05$.

6.3 Results

6.3.1 Sensitivity of mechanobiological parameters

Figure 6.6 shows the average percentage change in density in all elements when increasing and decreasing each parameter by 50%. It is clear that some parameters are less sensitive, with a change in density less than 10% despite a 50% increase or decrease of the input parameters (d_0, d_k, u_k, λ, Sk_o, γ_1 and γ_2). Osteocyte network connectivity (d_0) and osteocyte density (d_k) are used in Equation 6.2. This exponential was always going to be between 0 and 1, meaning any changes in d and dk do not alter the overall response. Osteocyte mechanosensitivity (u_k) started off very low as it was introduced as a dimmer switch between 0 and 1 and was set to 0.5. This value was too small for this parameter to increase or decrease the mechanical stimulus and density by more than 10%. The adaption velocity (λ) dictated how fast the system responds to the mechanical changes. This parameter should have a low sensitivity as bone remodelling occurs over a long period meaning the effect of λ is spread across the time. If bone remodelling was a shorter process (days instead of months), the effect

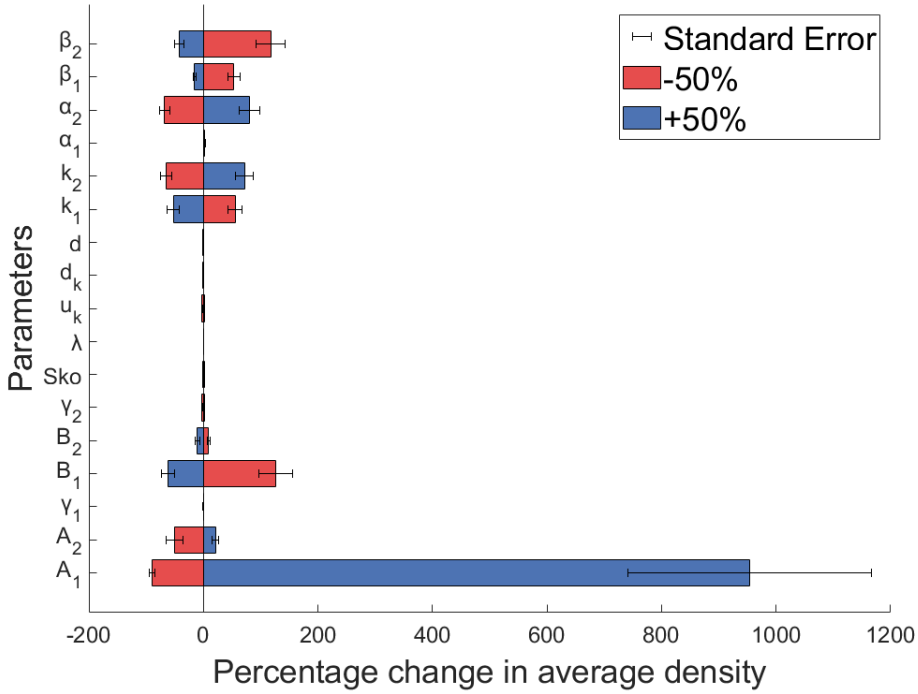

Figure 6.6. Change in average density when increasing and decreasing each parameter by 50% to understand the sensitivity of each parameter

of λ would be more apparent. The difference in mechanical signal from changes in Sk_o were not large enough to affect the osteoblast and osteoclast populations which drove the change in density, hence why Sk_o had a low sensitivity (<10%). γ_1 and γ_2 were exponential decay parameters that determined the influence of the mechanical stimulus S on the rates of osteoblast and osteoclast differentiation (g12 and g21). These parameters sat within Equation 6.3 as $e^{-\gamma_1 S(t)}$ and $e^{-\gamma_2|S(t)|}$ so doubling gamma still gave a very similar value to the initial estimate.

It is also noticeable that A_1 was very sensitive to a positive change (+50% in A_1). A_1 was the dominant factor in g12 as the exponential element was always close to 1. Equation 6.4 then used g12 as an exponential to the osteoclast population (x_C^{g12}). As A_1 was the dominant factor in g12, if A_1 was doubled, x_C^{g12} would increase by a factor of 76, also increasing the population of active osteoblasts by a factor of 76 for every iteration. This induced a 'runaway' effect where the density of each element was then significantly increased, hence the large variation in the positive change in A_1. This did not happen for the decrease in A_1 as the system was osteoblast dominant and therefore could recover from a decrease in osteoblast recruitment. A_2 also did not have this effect, which was most likely due to the initial osteoclast number being 1 and therefore there was not the 'runaway' effect we observed with A_1.

Figure 6.7 shows a zoomed in version of the sensitivity results for k_1, k_2, α_1, α_2, β_1 and β_2. Most of these parameters had ~50% change in density, both when increasing and decreasing the parameter by 50%, as would be expected for a balanced model. The only parameter which seems to have little effect is α_1. α_1 influenced the number of osteoclasts produced per timestep but the dominant factor in this equation was most likely x_B^{g21} as the number of initial osteoblasts at each timestep was much larger than the number of osteoclasts. Therefore, the effect of α_1 was dampened. All six of these parameters have important links to biological processes that can be monitored in clinic via blood BTMs and could be altered depending on patient specific data. α_1 and α_2 control the osteoclast and osteoblast differentiation rate, β_1 and β_2 control the osteoclast and osteoblast apoptosis rate and k_1 and k_2 control the rate of resorption and formation. For this reason, these six parameters were chosen for optimisation.

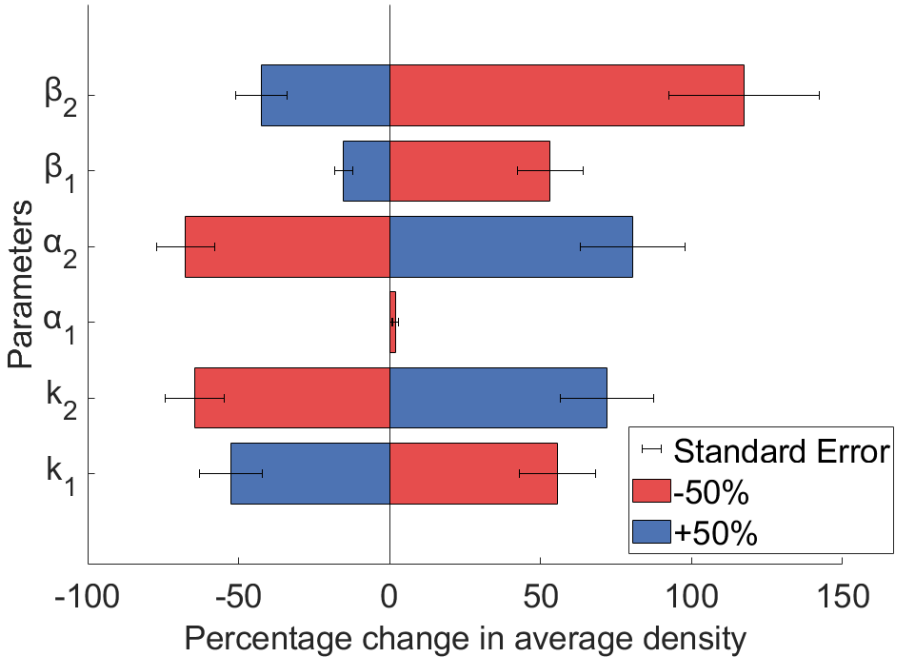

Figure 6.7. Close up view of the average change in density of k1, k2, α_1, α_2, β_1 and β_2 when increasing and decreasing each parameter by 50%.

6.3.2 Optimisation of mechanobiological model parameters

Both k_1 and k_2 decreased from controls to MM controls and again to the MM lesion group (Figure 6.8). Despite this difference being insignificant, this suggests that in MM vertebra with lesions, both bone formation and resorption rates were altered significantly, with k_1 decreasing more sharply than k_2. The sharp decline in k_1 suggested reduced bone resorption in the MM lesion group, contributing to the increased bone apposition post treatment. The decrease in k_1 and k_2 suggested the rate of turnover is slower in the MM patients but whether formation and resorption were balanced or not was unclear from this figure. Therefore, the ratio between k_1 and k_2 was calculated to understand if there was an imbalance in formation and resorption. Figure 6.9 shows the ratio of k_1 to k_2 in each group, with it decreasing slightly between controls to the MM control group and again to the MM lesion group. This difference was not significant, but it showed there was a trend towards more osteoblastic activity compared to osteoclastic activity in MM patients and particularly the vertebrae with lesions.

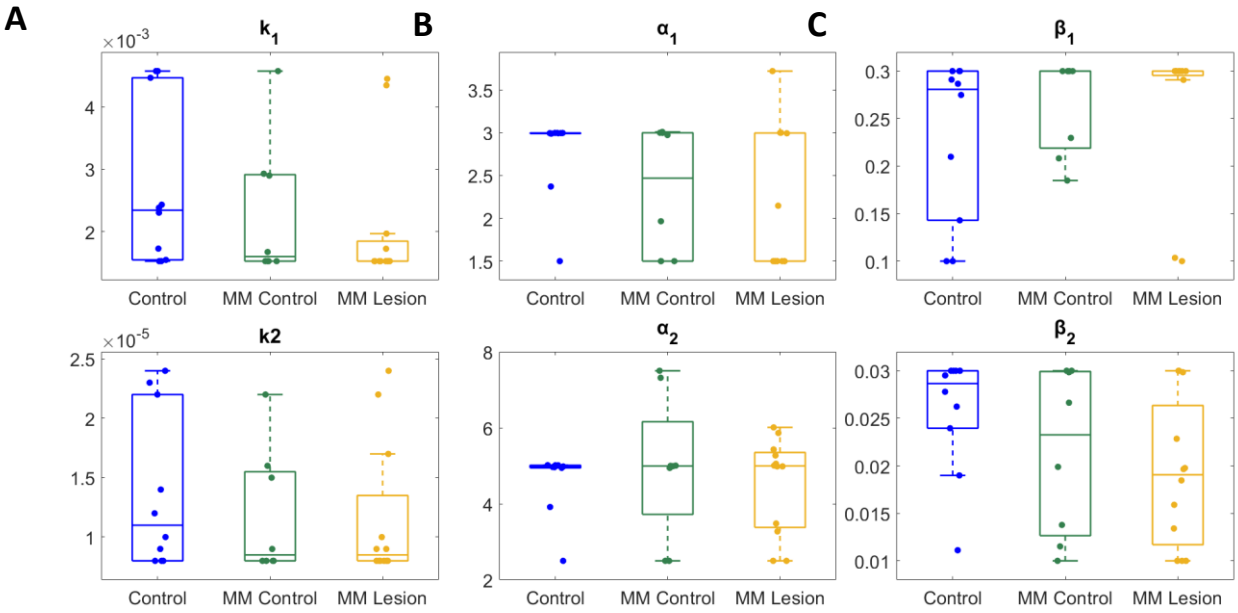

Figure 6.8. Box plots of optimised parameters in the control, MM control and MM lesion groups for (A) k_1 and k_2 (B) α_1 and α_2 and (C) β_1 and β_2.

For the differentiation rates, α_1 showed a decrease from control to MM groups while α_2 showed a very similar median value for all three groups. For both α_1 and α_2, the control group had a much smaller range than the other two groups, suggesting these parameters could be fixed for the controls. When looking at the ratio between α_1 and α_2, the MM lesion group had a much lower ratio than the controls. This suggests that the number of osteoblasts differentiating was higher than osteoclasts in the MM lesion group, however this was not significant. For the apoptosis rates, β_1 was relatively stable across the groups, with no significant differences, but showed a slight increase in MM Control and MM Lesion, indicating that osteoclasts were being removed quicker. β_2 showed more variability but tended to decrease in the MM Lesion group, suggesting that osteoblasts were being removed at a slower rate. However, with reduced osteoblast production this could balance overall osteoblast activity. The ratio between β_1 and β_2 had a small increase from Control to MM Control and a large jump to the MM lesion subgroup. This suggested the rate of osteoclast apoptosis was faster than osteoblasts apoptosis meaning there were more active osteoblasts.

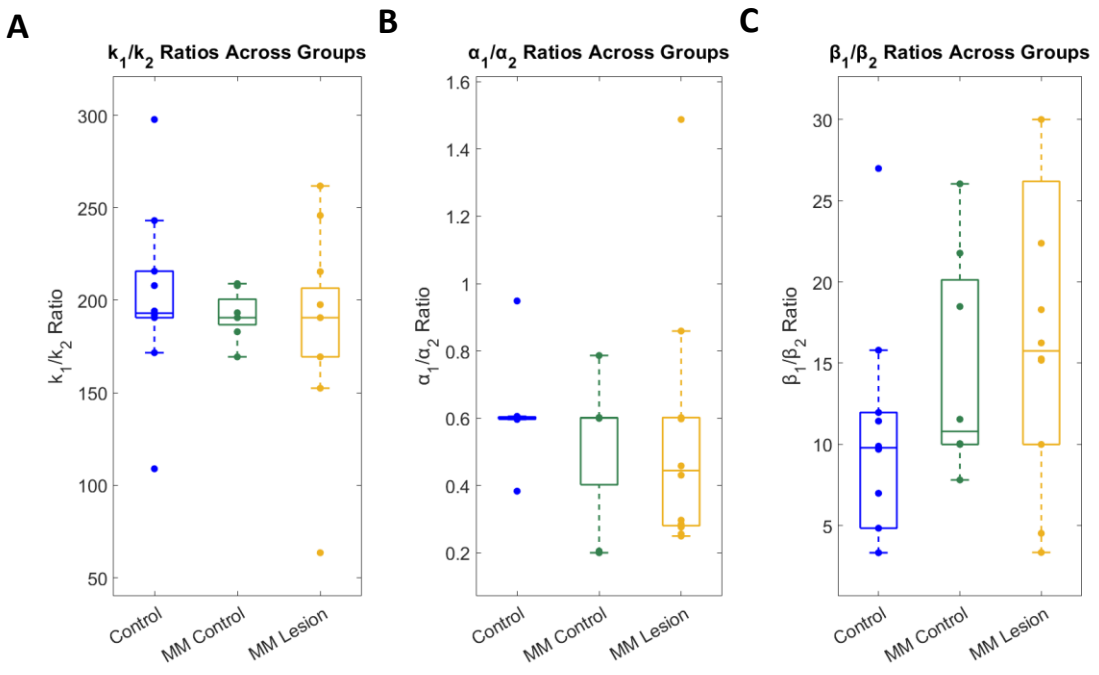

Figure 6.9. Ratio of (A) resorption to formation (k_1/k_2) (B) formation of osteoclasts to formation of osteoblasts (α_1/α_2) and (C) apoptosis rate of osteoclasts to apoptosis rate of osteoblasts (β_1/β_2).

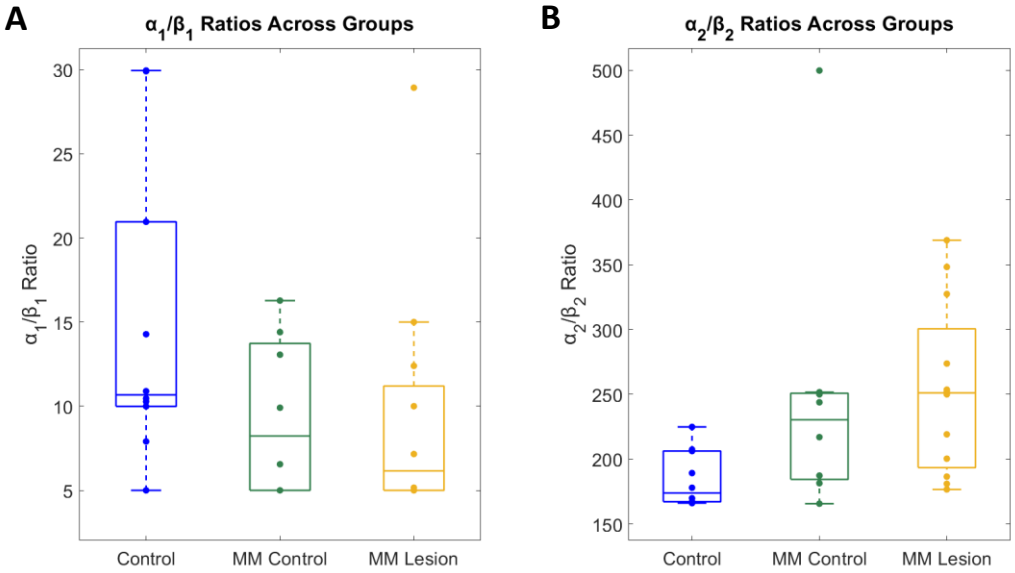

Figure 6.10. Ratio of (A) osteoclast formation to osteoclast apoptosis (α_1/β_1) (B) ratio of osteoblast formation to osteoblast apoptosis (α_2/β_2)

When assessing the differentiation to apoptosis ratio (Figure 6.10), osteoclasts had a lower ratio in the MM lesion group compared to the control and MM control, suggesting there was more osteoclast apoptosis than differentiation, suggesting less osteoclastic activity. On the

other hand, the α_2/β_2 ratio increased through the groups, suggesting more differentiation compared to apoptosis of osteoblasts, and hence more bone apposition in the MM lesion group.

6.3.3 Mechanobiological Predictions

Figure 6.11 shows the minimum principal strain at baseline, follow-up and predicted follow-up for a representative control patient (A), an MM patient with no lesion (B) and an MM patient with a large lesion (C). For the control patient, the model captures most changes from baseline to follow up as seen from the distribution of the maximum compressive strain (red regions) at predicted follow up, particularly in the axial plane. The model's ability to predict mechanical properties is also shown from the similar values for failure load and failure strength for follow up and predicted follow up.

For the example MM vertebra with no lesions, similarly to the control, the model captures most changes from baseline to follow up capturing the change in compressive strain (Figure 6.11). In the sagittal and coronal view, there are some slight discrepancies in magnitude of strain, where the high compressive strains at Follow-up are not seen in the Predicted. However, despite the local differences, the model is still able to predict the global changes as there is no significant difference in the failure load and failure strength between Follow-up and Predicted (Figure 6.12).

For the example MM patients' vertebra with a large lesion, the predicted distribution does not accurately capture the observed changes in strain, with substantial differences between the compressive strain distribution for Follow-up and Predicted (Figure 6.11). This is particularly clear in the lesion region, characterised by a region low bone density ($\rho < 0.1$ g/cm^3), highlighted at Baseline, where the compressive strains are much lower in the Predicted model compared to the actual Follow-up. In comparison to the example MM vertebra with no lesion, these discrepancies for the vertebra with a large lesion do follow through to the global properties as the prediction of failure load and failure strength (FS) is far from the actual Follow-up (Follow-up FL: 2233 N, Predicted FL: 2695 N, Follow-up FS: 3.11 MPa, Predicted FS: 3.75 MPa). These findings suggest that the more complex bone

characteristics such as lesions, require further input to the model in order to predict the changes in these particular vertebrae.

The results seen in the individual patients in Figure 6.11 are representative of the overall dataset. As seen from Figure 6.12, where, for both density and failure load, the lines representing each patient are almost all horizontal and there was no significant difference between Follow-up and Predicted (average percentage difference BMD: 2.13 ±2.36% NS, average percentage difference FL: 3.64 ±3.72% NS). This confirms the model predicted well for the control group.

For the MM group, the density was predicted well, as seen by the individual patient lines being mainly horizontal with no significant difference between Follow-up and Predicted (average percentage difference BMD: 3.49 ±4.63% NS). Figure 6.13 shows that the majority of the variability in the control, MM non lesion and MM lesion groups can be explained by a linear regression analysis (control: $R^2 = 0.98$, $p < 0.001$, MM non lesion: $R^2 = 0.93$, $p < 0.001$, MM lesion: $R^2 = 0.91$, $p < 0.001$). However, for failure load, the difference between Follow-up and Predicted is significant and it is clear from the patient lines there are large discrepancies (average percentage difference FL: 18.67 ±16.83% p = 0.01). Looking further into this data, if the group is split into two, where green is no visible lesions and yellow is lytic lesions, it is clear that the larger discrepancies between Follow-up and Predicted are in the lesion group. An upwards trend can also be seen, where for the lesion group, most of the patients' predictions are greater than the Follow-up. These observations are consistent with the linear regression analysis of the failure load, shown in Figure 6.13, where the variability is higher in the MM lesion group compared to the MM non-lesion and the controls (control: $R^2 = 0.99$, $p < 0.001$, MM non lesion: $R^2 = 0.94$, $p < 0.001$, MM lesion: $R^2 = 0.85$, $p < 0.001$). The prediction of strains in the vertebra with a large lesion (Figure 6.1 C) provides an explanation for this result, as lower strain is indicative of less compression which would correspond to a higher failure load, as seen in Figure 6.12.

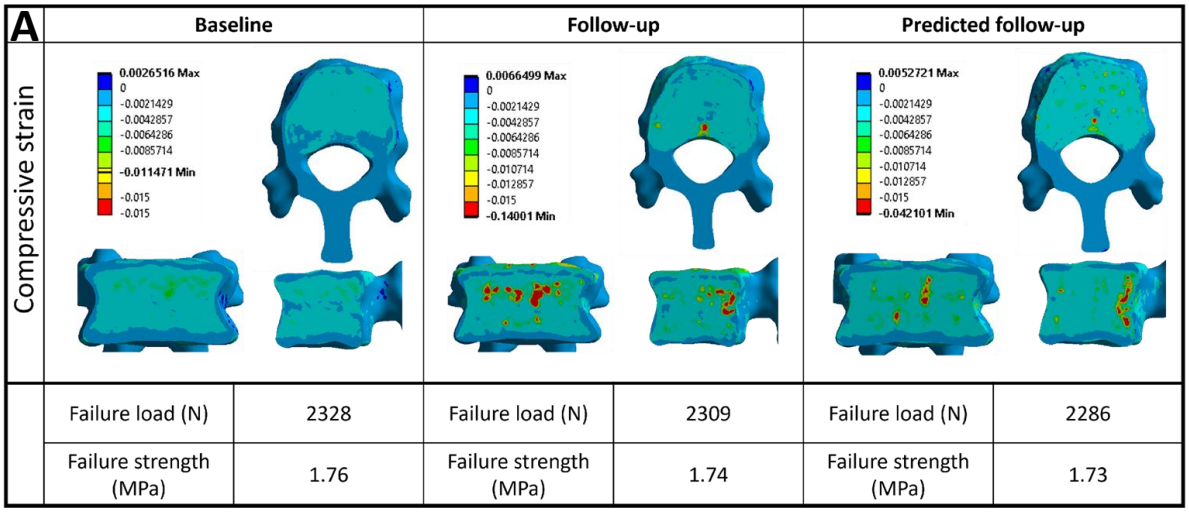

Failure load (N)	2328	Failure load (N)	2309	Failure load (N)	2286
Failure strength (MPa)	1.76	Failure strength (MPa)	1.74	Failure strength (MPa)	1.73

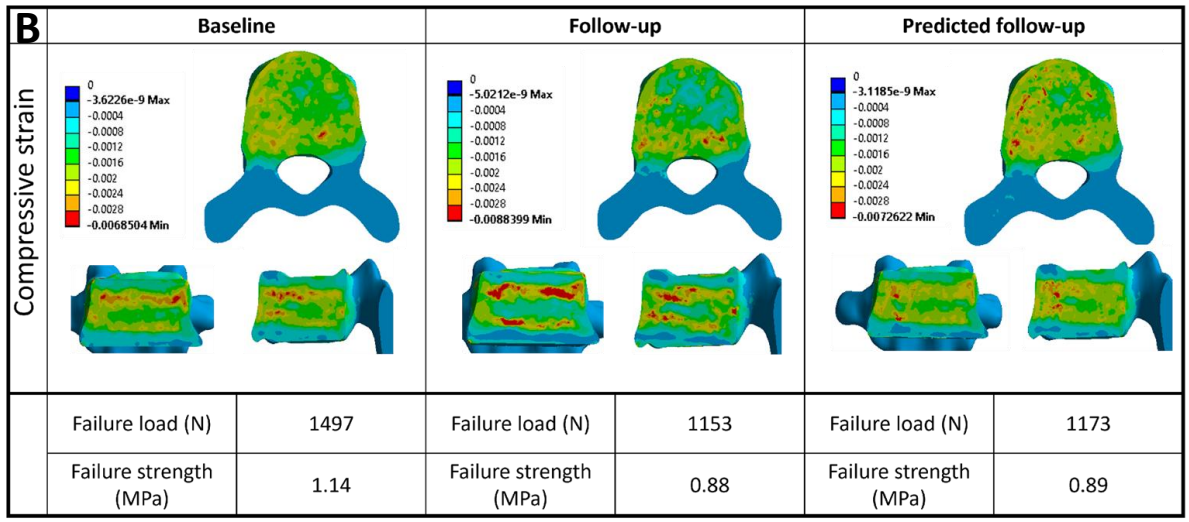

Failure load (N)	1497	Failure load (N)	1153	Failure load (N)	1173
Failure strength (MPa)	1.14	Failure strength (MPa)	0.88	Failure strength (MPa)	0.89

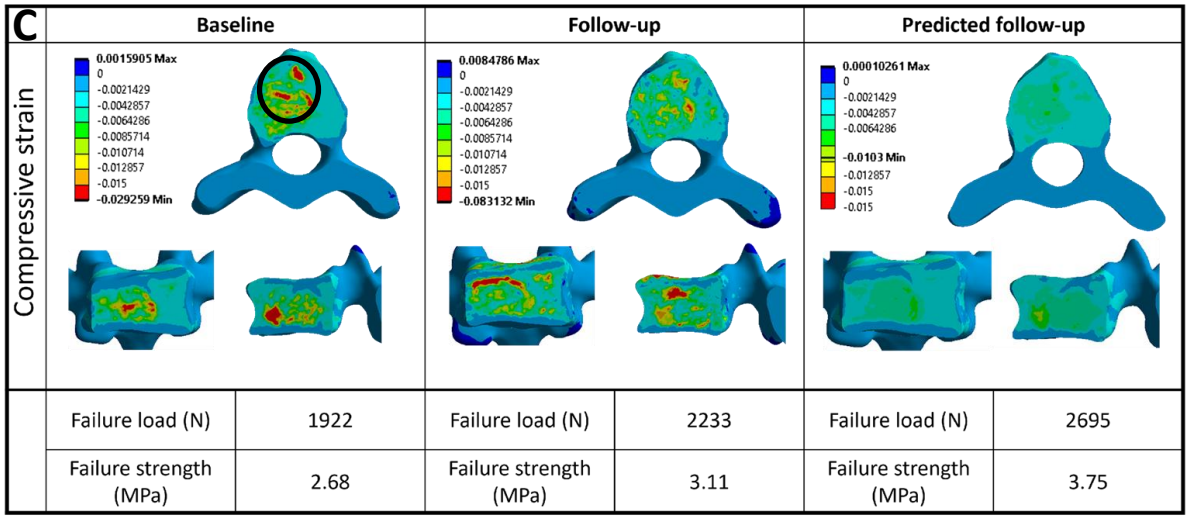

Failure load (N)	1922	Failure load (N)	2233	Failure load (N)	2695
Failure strength (MPa)	2.68	Failure strength (MPa)	3.11	Failure strength (MPa)	3.75

Figure 6.11 - Compressive strain distributions at baseline, follow-up and predicted follow-up in all three planes for an example control patient (A), MM patient with no lytic lesions (B) and an MM patient with a large lytic lesion (C).

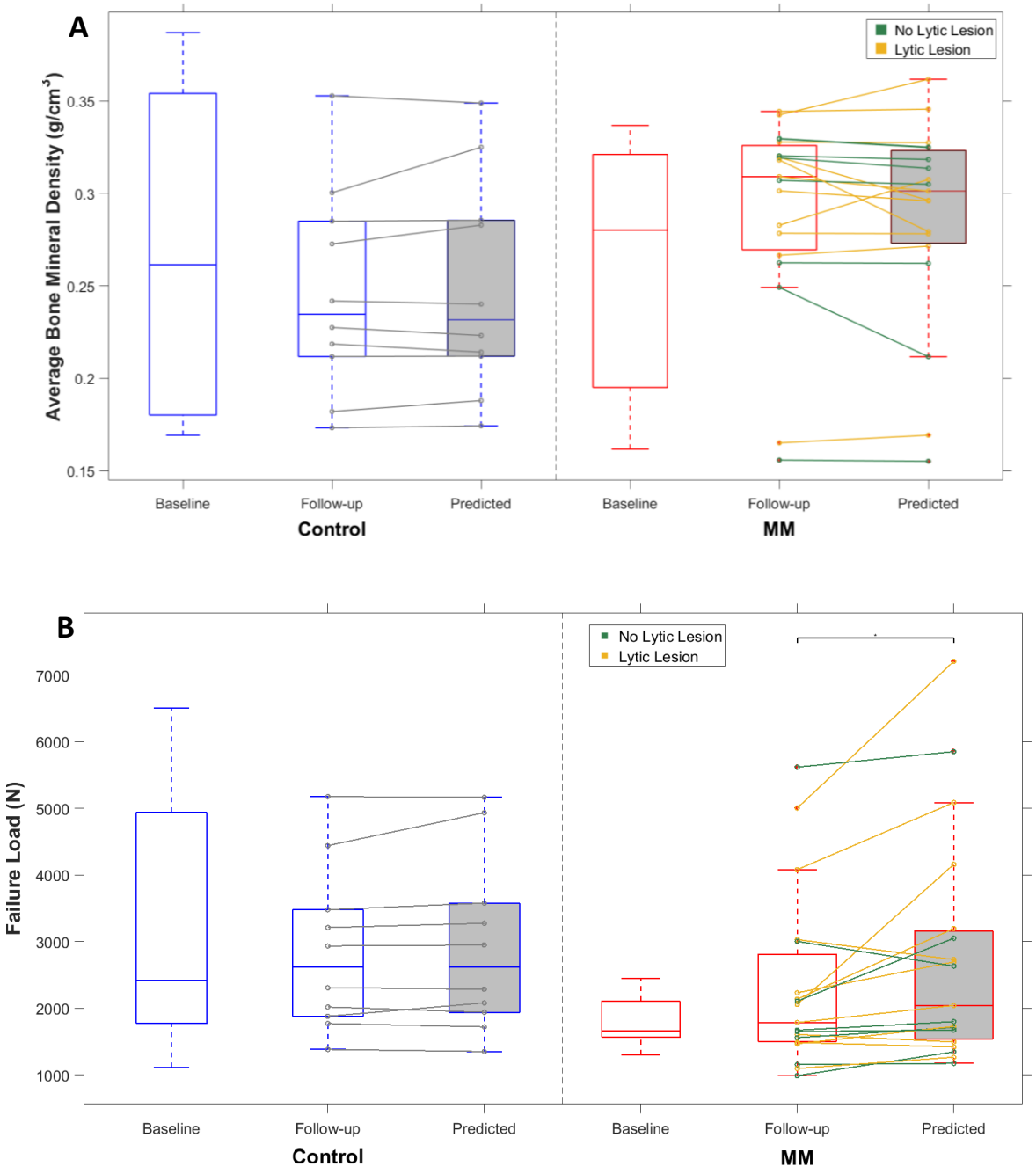

Figure 6.12 - Box plot of the (A) average bone mineral density and (B) failure load at baseline, follow-up and predicted follow-up for the control group (blue) and the MM group (red). The MM group was split into two to represent patients with no visible lytic lesions (green) and lytic lesions (yellow). A horizontal line represents data for a single patient connecting follow-up to predicted follow-up. * indicates p < 0.05

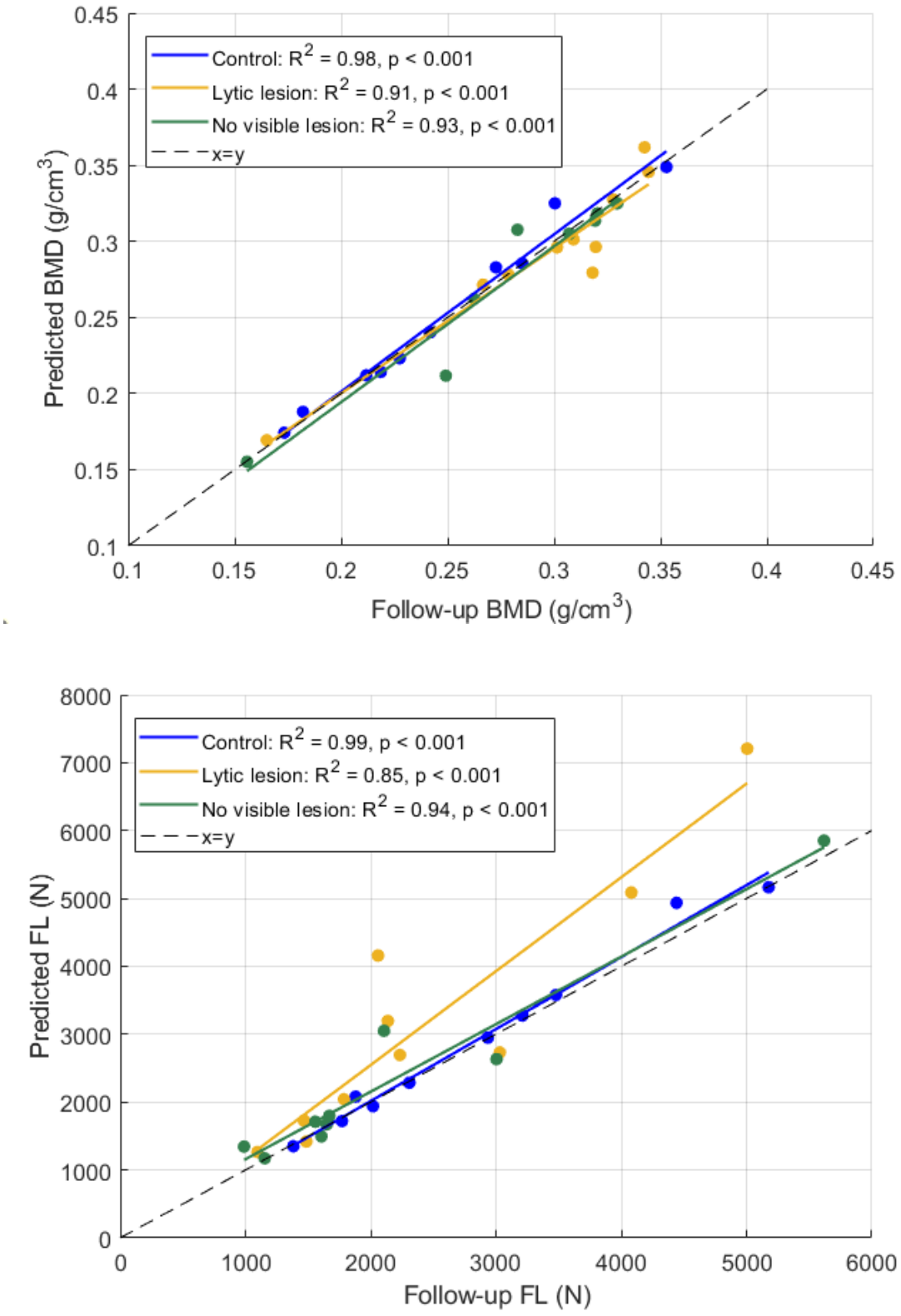

Figure 6.13 – Linear regression analysis between the follow-up and predicted (A) average bone mineral density (BMD) and (B) failure load (FL). Control data shown in blue, MM non-lesion group shown in green and MM lesion group shown in yellow.

To ensure the model was not affected by the vertebral level, the error in prediction was calculated for each vertebral level included in the model (Figure 6.14). The largest mean absolute error (MAE) occurs at L4 (MAE: 2100 N), followed by L3 (MAE: 1001 N) and T10 (MAE: 864 N). As the model was developed using the T12 control vertebra and the loading assumptions were based at L4/L5, it is clear the model is not affected by the distance away from T12.

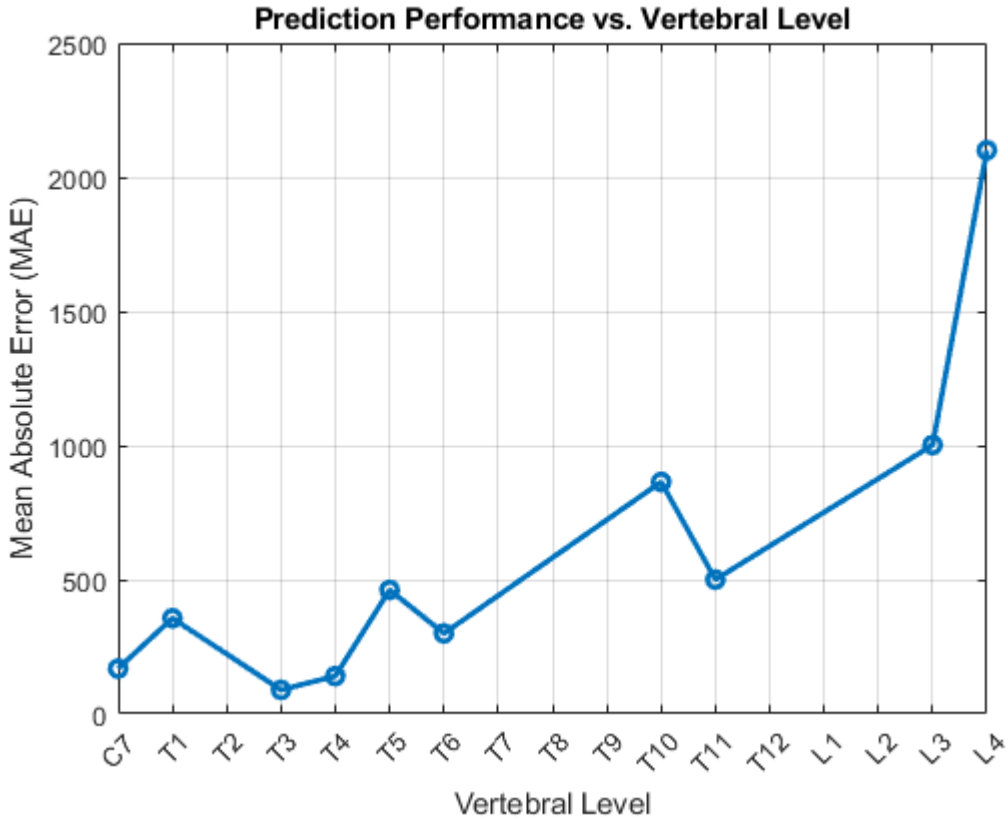

Figure 6.14 - Mean absolute error of the failure load at each vertebral level evaluated within this study

6.4 Discussion

The work in this chapter developed a mechanobiological model to predict the change in densitometric and mechanical properties of vertebra in patients with multiple myeloma following anti-cancer and bracing treatment. Overall, the model predicted the densitometric and mechanical properties well for the control patients and the MM patients' vertebrae with

no lesions. However, the model tends to overestimate the mechanical properties of MM vertebrae with lesions compared to the Follow-up.

The biological regulation algorithm controlled the interaction and activity of bone cells depending on mechanical stimulus (SED/density) from the finite element model. This algorithm performed well regarding timeline of activation and activity of osteoclasts and osteoblasts compared with literature (Cowin, 2001). With osteoclasts being differentiated first and resorbing bone for the first 20-30 days (Agerbzk *et al.*, 1991) followed by osteoblast differentiation and bone formation up to around 180 days totalling around 200 days for the full remodelling cycle (Eriksen, 2010). The period between the end of osteoblast activity and end of time steps is classed as the period of remineralisation. In this period, the model does not carry out any further calculations but in reality, this period is where the bone mineralises (Boivin *et al.*, 2009). For the control patients, this period is always ~165 days, however, for the myeloma patients, as the time between baseline and follow-up varies, this period is shortened or lengthened depending on when the follow-up was. This is a limitation of the current model as it does not account for more than one remodelling cycle, which would be the case if the time between scans is more than a year.

SED/density was chosen as the mechanical stimulus input for the mechanobiological algorithm. In the control patients' vertebra and MM patients' vertebra with no lesions, the SED was highest in the cortical shell. However, for MM patient's vertebra with lesions, the SED was also high around the lesion region, even if this fell within the trabecular portion of the vertebral body. If SED alone was used as the mechanical stimulus for the mechanobiological algorithm, the areas with high SED would increase in density and the areas with low SED would decrease in density. This would be an issue for the region where the lesion lies as no remodelling would occur here. However, from literature, bone apposition has been reported in the lesion region adjacent to mineralised tissue (Malhotra, Butler, *et al.*, 2016; Malhotra, Lui, *et al.*, 2016; Mohan *et al.*, 2021). The combination of SED/density allows for an increase in mineral in the lesion region where there is low density but also at the high stress zones, and therefore high SED, around the lesion.

The model works well for the control and MM vertebrae with no lesions when predicting the strain distribution in the vertebral body. However, for the MM vertebrae with a large lesion,

the strain map fails to capture the change from baseline to follow-up. A limitation of the model is that, when applied to elements representing lesions, it incorrectly assumes a starting population of osteoblasts. Therefore, when there is a very low-density element, the ratio of SED/density is high, the number of osteoblasts differentiated is high leading to an increase in density. This element then has a higher density than it should, decreasing the strain within that region. In reality, bone will form adjacent to already formed bone, not in the centre of the lesion, reducing the size of the lesion over time. See Appendix 1 for the attempts at adjusting the model to mitigate this limitation.

The parameters used within the biological regulation algorithm are mostly taken from the literature (Komarova *et al.*, 2003; Hambli, 2014). The parameters that were optimised for each patient accounted for the patient specific variations in bone remodelling rates, improving the predictive ability of the model. However, the parameters that were left as the initial chosen values were not optimised for this model. Due to a slightly different set-up to the model it was based on, there was an imbalance between formation and resorption, with formation having a much more amplified response. As can be seen in the sensitivity study where, when the parameters related to osteoblast differentiation and activity are altered, the density changes were notably larger (>50%). The model requires further improvement for the vertebra with larger lesions and therefore, future work could include a perturbation study to ascertain the value at which the parameters induce a change, from the originally calculated density, of greater than 10%. This will ensure that the parameters that should be influencing the change in density are having the desired effect.

When comparing the interactions and activity of the bone cells in the control versus MM patients, it can be seen that the MM lytic group had a higher osteoblast differentiation to apoptosis ratio and a lower osteoclast differentiation to apoptosis ratio than both the MM controls with no lesions and the healthy controls. This suggests that there is a higher number of active osteoblasts and a lower number of active osteoclasts in the MM lytic vertebrae. However, when looking at the ratio between resorption and formation, the ratios are very similar for all groups, suggesting a similar balance in formation and resorption in all groups. This means that the driving factor for more formation within the MM lytic group is the larger number of osteoblasts forming and less active osteoclasts resorbing.

The overall results showed no significant difference between the follow-up and predicted for the average bone mineral density for controls and MM patients. This strong prediction was supported by the linear regression analysis explaining 98% of the variance for the controls and 93% and 91% for the MM non-lesion group and MM lesion group, respectively. This is expected as the optimisation stage adjusted the parameters to fit the algorithm to the follow-up density in each element. As the average minimum standard error is optimised, out of the ~500,000 elements, there could be a small number of elements with a large error, but the rest of the elements have errors so small that the average standard error is below the threshold for convergence. This could be another reason for the discrepancies in the MM patients with large lesions as the lesion region could be the source of high errors which are cancelled out by the rest of the vertebra. The worst prediction of BMD was one of the MM non-lesion patients. Nevertheless, this error was not amplified when predicting the failure load suggesting the distribution of density is more important than the average. The prediction of failure load was not significantly different to the follow-up for the control and MM control patients, with some small discrepancies compared to the density prediction. The prediction for the MM large lesion group was significantly different to the follow-up, the majority of these patients' failure loads were overestimated due to the high mechanical stimulus in the lesion region as mentioned earlier.

There were some limitations to the current model. The boundary condition used for loading was a uniaxial compressive load using displacement control applied to the superior endplate. Uniaxial loading has been used in other validated FE studies to assess the mechanical properties of vertebra (Imai *et al.*, 2006; Zeinali, Hashemi and Akhlaghpoor, 2010; Dall'Ara *et al.*, 2012). In addition, the majority of the loading experienced by vertebrae is uniaxial from the vertebra above with some bending moment caused by the curvature of the spine. The loading conditions would have an effect on the magnitude of mechanical stimulus each remodelling site (element) receives and therefore, inducing bone apposition and resorption in the incorrect locations. Future work could include the comparison of different loading conditions, such as anterior bending, to assess the effect on the predictive power of the model.

Another limitation comes from the assumption that there is no new mechanical stimulus over the biological regulation algorithm. The mechanical stimulus tends towards zero over time

and is not updated depending on changes in bone density, i.e. if resorption has occurred and the density decreases, it is likely that the SED will then increase changing the bone cell dynamics and activity within that element. However, as the parameters in the model are optimised for the CT based density at follow-up, there is no way to add additional points for the evaluation of SED based on the changes after so many months. This would make the optimisation void and more difficult to estimate these parameters for each patient. As remodelling cycles are typically 180-200 days (Eriksen, 2010), a simple relationship between SED and change in density could be acquired and applied after this period to estimate the change in SED and therefore mechanical stimulus after the first remodelling cycle. Changing the loading before this point would overcomplicate the bone cell dynamics and interactions, causing the remodelling cycle to not behave in the desired way. To further inform the model of changes in remodelling, serum BTMs such as P1NP (Pro-collagen 1 N-terminal propeptide), CTX (carboxy-terminal collagen crosslinks) and sclerostin could be used at interim points during baseline and follow-up. This would allow for more patient specific data on remodelling throughout the cycle without the need for more CT scans.

6.5 Conclusion

In summary, the newly developed model predicted well the bone mineral density and mechanical properties for the control and MM with no lesions while it needs improvement for the MM patients with large lesions. This confirmed the third hypothesis of this thesis that "Normal mechanobiology principles cannot explain the bone changes in MM patients' vertebrae treated non-surgically". Additional investigations into the accuracy of the model including the alteration of the biological regulatory algorithm to ensure no remodelling can occur in the centre of the lesion was subsequently conducted and results of this can be seen in the Appendix 1 showing a promising improvement to the predictive accuracy. Furthermore, modifying the model to incorporate clinical BTM data could both increase the predictive ability and enhance the clinical utility. In the final chapter, we will evaluate the use of BTMs to inform the model of changes in remodelling at interim points between baseline and follow-up.

7 CLINICAL BIOMARKERS FOR PHYSIOLOGICALLY INFORMED MECHANOBIOLOGICAL MODELS

Chapter 6 details the mechanobiological model and its predictions on the multiple myeloma (MM) vertebra using patient specific optimisation of the bone remodelling parameters based on CT data at baseline and follow-up. Therefore, this model cannot be applied to prospective data to predict changes in the bone without a follow-up CT. As alluded to in chapter 6, the hypothesis behind this chapter is "Mechanobiological models incorporating bone turnover markers can predict bone changes in vertebrae of patients with multiple myeloma". Therefore, the aim of this chapter was to develop a preliminary study to evaluate the possibility of using Bone Turnover Markers (BTMs) at early time points (1,2 and 3 months after baseline) to predict key parameters in the mechanobiological algorithm and thus assess their ability to inform the model to predict the density and failure load after 12 months. This chapter uses a new unique clinical dataset composed of time-series CT scans and serum BTMs from the same patients acquired from Sheffield Teaching Hospitals.

7.1 Introduction

BTMs, particularly P1NP (Procollagen Type I N-terminal Propeptide) and CTX (Carboxy-terminal collagen-crosslinks), have been used clinically to evaluate bone turnover and the effect on fracture risk for patients with osteoporosis (Kuo and Chen, 2017) and MM (Kowalska *et al.*, 2010). A description of these biomarkers along with the current guidance for use in monitoring disease progression can be found in Section 2.3.2.

The role of serum P1NP and CTX in fracture prediction has been investigated two meta-analyses (Johansson *et al.*, 2014; Tian *et al.*, 2019). These studies both found a significant but modest association between BTMs and future fracture risk before (Johansson *et al.*, 2014) and after (Tian *et al.*, 2019) adjusting for BMD and clinical risk factors such as age and body weight. Most clinical trials have used bone turnover markers to monitor osteoporosis treatment but the use has not been widely adopted in routine clinical practice (Lorentzon *et al.*, 2019). BTMs have also been used to monitor treatment effects, particularly antiresorptives such as bisphosphonates, which reduce bone resorption by inhibiting osteoclasts, and relating this to fracture risk (Cummings *et al.*, 2009). The efficacy of using

biomarkers in monitoring bisphosphonates was assessed in the TRIO study. These authors recommended a 3-month measurement of P1NP and β-CTX, a β-isomerized form of CTX unique to bone, as this is where the change in CTX and P1NP due to treatment should be apparent (Diez-Perez *et al.*, 2017).

In MM, Kowalska et al. looked at the relationship between CTX, P1NP, and Osteocalcin (OC) and disease progression (metastatic stage) and found that P1NP and OC were correlated with disease progression, but CTX was not (Kowalska et al., 2010). Ting et al. also used CTX and P1NP to relate levels to disease progression, treatment, remission and relapse. (Ting *et al.*, 2016). These authors concluded that CTX has a role in routine treatment monitoring and predicting relapse of myeloma bone disease, even in patients on bisphosphonates. Elevated sclerostin was also found to correlate with advanced disease features and abnormal bone remodelling in myeloma (Terpos *et al.*, 2012).

As mentioned in chapter 2 and chapter 6, the mechanobiological models developed for MM in this thesis are mathematical models based on patient imaging data, but not on clinical biochemical data. In the literature and this thesis thus far, patient specific biological data has not been employed to predict changes in bone density of MM patients. As there is a known relationship between biomarkers and bone remodelling, the goal of this final study was to evaluate the ability of multiscale biomechanical models, that incorporate bone biomarkers, to predict spatio-temporal bone adaptation in the vertebra of MM patients. This would enable the model to predict changes in prospective data without the need for a follow-up CT.

7.2 Patient Data

Seven MM patients were included in the study with baseline and follow-up (12 months) CT scans. The patient data is detailed in Table 7.1, where the vertebrae were split into either ‘no lesion’, ‘small lesion’ where the lesion is <50% of the vertebral body and ‘large lesion’ where the lesion is >50% of the vertebral body. Two CT scanners were used; Toshiba Aquillon ONE and Toshiba Aquillon PRIME SP both using a voltage of 120 kV and a pixel size of 1 mm. The Toshiba Aquillon ONE scanner had a slice thickness of 2 mm, and the Toshiba Aquillon PRIME SP had a slice thickness of 2 mm. Biomarker data for P1NP, CTX and Sclerostin was obtained for 5 patients (Table 7.1) at 1, 2 and 3 months after baseline (for more information on this dataset see Chapter 2).

Table 7.1. Patient data including Patient ID, age, sex, vertebral level segmented, whether the vertebra has a lesion (no lesion, small lesion: <50% of vertebral body and large lesion: >50% of vertebral body) and whether the patient has bone turnover marker (BTM) data.

Patient ID	Age	Sex	Level	Lesion?	BTM data
BRATS001	63	M	T4	large	1, 2 and 3 months
BRATS002	66	M	T2	no	N/A
BRATS003	64	M	T8	small	N/A
BRATS005	68	M	T12	no	1, 2 and 3 months
BRATS006	60	F	T12	large	1, 2 and 3 months
BRATS009	64	M	T12	small	1, 2 and 3 months
BRATS011	66	F	T11	small	1, 2 and 3 months

7.3 Methods

Three-dimensional finite element (FE) models of vertebrae were generated from baseline and follow-up computed tomography (CT) scans for the selected vertebra for each patient (Table 1). CT images were calibrated with a phantomless approach (see chapter 2). The 3D reconstruction of CT scans, meshing, alignment and assignment of material properties are detailed in Chapter 2. Static simulation up to 0.15% strain was applied uniaxially to the superior endplate, while the inferior endplate was fixed. To evaluate the failure load (FL), separate non-linear models were ran at Baseline, Follow-up and the mechanobiological Predicted model with an applied strain of 1.9% and FL was defined as the load at 1.9% strain (Crawford, Cann and Keaveny, 2003; Wang *et al.*, 2012; Keaveny *et al.*, 2014).

The mechanobiological model from Chapter 6 was applied to this dataset, optimising the six parameters (k1, k2, α_1, α_2, β_1, β_2) for each patient. Then, a multiple linear regression analysis using leave one out cross validation (LOOCV) (Bradshaw *et al.*, 2023) was performed in MATLAB (R2024a). The multiple linear regression assessed the relationships between the three BTMs and each of the optimised parameters (k1, k2, α_1, α_2, β_1, β_2), as well as between the three BTMs and both BMD and failure load at 1, 2, and 3 months after baseline, separately. LOOCV was chosen due to the very small sample size, and despite its tendency to over predict outcomes (Adin *et al.*, 2024), it is the best choice for this study as no other

methods are viable at this scale. LOOCV uses all but one patient to train the model and then tests on the final patient, increasing the training dataset for small cohort sizes (Bradshaw *et al.*, 2023). It repeats this for all patients, increasing the robustness of the relationship compared to a simple linear regression. Following this analysis, parameters with a strong positive correlation between follow-up and predicted ($r > 0.8$) were then estimated using the linear regression equations utilising the BTMs (Equation 7.1). All other parameters that had a negative, moderate or weak correlation ($-1 < r < 0.8$) were averaged across the cohort.

$$P = \varphi_0^P + \varphi_{CTX}^P \cdot CTX + \varphi_{P1NP}^P \cdot P1NP + \varphi_{Sclerostin}^P \cdot Sclerostin$$

Equation 7.1

Where, P is the parameter to be predicted (k1, k2, α_1, α_2, β_1, β_2) , φ_0^P is the intercept, φ_{CTX}^P is the proportionality coefficient for CTX, φ_{P1NP}^P is the proportionality coefficient for P1NP, $\varphi_{Sclerostin}^P$ is the proportionality coefficient for Sclerostin.

7.3.1 Statistics

To evaluate the significant differences between the predicted and follow-up for density and failure load (FL), Wilcoxon paired test was conducted with significance at $p < 0.05$. To assess the relationship between actual and predicted model parameters, a linear regression was performed. The Pearson's correlation coefficients with corresponding p-values of the predictions were calculated for all linear regressions. Where an $r \leq 0.5$ represents a weak correlation, $0.5 < r < 0.8$ is moderate correlation and $0.8 < r \leq 1$ is a strong correlation, significance was considered where $p < 0.05$.

7.4 Results

The original mechanobiological model was evaluated for this new dataset. Figure 7.2 shows the results for Baseline, Follow-up and Predicted for BMD and failure load. The prediction of density was good across the seven patients with no significant difference between Follow-up and Predicted (average percentage difference: 3.0 ±3.0% $p > 0.05$). Similarly, for the FL, the prediction was good with no significant difference between Follow-up and Predicted (average percentage difference: 11 ±10% $p > 0.05$).

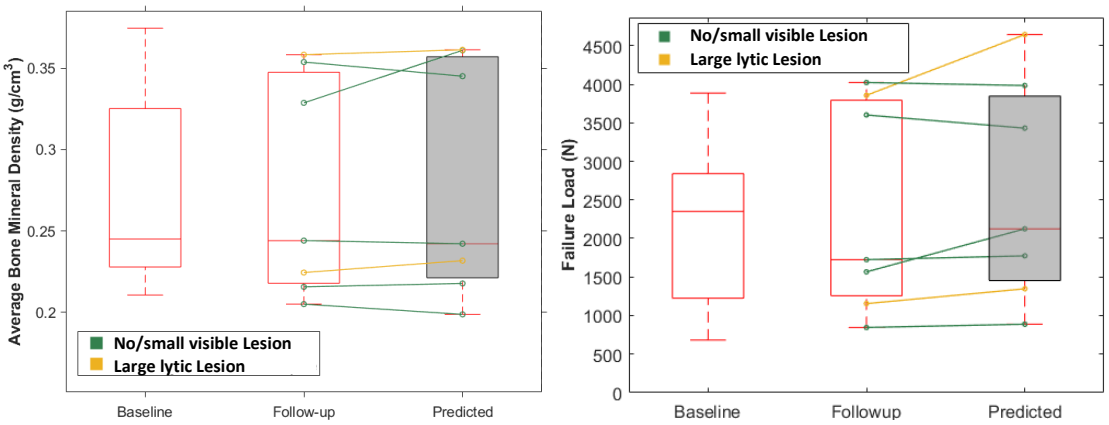

Figure 7.2 - Box plot of the (left) average bone mineral density and (right) failure load at Baseline, Follow-up and Predicted follow-up. The group was split into two to represent vertebrae with no/small visible lytic lesions (green) and large lytic lesions (yellow). A horizontal line represents data for a single patient connecting Follow-up to predicted Follow-up.

The linear regression using LOOCV revealed the weak predictive ability of BTMs for BMD and FL at all months apart from month 2 for FL where r = 0.99 ($p < 0.01$) (see Appendix 2 Figure 9.10). For the models optimised parameters, k_1 and k_2 were predicted well at month 1 using the linear regression equation from the LOOCV analysis (k_1: r = 0.85, %RMSE = 0.199%, p = 0.07, k_2: = 0.93, %RMSE = 0.214%, p = 0.02, Figure 7.1). For all other parameters, the relationship between the predicted vs actual was weak at all months ($r \leq 0.8$, $p > 0.05$ Appendix 2 Figure 9.11).

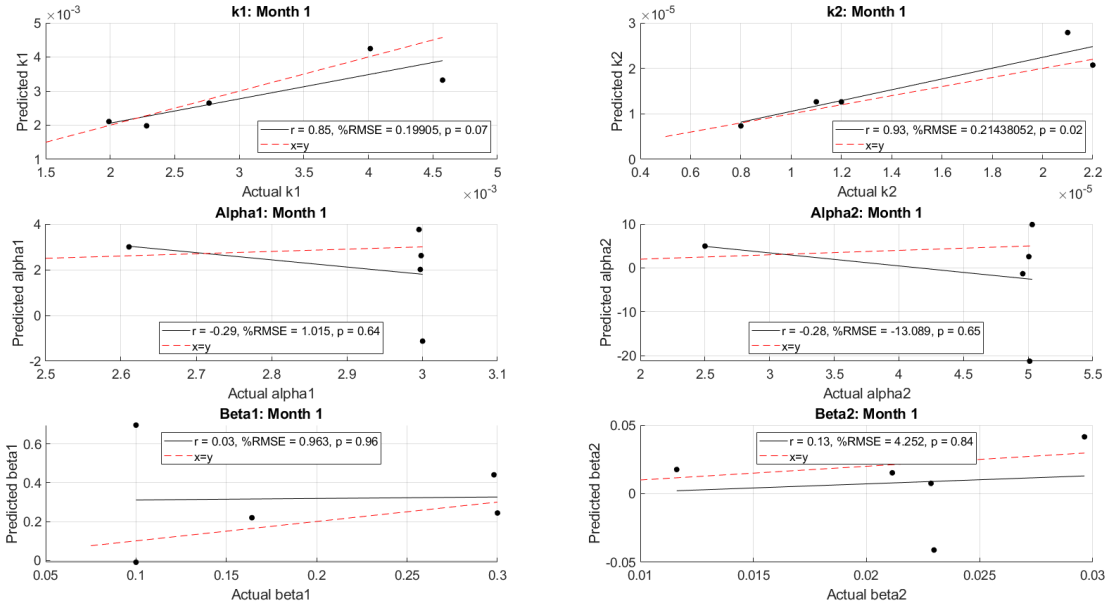

Figure 7.1 – Results of the linear regression, predicting parameters k1, k2, α_1, α_2, β_1, β_2 at 1 month after baseline using the equation derived from the LOOCV multiple linear regression analysis. 'Actual' is the parameter calculated from the optimisation of the original model and 'Predicted' is the predicted parameter using the BTM data

The model was then evaluated with averaged parameters for α_1, α_2, β_1 and $\beta_2$and with estimated k_1 and k_2 from the averaged linear regression equations calculated from the previous step, see Figure 7.3. The BTM incorporated mechanobiological model predicted the BMD and FL well for three patients' vertebra, BRATS001, BRATS005, BRATS009 (average percentage difference BMD: 3.95 ±3.27%, FL: 7.1 ±8.5%). However, for the other two patients' vertebra, BRATS006 and BRATS011, the BTM model predictions were further from the actual Follow-up values (average percentage difference BMD: 15.3 ±0%, FL: 41.2 ±5.3%). The vertebra in BRATS006 had a large lytic lesion and was over predicted by 15% in BMD and 45% in FL. The vertebra in BRATS011 had lots of small lesions present at follow-up which were not as clear at baseline and was underpredicted by 15% in BMD and 38% in FL (Figure 7.3). This prediction could also have been affected by the image quality, as seen from Figure 7.4 where the resolution is lower at baseline (B) than follow-up (C).

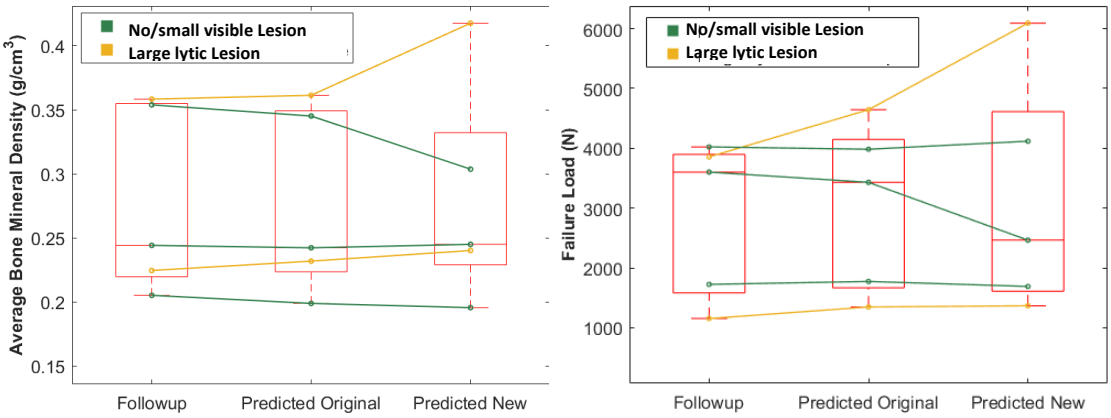

Figure 7.3 - Box plot of the (left) average bone mineral density and (right) failure load at follow-up, original models predicted follow-up and the new models predtiction incorporating the BTMs. The group was split into two to represent vertebrae with no/small visible lytic lesions (green) and large lytic lesions (yellow). A horizontal line represents data for a single patient connecting follow-up to predicted follow-up to new predicted follow-up.

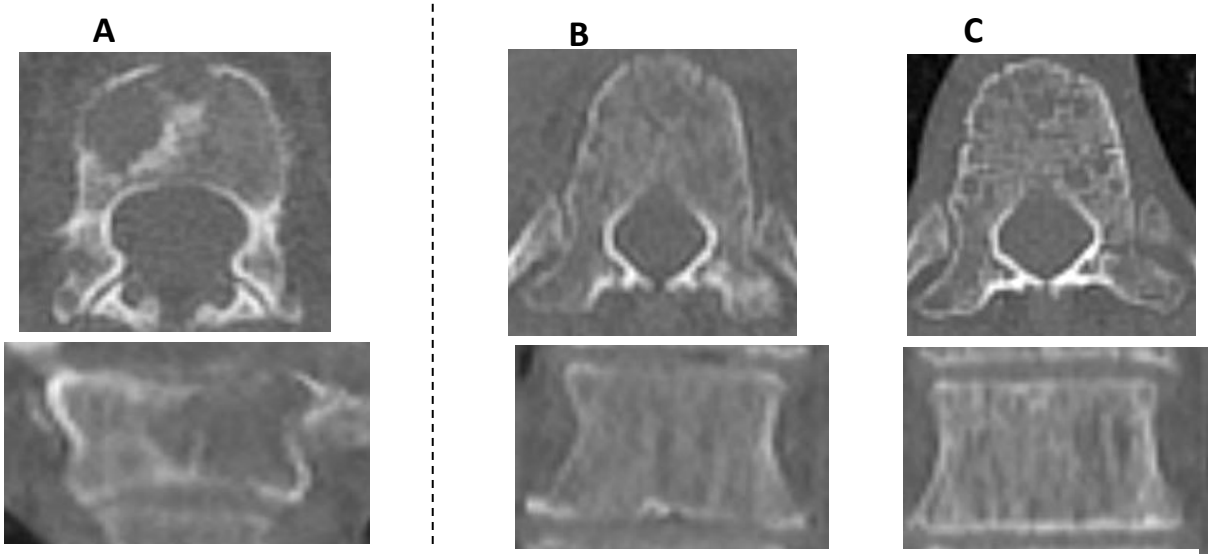

Figure 7.4. CT images of (A) BRATS006 baseline CT of selected vertebra highlighting the large lytic lesion (B) Baseline CT of BRATS011 showing no visible lesions (C) Follow-up CT of BRATS011 showing small lesions.

7.5 Discussion

The model developed in this chapter is the first to incorporate biomarkers for prediction of change in mechanical properties of vertebra with MM. Using biomarkers alone, the model successfully predicted three of the five patients' change in density and mechanical properties as later measured using CT. While the model faced limitations in patients with large lytic lesions and or active new lesion formation, it nonetheless demonstrated the possibility of predicting patient disease trajectory using blood biomarkers added to mechanobiological models.

A strong correlation was found between the biomarkers and parameters k1 and k2 after one month using the LOOCV method. LOOCV is a useful tool for small cohorts as it allows for maximisation of the limited data and improves confidence in the parameter relationships compared to a standard linear regression (Bradshaw *et al.*, 2023). Since k_1 and k_2 relate directly to the formation and resorption processes, their strong predictive value aligns with the expected mechanobiological impact of bone turnover in multiple myeloma. The range of values of k_1 and k_2 was also larger and more evenly distributed than the α_1 and α_2, making it easier to form a relationship between biomarkers and parameter. For β_1 and β_2, there was a large range of values, but no relationship was found. The lack of predictive power in the

parameters associated with cellular production and removal rates implies that these processes were less sensitive to biomarker fluctuations in this patient cohort. These production and removal rates may vary more gradually and therefore changes were unable to be captured in biomarkers measured within 3 months.

In contrast, k_1 and k_2 had the highest predictive power at one month which suggests they might be tied to an early mechanobiological response that carried the changes in bone up to 12 months. As with most MM patients, this cohort was treated with anti-resorptives, which significantly reduce osteoclast activity, and therefore CTX, within the first month before settling out (Orford *et al.*, 2024). Therefore, to predict changes after 12 months, it is possible that only the first month is needed, as if any changes were to occur these would happen within this early time period. However, this would need to be tested on a larger cohort to generalise the findings. Similar to other studies in MM where CTX was found to be a significant predictor of bone turnover over P1NP (Ting *et al.*, 2016), CTX had the largest coefficient in the two equations used to predict k_1 and k_2 (see Appendix) suggesting its effect is more significant in our model.

The two patients that the model underperformed for had more complex bone characteristics than the other three patients. One of the patients' vertebra had a large lesion. As discussed in Chapter 6, the model often predicts the BMD and FL higher than the Follow-up in vertebrae with large lesions due to the assumption that lytic tissue is treated the same as bone. When high strains are present, more formation occurs, increasing the density and Young's modulus, and thus decreasing the strain in that region and increasing the failure load. To test whether this is the issue within this cohort using the estimated and averaged parameters, rather than an anomaly, more patient imaging and biomarker data is needed. If this issue persists, the alteration developed in Chapter 6 (Appendix) could be applied to ameliorate this effect. The vertebrae for BRATS011 had new lesion formation. At present, the model changes the density of each element based on the SED, and the resulting interaction of bone cells. This is based on normal bone remodelling and has no additional myeloma-related input to predict the formation of lytic lesions. The model could be developed to include a parameter or equations to predict lesion formation. However, at present no data is available on the number of MM cells in these patients and the likelihood, size and location of the lesions.

The main limitation of the current study is the small cohort size. With a larger cohort size, the significance of the relationship between actual and predicted k1 and k2 may change. As the other four parameters are currently averaged, a larger cohort size would allow for further exploration of these relationships, confirming if these parameters can be predicted. A larger cohort size would also incorporate a more diverse dataset with more vertebrae with large lesions and new lesion formation to confirm if the model struggles with these more complex bone characteristics or whether those two patients are indeed anomalies. Another limitation is the number of datapoints available for the BTMs. Currently, 1, 2 and 3 months are evaluated, with only 1 month having a significant predictive ability. With more patients, the predictive ability for the other two months may change. It would be interesting to see how early k1 and k2 could be predicted as studies suggest that changes in CTX occur as early as 7 days (Orford *et al.*, 2024). Having more datapoints would also mean the model could be updated more often based on the new data to give more accurate predictions for ongoing monitoring. However, if 12-month changes can be predicted with BTMs at 1 month, it would reduce the number of hospital visits the patient needs as well as cost and hospital resources.

7.6 Conclusion

Bone health in multiple myeloma is a major concern. As highlighted in chapter 2, the management of mechanical instability is not well standardised and most often down to the clinician's opinion, alongside the SINS score of the vertebra, on what treatment plan is adopted. Most 'large lesion' vertebrae in this study would be classified as SINS >10 in the potentially unstable or unstable category, making it difficult to decide which treatment is best for improving spinal instability. Most clinicians would choose to perform surgery on the vertebra deemed as unstable or potentially unstable as well as the adjacent vertebra (Pennington *et al.*, 2019). The bracing treatment, mentioned in Chapter 2, is not as commonly adopted due to the lack of scientific basis for patients regaining strength and stability. Predicting the change in bone density and strength is difficult as the mechanism driving the remineralisation is unknown and appears not to be governed by normal mechano-adaptation rules alone, in addition to patient variations in remodelling cycles. The ability to predict these changes in bone would enable more confident decision making when treating spinal

instability. By incorporating biomarkers, which inform us of changes in bone remodelling, we have begun to understand these mechanisms and predict these changes.

The model developed sets the foundation for further study of this unique patient population by predicting bone changes effectively in most cases and offers valuable insights into how early mechanobiological responses affect mechanical properties after 12 months. This preliminary study suggests confirmation of Hypothesis 4 "Mechanobiological models incorporating bone turnover markers can predict bone changes in vertebrae of patients with multiple myeloma". However, more data is needed to objectively confirm this. This first attempt at creating a biomarker-informed mechanobiological model to predict patient-specific bone changes represents a promising step towards understanding multiple myeloma disease progression and informing better clinical decision making and patient outcomes.

8 DISCUSSION AND CONCLUSIONS

8.1 Introduction

This chapter summarises the main findings of this thesis, drawing together the insights obtained from the assessment of the changes in vertebral mechanical properties in cancer patients following treatment. Recommendations for further work and future perspectives in the field are also discussed.

8.2 Main Findings of the Thesis

The research in this thesis focussed on developing subject specific finite element (FE) models to assess the change in mechanical properties in cancer patients following treatment and coupling these biomechanical models with mechanobiological principles to predict these changes. The key contributions of each chapter are summarised below:

The first study of this thesis developed a finite element modelling pipeline to assess the mechanical properties of vertebrae with and without metastatic lesions. The pipeline was based on existing methods but modified and optimised for vertebral models from clinical CT scans with and without metastatic lesions. The segmentation reproducibility study concluded high reproducibility of the manual segmentation technique, with and without metastatic lesions, with the vertebrae without lesions having a slightly higher reproducibility. The importance of higher image quality and resolution for more reproducible segmentations was also concluded. Where a significant relationship between the combined effect of slice thickness and pixel size versus the DICE similarity score (DSC) and the Hausdorff distance was found. The comparison between phantomless and phantom calibration evaluated the use of different combinations of internal materials. The combination of aorta and air for calibrating the CT scan yielded the best result, producing the most similar volumetric bone mineral density to the phantom calibration method. Finally, the mesh refinement study concluded the use of a maximum of 1 mm element edge length was applicable to the FE pipeline used in this thesis.

The second study utilised the FE pipeline from Chapter 3 to analyse the effect of androgen deprivation therapy (ADT) on the bone mineral density (BMD) and mechanical properties of non-metastatic prostate cancer patients. This study concluded a significant decrease in

densitometric (areal BMD: -4%, volumetric BMD: -17%, integral volumetric BMD: -11%) and mechanical properties (stiffness: -14%, $p < 0.01$; failure load: -16%, $p < 0.01$; normalised stiffness: -14%, $p < 0.01$; failure strength: -16%, $p < 0.01$) of vertebrae following 12-months of ADT. These findings proved our hypothesis that "The vertebral strength of prostate cancer patients reduces when administered with ADT". Additionally, the regression analysis confirmed a stronger correlation of both trabecular vBMD ($r = 0.78$-0.92, $p < 0.001$) and integral vBMD ($r = 0.88$-0.96, $p < 0.001$) with the mechanical properties than the aBMD ($r = 0.28$-0.44, $p < 0.01$) suggesting that the determination of the vBMD might be of higher value when assessing patient bone strength at specific vertebral levels in clinical practice.

The third study also utilised the FE pipeline developed in Chapter 3 to estimate the mechanical properties of vertebrae with and without lytic lesions following treatment with orthopaedic bracing. This study concluded that the patients' vertebrae with large lytic lesions (size >50% of the vertebral body) had significant remineralisation and increase in mechanical properties evaluated at follow-up. For vertebrae without metastatic lesions or with small lesions (size <50% of the vertebral body) there was no significant increase in bone mineral density or mechanical properties evaluated at follow-up. This therefore confirmed the hypothesis "The remineralisation following bracing treatment for MM patients leads to an increase in vertebral strength". Moreover, a patient-by-patient analysis was conducted to evaluate the prediction of the change in mechanical properties using QCT derived volumetric BMD, and it was found that this prediction was only possible when any changes in mineral was contained within the vertebral body and not towards the cortical shell. This was due to the fact that vBMD is measured in the trabecular portion of the vertebral body and does not take account of the cortical bone. The changes in BMD, particularly those with large lesions, is not well understood, whether these changes are driven through normal remodelling or whether there was an additional biological mechanism influenced by the myeloma cells was still unknown.

The fourth study in this thesis attempted to predict the changes in densitometric and mechanical properties over time of MM vertebrae with and without metastatic lesions. The model was developed by coupling the organ level FE models of vertebrae with cell-level behaviours of bone cells influenced by the mechanical stimulus, which adjusted material properties based on biological pathways described by differential equations. The model's parameters were optimised based on the density at the follow-up CT. The model was able to

predict the changes in BMD and mechanical properties in the non-cancer control patients (average percentage difference BMD: 2.13 ±2.36%, average percentage difference FL: 3.64 ±3.72%). The model also predicted the BMD well for all the MM vertebrae (average percentage difference BMD: 3.49 ±4.63%). However, for the failure load, the model struggled when predicting, particularly those vertebrae with metastatic lesions (average percentage difference FL: 18.67 ±16.83% p = 0.01). The current model needed improvements to better predict the changes in vertebrae with larger lytic lesions. This was due to the algorithm being able to alter bone in the central region of the lytic lesion, which does not happen during the remineralisation seen in other case studies. The data in Appendix 1 demonstrates how the model was modified to allow only elements with at least one adjacent element with the density of bone to remodel. This change ensured that bone formation occurred only from the edges of the lesion inward. This adjustment improved the prediction of the failure load, but further work was still necessary to ensure the location of the changes in mineral were more accurate.

The fifth study utilised the mechanobiological model from Chapter 6 and incorporated bone turnover markers (BTMs) to allow for the prediction without the need for a follow-up CT. The model was able to predict the BMD and failure load well in three out of the five patients (average percentage difference BMD: 3.95 ±3.27%, FL: 7.1 ±8.5%). However, for the other two patients' vertebra (labelled BRATS006 and BRATS011) the model predictions were further from the actual Follow-up values (average percentage difference BMD: 15.3 ±0%, FL: 41.2 ±5.3%). The two vertebrae for BRATS006 and BRATS011 were identified in having more complex bone characteristics. BRATS006 had a large lytic lesion (>50% of the vertebral body). This limitation was addressed in Chapter 6 and for future assessments on new datasets, the updated version of the model, ensuring remodelling occurs from the edges of the lesion inward, to better predict vertebrae with large lesions would be employed. BRATS011 had new lesion formation as well as poorer quality scan at baseline. Both factors influenced the ability to predict the follow-up for this patient. Overall, the model developed sets a firm foundation in predicting bone changes effectively in most cases and offers valuable insights into how early mechanobiological responses affect mechanical properties after 12 months. This is the first attempt at creating a biomarker-informed mechanobiological model to predict patient-specific bone changes in multiple myeloma. This is a promising step forward towards

understanding the downstream effects of current clinical treatments, and to predicting future densitometric and mechanical properties, which will aid in clinical decision-making.

8.3 Future work

8.3.1 Further development of the FE pipeline

While this thesis has made significant strides in developing a robust finite element (FE) analysis pipeline, several areas require further investigation to enhance its applicability and accuracy. One key aspect is the variability inherent in clinical CT scan quality. Since clinical CTs are acquired using different scanning protocols and resolutions, the segmentation reproducibility of the images may be affected, as alluded to in Chapter 3. Initial evaluations have been conducted in this thesis, but a more extensive study involving a large cohort of scans with varying protocols is necessary. This would allow for a comprehensive analysis of how image quality impacts segmentation reproducibility, ultimately providing guidelines on the optimal resolution required for reliable segmentation of vertebrae.

Another extension of this work involves assessing the effect of segmentation reproducibility on FE-predicted mechanical properties. Since FE analyses depend on the accuracy of segmented geometries, inconsistencies or errors in segmentation could propagate through the pipeline and influence mechanical property predictions. Ongoing studies in our group aim to quantify this impact and ensure that the FE pipeline remains robust despite segmentation variability.

Furthermore, the calibration method used in CT-based FE analysis is a critical factor in predicting mechanical properties. This study is currently being extended to compare phantomless and phantom calibration techniques to determine how different calibration methods influence FE-predicted mechanical behaviour. By systematically evaluating these methods, this research aims to establish whether phantomless calibration could be used for CT calibration in FE studies, enabling the use of retrospective CT datasets that do not feature a phantom.

Lastly, expanding the loading conditions tested within the FE framework is crucial for understanding vertebral stability under different mechanical scenarios. While current analyses focus on uniaxial compression as the standard mode of physiological loading, future

work will incorporate additional loading conditions, such as torsion, bending, and eccentric compression. These studies will provide a more comprehensive understanding of how lytic vertebrae respond to various mechanical stimuli, possibly aiding the prediction of mechanical properties using the mechanobiological models developed in Chapter 6.

8.3.2 Improving the mechanobiological model to better predict changes in the vertebrae with large lesions

Building upon the findings in Chapter 6 and the conclusions of this thesis, further improvements to the mechanobiological model are necessary to enhance its predictive capability, particularly for vertebrae with large lesions. The supplementary analyses in this thesis indicated that vertebrae with substantial lesions tend to exhibit increased mineralization around the lesion margins compared to the rest of the vertebral body. This trend has been observed in multiple cases and warrants further investigation to refine the model's ability to capture these biomechanical adaptations.

A potential avenue for improving the model involves tuning the formation parameters when a lesion exceeds a critical threshold (>50% of the vertebral body). In such cases, elements within the lesion that have low density but are adjacent to high-density regions would have increased formation parameters. By incorporating these refinements, the model could more accurately simulate the biological response to large lesions, leading to improved clinical predictions.

8.3.3 Extension of the biomarker incorporated mechanobiological model

The integration of biomarker data into the mechanobiological model represents a promising step toward personalised predictions of vertebral changes. Our clinical collaborators are currently working on acquiring additional patient data, including higher-quality CT scans and comprehensive biomarker profiles. This expanded dataset will facilitate more robust validation of the model and enable a deeper investigation into its predictive power.

A key question to be addressed is whether the model can make reliable predictions based solely on baseline CT and biomarker data or if additional input parameters are necessary for accurate predictions. By analysing a larger cohort, this research will determine whether certain biomarkers serve as strong independent predictors or if their predictive power is

enhanced in conjunction with other clinical factors. Ultimately, this extension of the model could pave the way for improved patient-specific prognostics and treatment strategies.

8.4 Conclusion

In conclusion, this thesis presents the computational studies conducted throughout the author's PhD studies in the field of vertebral biomechanics and mechanobiology of oncology patients. A comprehensive literature review was presented, followed by the rationale and motivation for the studies carried out. The methods and results of each study, along with a discussion of the implications for the fields of research were detailed in each chapter.

The studies presented provide novel insight into how the treatment and disease progression of oncology patients affect the biomechanical properties of vertebrae. The first study developed a FE pipeline, enabling the assessment of vertebral strength in cancer patients through time-series CT scans. This provides a new approach for evaluating bone health in metastatic disease and offers potential for more personalised treatment planning. Additionally, by demonstrating the significant decrease in vertebral mechanical properties following androgen deprivation therapy (ADT) in prostate cancer patients, this research emphasised the importance of monitoring bone strength during cancer treatment, ultimately contributing to better-informed clinical practices and patient care strategies. The application of the FE pipeline to multiple myeloma patients revealed the varied effects of remineralisation on bone stability, highlighting the need for individualised treatment monitoring and further mechanistic investigation. The development of a mechanobiological model attempted to explore this remineralisation phenomenon by integrating FE analysis with bone adaptation mechanisms. To improve the clinical applicability of the model, bone turnover markers were incorporated into the mechanobiological model. This significantly enhanced its predictive capabilities, enabling patient-specific predictions from baseline CT scans and offering a transformative approach to clinical decision-making and treatment monitoring in MM. Thus, the findings of this thesis provide valuable insight into the mechanisms behind the mineral and mechanical changes in vertebra with lytic lesions, enabling further development of predictive tools to guide clinical treatments.

8.5 References

Abrahamsen, B. *et al.* (2007) 'Fracture risk in Danish men with prostate cancer: A nationwide register study', *BJU International*, 100(4), pp. 749–754. doi: 10.1111/j.1464-410X.2007.07163.x.

Adin, A. *et al.* (2024) 'Automatic cross-validation in structured models: Is it time to leave out leave-one-out?', *Spatial Statistics*, 62(November 2023), pp. 1–17. doi: 10.1016/j.spasta.2024.100843.

Agerbæk, M. O. *et al.* (1991) 'A reconstruction of the remodelling cycle in normal human cortical iliac bone', *Bone and Mineral*, 12(2), pp. 101–112. doi: 10.1016/0169-6009(91)90039-3.

Agerbzk, M. O. *et al.* (1991) *A reconstruction of the remodelling cycle in nor human cortical iliac bone*, *Bone and Mineral*.

Agur, A. ., Dalley, A. . and Grant, J. C. . (2013) *Grant's atlas of anatomy*. Lippincott Williams & Wilkins.

Aldieri, A. *et al.* (2024) 'Development and validation of a semi-automated and unsupervised method for femur segmentation from CT', *Scientific Reports*, 14(1). doi: 10.1038/s41598-024-57618-6.

Aligizakis, A. *et al.* (2002) 'Functional outcome of burst fractures of the thoracolumbar spine managed non-operatively, with early ambulation, evaluated using the load sharing classification', *Acta Orthopaedica Belgica*, 68(3), pp. 279–287.

Almeida, M. *et al.* (2017) 'Estrogens and androgens in skeletal physiology and pathophysiology', *Physiological Reviews*, 97(1), pp. 135–187. doi: 10.1152/physrev.00033.2015.

Alqahtani, F. F. and Offiah, A. C. (2019) 'Diagnosis of osteoporotic vertebral fractures in children', *Pediatric Radiology*, 49(3), pp. 283–296. doi: 10.1007/s00247-018-4279-5.

Anastasilakis, A. D. *et al.* (2013) 'Comparative effect of zoledronic acid versus denosumab on serum sclerostin and dickkopf-1 levels of naive postmenopausal women with low bone mass: A randomized, head-to-head clinical trial', *Journal of Clinical Endocrinology and Metabolism*,

98(8), pp. 3206–3212. doi: 10.1210/jc.2013-1402.

Anderson, G. and O'Sullivan, J. (2022) 'Increased fracture risk in prostate cancer: causes and consequences', *Trends in Urology & Men's Health*, 13(3), pp. 6–10. doi: 10.1002/tre.853.

Anitha, D. *et al.* (2017) 'Risk of vertebral compression fractures in multiple myeloma patients: A finite-element study', *Medicine (United States)*, 96(2). doi: 10.1097/MD.0000000000005825.

Anselmetti, G. C., Manca, A. and Montemurro, F. (2012) 'Percutaneous Vertebroplasty in Multiple Myeloma: Prospective Long-Term Follow-Up in 106 Consecutive Patients.', *Cardiovasc Intervent Radiol*, pp. 139–45.

Ashman, R. B. and Jae Young Rho (1988) 'Elastic modulus of trabecular bone material', *Journal of biomechanics*, 21(3), pp. 177–181. doi: 10.1016/0021-9290(88)90167-4.

El Badri, S. A. M., Salawu, A. and Brown, J. E. (2019) 'Bone Health in Men with Prostate Cancer: Review Article', *Current Osteoporosis Reports*, 17(6), pp. 527–537. doi: 10.1007/s11914-019-00536-8.

Bahia, M. T. *et al.* (2020) 'A bone remodeling model governed by cellular micromechanics and physiologically based pharmacokinetics', *Journal of the Mechanical Behavior of Biomedical Materials*, 104(October 2019), p. 103657. doi: 10.1016/j.jmbbm.2020.103657.

Balducci, M. *et al.* (2011) 'Impact of Radiotherapy on Pain Relief and Recalcification in Plasma Cell Neoplasms Long-Term Experience Balducci M, et al. Pain Relief and Recalcification by RT in Plasma Cell Neoplasms', *Strahlenther Onkol*, 187(2), pp. 114–123. doi: 10.1007/s00066-010-2155-9.

Baron, R. and Kneissel, M. (2013) 'WNT signaling in bone homeostasis and disease: from human mutations to treatments', *Nature Medicine*, 19(2), pp. 179–192. doi: 10.1038/nm.3074.

Bartenschlager, S. *et al.* (2021) 'BMD accuracy errors specific to phantomless calibration of CT scans of the lumbar spine'. doi: 10.1016/j.bone.2021.116304.

Bartl, R. and Bartl, C. (2019) 'Structure and Architecture of Bone.', in *The Osteoporosis Manual.* Springer, Cham. doi: https://doi.org/10.1007/978-3-030-00731-7_2.

Beaupré, G. S., Orr, T. E. and Carter, D. R. (1990) 'An approach for time-dependent bone modeling and remodeling—theoretical development', *Journal of Orthopaedic Research*, 8(5), pp. 651–661. doi: 10.1002/jor.1100080506.

Van Beek, E. *et al.* (1999) 'Farnesyl pyrophosphate synthase is the molecular target of nitrogen-containing bisphosphonates', *Biochemical and Biophysical Research Communications*, 264(1), pp. 108–111. doi: 10.1006/bbrc.1999.1499.

Behrens, B. A. *et al.* (2009) 'Numerical investigations on the strain-adaptive bone remodelling in the periprosthetic femur: Influence of the boundary conditions', *BioMedical Engineering Online*, 8, pp. 1–9. doi: 10.1186/1475-925X-8-7.

Belo, D., Reis, J. H. and Teixeira, J. C. (2021) 'Cervical spine multiple myeloma and isolated radiotherapy', *Journal of Surgical Case Reports*, 1, pp. 1–4. doi: 10.1093/jscr/rjaa563.

Betts, J. G. *et al.* (2022) 'Bone Tissue and the Skeletal System', in *Anatomy and Physiology 2e*. Houston, Texas: OpenStax. Available at: https://openstax.org/books/anatomy-and-physiology-2e/pages/1-introduction.

Bevill, G. and Keaveny, T. M. (2009) 'Trabecular bone strength predictions using finite element analysis of micro-scale images at limited spatial resolution', *Bone*, 44(4), pp. 579–584. doi: 10.1016/J.BONE.2008.11.020.

Bird, J. M. *et al.* (2011) 'Guidelines for the diagnosis and management of multiple myeloma 2011', *British Journal of Haematology*, 154(1), pp. 32–75. doi: 10.1111/j.1365-2141.2011.08573.x.

Bird, S. A. and Boyd, K. (2019) 'Multiple myeloma: an overview of management', *Palliative Care and Social Practice*. SAGE Publications Sage UK: London, England. doi: 10.1177/1178224219868235.

Blake, G. M. *et al.* (2009) 'Effect of increasing vertebral marrow fat content on BMD measurement , T -Score status and fracture risk prediction by DXA', 44, pp. 495–501. doi: 10.1016/j.bone.2008.11.003.

Bogduk, N. and Mercer, S. (2000) 'Biomechanics of the cervical spine. I: Normal kinematics', *Clinical Biomechanics*, 15(9ƒ), pp. 633–648. Available at: www.elsevier.com/locate/clinbiomech.

Boivin, G. *et al.* (2009) 'Influence of remodeling on the mineralization of bone tissue', in *Osteoporosis International*. Springer London, pp. 1023–1026. doi: 10.1007/s00198-009-0861-x.

Bonewald, L. F. (2011) 'The Amazing Osteocyte', *J Bone Miner Res*, 26, pp. 229–38. doi: 10.1002/jbmr.320.

Bonfield, W. and Datta, P. K. (1974) 'Young's modulus of compact bone', *Journal of biomechanics*, 7(2), pp. 147–149. doi: 10.1016/0021-9290(74)90053-0.

Bonfoh, N., Novinyo, E. and Lipinski, P. (2011) 'Modeling of bone adaptative behavior based on cells activities', *Biomechanics and Modeling in Mechanobiology*, 10(5), pp. 789–798. doi: 10.1007/s10237-010-0274-y.

Boszczyk, B. M., Boszczyk, A. A. and Putz, R. (2001) 'Comparative and functional anatomy of the mammalian lumbar spine', *Anatomical Record*, 264(2), pp. 157–168. doi: 10.1002/ar.1156.

Bradshaw, T. J. *et al.* (2023) 'A Guide to Cross-Validation for Artificial Intelligence in Medical Imaging', *Radiology: Artificial Intelligence*, 5(4). doi: 10.1148/ryai.220232.

Brinckmann, P., Biggemann, M. and Hilweg, D. (1989) 'Prediction of the compressive strength of human lumbar vertebrae', *Clinical Biomechanics*, 4(SUPPL. 2), pp. iii–27. doi: 10.1016/0268-0033(89)90071-5.

Brown, J. E. *et al.* (2020) 'Guidance for the assessment and management of prostate cancer treatment-induced bone loss. A consensus position statement from an expert group', *Journal of Bone Oncology*, 25, p. 100311. doi: 10.1016/j.jbo.2020.100311.

Buckley, J. M., Loo, K. and Motherway, J. (2007) 'Comparison of quantitative computed tomography-based measures in predicting vertebral compressive strength', *Bone*, 40(3), pp. 767–774. doi: 10.1016/j.bone.2006.10.025.

Budoff, M. J. *et al.* (2013) 'Measurement of phantomless thoracic bone mineral density on coronary artery calcium CT scans acquired with various CT scanner models', *Radiology*, 267(3), pp. 830–836. doi: 10.1148/radiol.13111987.

Burklein, D. B. *et al.* (2001) 'Correlation of thoracic and lumbar vertebral failure loads with in

situ vs. ex situ dual energy X-ray absorptiometry', *Journal of Biomechanics*, 35, pp. 579–587.

Burtis, C. A. (2015) *Tietz Fundamentals of Clinical Chemistry and Molecular Diagnostics*. 4th edn. Elsevier India.

Bussard, K. M., Gay, C. V. and Mastro, A. M. (2008) 'The bone microenvironment in metastasis; what is special about bone?', *Cancer and Metastasis Reviews*, 27(1), pp. 41–55. doi: 10.1007/s10555-007-9109-4.

Campbell, G. M. *et al.* (2017) 'Assessment of Bone Fragility in Patients With Multiple Myeloma Using QCT-Based Finite Element Modeling', *Journal of Bone and Mineral Research*, 32(1), pp. 151–156. doi: 10.1002/jbmr.2924.

Cancer Research UK (2014) *Myeloma survival statistics | Cancer Research UK*. Available at: https://www.cancerresearchuk.org/health-professional/cancer-statistics/statistics-by-cancer-type/myeloma/survival#ref-2 (Accessed: 11 July 2022).

Cancer Research UK (2019) *No Title*. Available at: https://www.cancerresearchuk.org/health-professional/cancer-statistics/statistics-by-cancer-type/prostate-cancer#heading-Two.

Capulli, M., Paone, R. and Rucci, N. (2014) 'Osteoblast and osteocyte: Games without frontiers', *Archives of Biochemistry and Biophysics*. Arch Biochem Biophys, pp. 3–12. doi: 10.1016/j.abb.2014.05.003.

Carpenter, R. D. *et al.* (2014) 'Inter-scanner differences in in vivo QCT measurements of the density and strength of the proximal femur remain after correction with anthropomorphic standardization phantoms', *Medical Engineering and Physics*, 36(10), pp. 1225–1232. doi: 10.1016/j.medengphy.2014.06.010.

Carter, D. R., Hayes, W. C. and Schurman, D. J. (1976) 'Fatigue life of compact bone—II. Effects of microstructure and density', *Journal of Biomechanics*, 9(4), pp. 211–218. doi: 10.1016/0021-9290(76)90006-3.

Carter, D. R., Orr, T. E. and Fyhrie, D. P. (1989) 'Relationships between loading history and femoral cancellous bone architecture', *Journal of Biomechanics*, 22(3), pp. 231–244. doi: 10.1016/0021-9290(89)90091-2.

Cawley, D. T. *et al.* (2019) 'Managing the cervical spine in multiple myeloma patients',

Hematological Oncology, 37(2), pp. 129–135. doi: 10.1002/hon.2564.

Cecchini, M. G. *et al.* (2005) 'Molecular and biological mechanisms of bone metastasis', *EAU Update Series*, 3(4), pp. 214–226. doi: 10.1016/J.EUUS.2005.09.006.

Cheng, P. *et al.* (2021) 'Automatic vertebrae localization and segmentation in CT with a two-stage Dense-U-Net', *Scientific Reports*, 11(1), pp. 1–13. doi: 10.1038/s41598-021-01296-1.

Christen, P. *et al.* (2014) 'Bone remodelling in humans is loaddriven but not lazy.', *Nat Commun*, 5, p. 4855.

Cierniak, R. (2011) 'Technical Concepts of X-ray Computed Tomography Scanners', in *X-Ray Computed Tomography in Biomedical Engineering.* London: Springer, pp. 21–62. doi: https://doi.org/10.1007/978-0-85729-027-4_3.

Clarke, B. (2008) 'Normal Bone Anatomy and Physiology The Skeleton', *Clin J Am Soc Nephrol*, 3, pp. 131–139. doi: 10.2215/CJN.04151206.

Clines, G. A. and Guise, T. A. (2005) 'Hypercalcaemia of malignancy and basic research on mechanisms responsible for osteolytic and osteoblastic metastasis to bone', *Endocrine-Related Cancer*, 12(3), pp. 549–583. doi: 10.1677/erc.1.00543.

Cole, J. H. and Van Der Meulen, M. C. H. (2011) 'Whole Bone Mechanics and Bone Quality', *Clinical Orthopaedics and Related Research*, 469(8), p. 2139. doi: 10.1007/S11999-011-1784-3.

Colucci, S. *et al.* (2009) 'Soluble decoy receptor 3 modulates the survival and formation of osteoclasts from multiple myeloma bone disease patients', *Leukemia*, 23(11), pp. 2139–2146. doi: 10.1038/leu.2009.136.

Confavreux, C. B. *et al.* (2021) 'Fracture risk evaluation of bone metastases: A burning issue', *Cancers*. Multidisciplinary Digital Publishing Institute (MDPI), p. 5711. doi: 10.3390/cancers13225711.

Cook, D. J. *et al.* (2012) 'Variability of manual lumbar spine segmentation', *International Journal of Spine Surgery*, 6(1), pp. 167–173. doi: 10.1016/j.ijsp.2012.04.002.

Cook, R. D. *et al.* (2001) 'Concepts and Applications of Finite Element Analysis'. doi: 10.1016/b978-0-08-052402-3.50011-3.

Costa, M. C. *et al.* (2019) 'Biomechanical assessment of vertebrae with lytic metastases with subject-specific finite element models', *Journal of the Mechanical Behavior of Biomedical Materials*, 98(June), pp. 268–290. doi: 10.1016/j.jmbbm.2019.06.027.

Cowin, S. . (2001) *Bone mechanics handbook, second edition*, *Bone Mechanics Handbook, Second Edition*. Edited by S. C. Cowin. doi: 10.1016/s0021-9290(01)00251-2.

Cowin, S. C. and Van Buskirk, W. C. (1979) 'Surface bone remodeling induced by a medullary pin', *Journal of Biomechanics*, 12(4), pp. 269–276. doi: 10.1016/0021-9290(79)90069-1.

Cowin, S. C., Moss-Salentijn, L. and Moss, M. L. (1991) 'Candidates for the Mechanosensory System', *Journal of Biomechanical Engineering*, 113, pp. 191–197. Available at: http://asmedigitalcollection.asme.org/biomechanical/article-pdf/113/2/191/5502120/191_1.pdf (Accessed: 23 June 2022).

Crane, J. L., Xian, L. and Cao, X. (2016) 'Role of TGF-β Signaling in Coupling Bone Remodeling', in *Methods in Molecular Biology*. Humana Press Inc., pp. 287–300. doi: 10.1007/978-1-4939-2966-5_18.

Crawford, R. P., Cann, C. E. and Keaveny, T. M. (2003) 'Finite element models predict in vitro vertebral body compressive strength better than quantitative computed tomography', *Bone*, 33(4), pp. 744–750. doi: 10.1016/S8756-3282(03)00210-2.

Cummings, S. R. *et al.* (2009) 'Denosumab for prevention of fractures in postmenopausal women with osteoporosis', *Obstetrical and Gynecological Survey*, 64(12), pp. 805–807. doi: 10.1097/01.ogx.0000363236.41902.96.

Cummings, S. R., Bates, D. and Black, D. M. (2002) 'Clinical use of bone densitometry: Scientific review', *Journal of the American Medical Association*, 288(15), pp. 1889–1897. doi: 10.1001/jama.288.15.1889.

Currey, J. D. (1979) 'Mechanical properties of bone tissues with greatly differing functions', *Journal of biomechanics*, 12(4), pp. 313–319. doi: 10.1016/0021-9290(79)90073-3.

Currey, J. D. (2001) 'Bone strength: what are we trying to measure?', *Calcified tissue international*, 68(4), pp. 205–210. doi: 10.1007/S002230020040.

Dahl, A. C. E. and Thompson, M. S. (2011) 'Mechanobiology of Bone', *Comprehensive*

Biotechnology, Second Edition, 5, pp. 217–236. doi: 10.1016/B978-0-08-088504-9.00419-0.

Dai, J. *et al.* (2005) 'Bone Morphogenetic Protein-6 Promotes Osteoblastic Prostate Cancer Bone Metastases through a Dual Mechanism', *Cancer Research*, 65(18), pp. 8274–8285. doi: 10.1158/0008-5472.CAN-05-1891.

Dall'Ara, E. *et al.* (2012) 'QCT-based finite element models predict human vertebral strength in vitro significantly better than simulated DEXA', *Osteoporosis International*, 23(2), pp. 563–572. doi: 10.1007/s00198-011-1568-3.

Dalla Via, J. *et al.* (2019) 'Bone mineral density, structure, distribution and strength in men with prostate cancer treated with androgen deprivation therapy', *Bone*, 127(June), pp. 367–375. doi: 10.1016/j.bone.2019.06.005.

Dao, T. T. (2017) 'Advanced computational workflow for the multi-scale modeling of the bone metabolic processes', *Medical and Biological Engineering and Computing*, 55(6), pp. 923–933. doi: 10.1007/s11517-016-1572-z.

Delank, K. S. *et al.* (2011) 'The Treatment of Spinal Metastases', *Deutsches Ärzteblatt International*, 108(5), p. 71. doi: 10.3238/ARZTEBL.2011.0071.

Demirbağ Kabayel, D. (2016) 'The role of quantitative computed tomography and magnetic resonance imaging in diagnosis and follow-up of osteoporosis: A review', *Turkiye Fiziksel Tip ve Rehabilitasyon Dergisi*, 62(3), pp. 288–295. doi: 10.5606/tftrd.2016.33407.

DeVries, N. A. *et al.* (2008) 'Validation of phalanx bone three-dimensional surface segmentation from computed tomography images using laser scanning', *Skeletal Radiology*, 37(1), pp. 35–42. doi: 10.1007/s00256-007-0386-3.

Diez-Perez, A. *et al.* (2017) 'International Osteoporosis Foundation and European Calcified Tissue Society Working Group. Recommendations for the screening of adherence to oral bisphosphonates', *Osteoporosis International*, 28(3), pp. 767–774. doi: 10.1007/s00198-017-3906-6.

Downey, P. A. and Siegel, M. I. (2006) 'Bone biology and the clinical implications for osteoporosis', *Physical Therapy*. American Physical Therapy Association, pp. 77–91. doi: 10.1093/ptj/86.1.77.

Dunlop, J. W. C. *et al.* (2009) 'New suggestions for the mechanical control of bone remodeling', *Calcified Tissue International*, 85(1), pp. 45–54. doi: 10.1007/s00223-009-9242-x.

Dunlop, R. B., Adams, M. A. and Hutton, W. C. (1984) 'Disc space narrowing and the lumbar facet joints', *https://doi.org/10.1302/0301-620X.66B5.6501365*, 66(5), pp. 706–710. doi: 10.1302/0301-620X.66B5.6501365.

Duvauferrier, R. *et al.* (2013) 'Current role of CT and whole body MRI in multiple myeloma', *Diagnostic and Interventional Imaging*, pp. 169–183. doi: 10.1016/j.diii.2012.12.001.

Edmondston, S. J. and Singer, K. P. (1997) 'Thoracic spine: Anatomical and biomechanical considerations for manual therapy', *Manual Therapy*, 2(3), pp. 132–143. doi: 10.1054/math.1997.0293.

Engelke, K. *et al.* (2008) 'Clinical Use of Quantitative Computed Tomography and Peripheral Quantitative Computed Tomography in the Management of Osteoporosis in Adults: The 2007 ISCD Official Positions', *Journal of Clinical Densitometry*, 11(1), pp. 123–162. doi: 10.1016/J.JOCD.2007.12.010.

Engelke, K., van Rietbergen, B. and Zysset, P. (2016) 'FEA to Measure Bone Strength: A Review', *Clinical Reviews in Bone and Mineral Metabolism*, 14(1), pp. 26–37. doi: 10.1007/s12018-015-9201-1.

Eriksen, E. F. (2010) 'Cellular mechanisms of bone remodeling', *Reviews in Endocrine and Metabolic Disorders*, pp. 219–227. doi: 10.1007/s11154-010-9153-1.

Eswaran, S. K. *et al.* (2006) 'Cortical and Trabecular Load Sharing in the Human Vertebral Body', *J Bone Miner Res*, 21(2), pp. 307–314.

Faghani, S. *et al.* (2023) 'A deep learning algorithm for detecting lytic bone lesions of multiple myeloma on CT', *Skeletal Radiology*, 52(1), pp. 91–98. doi: 10.1007/s00256-022-04160-z.

Fahed, Z. *et al.* (2015) 'Management of neoplastic spinal tumors in a spine surgery care unit', *Clinical Neurology and Neurosurgery*, 128, pp. 35–40. doi: 10.1016/j.clineuro.2014.10.021.

Fedorov, A. *et al.* (2012) '3D Slicer as an Image Computing Platform for the Quantitative Imaging Network', *Magnetic resonance imaging*, 30(9), p. 1323. doi:

10.1016/J.MRI.2012.05.001.

Feller, L., Kramer, B. and Lemmer, J. (2011) 'A short account of metastatic bone disease', *Cancer Cell International*, 11(1), pp. 1–6. doi: 10.1186/1475-2867-11-24/METRICS.

Feng, X. and McDonald, J. M. (2011) 'Disorders of Bone Remodeling', *https://doi.org/10.1146/annurev-pathol-011110-130203*, 6, pp. 121–145. doi: 10.1146/ANNUREV-PATHOL-011110-130203.

Fields, A. J. *et al.* (2009) 'Role of trabecular microarchitecture in whole-vertebral body biomechanical behavior', *Journal of Bone and Mineral Research*, 24(9), pp. 1523–1530. doi: 10.1359/jbmr.090317.

Fields, A. J. *et al.* (2011) 'Influence of vertical trabeculae on the compressive strength of the human vertebra', *Journal of Bone and Mineral Research*, 26(2), pp. 263–269. doi: 10.1002/jbmr.207.

Flouzat-Lachaniette, C. H. *et al.* (2013) 'Treatment of spinal epidural compression due to hematological malignancies: A single institution's retrospective experience', *European Spine Journal*, 22(3), pp. 548–555. doi: 10.1007/S00586-012-2562-Y.

Frost, H. M. (1987) 'Bone "mass" and the "mechanostat": A proposal', *The Anatomical Record*, 219(1), pp. 1–9. doi: 10.1002/AR.1092190104.

Galán-Olleros, M. *et al.* (2021) 'Orthopedic Surgical Treatment and Perioperative Complications in Multiple Myeloma Bone Disease: Analysis of a Series (2009–2018)', *Annals of Surgical Oncology*, 28(2), pp. 1158–1166. doi: 10.1245/s10434-020-08819-6.

Galbusera, F. *et al.* (2018) 'The Role of the Size and Location of the Tumors and of the Vertebral Anatomy in Determining the Structural Stability of the Metastatically Involved Spine: a Finite Element Study', *Translational Oncology*, 11(3), pp. 639–646. doi: 10.1016/j.tranon.2018.03.002.

Gao, C. *et al.* (2015) 'Nanotechnology for treating osteoporotic vertebral fractures', *International Journal of Nanomedicine*, 10, pp. 5139–5157. doi: 10.2147/IJN.S85037.

Garavelli, C. *et al.* (2022) 'Experimental validation of a subject-specific finite element model of lumbar spine segment using digital image correlation', *PLoS ONE*, 17(9 9), pp. 1–17. doi:

10.1371/journal.pone.0272529.

Gatta, G. *et al.* (2017) 'Burden and centralised treatment in Europe of rare tumours: results of RARECAREnet—a population-based study', *The Lancet Oncology*, 18(8), pp. 1022–1039. doi: 10.1016/S1470-2045(17)30445-X.

Genant, H. K. and Boyd, D. (1977) 'Quantitative bone mineral analysis using dual energy computed tomography', *Investigative Radiology*, pp. 545–551. doi: 10.1097/00004424-197711000-00015.

Giuliani, N., Rizzoli, V. and Roodman, G. D. (2006) 'Multiple myeloma bone disease: Pathophysiology of osteoblast inhibition', *Blood*. American Society of Hematology, pp. 3992–3996. doi: 10.1182/blood-2006-05-026112.

Gleeson, T. G. *et al.* (2009) 'Accuracy of whole-body low-dose multidetector CT (WBLDCT) versus skeletal survey in the detection of myelomatous lesions, and correlation of disease distribution with whole-body MRI (WBMRI)', *Skeletal Radiology*, 38(3), pp. 225–236. doi: 10.1007/S00256-008-0607-4/FIGURES/9.

Goel, V. K. *et al.* (1995) 'Cancellous bone young's modulus variation within the vertebral body of a ligamentous lumbar spine—application of bone adaptive remodeling concepts', *Journal of Biomechanical Engineering*, 117(3), pp. 266–272. doi: 10.1115/1.2794180.

Gokaraju, K. *et al.* (2016) 'Multiple myeloma presenting with acute bony spinal cord compression and mechanical instability successfully managed nonoperatively', *Spine Journal*, 16(8), pp. e567–e570. doi: 10.1016/j.spinee.2016.03.011.

Gokaraju, K. *et al.* (2019) 'Spinal fusion from nonoperative management of lytic myelomatous vertebrae', *Spine Journal*, 19(2), pp. e4–e5. doi: 10.1016/j.spinee.2015.04.034.

Goldman, L. W. (2007) 'Principles of CT and CT technology', *Journal of Nuclear Medicine Technology*, pp. 115–128. doi: 10.2967/jnmt.107.042978.

Grashuis, J. L., Bolotin, H. H. and Sieva, H. (2003) 'Patient-Specific DXA Bone Mineral Density Inaccuracies: Quantitative Effects of Nonuniform Extraosseous Fat Distributions ¨', 18(6), pp. 1020–1027.

Greenspan, S. L. *et al.* (2005) 'Bone loss after initiation of androgen deprivation therapy in

patients with prostate cancer', *Journal of Clinical Endocrinology and Metabolism*, 90(12), pp. 6410–6417. doi: 10.1210/jc.2005-0183.

Griffith, J. F. and Genant, H. K. (2008) 'Bone mass and architecture determination: state of the art', *Best Practice & Research Clinical Endocrinology & Metabolism*, 22(5), pp. 737–764. doi: 10.1016/J.BEEM.2008.07.003.

Groenen, K. H. J. *et al.* (2018) 'Case-specific non-linear finite element models to predict failure behavior in two functional spinal units', *Journal of Orthopaedic Research*, 36(12), pp. 3208–3218. doi: 10.1002/jor.24117.

Gupta, D. *et al.* (2001) *Adherence of multiple myeloma cells to bone marrow stromal cells upregulates vascular endothelial growth factor secretion: therapeutic applications*, *Leukemia*. Available at: www.nature.com/leu.

Hall, S. and Stephens, J. (2018) *Anatomy and Physiology*. Fifth. Elsevier.

Hambli, R. (2014) 'Connecting mechanics and bone cell activities in the bone remodeling process: An integrated finite element modeling', *Frontiers in Bioengineering and Biotechnology*, 2(APR), pp. 1–12. doi: 10.3389/fbioe.2014.00006.

Hambli, R. *et al.* (2016) 'Prediction of denosumab effects on bone remodeling: A combined pharmacokinetics and finite element modeling', *Journal of the Mechanical Behavior of Biomedical Materials*, 60, pp. 492–504. doi: 10.1016/j.jmbbm.2016.03.010.

Hameed, A. *et al.* (2014) 'Bone Disease in Multiple Myeloma: Pathophysiology and Management', *Cancer Growth and Metastasis*, 7, p. 33. doi: 10.4137/CGM.S16817.

Handforth, C. *et al.* (2024) 'The impact of androgen deprivation therapy on bone microarchitecture in men with prostate cancer: A longitudinal observational study (The ANTELOPE Study)', *Journal of Bone Oncology*, 47, p. 100611. doi: 10.1016/j.jbo.2024.100611.

Hart, N. H. *et al.* (2017) 'Mechanical basis of bone strength: Influence of bone material, bone structure and muscle action', *Journal of Musculoskeletal Neuronal Interactions*, pp. 114–139. Available at: http://www.ismni.org.

Heindel, W. *et al.* (2014) 'The diagnostic imaging of bone metastases', *Deutsches Ärzteblatt international*, 111(44), pp. 741–747. doi: 10.3238/arztebl.2014.0741.

Heller, M. (2022) 'Finite Element Analysis in Orthopedic Biomechanics', in Galbusera, F. and Innocenti, B. (eds) *Human Orthopaedic Biomechanics*. Elsevier, pp. 637–658. doi: 10.1016/B978-0-12-824481-4.00031-7.

Higano, C. S. (2008) 'Androgen-deprivation-therapy-induced fractures in men with nonmetastatic prostate cancer: What do we really know?', *Nature Clinical Practice Urology*, 5(1), pp. 24–34. doi: 10.1038/NCPURO0995.

Hinge, M. *et al.* (2016) 'Bone healing in multiple myeloma: A prospective evaluation of the impact of first-line anti-myeloma treatment', *Haematologica*, 101(10), pp. e419–e422. doi: 10.3324/haematol.2016.144477.

Hlaing, T. T. and Compston, J. E. (2014) 'Biochemical markers of bone turnover - uses and limitations', *Annals of Clinical Biochemistry*, 51(2), pp. 189–202. doi: 10.1177/0004563213515190.

Hofbauer, L. C. *et al.* (2000) 'Perspective The Roles of Osteoprotegerin and Osteoprotegerin Ligand in the Paracrine Regulation of Bone Resorption', *J Bone Miner Res*, 15, pp. 2–12.

Hou, F. J. *et al.* (1998) 'Human vertebral body apparent and hard tissue stiffness', *Journal of Biomechanics*, 31(11), pp. 1009–1015. doi: 10.1016/S0021-9290(98)00110-9.

Huiskes, R. *et al.* (1987) 'Adaptive bone-remodeling theory applied to prosthetic-design analysis', *Journal of Biomechanics*, 20(11–12), pp. 1135–1150. doi: 10.1016/0021-9290(87)90030-3.

Huiskes, R. *et al.* (2000) 'Effects of mechanical forces on maintenance and adaptation of form in trabecular bone', *Nature*, 405(6787), pp. 704–706. doi: 10.1038/35015116.

Hussein, A. I. *et al.* (2018) 'Differences in Trabecular Microarchitecture and Simplified Boundary Conditions Limit the Accuracy of Quantitative Computed Tomography-Based Finite Element Models of Vertebral Failure', *Journal of Biomechanical Engineering*, 140(2), pp. 1–11. doi: 10.1115/1.4038609.

Imai, K. *et al.* (2006) 'Nonlinear finite element model predicts vertebral bone strength and fracture site', *Spine*, 31(16), pp. 1789–1794. doi: 10.1097/01.brs.0000225993.57349.df.

Imai, K. *et al.* (2008) 'In vivo assessment of lumbar vertebral strength in elderly women using

computed tomography-based nonlinear finite element model', *Spine*, 33(1), pp. 27–32. doi: 10.1097/BRS.0B013E31815E3993.

Imai, K. (2015) 'Computed tomography-based finite element analysis to assess fracture risk and osteoporosis treatment', *World Journal of Experimental Medicine*, 5(3), p. 182. doi: 10.5493/wjem.v5.i3.182.

Izzo, R. *et al.* (2013) 'Biomechanics of the spine. Part I: Spinal stability', *European Journal of Radiology*, 82(1), pp. 118–126. doi: 10.1016/j.ejrad.2012.07.024.

Jackman, T. M. *et al.* (2015) 'Quantitative, 3D Visualization of the Initiation and Progression of Vertebral Fractures Under Compression and Anterior Flexion'. doi: 10.1002/jbmr.2749.

Jemal, A. *et al.* (2010) 'Cancer Statistics, 2010', *CA: A Cancer Journal for Clinicians*, 60(5), pp. 277–300. doi: 10.3322/CAAC.20073.

Johansson, H. *et al.* (2014) 'A meta-analysis of reference markers of bone turnover for prediction of fracture', *Calcified Tissue International*, 94(5), pp. 560–567. doi: 10.1007/s00223-014-9842-y.

Keaveny, T. M. *et al.* (1993) 'Theoretical analysis of the experimental artifact in trabecular bone compressive modulus', *Journal of biomechanics*, 26(4–5), pp. 599–607. doi: 10.1016/0021-9290(93)90021-6.

Keaveny, T. M. *et al.* (2007) 'Effects of Teriparatide and Alendronate on Vertebral Strength as Assessed by Finite Element Modeling of QCT Scans in Women With Osteoporosis', *Journal of Bone and Mineral Research*, 22(1), pp. 149–157. doi: 10.1359/JBMR.061011.

Keaveny, T. M. *et al.* (2014) 'Femoral and Vertebral Strength Improvements in Postmenopausal Women With Osteoporosis Treated With Denosumab', *Journal of Bone and Mineral Research*, 29(1), pp. 158–165. doi: 10.1002/JBMR.2024.

Keaveny, T. M., Morgan, E. F. and Yeh, O. C. (1981) 'BONE MECHANICS', in, pp. 360–366. doi: 10.1016/S0140-6736(00)62141-4.

Keaveny, T. M., Morgan, E. F. and Yeh, O. C. (2004) *BONE MECHANICS*. Available at: www.digitalengineeringlibrary.com.

Khosla, S., Joseph Melton, L. and Lawrence Riggs, B. (2002) 'Clinical review 144: Estrogen and

the male skeleton', *Journal of Clinical Endocrinology and Metabolism*, 87(4), pp. 1443–1450. doi: 10.1210/jc.87.4.1443.

Kiratli, B. J. *et al.* (2001) 'Progressive decrease in bone density over 10 years of androgen deprivation therapy in patients with prostate cancer', *Urology*, 57(1), pp. 127–132. doi: 10.1016/S0090-4295(00)00895-5.

Kishan, A. U. *et al.* (2022) 'Androgen deprivation therapy use and duration with definitive radiotherapy for localised prostate cancer: an individual patient data meta-analysis', *The Lancet Oncology*, 23(2), pp. 304–316. doi: 10.1016/S1470-2045(21)00705-1.

Komarova, S. V. *et al.* (2003) 'Mathematical model predicts a critical role for osteoclast autocrine regulation in the control of bone remodeling', *Bone*, 33(2), pp. 206–215. doi: 10.1016/S8756-3282(03)00157-1.

Kopperdahl, D. L. and Keaveny, T. M. (1998) 'Yield strain behavior of trabecular bone', *Journal of Biomechanics*, 31(7), pp. 601–608. doi: 10.1016/S0021-9290(98)00057-8.

Kopperdahl, D. L., Morgan, E. F. and Keaveny, T. M. (2002) 'Quantitative computed tomography estimates of the mechanical properties of human vertebral trabecular bone', *Journal of Orthopaedic Research*, 20(4), pp. 801–805. doi: 10.1016/S0736-0266(01)00185-1.

Kowalska, M. *et al.* (2010) 'Procollagen I amino-terminal propeptide as a potential marker for multiple myeloma', *Clinical Biochemistry*, 43(6), pp. 604–608. doi: 10.1016/j.clinbiochem.2009.12.018.

Kuo, T. R. and Chen, C. H. (2017) 'Bone biomarker for the clinical assessment of osteoporosis: Recent developments and future perspectives', *Biomarker Research*, 5(1), pp. 5–13. doi: 10.1186/S40364-017-0097-4.

Lee, D. C. *et al.* (2017) 'Phantomless calibration of CT scans for measurement of BMD and bone strength-Inter-operator reanalysis precision'. doi: 10.1016/j.bone.2017.07.029.

Lemaire, V. *et al.* (2004) 'Modeling the interactions between osteoblast and osteoclast activities in bone remodeling', *Journal of Theoretical Biology*, 229(3), pp. 293–309. doi: 10.1016/J.JTBI.2004.03.023.

Lerebours, C. *et al.* (2016) 'A multiscale mechanobiological model of bone remodelling

predicts site-specific bone loss in the femur during osteoporosis and mechanical disuse', *Biomechanics and Modeling in Mechanobiology*, 15(1), pp. 43–67. doi: 10.1007/s10237-015-0705-x.

Li, M. *et al.* (2015) 'A comparison study on the efficacy of SpinoMed and soft lumbar orthosis for osteoporotic vertebral fracture', *Prosthetics and Orthotics International*, 39(4), pp. 270–276. doi: 10.1177/0309364614528204.

Liang, Y. W. *et al.* (2024) 'The Quantitative Evaluation of Automatic Segmentation in Lumbar Magnetic Resonance Images', *Neurospine*, 21(2), pp. 665–675. doi: 10.14245/ns.2448060.030.

Liebschner, M. A. K. *et al.* (2003) 'Finite element modeling of the human thoracolumbar spine', *Spine*, 28(6), pp. 559–565. doi: 10.1097/01.BRS.0000049923.27694.47.

Lin, C. L., Lin, Y. H. and Chang, S. H. (2010) 'Multi-factorial analysis of variables influencing the bone loss of an implant placed in the maxilla: Prediction using FEA and SED bone remodeling algorithm', *Journal of Biomechanics*, 43(4), pp. 644–651. doi: 10.1016/j.jbiomech.2009.10.030.

Lin, J. K. *et al.* (2023) 'Validation of Biomechanical Computed Tomography for Fracture Risk Classification in Metastatic Hormone-sensitive Prostate Cancer', *European Urology Oncology*, (xxxx), pp. 1–10. doi: 10.1016/j.euo.2023.10.016.

Lirette, L. S. *et al.* (2014) 'Coccydynia: An overview of the anatomy, etiology, and treatment of coccyx pain', *Ochsner Journal*, 14(1), pp. 84–87.

Liu, X. *et al.* (2021) 'Detection and Segmentation of Pelvic Bones Metastases in MRI Images for Patients With Prostate Cancer Based on Deep Learning', *Frontiers in Oncology*, 11(November), pp. 1–11. doi: 10.3389/fonc.2021.773299.

Lorentzon, M. *et al.* (2019) 'Algorithm for the Use of Biochemical Markers of Bone Turnover in the Diagnosis, Assessment and Follow-Up of Treatment for Osteoporosis', *Advances in Therapy*, 36(10), pp. 2811–2824. doi: 10.1007/s12325-019-01063-9.

Lu, Y. *et al.* (2014) 'Finite element analyses of human vertebral bodies embedded in polymethylmethalcrylate or loaded via the hyperelastic intervertebral disc models provide equivalent predictions of experimental strength', *Journal of Biomechanics*, 47(10), pp. 2512–

2516. doi: 10.1016/j.jbiomech.2014.04.015.

Luisi, S. *et al.* (2001) 'Expression and secretion of activin A: possible physiological and clinical implications', *European Journal of Endocrinology*, 145, p. 225236. Available at: https://academic.oup.com/ejendo/article/145/3/225/6750414.

Macedo, F. *et al.* (2017) 'Bone Metastases: An Overview', *Oncology Reviews*, 11(1), pp. 43–49. doi: 10.4081/ONCOL.2017.321.

Mahnken, A. H. *et al.* (2002) 'Multidetector CT of the spine in multiple myeloma: Comparison with MR imaging and radiography', *American Journal of Roentgenology*, 178(6), pp. 1429–1436. doi: 10.2214/ajr.178.6.1781429.

Majcher, K. B. *et al.* (2024) 'Magnetic resonance imaging based finite element modelling of the proximal femur: a short-term in vivo precision study', *Scientific Reports*, 14(1). doi: 10.1038/s41598-024-57768-7.

Malhotra, K., Butler, J. S., *et al.* (2016) 'Spinal disease in myeloma: Cohort analysis at a specialist spinal surgery centre indicates benefit of early surgical augmentation or bracing', *BMC Cancer*, 16(1). doi: 10.1186/s12885-016-2495-7.

Malhotra, K., Lui, D. F., *et al.* (2016) 'Successful nonsurgical treatment for highly unstable fracture subluxation of the spine secondary to myeloma', *Spine Journal*, 16(8), pp. e547–e551. doi: 10.1016/j.spinee.2016.03.008.

Mansoorinasab, M. and Abdolhoseinpour, H. (2018) 'A review and update of vertebral fractures due to metastatic tumors of various sites to the spine: Percutaneous vertebroplasty', *Interventional Medicine and Applied Science*, 10(1), pp. 1–6. doi: 10.1556/1646.10.2018.03.

Maquer, G., Dall'Ara, E. and Zysset, P. K. (2012) 'Removal of the cortical endplates has little effect on ultimate load and damage distribution in QCT-based voxel models of human lumbar vertebrae under axial compression', *Journal of Biomechanics*, 45(9), pp. 1733–1738. doi: 10.1016/j.jbiomech.2012.03.019.

Martin, M. *et al.* (2020) 'Assessment of romosozumab efficacy in the treatment of postmenopausal osteoporosis: Results from a mechanistic PK-PD mechanostat model of bone remodeling', *Bone*, 133(January), p. 115223. doi: 10.1016/j.bone.2020.115223.

Matsumoto, T. *et al.* (2009) 'Prediction of vertebral strength under loading conditions occurring in activities of daily living using a computed tomography-based nonlinear finite element method', *Spine*, 34(14), pp. 1464–1469. doi: 10.1097/BRS.0b013e3181a55636.

Matsuura, Y. *et al.* (2014) 'Specimen-Specific Nonlinear Finite Element Modeling to PredictVertebrae Fracture Loads after Vertebroplasty', *Spine*, 39(22), pp. e1291–e1296.

Matuschek, C. *et al.* (2015) 'Effects of Radiotherapy in the treatment of multiple myeloma: A retrospective analysis of a Single Institution', *Radiation Oncology*, 10(1), pp. 1–9. doi: 10.1186/S13014-015-0374-Z/TABLES/5.

McNamara, L. M. and Prendergast, P. J. (2007) 'Bone remodelling algorithms incorporating both strain and microdamage stimuli', *Journal of Biomechanics*, 40(6), pp. 1381–1391. doi: 10.1016/J.JBIOMECH.2006.05.007.

Mellal, A. *et al.* (2004) 'Stimulating effect of implant loading on surrounding bone. Comparison of three numerical models and validation by in vivo data', *Clinical Oral Implants Research*, 15(2), pp. 239–248. doi: 10.1111/j.1600-0501.2004.01000.x.

Mellon, S. J. and Tanner, K. E. (2012) 'Bone and its adaptation to mechanical loading: A review', *International Materials Reviews*. Taylor & Francis, pp. 235–255. doi: 10.1179/1743280412Y.0000000008.

Melton, L. J. *et al.* (2007) 'Structural determinants of vertebral fracture risk', *Journal of Bone and Mineral Research*, 22(12), pp. 1885–1892. doi: 10.1359/jbmr.070728.

Melton, L. J. *et al.* (2010) 'Relation of vertebral deformities to bone density, structure, and strength', *Journal of Bone and Mineral Research*, 25(9), pp. 1922–1930. doi: 10.1002/JBMR.150.

Mercadante, S. (1997) 'Malignant bone pain: Pathophysiology and treatment', *Pain*, 69(1–2), pp. 1–18. doi: 10.1016/S0304-3959(96)03267-8.

Michalski, A. S. *et al.* (2020) 'CT-based internal density calibration for opportunistic skeletal assessment using abdominal CT scans', *Medical Engineering and Physics*, 78, pp. 55–63. doi: 10.1016/j.medengphy.2020.01.009.

Millner, M. R. *et al.* (1978) 'Determination of effective energies in CT calibration', *Medical*

Physics, 5(6), pp. 543–545. Available at: https://aapm.onlinelibrary.wiley.com/doi/epdf/10.1118/1.594488.

Mizrahi, J., Silva, M. J. and Hayes, W. C. (1992) 'Finite element stress analysis of simulated metastatic lesions in the lumbar vertebral body', *Journal of Biomedical Engineering*, 14(6), pp. 467–475. doi: 10.1016/0141-5425(92)90098-6.

Moester, M. J. C. *et al.* (2010) 'Sclerostin: Current knowledge and future perspectives', *Calcified Tissue International*, 87(2), pp. 99–107. doi: 10.1007/s00223-010-9372-1.

Mohan, M. *et al.* (2021) 'Bone remineralization of lytic lesions in multiple myeloma – The Arkansas experience', *Bone*, 146, p. 115876. doi: 10.1016/J.BONE.2021.115876.

Molloy, S. *et al.* (2015) 'Optimizing the management of patients with spinal myeloma disease', *British Journal of Haematology*, 171(3), pp. 332–343. doi: 10.1111/bjh.13577.

Morgan, E. F. *et al.* (2001) 'Nonlinear Behavior of Trabecular Bone at Small Strains', *Journal of Biomechanical Engineering*, 123(1), pp. 1–9. doi: 10.1115/1.1338122.

Morgan, E. F., Bayraktar, H. H. and Keaveny, T. M. (2003) 'Trabecular bone modulus–density relationships depend on anatomic site', *Journal of Biomechanics*, 36(7), pp. 897–904. doi: 10.1016/S0021-9290(03)00071-X.

Morgan, E. F. and Keaveny, T. M. (2001) 'Dependence of yield strain of human trabecular bone on anatomic site', *Journal of Biomechanics*, 34(5), pp. 569–577. doi: 10.1016/S0021-9290(01)00011-2.

Mose, S. *et al.* (2000) 'Originalarbeit Strahlentherapie und Onkologie Wertigkeit der Radiotherapie in der Behandlung des multiplen Myeloms', *Strahlenther Onkol*, 176, p. 506.

Mundy, G. R. (2002) 'Metastasis to bone: causes, consequences and therapeutic opportunities', *Nature Reviews Cancer 2002 2:8*, 2(8), pp. 584–593. doi: 10.1038/nrc867.

Nazarian, A. *et al.* (2008) 'Bone volume fraction explains the variation in strength and stiffness of cancellous bone affected by metastatic cancer and osteoporosis', *Calcified Tissue International*, 83(6), pp. 368–379. doi: 10.1007/s00223-008-9174-x.

Niebur, G. L. *et al.* (1999) 'Convergence Behavior of High-Resolution Finite Element Models of Trabecular Bone', *Journal of Biomechanical Engineering*, 121(6), pp. 629–635. doi:

10.1115/1.2800865.

Niebur, G. L. *et al.* (2000) 'High-resolution finite element models with tissue strength asymmetry accurately predict failure of trabecular bone', *Journal of Biomechanics*, 33(12), pp. 1575–1583. doi: 10.1016/S0021-9290(00)00149-4.

Nishio, M. *et al.* (2021) 'Lung Cancer Segmentation With Transfer Learning: Usefulness of a Pretrained Model Constructed From an Artificial Dataset Generated Using a Generative Adversarial Network', *Frontiers in Artificial Intelligence*, 4(July), pp. 1–10. doi: 10.3389/frai.2021.694815.

Nucci, M. and Anaissie, E. (2009) 'Infections in patients with multiple myeloma in the era of high-dose therapy and novel agents', *Clinical Infectious Diseases*, 49(8), pp. 1211–1225. doi: 10.1086/605664/2/49-8-1211-TBL005.GIF.

Oranger, A. *et al.* (2013) 'Cellular Mechanisms of Multiple Myeloma Bone Disease', *Clinical and Developmental Immunology*, 2013. doi: 10.1155/2013/289458.

Orford, N. R. *et al.* (2024) 'A pilot feasibility randomised controlled trial of bone antiresorptive agents on bone turnover markers in critically ill women', *Scientific Reports*, 14(1), pp. 1–10. doi: 10.1038/s41598-024-52607-1.

Ott, S. M. (2018) 'Cortical or Trabecular Bone: What's the Difference?', *American Journal of Nephrology*. S. Karger AG, pp. 373–375. doi: 10.1159/000489672.

Pahr, D. H. and Zysset, P. K. (2009) 'A comparison of enhanced continuum FE with micro FE models of human vertebral bodies', *Journal of Biomechanics*, 42(4), pp. 455–462. doi: 10.1016/j.jbiomech.2008.11.028.

Pant, A. *et al.* (2021) 'Integration of mechanics and biology in computer simulation of bone remodeling', *Progress in Biophysics and Molecular Biology*, 164, pp. 33–45. doi: 10.1016/J.PBIOMOLBIO.2021.05.001.

Park, T. *et al.* (2022) 'Automated segmentation of the fractured vertebrae on CT and its applicability in a radiomics model to predict fracture malignancy', *Scientific Reports*, 12(1), pp. 1–11. doi: 10.1038/s41598-022-10807-7.

Pennington, Z. *et al.* (2019) 'SINS Score and Stability: Evaluating the Need for Stabilization

Within the Uncertain Category', *World Neurosurgery*, 128, pp. e1034–e1047. doi: 10.1016/j.wneu.2019.05.067.

Pfeifer, M., Begerow, B. and Minne, H. W. (2004) 'Effects of a New Spinal Orthosis on Posture, Trunk Strength, and Quality of Life in Women with Postmenopausal Osteoporosis: A Randomized Trial', *American Journal of Physical Medicine and Rehabilitation*, 83(3), pp. 177–186. doi: 10.1097/01.PHM.0000113403.16617.93.

Pickhardt, P. J. *et al.* (2013) 'Opportunistic screening for osteoporosis using abdominal computed tomography scans obtained for other indications', *Annals of Internal Medicine*, 158(8), pp. 588–595. doi: 10.7326/0003-4819-158-8-201304160-00003.Opportunistic.

Pickhardt, P. J. *et al.* (2015) 'Comparison of Femoral Neck BMD Evaluation Obtained Using Lunar DXA and QCT With Asynchronous Calibration From CT Colonography', *Journal of Clinical Densitometry*, 18(1), pp. 5–12. doi: 10.1016/J.JOCD.2014.03.002.

Pivonka, P. *et al.* (2008) 'Model structure and control of bone remodeling: A theoretical study', *Bone*, 43(2), pp. 249–263. doi: 10.1016/j.bone.2008.03.025.

Pivonka, P. *et al.* (2010) 'Theoretical investigation of the role of the RANK-RANKL-OPG system in bone remodeling', *Journal of Theoretical Biology*, 262(2), pp. 306–316. doi: 10.1016/j.jtbi.2009.09.021.

Proudfoot, J. (2003) 'Pediatric Thoracolumbar Spinal Injury: Frequently Hidden, but Not Harmless | 2003-06-01 | AHC Media: Continuing Medical Education Publishing | Relias Media - Continuing Medical Education Publishing', *Pediatric Emergency Medicine Reports*, 8(6), p. 59.

Qiang, Y. W. *et al.* (2008) 'Myeloma-derived Dickkopf-1 disrupts Wnt-regulated osteoprotegerin and RANKL production by osteoblasts: a potential mechanism underlying osteolytic bone lesions in multiple myeloma', *Blood*, 112(1), p. 196. doi: 10.1182/BLOOD-2008-01-132134.

Quidet, M. *et al.* (2018) 'Evaluation of the Relevance of Surgery in Patients with Multiple Myeloma Harboring Symptomatic Spinal Involvement: A Retrospective Case Series', *World Neurosurgery*, 114, pp. e356–e365. doi: 10.1016/j.wneu.2018.02.184.

Rao, G. *et al.* (2006) 'Multiple myeloma of the cervical spine: Treatment strategies for pain

and spinal instability', *Journal of Neurosurgery: Spine*, 5(2), pp. 140–145. doi: 10.3171/spi.2006.5.2.140.

Rasband, W. . (1997) *ImageJ*, *U. S. National Institutes of Health*. Bethesda, Maryland, USA. Available at: https://imagej.nih.gov/ij/.

Rathnayaka, K. *et al.* (2011) 'Effects of CT image segmentation methods on the accuracy of long bone 3D reconstructions', *Medical Engineering and Physics*, 33(2), pp. 226–233. doi: 10.1016/j.medengphy.2010.10.002.

Rawla, P. (2019) 'Epidemiology of Prostate Cancer', *World Journal of Oncology*, 10(2), p. 63. doi: 10.14740/WJON1191.

Ritzel, H. *et al.* (1997) 'The Thickness of Human Vertebral Cortical Bone and its Changes in Aging and Osteoporosis: A Histomorphometric Analysis of the Complete Spinal Column from Thirty-Seven Autopsy Specimens', *Journal of Bone and Mineral Research*, 12(1), pp. 89–95. doi: 10.1359/JBMR.1997.12.1.89.

Roland Dürr, H. *et al.* (2002) 'Multiple myeloma: Surgery of the spine. Retrospective analysis of 27 patients', *Spine*, 27(3), pp. 320–325. doi: 10.1097/00007632-200202010-00023.

Roodman, G. D. (2009) 'SPOTLIGHT REVIEW Pathogenesis of myeloma bone disease', *Leukemia*, 23, pp. 435–441. doi: 10.1038/leu.2008.336.

Ruimerman, R. *et al.* (2003) 'A 3-dimensional computer model to simulate trabecular bone metabolism.', *Biorheology*, 40(1,2,3), pp. 315–320.

Saffarzadeh, M. *et al.* (2016) 'Multicenter analysis of CIREN occupant lumbar bone mineral density and correlation with age and fracture incidence', *Traffic Injury Prevention*, 17(S1), pp. 34–41. doi: 10.1080/15389588.2016.1203429.

Saillard, E. *et al.* (2024) 'Finite element models with automatic computed tomography bone segmentation for failure load computation', *Scientific Reports*, 14(1). doi: 10.1038/s41598-024-66934-w.

Saladin, K. ., Gan, C. . and Cushman, H. . (2017) *Anatomy & Physiology: The Unity of Form and Function*. 8th edn. McGraw-Hill US Higher Ed.

Sato, M. *et al.* (2024) 'Impact of Androgen Deprivation Therapy on Lumbar Spine Bone Health

Using Quantitative Computed Tomography in a Propensity-Matched Cohort of Patients With Prostate Cancer', *JU Open Plus*, 2(6). doi: 10.1097/ju9.0000000000000158.

Saylor, P. J. *et al.* (2011) 'Factors Associated With Vertebral Fractures in Men Treated With Androgen Deprivation Therapy for Prostate Cancer Abbreviations and Acronyms ADT androgen deprivation therapy BMD bone mineral density BMI body mass index BSAP bone specific alkaline phosphatase CTX C-telopeptide GnRH gonadotropin-releasing hormone', *The Journal of Urology*, 186, pp. 482–486. doi: 10.1016/j.juro.2011.03.111.

von Schacky, C. E. *et al.* (2021) 'Multitask deep learning for segmentation and classification of primary bone tumors on radiographs', *Radiology*, 301(2), pp. 398–406. doi: 10.1148/radiol.2021204531.

Schäfer, R. *et al.* (2023) 'The mechanical loading of the spine in physical activities', *European Spine Journal*, 32(9), pp. 2991–3001. doi: 10.1007/s00586-023-07733-1.

Scheiner, S. *et al.* (2014) 'Mathematical modeling of postmenopausal osteoporosis and itstreatment by the anti-catabolic drug denosumab', *Int. J. Numer. Meth. Biomed. Engng.*, 30, pp. 1–27.

Scheiner, S., Pivonka, P. and Hellmich, C. (2013) 'Coupling systems biology with multiscale mechanics, for computer simulations of bone remodeling', *Computer Methods in Applied Mechanics and Engineering*, 254, pp. 181–196. doi: 10.1016/j.cma.2012.10.015.

Schileo, E. *et al.* (2008) 'An accurate estimation of bone density improves the accuracy of subject-specific finite element models', *Journal of Biomechanics*, 41(11), pp. 2483–2491. doi: 10.1016/J.JBIOMECH.2008.05.017.

Schileo, E. and Taddei, F. (2021) 'Finite Element Assessment of Bone Fragility from Clinical Images', *Current Osteoporosis Reports*, 19(6), pp. 688–698. doi: 10.1007/s11914-021-00714-7.

Schneider, C. A., Rasband, W. S. and Eliceiri, K. W. (2012) 'NIH Image to ImageJ: 25 years of image analysis', *Nature Methods*, 9(7), pp. 671–675. Available at: https://doi.org/10.1038/nmeth.2089.

Schriefer, J. L. *et al.* (2005) 'Cellular accommodation and the response of bone to mechanical loading', *Journal of Biomechanics*, 38(9), pp. 1838–1845. doi:

10.1016/j.jbiomech.2004.08.017.

Schulte, F. A. *et al.* (2013) 'Strain-adaptive in silico modeling of bone adaptation - A computer simulation validated by in vivo micro-computed tomography data', *Bone*, 52(1), pp. 485–492. doi: 10.1016/j.bone.2012.09.008.

Schwaiger, B. J. *et al.* (2017) 'Vertebral and femoral bone mineral density and bone strength in prostate cancer patients assessed in phantomless PET/CT examinations', *Bone*, 101, pp. 62–69. doi: 10.1016/j.bone.2017.04.008.

Schwiedrzik, J. J. (2014) *Experimental, theoretical and numerical investigation of the nonlinear micromechanical properties of bone*.

Seifert-Klauss, V. *et al.* (2012) 'Bone loss in premenopausal, perimenopausal and postmenopausal women: results of a prospective observational study over 9 years', *https://doi.org/10.3109/13697137.2012.658110*, 15(5), pp. 433–440. doi: 10.3109/13697137.2012.658110.

Shahinian, V. B. *et al.* (2005) 'From the Departments of General Internal Medicine', *N Engl J Med*, 352(2), pp. 154–164. Available at: www.nejm.org.

Shore, N. D. (2020) *Management Review Current and Future Management of Locally Advanced and Metastatic Prostate Cancer KEY WORDS Prostate cancer • Metastatic prostate cancer • Locally advanced prostate cancer • Androgen deprivation therapy • Chemotherapy*, *Rev Urol*.

Smith, M. R. *et al.* (2001) 'PAMIDRONATE TO PREVENT BONE LOSS DURING ANDROGEN-DEPRIVATION THERAPY FOR PROSTATE CANCER Background Treatment with a gonadotropin-releas', *N Engl J Med*, 948(13). Available at: www.nejm.org.

Smith, M. R. *et al.* (2005) 'Gonadotropin-releasing hormone agonists and fracture risk: A claims-based cohort study of men with nonmetastatic prostate cancer', *Journal of Clinical Oncology*, 23(31), pp. 7897–7903. doi: 10.1200/JCO.2004.00.6908.

Smith, M. R. *et al.* (2006) 'Risk of clinical fractures after gonadotropin-releasing hormone agonist therapy for prostate cancer', *Journal of Urology*, 175(1), pp. 136–139. doi: 10.1016/S0022-5347(05)00033-9.

Snowden, J. A. *et al.* (2011) 'Guidelines for supportive care in multiple myeloma 2011', *British Journal of Haematology*, 154(1), pp. 76–103. doi: 10.1111/j.1365-2141.2011.08574.x.

Stadelmann, M. A. *et al.* (2020) 'Conventional finite element models estimate the strength of metastatic human vertebrae despite alterations of the bone's tissue and structure', *Bone*, 141, p. 115598. doi: 10.1016/J.BONE.2020.115598.

Suarez-Almazor, M. E. *et al.* (2022) 'Association of Bone Mineral Density Testing with Risk of Major Osteoporotic Fractures among Older Men Receiving Androgen Deprivation Therapy to Treat Localized or Regional Prostate Cancer', *JAMA Network Open*, 5(4), pp. 1–16. doi: 10.1001/jamanetworkopen.2022.5432.

Suva, L. J., Griffin, R. J. and Makhoul, I. (2009) 'Mechanisms of bone metastases of breast cancer', *Endocrine-Related Cancer*, 16(3), pp. 703–713. doi: 10.1677/ERC-09-0012.

Taha, A. A. and Hanbury, A. (2015) 'Metrics for evaluating 3D medical image segmentation: Analysis, selection, and tool', *BMC Medical Imaging*, 15(1). doi: 10.1186/s12880-015-0068-x.

Taichman, R. S. (2005) 'Blood and bone: two tissues whose fates are intertwined to create the hematopoietic stem-cell niche Introduction and historical perspective'. doi: 10.1182/blood-2004-06.

Takasu, M. *et al.* (2011) 'Multiple Myeloma: Microstructural Analysis of Lumbar Trabecular Bones in Patients without Visible Bone Lesions-Preliminary Results 1 Conclusion: Signifi cant differences were observed in spinal microarchi-tecture between control subjects and multiple myeloma patients without pathologic fractures. Independent predic-tors of multiple myeloma included TbTh and FD in male patients and DA in female patients', 260(2). doi: 10.1148/radiol.11101746.

Tatoń, G. *et al.* (2013) 'Combining areal DXA bone mineral density and vertebrae postero-anterior width improves the prediction of vertebral strength', *Skeletal Radiology*, 42(12), pp. 1717–1725. doi: 10.1007/s00256-013-1723-3.

Terpos, E. *et al.* (2012) 'Elevated circulating sclerostin correlates with advanced disease features and abnormal bone remodeling in symptomatic myeloma: Reduction post-bortezomib monotherapy', *International Journal of Cancer*, 131(6), pp. 1466–1471. doi: 10.1002/ijc.27342.

Terpos, E. *et al.* (2021) 'Treatment of multiple myeloma-related bone disease: recommendations from the Bone Working Group of the International Myeloma Working Group', *Policy Review Lancet Oncol*, 22, pp. 119–149. doi: 10.1016/S1470-2045(20)30559-3.

Terpos, E., Christoulas, D. and Gavriatopoulou, M. (2018) 'Biology and treatment of myeloma related bone disease', *Metabolism: Clinical and Experimental*, 80, pp. 80–90. doi: 10.1016/J.METABOL.2017.11.012.

The Editors of Encyclopaedia Britannica (2020) 'osteocyte | Definition, Function, Location, & Facts | Britannica', *Encyclopædia Britannica*.

Tian, A. *et al.* (2019) 'Reference markers of bone turnover for prediction of fracture: A meta-analysis', *Journal of Orthopaedic Surgery and Research*, 14(1), pp. 4–13. doi: 10.1186/s13018-019-1100-6.

Tian, E. *et al.* (2009) 'The Role of the Wnt-Signaling Antagonist DKK1 in the Development of Osteolytic Lesions in Multiple Myeloma', *http://dx.doi.org/10.1056/NEJMoa030847*, 349(26), pp. 2483–2494. doi: 10.1056/NEJMOA030847.

Ting, K. R. *et al.* (2016) 'Clinical utility of C-terminal telopeptide of type 1 collagen in multiple myeloma', *British Journal of Haematology*, 173(1), pp. 82–88. doi: 10.1111/bjh.13928.

Tobeiha, M. *et al.* (2020) 'RANKL/RANK/OPG Pathway: A Mechanism Involved in Exercise-Induced Bone Remodeling', *BioMed Research International*. Hindawi Limited. doi: 10.1155/2020/6910312.

Tschirhart, C. E., Finkelstein, J. A. and Whyne, C. M. (2007) 'Biomechanics of vertebral level, geometry, and transcortical tumors in the metastatic spine', *Journal of Biomechanics*, 40, pp. 46–54. doi: 10.1016/j.jbiomech.2005.11.014.

Tschirhart, C. E., Nagpurkar, A. and Whyne, C. M. (2004) 'Effects of tumor location, shape and surface serration on burst fracture risk in the metastatic spine', *Journal of Biomechanics*, 37, pp. 653–660. doi: 10.1016/j.jbiomech.2003.09.027.

Utzschneider, S. *et al.* (2011) 'Surgical therapy of skeletal complications in multiple myeloma', in *International Orthopaedics*, pp. 1209–1213. doi: 10.1007/s00264-010-1127-0.

Vasikaran, S. *et al.* (2011) 'International Osteoporosis Foundation and International

Federation of Clinical Chemistry and Laboratory Medicine Position on bone marker standards in osteoporosis', *Clinical Chemistry and Laboratory Medicine*, 49(8), pp. 1271–1274. doi: 10.1515/CCLM.2011.602.

de Visser, K. E. and Joyce, J. A. (2023) 'The evolving tumor microenvironment: From cancer initiation to metastatic outgrowth', *Cancer Cell*. Cell Press, pp. 374–403. doi: 10.1016/j.ccell.2023.02.016.

Vivanco, J., Anderson, P. A. and Smith, E. L. (2014) 'Dependence of Anisotropy of Human Lumbar Vertebral Trabecular Bone on Quantitative Computed Tomography-Based Apparent Density', 136(September), pp. 1–10. doi: 10.1115/1.4027663.

Wang, C. *et al.* (2011) 'Simulated evolution of the vertebral body based on basic multicellular unit activities', *Journal of Bone and Mineral Metabolism*, 29(4), pp. 466–476. doi: 10.1007/s00774-010-0244-6.

Wang, C. *et al.* (2014) 'Simulation of bone remodelling in orthodontic treatment', *http://dx.doi.org/10.1080/10255842.2012.736969*, 17(9), pp. 1042–1050. doi: 10.1080/10255842.2012.736969.

Wang, X. *et al.* (2012) 'Prediction of new clinical vertebral fractures in elderly men using finite element analysis of CT scans', *Journal of Bone and Mineral Research*, 27(4), pp. 808–816. doi: 10.1002/jbmr.1539.

Wang, Y. *et al.* (2011) 'Computational Modeling of Interactions between Multiple Myeloma and the Bone Microenvironment', *PLOS ONE*, 6(11), p. e27494. doi: 10.1371/JOURNAL.PONE.0027494.

Weaver, A. A. *et al.* (2015) 'Lumbar Bone Mineral Density Phantomless Computed Tomography Measurements and Correlation with Age and Fracture Incidence', *Traffic Injury Prevention*, 16, pp. S153–S160. doi: 10.1080/15389588.2015.1054029.

Webster, D. *et al.* (2015) 'Strain energy density gradients in bone marrow predict osteoblast and osteoclast activity: A finite element study', *Journal of Biomechanics*, 48(5), pp. 866–874. doi: 10.1016/j.jbiomech.2014.12.009.

Wehrli, F. W. *et al.* (2006) 'Quantitative MRI for the assessment of bone structure and function', *NMR in Biomedicine*, pp. 731–764. doi: 10.1002/nbm.1066.

Weinans, H. *et al.* (2000) '"nite element models', *Journal of Biomechanics*, 33.

Weinans, H., Huiskes, R. and Grootenboer, H. J. (1992) 'The behavior of adaptive bone-remodeling simulation models', *Journal of Biomechanics*, 25(12), pp. 1425–1441. doi: 10.1016/0021-9290(92)90056-7.

Westendorf, J. J., Kahler, R. A. and Schroeder, T. M. (2004) 'Wnt signaling in osteoblasts and bone diseases', *Gene*, 341(1–2), pp. 19–39. doi: 10.1016/J.GENE.2004.06.044.

White, A. A. and Panjabi, M. M. (1978) 'The basic kinematics of the human spine: A review of past and current knowledge', *Spine*, pp. 12–20. doi: 10.1097/00007632-197803000-00003.

Whyne, C. M. *et al.* (2000) 'Biphasic material properties of lytic bone metastases', *Annals of Biomedical Engineering*, 28(9), pp. 1154–1158. doi: 10.1114/1.1313773.

Whyne, C. M., Hu, S. S. and Lotz, J. C. (2001) 'Parametric finite element analysis of vertebral bodies affected by tumors', *Journal of Biomechanics*, 34, pp. 1317–1324.

Whyne, C. M., Hu, S. S. and Lotz, J. C. (2003) 'Burst fracture in the metastatically involved spine: Development, validation, and parametric analysis of a three- dimensional poroelastic finite-element model', *Spine*, 28(7), pp. 652–660. doi: 10.1097/00007632-200304010-00007.

Winkler, D. G. *et al.* (2003) 'Osteocyte control of bone formation via sclerostin, a novel BMP antagonist', *EMBO Journal*, 22(23), pp. 6267–6276. doi: 10.1093/emboj/cdg599.

Winterbottom, A. P. and Shaw, A. S. (2009) 'Imaging patients with myeloma', *Clinical Radiology*, 64(1), pp. 1–11. doi: 10.1016/j.crad.2008.07.006.

Wolff, J. (1892) *The law of bone transformation*. Berlin: Hirschwald.

Wong, S. K. *et al.* (2019) 'Prostate cancer and bone metastases: The underlying mechanisms', *International Journal of Molecular Sciences*, 20(10). doi: 10.3390/ijms20102587.

Wysocki, M. A. and Doyle, S. (2022) 'Enhancing biomedical data validity with standardized segmentation finite element analysis', *Scientific Reports*, 12, p. 9860. Available at: https://doi.org/10.1038/s41598-022-13961-0.

Xu, L. *et al.* (2018) 'Automated Whole-Body Bone Lesion Detection for Multiple Myeloma on 68 Ga-Pentixafor PET/CT Imaging Using Deep Learning Methods', *Contrast Media and Molecular Imaging*, 2018. doi: 10.1155/2018/2391925.

Yee, A. J. and Raje, N. S. (2018) 'Denosumab for the treatment of bone disease in solid tumors and multiple myeloma', *Future Oncology*, 14(3), pp. 195–203. doi: 10.2217/fon-2017-0403.

Zeinali, A., Hashemi, B. and Akhlaghpoor, S. (2010) 'Noninvasive prediction of vertebral body compressive strength using nonlinear finite element method and an image based technique', *Physica Medica*, 26(2), pp. 88–97. doi: 10.1016/j.ejmp.2009.08.002.

Zhang, X., Jiang, P. and Wang, C. (2023) 'The role of prostate-specific antigen in the osteoblastic bone metastasis of prostate cancer: a literature review', *Frontiers in Oncology*. Frontiers Media SA. doi: 10.3389/fonc.2023.1127637.

Zhou, L. *et al.* (2021) 'Measuring the global, regional, and national burden of multiple myeloma from 1990 to 2019', *BMC Cancer*, 21(1). doi: 10.1186/s12885-021-08280-y.

Zysset, P. *et al.* (2015) 'Clinical Use of Quantitative Computed Tomography-Based Finite Element Analysis of the Hip and Spine in the Management of Osteoporosis in Adults: The 2015 ISCD Official Positions-Part II', *Journal of Clinical Densitometry*, 18(3), pp. 359–392. doi: 10.1016/j.jocd.2015.06.011.

Zysset, P. K. *et al.* (2013) 'Finite element analysis for prediction of bone strength', *BoneKEy reports*, 2. doi: 10.1038/BONEKEY.2013.120.

9 APPENDIX

9.1 Appendix 1

9.1.1 Data table for MM patients

			Average BMD				Failure Load (N)			
MM	Control/ Lytic (C/L)	Level	Baseline	Follow-up	Predicted	% diff follow-up/ predicted	Baseline	Follow-up	Predicted	% diff follow-up/ predicted
P1a	C	T4	0.3182	0.3204	0.3184	0.63	1622.6	1558.2	1711.6	9.38
	L	T5	0.3099	0.3425	0.3618	5.48	1922.3	2233.2	2695.1	18.74
P3	C	T10	0.1763	0.1558	0.1552	0.39	1497.4	1153.9	1173.6	1.69
	L	T11	0.1907	0.1651	0.1693	2.51	2134.1	1466.9	1728.4	16.37
P3a	C	T10	0.1815	0.2492	0.2117	16.27	1802.9	3004.5	2633.4	13.16
	L	T11	0.1785	0.2666	0.2715	1.82	1959.1	4080.5	5087.5	21.97
P5	C	T4	0.3368	0.3295	0.3248	1.44	1664.8	1649.4	1674	1.48
	L	T6	0.3139	0.3196	0.2963	7.57	2451.5	3030.9	2731.1	10.41
P5a	C	T1	0.3221	0.3193	0.3136	1.80	1355.7	988.97	1345.4	30.54
	L	C7	0.3335	0.3091	0.3013	2.56	1545.1	1096.3	1265.2	14.30
P8	C	T3	0.3292	0.2828	0.3076	8.40	2271.4	1606.9	1494.7	7.23
	C	T4	0.3336	0.3071	0.305	0.69	2158.4	1670.3	1799.2	7.43
P9	L	L3	0.2848	0.3278	0.3275	0.092	1621	2136.8	3195.7	39.71
P9a	C	T11	0.2083	0.3297	0.3251	1.41	2243.9	5618.8	5852.	4.07
	L	T10	0.1617	0.3444	0.3456	0.35	1612	5005.1	7207.1	36.06
P11	C	L3	0.2277	0.2625	0.2622	0.11	1640.9	2106.2	3050.9	36.64
	L	L4	0.248	0.2785	0.2782	0.11	2026.3	2058.9	4159.5	67.56
P12	L	T4	0.2679	0.3014	0.296	1.81	1507.9	1786.5	2042.9	13.39
	L	T5	0.2802	0.3181	0.2794	12.95	1302.7	1486.1	1419.5	4.58

9.1.2 Model adjustments

9.1.2.1 Adjustment 1: Linear Adjustment

As is clear from the studies in Chapter 6, the MM group is less well predicted compared to the non-cancer controls from the ANTELOPE trial and the MM vertebrae with no lesions. Making changes to the remodelling algorithm requires rerunning all models through the entire mechanobiological model which is time consuming. Therefore, it was proposed to attempt a simple linear adjustment to the density of each element in the models of the MM vertebra with large lesions. This simple adjustment means that the models only require a final simulation in Ansys to calculate the mechanical properties. For this adjustment, a sample of 7 MM patients with lytic vertebrae were used.

Method

To calculate the linear adjustment applied to the density, a linear regression study was conducted. The MM group was split into two, as done previously in this chapter, to evaluate the patients with and without lytic lesions separately. Figure 9.1 shows the linear regression relationship for the MM controls (green) and MM patients with lytic lesions (yellow). From the regression analysis, it was clear that the lesion group had much more variation as well as a poorer correlation (higher RMSE). The linear regression equation used to adjust the density is shown below in Equation 6.9.

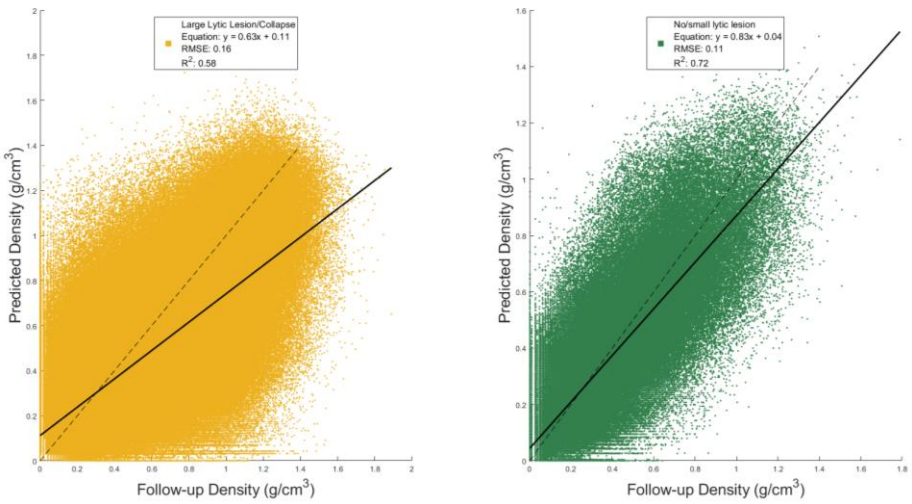

Figure 9.1 - Linear regression between the follow-up and predicted density for the vertebrae with lesinos (yellow) and vertebrae without lesions (green)

$$y = 0.63x + 0.11$$

Equation 6.9

Where y is the new predicted density and x is the original predicted density.

Using this equation for all patients, the predicted density for each element was adjusted. From this new predicted density, the Young's modulus was calculated and the model with the new material properties was re-evaluated in Ansys to estimate the reaction force at 0.15% strain (Figure 9.2).

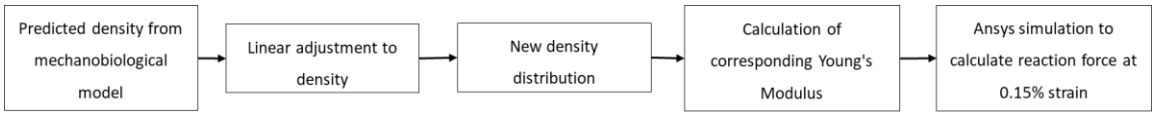

Figure 9.2 – Flow chart of the method for adjustment 1.

Results

In the original model, the average density was predicted well ($p < 0.5$). This was due to the optimisation of the average bone mineral density; however, the individual elements standard error was not optimised. Therefore, when plotting the graphs in Figure 9.1, there is a large RMSE for both vertebra with large lesions (RMSE: 0.16) and vertebra with no or small lesions (RMSE: 0.11). It was clear from the linear regression that most patients' average density would increase as the gradient of the line would increase through the adjustment (Figure 9.1). This result can be seen in Figure 9.3 where the average density of the new prediction for each vertebrae was now overestimated compared to the follow-up (Figure 9.1, $p < 0.05$). Despite one patients prediction improving by 1.36%, there was a similar result for the reaction force, where all other patients' predictions worsened (average original percentage difference between Follow-up and Predicted Follow-up Reaction Force: 31.41%, average new percentage difference between Follow-up and Predicted Follow-up Reaction Force: 48.1%) (Figure 9.3). The patients' vertebrae that improved in prediction was collapsed and had large regions of hypermineralisation. These regions with hypermineralisation would have high density and low strain and therefore there would have been little change in the density through the original mechanobiological model. With the linear adjustment, this increased the density of the elements with high density (Figure 9.1), increasing the prediction of the failure load. For all patients, the predicted BMD and FL is higher than the

follow-up. This reinforces the conclusion from this chapter, that the model increased the density for the vertebra with lesions more than what the follow-up density was. The model, therefore, needs further improvement, focussing on local improvements in the vertebrae with large lesions.

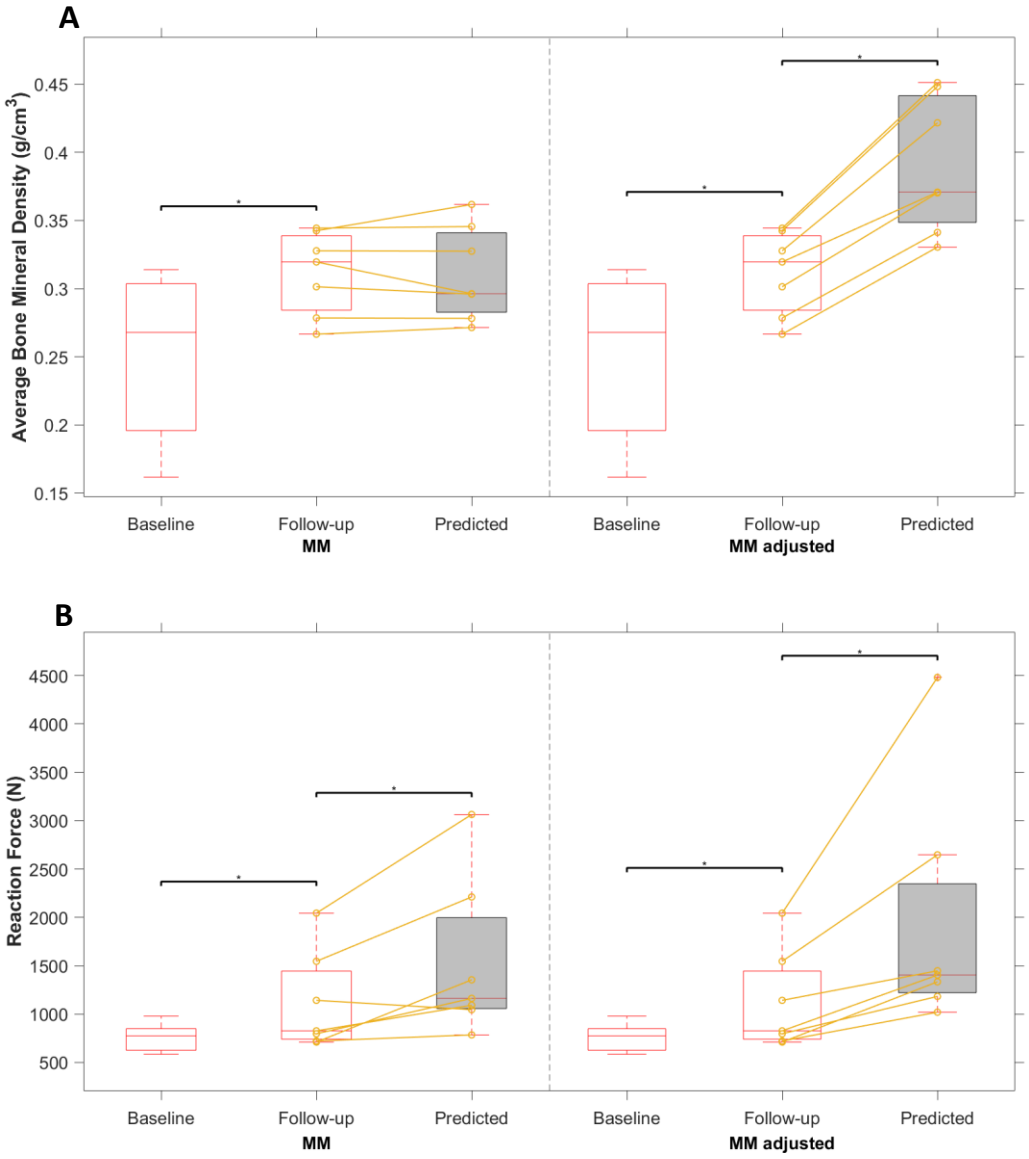

Figure 9.3 - Box plot of the (A) average bone mineral density and (B) reaction force at 0.15% strain with the original prediction from earlier in the chapter on the left and the new prediction with the linear adjustment on the right.

9.1.2.2 Adjustment 2: Bone cell removal in lesion region

As adjustment 1 has shown, a more patient-specific approach to improve the prediction of the vertebra with larger lesions is necessary. Metastatic lytic tissue is primarily composed of tumour cells, fibroblasts and immune cells (de Visser and Joyce, 2023). Therefore, it was assumed that, within this region, there were no osteoclasts or osteoblasts meaning no bone remodelling. This was implemented in the model to evaluate whether the removal of initial osteoblasts and osteoclasts improved the prediction of density and failure load for the vertebra with large lesions.

Method

For this adjustment, a sample subset of 7 MM patients from the RNOH dataset was included. To remove bone cells in the lesion region, a rule was enforced so that if the density of the element was <0.1 g/cm^3, there were no osteoblasts or osteoclasts for the first time step. After this time step, the model would run as normal and bone cells could populate these elements depending on the local mechanical stimulus experienced by each element. The material properties were then remapped onto the 3D model and re-run in Ansys to evaluate the failure load at 1.9% strain.

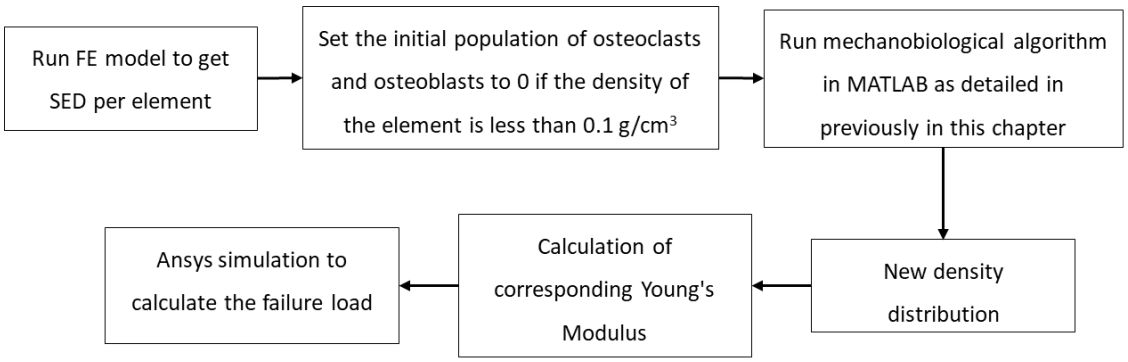

Figure 9.4 – Flow chart of the pipeline for adjustment 2.

Results

The prediction of average bone mineral density does not improve through this adjustment, but the difference between follow-up and predicted remains insignificant (Figure 9.5, $p > 0.5$). However, this was expected as the algorithm and parameters were optimised to match the predicted average density to the follow-up average density. The difference between follow-up and predicted for the adjusted model is now not significant which suggests the model has

improved in prediction (Figure 9.5). However, the prediction only improves in one patient (P9a) while the prediction for the rest of the cohort gets worse (average original percentage difference between Follow-up and Predicted Follow-up: 24.73%, average new percentage difference between Follow-up and Predicted Follow-up: 27.98%). The most likely reason for the insignificant difference is the small sample size for this sub-study.

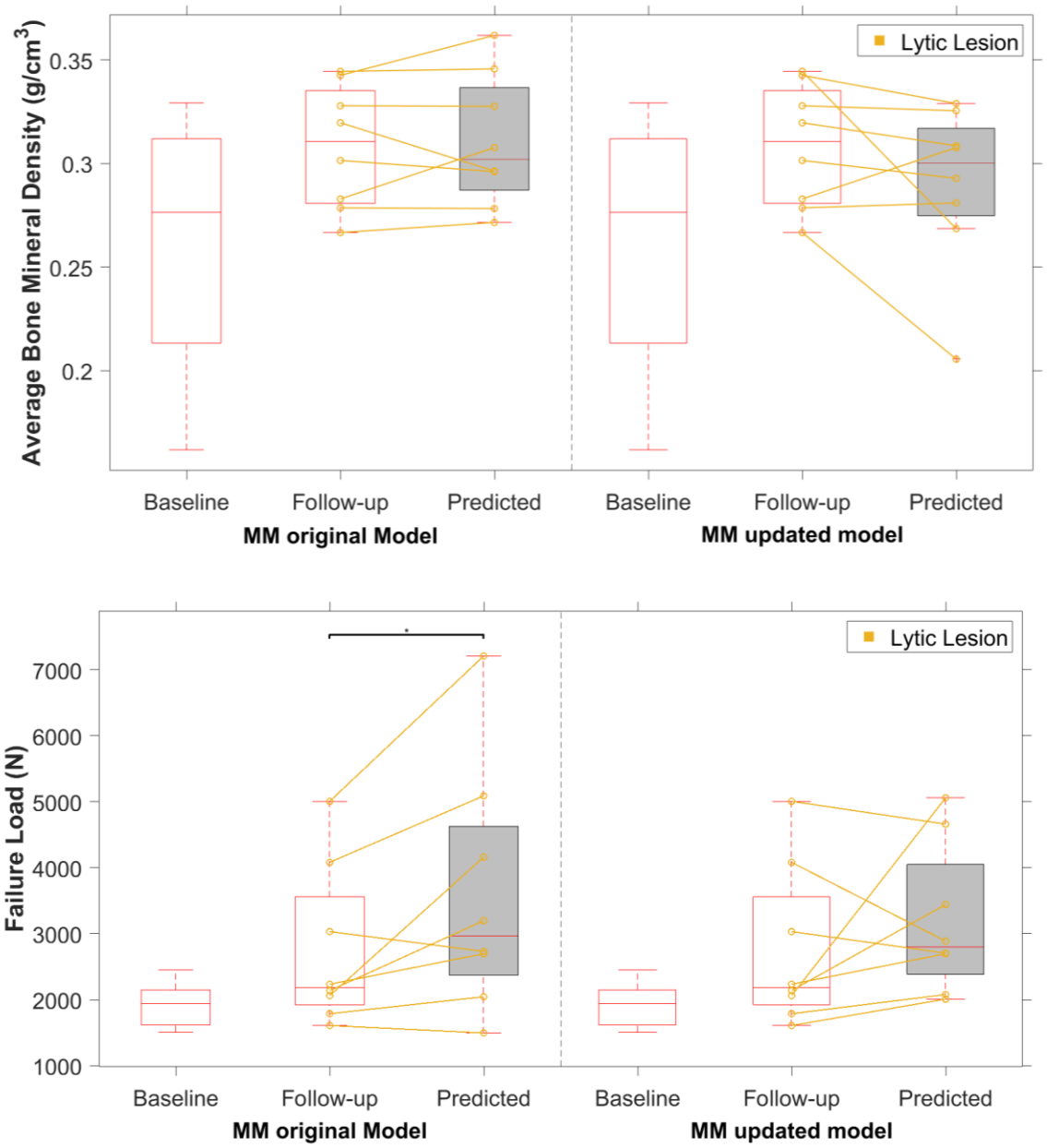

Figure 9.5 – Box plot of the second adjustment for the average bone mineral density (top) and the failure load (bottom), comparing the original models prediction (left) and the new adjustments prediction (right).

A

	Follow-up	Original: Predicted	Adjustment 2: Predicted
Failure Load (N)	2233	2695	2511
Average Density (g/cm³)	0.3425	0.3618	0.3289
Density distribution (g/cm³)	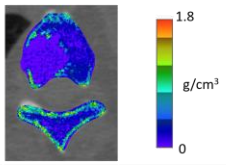	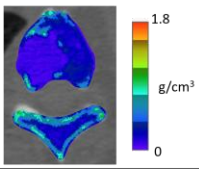	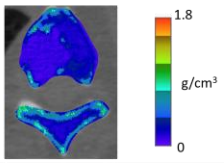
EPEL3 distribution@1.9% strain (mm/mm)	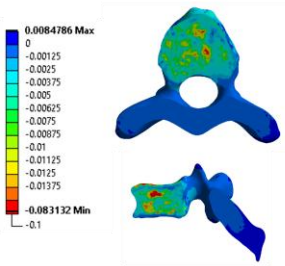	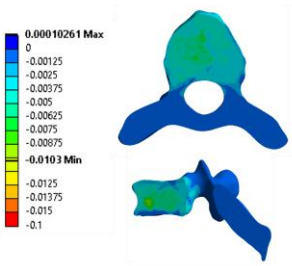	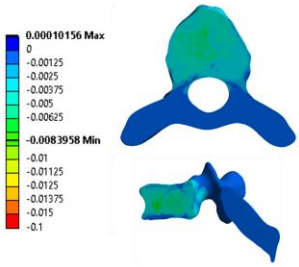

B

	Follow-up	Original: Predicted	Adjustment 2: Predicted
Failure Load (N)	3031	2731	2704
Average Density (g/cm³)	0.3196	0.2963	0.3085
Density distribution (g/cm³)	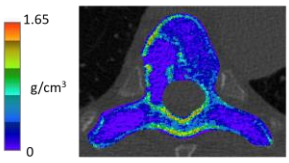	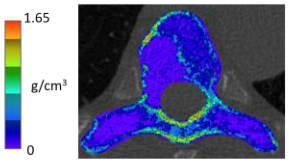	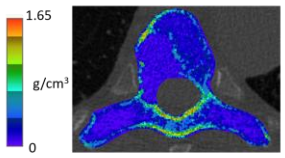
EPEL3 distribution@1.9% strain (mm/mm)	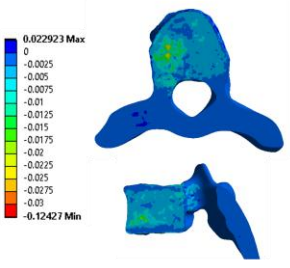	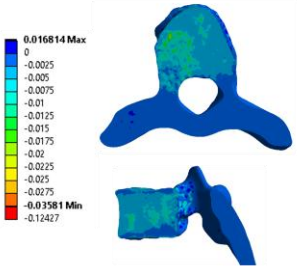	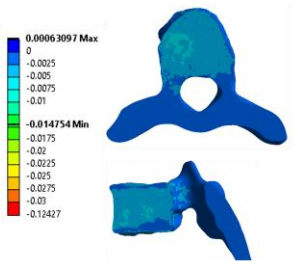

Figure 9.6 – Two example patients A and B, detailing the failure load, average density, the density distribution and the compressive strain distribution at follow-up, the original models prediction and the new adjustment 2 prediction.

Figure 9.6 shows the distribution of density and compressive strain at Follow-up, Original Predicted and Improvement 2 Predicted in two example patients vertebra with a large lesion. In the first example patient (A), the density distribution is very similar between Original Predicted and Improvement 2 Predicted, however the average density was slightly lower in the improvement than originally prredicted (Original model predicted density: 0.3618 g/cm³, Adjustment 2 predicted density: 0.3289 g/cm³). The compressive strain distribution also looks very similar to the original prediction. Nevertheless, the failure load was predicted closer to the Follow-up with the adjustment compared to the original models

prediction (Follow-up FL: 2233 N, Original model predicted FL: 2695 N, Adjustment 2 predicted FL: 2511 N). For the second example patient (Figure 8.6 B), the density distribution around the lesion has not been captured with the models original prediction or the adjustments prediction. In addition, within the lesion region, the density is higher with adjustment 2's prediction compared to the follow-up scan which decreased the compressive strains within that region.

9.1.2.3 Improvement 3: Preventing remodelling in lytic tissue

As mentioned previously, within the lesion region there are thought to be no bone cells and therefore, no remodelling can occur. Adjustment 2 was not substantial enough to improve the prediction of the vertebra with lytic lesions. Therefore, adjustment 3 ensured that any lytic tissue could not remodel unless it was adjacent to bone tissue.

Method

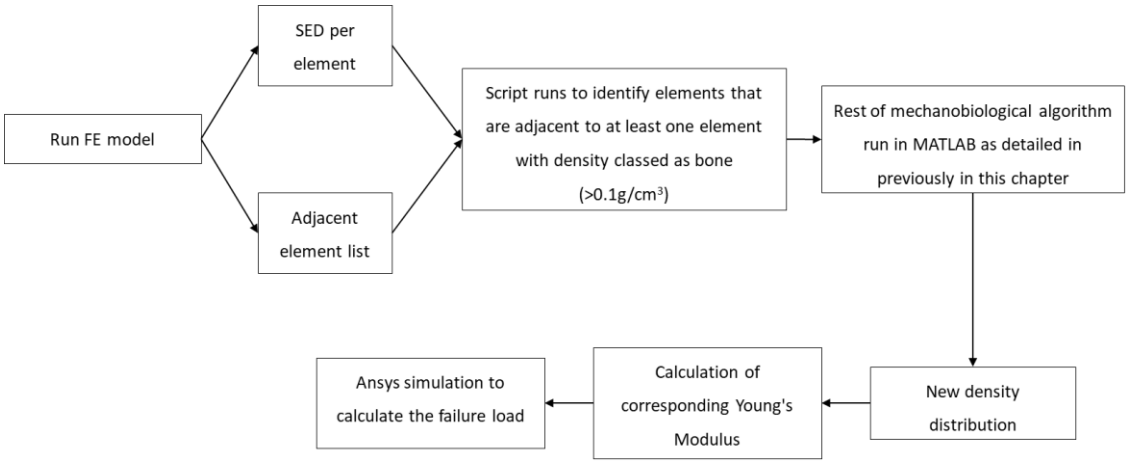

Figure 9.7 – Flow chart of method for adjustment 3

For this adjustment, all vertebra with lytic lesions were modelled (n=11). To model the lesion separately from the bone, adjacent elements were exported from Ansys and imported into the MatLab code for the mechanobiological algorithm. The algorithm then analysed for each element whether it was surrounded by at least one other element with density >0.1g/cm^3 and if it was, that element could remodel. If the element could remodel, the rest of the mechanobiological algorithm was applied, otherwise it was left as the density at the baseline scan. The rest of the algorithm was run to predict the material properties, which were then imported into the 3D model where the failure load was predicted.

Results

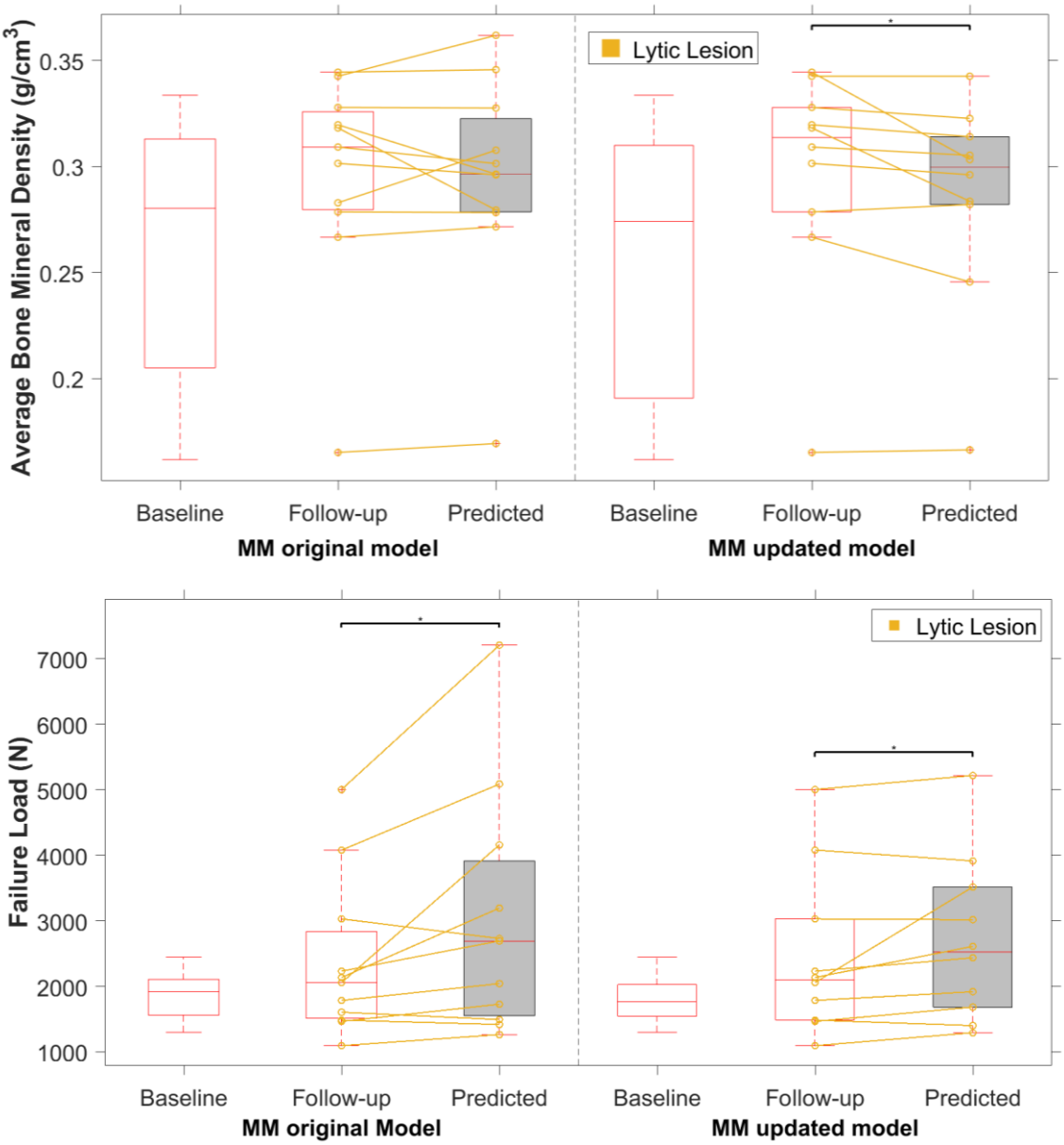

Figure 9.8 – Box plot of the third adjustment for the average bone mineral density (top) and the failure load (bottom), comparing the original models prediction (left) and the new adjustments prediction (right).

The average bone mineral density prediction is now significantly different to the follow-up (Figure 9.8, $p<0.05$). However, the most important result was the failure load as this represents the mechanical integrity of the vertebra and gives insights into the fracture risk. For this improvement, the failure load prediction is still significantly different ($p < 0.05$), however, the average prediction improved compared to the original prediction (average

original difference between follow-up and predicted: 24.31%, average new difference between follow-up and predicted: 13.32%), with only two patients' predictions minorly worsening (original percentage difference: 14.3%, new percentage difference: 16.53% and original percentage difference: 4.58%, new percentage difference: 5.81%).

Figure 9.9 the density and compressive strain distributions in two example patients (A and B). For the first example patient, the density distribution is similar for both predictive models except the lesion region which is better predicted by the improvement. This can be seen as

A

	Follow-up	Original: Predicted	Adjustment 3: Predicted
Failure Load (N)	2233	2695	2437
Average Density (g/cm³)	0.3425	0.3618	0.3425
Density distribution (g/cm³)	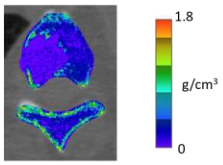	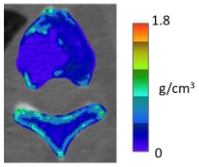	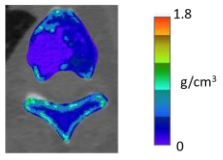
EPEL3 distribution @1.9% strain (mm/mm)	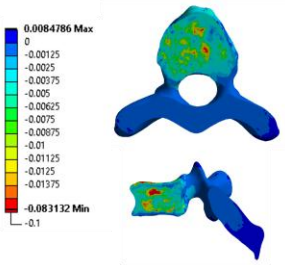	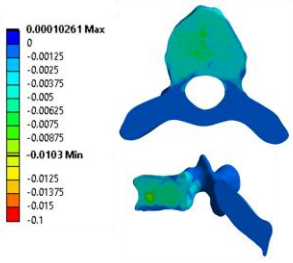	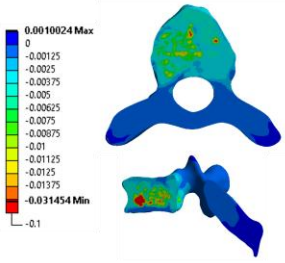

B

	Follow-up	Original: Predicted	Improvement 3: Predicted
Failure Load (N)	3031	2731	3018
Average Density (g/cm³)	0.3196	0.2963	0.314
Density distribution (g/cm³)	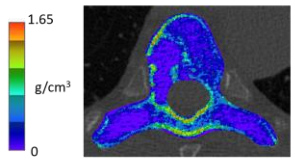	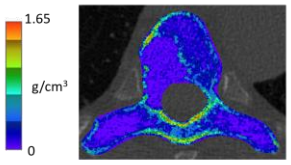	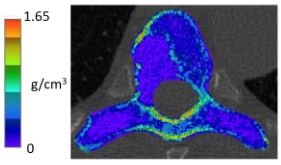
EPEL3 distribution@1.9% strain (mm/mm)	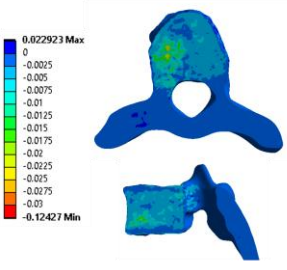	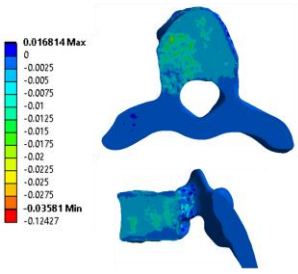	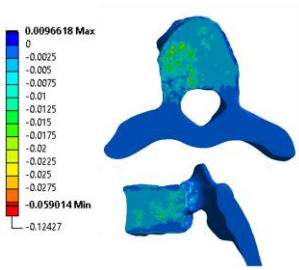

Figure 9.9 – Two example patients A and B, detailing the failure load, average density, the density distribution and the compressive strain distribution at follow-up, the original models prediction and the new adjustment 3 prediction.

the lesion region is a lower density (lighter purple). The distribution of compressive strain represents this lower density as there are higher strains within the lesion region in the improvement prediction. This compressive strain distribution also more closely follows the distribution at Follow-up. This improvement of compressive strain distribution follows through to the predicted mechanical properties where the prediction of FL is closer to Follow-up (Follow-up FL: 2233 N, Original predicted FL: 2695 N, Improvement 3 predicted FL: 2437 N).

In conclusion, this section has explored several adjustments to the original mechanobiological model to improve the prediction of failure load. While initial linear scaling of predicted density and the removal of bone cells within the lesion proved ineffective, preventing any remodelling within the central region of the lesion demonstrated a positive impact on predictive accuracy. This adjustment suggested the assumption that bone remodelling does not occur in the central region of the lesion was correct, and that this absence of remodelling plays a crucial role in capturing the mechanical behaviour and ultimate failure of the bone.

9.2 Appendix 2

Table 9.1 - Multiple Linear Regression equation coefficients for k_1 at one month after baseline for all five patients. Average coefficients used to calculate the final predictions of k_1 for each patient based on the patient's CTX, P1NP and Sclerostin levels.

Coefficient	P1 out	P2 out	P3 out	P4 out	P5 out	Average
Intercept	0.0058	0.0053	0.0051	0.0052	0.005534	0.005387
CTX	0.0008211	0.0008140	-0.0007509	-0.0001039	0.001317	0.0004194
P1NP	0.0000194	0.0000177	0.0000203	0.0000254	0.0000153	0.0000196
Sclerostin	-0.0001612	-0.0001407	-0.0001283	-0.0001485	-0.0001491	-0.0001456

Table 9.2 - Multiple Linear Regression equation coefficients for k_1 at one month after baseline for all five patients. Average coefficients used to calculate the final predictions of k_1 for each patient based on the patient's CTX, P1NP and Sclerostin levels.

Coefficient	P1 out	P2 out	P3 out	P4 out	P5 out	Average
Intercept	3.064E-05	3.322E-05	3.436E-05	3.411E-05	3.211E-05	3.289E-05
CTX	8.444E-06	8.482E-06	1.708E-05	1.353E-05	5.719E-06	1.065E-05
P1NP	7.009E-08	7.931E-08	6.500E-08	3.720E-08	9.230E-08	6.878E-08

Sclerostin	8.859E-07	9.983E-07	1.067E-06	9.558E-07	-9.522E-07	9.717E-07

Table 9.3 - Baseline, follow-up and Predicted BMD for all five patients with percentage differences between follow-up and the original prediction and the follow-up and the BTM incorporated prediction.

	Baseline (g/cm^3)	Follow-up (g/cm^3)	Predicted – Original model (g/cm^3)	Difference between follow-up and predicted original (%)	Predicted - BTM incorporate (g/cm^3)	Difference between follow-up and predicted BTM incorporate (%)
BRATS001	0.2251	0.2245	0.2318	3.19	0.2401	6.72
BRATS005	0.2363	0.2051	0.1988	3.12	0.1955	4.79
BRATS006	0.2999	0.3583	0.3613	0.83	0.4176	15.29
BRATS009	0.2451	0.2441	0.2422	0.78	0.2449	0.33
BRATS011	0.3336	0.3538	0.3451	2.49	0.3036	15.27

Table 9.4 - Baseline, follow-up and Predicted BMD for all five patients with percentage differences between follow-up and the original prediction and the follow-up and the BTM incorporated prediction.

	Baseline (N)	Follow-up (N)	Predicted – Original model (N)	Difference between follow-up and predicted original (%)	Predicted – BTM incorporated (N)	Difference between follow-up and predicted BTM incorporated (%)
BRATS001	965.77	1153.5	1346.3	15.43	1367.1	16.95
BRATS005	2617.6	1724.6	1773.7	2.81	1690.2	2.01
BRATS006	2350.8	3856.6	4645.3	18.55	6092.6	44.95
BRATS009	3884.6	4023.3	3984	0.98	4118.7	2.34
BRATS011	2914	3601.9	3430.7	4.87	2464.2	37.51

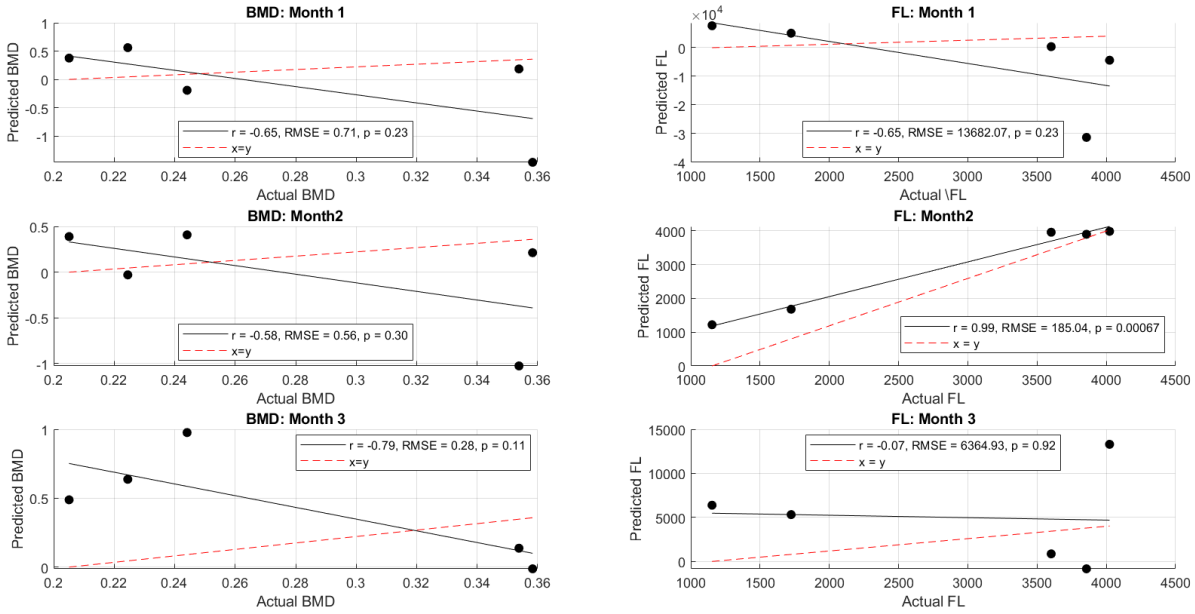

Figure 9.10 - Results of the linear regression, predicting BMD and failure load at 1, 2 and 3 months after baseline using the equation derived from the LOOCV multiple linear regression analysis. 'Actual' is the parameter calculated from the optimisation of the original model and 'Predicted' is the predicted parameter using the BTM data.

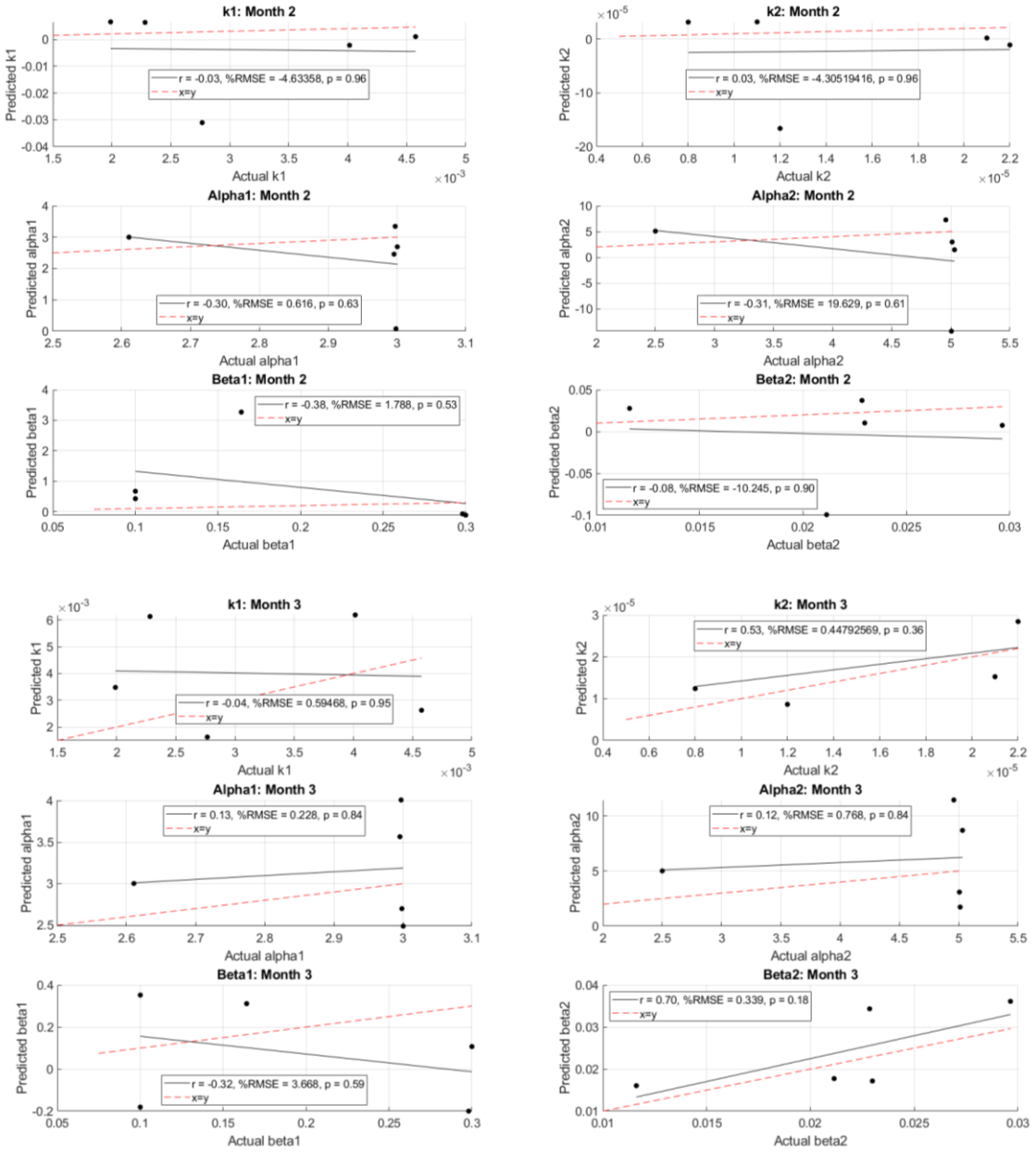

Figure 9.11 – Results of the linear regression, predicting parameters k1, k2, α_1, α_2, β_1, β_2 at 2 and 3 months after baseline using the equation derived from the LOOCV multiple linear regression analysis. 'Actual' is the parameter calculated from the optimisation of the original model and 'Predicted' is the predicted parameter using the BTM data.